Behaviour of ferrocement columns under static and cyclic loading

A thesis submitted to The University of Manchester for the degree of
Doctor of Philosophy
in the Faculty of Engineering and Physical Sciences

2013

Jianqi Wang
BEng, MSc

SCHOOL OF MECHANICAL, AEROSPACE AND CIVIL ENGINEERING

DECLARATION

No portion of the work referred to in this dissertation has been submitted, in support of an application, for another degree or qualification of this or any other university or institution of learning.

Jianqi Wang

ACKNOWLEDGEMENTS

I would like to thank Parthasarathi Mandal and Paul Nedwell for their excellent supervision, valuable guidance, constructive discussions and encouragement throughout the period my research at Manchester.

I would also like to thank John Mason, David Mortimer, Shichuan Tian, Lu Chen and Chao Han for their generous help with the experiment tests in this dissertation study.

Finally, I would like to thank my family for their moral support and their encouragement throughout my studies.

COPYRIGHT STATEMENT

ABSTRACT

This thesis presents the results of an experimental, numerical and analytical study to develop a design method for ferrocement columns and reinforced concrete columns strengthened using ferrocement jackets. Two groups tests were conducted, comprising five static loading tests and three cyclic load tests. The static tests had one reinforced concrete column, two ferrocement columns and two strengthened reinforced concrete columns. The cyclic loading tests were conducted on one reinforced concrete column and two ferrocement columns. For both sets of tests, the loading applications included two steps, first axial load and then lateral load.

The experimental data were used for validation of the finite element models that were developed using the ABAQUS software package. The validated models were used as part of a comprehensive parametric study to investigate the effects of a number of design parameters including the effects of material strength, reinforcement geometry and arrangement, and the influence of the axial load.

The main conclusions from the experiments and the parametric studies were that the number of layers of mesh in the ferrocement has a significant effect on the peak lateral load capacity of a column and ferrocement can be used as a strengthening or retrofitting material. Based on the results from the experimental and numerical studies, it was observed that the existing design methods significantly underestimate the peak lateral load capacity.

It is found that the ACI design guideline for ferrocement columns is conservative because the transverse wires in the ferro-mesh provide confinement. The ferro-mesh transverse direction has very fine wire as confinement. Therefore, ferrocement has a high potential for use as a repair/strengthening material. The detailed parametric study data was condensed into a dimensionless interaction diagrams that can be used for the design of new ferrocement columns as well as strengthening of reinforced concrete columns using ferrocement jackets.

CONTENT

List of Figures

List of Tables

List of Notations

A	Amplitude
A_c	Gross cross sectional area of the matrix section
A_{cy}	Cross sectional area of the cylinder
A_{mesh}	Total surface area of reinforcement mesh
A_r	Effective area of reinforcement
A_s	Cross section area of tension steel
A_{sc}	Cross section area of compression steel
b	Width of concrete section
c	Distance from top surface to neutral axis (N.A)
C_m	Compression force for matrix
C_s	Compression force for reinforcement
d	Distance from top surface to tension steel
d'	Distance from top surface to compression steel
d_c	Compressive damage variable
$d_{peak\ load}$	The peak load of the specimen under static loading
d_{si}	Distance from extreme compression to each layer of mesh
d_t	Tensile damage variable
D	Diameter of cylinder
E	Young's Modulus
E_{cm}	Young's modulus of concrete, $22\ (0.1\ f_{cm})^{0.3}$
E_s	Young's modulus of reinforcement
E_0	Initial elastic stiffness
f'_c	Specified compressive strength of concrete
f_{cm}	Compressive strength
f_{com}	Overall column strength from concrete and matrix properties, $f_{com} = \eta f_c + (1-\eta) f_m$
f_{ctm}	Tensile stress of concrete
f_y	Reinforcement yield stress
F	Force

F_1, F_2	Assumed forces balancing the lateral forces: F_1 position at the edge of the concrete, F_2 position at 200 mm from the edge
F_c	Maximum load at failure
F_{cc}	Force of compression concrete
F_{sc}	Force of compression steel bar
F_{st}	Force of tension steel bar
F_t	Maximum loading at failure
G	The potential plastic flow
h	Height of concrete section
I	Second moment of area
k_1, k_2	The stiffness of F_1 and F_2
k_θ	Rotation stiffness
K	The ratio of the second stress invariant on the tensile meridian, $q\ (TM)$, to the compressive meridian, $q\ (CM)$, adapted for different evolutions of strength under tension and compression
L	Length from point O to actuator load position
L_{cy}	Length of cylinder
m_1, m_2	The distances from point F_1 and F_2 to point O. Point O has zero displacement when lateral load applied
M	Bending moment
n	Approximate function of compressive strength of matrix, $n = 0.4 \times 10^{-3} \times 150\ f_{cm} + 1.0$
n_1, n_2	The displacements at the edges
P	Axial load
P_{bal}	Axial load at balance
P_0	Pure load of column
p	The effective hydrostatic stress
q	The Von Mises equivalent effective stress
S_r	Specific surface
S_{rl}	Specific surface in longitudinal direction
S_{rt}	Specific surface in transverse direction
T_s	Tensile force of reinforcement

V	Lateral load
$V_{composite}$	The volume of composite
V_{max}	The ultimate lateral loading
V_{mesh}	Total volume of reinforcement mesh
V_r	Volume fraction
V_{rl}	Volume fraction in longitudinal direction
V_{rt}	Volume fraction in transverse direction
α	Depth of equivalent rectangular stress block
β_1	Factor relating depth of equivalent rectangular compressive stress block to neutral axis (N.A) depth
Δ_A	Cantilever deformation one the underside of point Li-A
Δ_p	Displacement of the column at peak load
Δ_u	Displacement of the column in the descending branch corresponding to 0.85 of the maximum load
Δ_{yI}	Effective yielding displacement
ε_c	Compression strain of concrete
ε_{cr}	Strain at cracking, f_{ctm}/E_0
ε_c^{el}	Elastic compression strain
ε_{c1}	Compressive strain at peak stress, $0.0007\ f_{cm}^{0.31} < 0.0028$
ε_{cu}	Ultimate strain of concrete
ε_{cu1}	Ultimate strain, 0.0035 for $f_{cm} < 58\ MPa$
ε_s	Strain of tension steel bar
ε_{sc}	Strain of compression steel bar
ε_t	The lateral strain at yield stress
ε_t^{el}	Elastic tensile strain
$\tilde{\varepsilon}_c^{in}$	Inelastic compressive strain of concrete
$\tilde{\varepsilon}_c^{pl}$	Plastic compressive strain
$\tilde{\varepsilon}_t^{ck}$	Cracking strain of concrete
$\tilde{\varepsilon}_t^{pl}$	Plastic tensile strain
ε_{tc}	Tensile strain of concrete
ε_y	The strain at yield stress
ε_{yc}	Strain of steel at yield

ε_{0c}^{el}	Elastic compressive strain of concrete at yield, σ_c/E_0
ε_{0t}^{el}	Elastic tensile strain of concrete at yield, σ_t/E_0
ϵ	Eccentricity, defined as the rate of plastic potential function approaches at the asymptote line. The default is $\epsilon = 0.1$
η	Global factor of reinforcement mesh in the loading direction (Chapter 2); Ratio of compression strain with strain at peak load, $\varepsilon_c/\varepsilon_{c1}$ (Chapter 5)
η_l	Global factor of reinforcement mesh in longitudinal direction
η_t	Global factor of reinforcement mesh in transverse direction
η_θ	Global factor of reinforcement mesh in other angle directions
η'	Ratio of concrete to overall section
θ	Rotation in radian
μ	Viscosity parameter
μ_Δ	Deformation ductility
σ_c	Compression stress
σ_{c0}	Compression yield stress
σ_{cu}	Ultimate compression stress
σ_t	Tensile stress
σ_{t0}	Tensile failure stress
σ_y	The yield stress = 0.4 f_{cm}
υ	Poisson's ratio
ψ	Dilation angle, in the p–q plane at high confining pressure
$\sum C_{si}$	Total force of welded mesh under compression
$\sum T_{si}$	Total force of welded mesh under tension

CHAPTER 1 Introduction

1.1 Background

Ferrocement is one of the earliest versions of reinforced concrete, however, it's design has been mostly empirical and formal design guides have not been developed as they have been for more traditional reinforced concrete.

ACI 318 (ACI, 2008) and EC2 (CEN, 2004a) give detailed design guidelines for reinforced concrete structure, however ferrocement is not specifically covered, and the design guidelines for ferrocement produced by ACI Committee 549 (ACI 549) lacks detail in its' use as a repair and strengthening material. As a tool to aid research, finite element analysis has been used with reinforced concrete for a number of decades; however, its specific use with ferrocement has been extremely limited.

In the earthquake-resistant design of structures, overstrength and ductility are key factors that influence safety. Ductility of the whole structure depends on the ductility of each individual member, for example: beams, columns, or floors. It also depends on the configuration of the structure. The appearance of cracks is quite common in structures that survive an earthquake. Some cracks may be cosmetic in nature and do not need any special attention. Nevertheless, often they show sufficient damage to require retrofit strengthening. Repairing and retrofitting concrete structures has become quite common in the construction industry due to the financial benefits, whether in terms of direct or in-direct costs, compared to the alternative of demolition and total or partial re-construction. Various materials have been used for repair and strengthening, for example steel bar and plate, fibre reinforced polymers (FRP) and ferrocement. For this study, the author used ferrocement column and strengthen reinforced concrete using ferrocement jacket columns subjected to static and cyclic loading. The performance of the strengthened columns was compared with equivalent unaltered reinforced concrete and ferrocement columns.

According to the ACI Committee 549 (ACI, 1988), ferrocement is a type of thin wall reinforced concrete commonly constructed of hydraulic cement mortar reinforced with closely spaced layers of continual and relatively small size wire mesh. This study investigates the use of ferrocement for retrofitting existing reinforced concrete structures as well as its use as a construction material for new structures in seismically active zones.

Ferrocement has been used as a strengthening and repairing material, especially for speedy repairs and strengthening measures for civil engineering structures worldwide (ACI, 1997a, Nedwell et al., 1994, FS, 2013). Reinforced concrete columns can be easily and effectively strengthened using ferrocement jacket. The advantages of using ferrocement wrapping are its adaptability, high strength to weight ratio, superior cracking characteristics, good bond with existing concrete surface, improved ductility and impact resistance when compared to conventional strengthening materials such as steel plates. Ferrocement behaves as a homogeneous elastic material over a wide limit because the uniformly distributed mesh reinforcement results in a better crack-resisting mechanism.

For the experimental work described in this thesis, two types of loading were applied to the specimens, namely static and cyclic. Five columns were tested under static loading and three had cyclic loading applied.

As mentioned earlier, the ductility of a whole structure depends on the ductility of its individual elements. For notionally one-dimensional elements, like beams and columns, curvature ductility is a good measure of the energy absorption capacity. In general, the curvature ductility of reinforced concrete sections can be increased by designing them to be under-reinforced, so that their rotational capacity stems from the yielding of the steel prior to fracture. To extract this ductility, concrete in the compression zones needs to remain intact. An effective way to achieve this is by increasing the confining pressure by using stirrups or concrete-filled tubes. Likewise, for ferrocement a number of material and geometric parameters may affect ductility.

1.2 Aims and objectives

The aim of this research project is to improve the knowledge and understanding of the behaviour of ferrocement short columns under combination loading and from this produce non-dimensional charts that can be used for design. The objective are:

1. A literature reviewer will be conducted to understand the current state of knowledge and to investigate whether information from similar applications is suitable for adaptation to the use with ferrocement.

2. A number of experimental tests will be designed and conducted to provide information for, and validation of, the finite element model with respect to static loading and to cyclic loading.

3. Finite element model will be proposed to investigate the test specimens and to perform parametric studies with regard to the main properties of both the base columns and the ferrocement strengthening.

4. Non-dimensional charts will be presented based on the above study to the ACI Committee 549 for potential inclusion into the Design Guide for Ferrocement.

1.3 Organization of the thesis

This thesis is divided into the following eight chapters:

Chapter 1 Introduction: This chapter gives a general introduction including the research background and the scope and outline of the thesis.

Chapter 2 Ferrocement: material behaviour and applications: This chapter presents a brief literature review including: the development of ferrocement, a description of the ferrocement constituents and their mechanical behaviour, basic mechanical behaviour of ferrocement, columns under combination of axial load and bending, strengthened reinforced concrete using ferrocement jacket, and use of FEA in ferrocement modelling.

Chapter 3 Experimental tests: This chapter presents the experiments in detail including material property tests of the matrix and reinforcement, fabrication of the ferrocement column specimens, design and construction of the equipment and test details.

Chapter 4 Experimental results: This chapter presents the results of columns tests, which include static loading and cyclic loading.

Chapter 5 Finite element modelling: This chapter present the details of the finite element modelling. The commercial package ABAQUS, was used to establish and validate finite element models against the experimental results.

Chapter 6 Parametric studies: This chapter presents a parametric study using FEA to investigate the behaviour under static loading for variation in geometric arrangements and material properties.

Chapter 7 Design guidelines: This chapter presents design guidelines for ferro-cement and reinforced concrete columns strengthened using ferrocement jackets.

Chapter 8 Conclusions and recommendations for future studies: This chapter summarizes the main conclusions from the work undertaken for this thesis and gives recommendations for future research.

CHAPTER 2 Ferrocement: material behaviour and applications

2.1 Ferrocement: definition and history

Ferrocement is defined by the American Concrete Institute (ACI) Committee 549R-97 in their "State of the Art Report" (ACI, 1997b) as:

> "Ferrocement is a type of thin wall reinforced concrete commonly constructed of hydraulic cement matrix reinforced with closed spaced layers of continuous and relatively small size wire mesh. The mesh may be made of metallic or other suitable material. The fineness of the matrix and its composition should be compatible with the opening and tightness of the reinforcing system it is meant to encapsulate."

The two fundamental constituents of ferrocement are the matrix and the reinforcing mesh. The requirements for using factored loads and load combinations are stipulated in Eurocode 2 (CEN, 2004a) or ACI 318 (ACI, 2008).

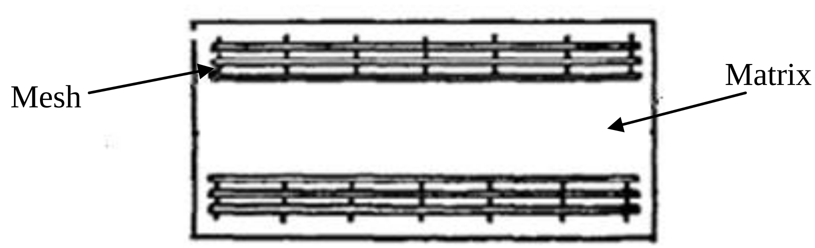

Figure 2-1: Typical meshes used in ferrocement application

There are many similarities between ferrocement and reinforced concrete; and these are summarized as follows:

1. Both ferrocement and reinforced concrete obey the same principles of mechanics and can be analysed using the same theories.
2. Both can be analysed using similar techniques, experimental tests or numerical simulations.
3. Both can be designed adopting the same philosophy; such as limit state design to satisfy both the ultimate and serviceability limit states.

However, the differences between ferrocement and reinforced concrete are also important. The main differences are:

1. Compared with reinforced concrete, ferrocement is homogenous and isotropic in two directions.
2. Ferrocement has good tensile strength and a high specific surface of reinforcement, maybe two orders of magnitude greater than that of reinforced concrete.
3. Due to the two-dimensional reinforcement of the mesh system, ferrocement has: (i) much better extensibility; (ii) smaller crack widths, (iii) higher durability under environmental exposure; and (iv) better impact and punching shear strength.

Ferrocement was first officially proposed in 1847 by Joseph Louis Lambot in France (ACI, 1997b). It was utilised in the construction of a rowboat using woven wires and matrix. In 1852, a patent was submitted in the name of “Ferrocement” which literally means “Iron Cement”.

In the early 1940s, an Italian architect, Pier Luigi Nervi (Nervi et al., 1956), resurrected the original ferrocement for the following reason:

> “The fundamental idea behind the new reinforced concrete material ferrocement is the well known and elementary fact that concrete can stand large strains, in the neighbourhood of the reinforcement and that

the magnitude of the strains depends on the distribution and subdivision of the reinforced through the mass of the concrete."

Professor Nervi established the preliminary characteristics of ferrocement through a series of tests. Nervi claimed successful use of ferrocement in roofs of buildings and warehouses in addition to its use in boat building. After the Second War, Nervi proceeded, following a series of tests, to design and construct several roofs, which remain models of the rational and aesthetic use of ferrocement in structural design. Also, Nervi built a 165 ton motor sail-boat "Irene", with a ferrocement hull with a thickness of 36 mm (Walkus and Kowalski, 1971).

In the 1960s, ferrocement began to be used in various countries such as the United Kingdom, China, India, Australia and New Zealand (ACI, 1988).

After 1972, several academic committees were set up to study the behaviour and development of ferrocement:

- 1972, an Ad Hoc Panel was set up by the USA National Academy of Science.
- 1974, Committee 549 was established by the American Concrete Institute (ACI).
- 1976, an International Ferrocement Information Centre (IFIC) was established at the Asian Institute of Technology, Bangkok, Thailand and in cooperation with the New Zealand Ferrocement Marine Association (NZFCMA) they published a quarterly journal called, "The Journal of Ferrocement". Unfortunately, the journal was terminated in 2006. In addition, from 1981 until 2012, ten international symposia were held in various parts of world, Cuba was taken the latest symposia, called FERRO10.
- 1991, the International Ferrocement Society (IFS) was formed to promote the use of ferrocement. In 2001, the Ferrocement Model Code

was introduced. The code provides a document that enables civil engineers to study and model their ferrocement designs.

- 2011, the Ferrocement Society (FS) was establish in India.

The ferrocement group ACI 549 (ACI, 1988) is still the most effective international committee, and published a design guide for ferrocement in 1989. This guide is still the most important reference design and is widely used by most designers.

In 2000, Professor Antoine Naaman of the University of Michigan produced the first (and to date the only) text book “Ferrocement and Laminated Cementitious Composites” (Naaman, 2000).

2.2 Application of ferrocement

Ferrocement is a highly versatile construction material that has a potentially wide range of practical applications. Ferrocement can be used to manufacture different shapes of structures around the world. In developing countries, ferrocement has been used for housing, sanitation, agriculture, fisheries, water resource projects (e.g. water transportation vessels) and to repair or strengthen old structures.

In addition, applications of ferrocement were used for boats, water tanks, shell structure, roof, retrofitting balcony and extension room. Six applications are shown in Figure 2-2.

Recently, many structures have been built using ferrocement. Morage (2012) worked on building a one-storey house using precast ferrocement elements in Haiti. In India, the Indian Ferrocement Society is blossoming and they have just held a ferrocement conference, on topics such as water tanks and ferrocement houses. In Cuba, a number of swimming pools have been constructed using ferrocement and some simple houses (Rivas and Hernandez, 2013).

(a): Ferrocement boat (b): Water tank

(c): Shell structure (d): Ferrocement roof

(e): New balcony (f): Extension room

Figure 2-2 Examples of ferrocement applications, (a): (BSS, 2011), (b): (Cambodia, 2010), (c): (Nedwell, 2009), (d): (Ferrocement.com, 2009), (e): (jadferrocements.net, 2010), (f): (jadferrocements.net, 2010)

Durability and maintenance are of great concern in civil engineering structures. To increase the durability of structures, ferrocement is a better option than reinforced concrete and masonry in some circumstances. Reinforced concrete or masonry walls often exhibit distress due to damaged or need retrofitting before the end of their design life following events such as earthquakes or fires. Examples of retrofitted structures using ferrocement are presented in a later section.

2.3 Constituent materials

The main components of ferrocement are the matrix and the reinforcing mesh. They are described as follows:

2.3.1 Matrix

The matrix is a mixture of cement, well-graded sand, water, and possibly some admixtures such as silica fume and superplasticizer. Similar to concrete, the matrix should have adequate workability, low permeability, and high compressive strength. The water-cement ratio, sand-cement ratio, quality of water, type of cement and curing conditions in addition to the casting and compaction can influence the mechanical properties of the matrix (Paul and Pama, 1978).

2.3.1.1 **Cement**

Ordinary Portland Cement (OPC) is commonly used. It should be kept fresh, be of uniform consistency and free of lumps and foreign matter. Moreover, it should be stored in dry conditions for as short duration as possible.

2.3.1.2 **Aggregates**

Normal-weight fine aggregate is commonly used in the matrix. Aggregates having high hardness, large strength and containing sharp silica can achieve the best strength results. However, the aggregate should be kept clean, inert, free of organic matter and deleterious substances and free of silt or clay. Additionally, EN 12350:2009 (BSI, 2009) requires that 80%-100% of the weight of the aggregate should pass the BS Sieve No.7 (2.36 mm).

2.3.1.3 **Water**

The water used in ferrocement should be fresh, clean and free from organic or harmful solutions. Unclean water may interfere with the setting of cement and will influence the strength or lead to staining on surfaces.

2.3.1.4 **Admixtures**

An admixture is defined as a material other than water, aggregate or hydraulic cement which might be introduced into a batch of ferrocement or matrix, during or immediately before its making (Dodson, 1990). It is used in a matrix to provide up to four benefits, which are reduced water requirement, increased strength, improvement in impermeability and better durability. The two main categories of admixtures are Chemical and Mineral admixtures.

Chemical admixtures are added in small quantities during the mixing process to modify the properties of the mixture, such as Superplasticizer and Chromium Trioxide (CrO_3). The Superplasticizer admixtures are known as high-range water reducing agents, which give as considerable increase in workability of the matrix and concrete for a constant water-cement ratio (Paillère, 1995). Chromium Trioxide (CrO_3) is known to reduce the reaction between the matrix and galvanized reinforcement (ACI, 1997b), however for health and safety, CrO_3 was not longer used.

Mineral admixtures can reduce energy costs, save raw materials and improve concrete and matrix properties, such as porosity, strength, permeability and durability. Various mineral admixtures are now commonly used in cement and concrete production, such as Silica-fume and Fly ash. Silica-fume has a high content of amorphous silicon dioxide and consists of very fine spherical particles. It is collected by filtering the gases escaping from the furnaces (Detwiler and Mehta, 1989, Hooton, 1993) and is used to improve cement properties such as compressive strength, bond strength and abrasion resistance. Fly ash, or natural pozzolan as pulverized particles, is another admixture added for changing the property of the concrete and matrix.

2.3.2 The property of the matrix

To produce a workable matrix, the weight ratio of sand to cement varies from 1.4 to 2.5, and the ratio of the water to cement is between 0.30 and 0.55. In general, a workable mix can completely penetrate and surround the mesh reinforcement and have acceptable amounts of shrinkage and porosity. Water-reducing admixtures can be used to enhance mix plasticity, especially where admixtures such as superplasticizer are used. Furthermore, the slump of fresh matrix should not exceed 50 mm.

From literature, various different moduli have been given for the matrix, for example, the Young's Modulus given may vary from 5 GPa to over 20 GPa, even based on the same sand-cement and water-cement mixtures (Arif and Kaushik, 1999, Mansur and Ong, 1987). As the matrix property varies among these studies, separate experimental studies are carried out to characterise this behaviour for the current study.

2.3.3 Reinforcement mesh

The reinforcement should be clean and free from deleterious materials such as dust, rust, paint, oil or similar substances. A wire mesh with closely spaced wires is the most popular reinforcement used in ferrocement structures. Generally, common wire meshes have square or hexagonal openings.

Meshes with square openings are available in woven or welded form. Other types of reinforcement are also used for some special applications or for specific performance or economy, such as expanded metal mesh. Typical types of mesh are shown in Figure 2-3.

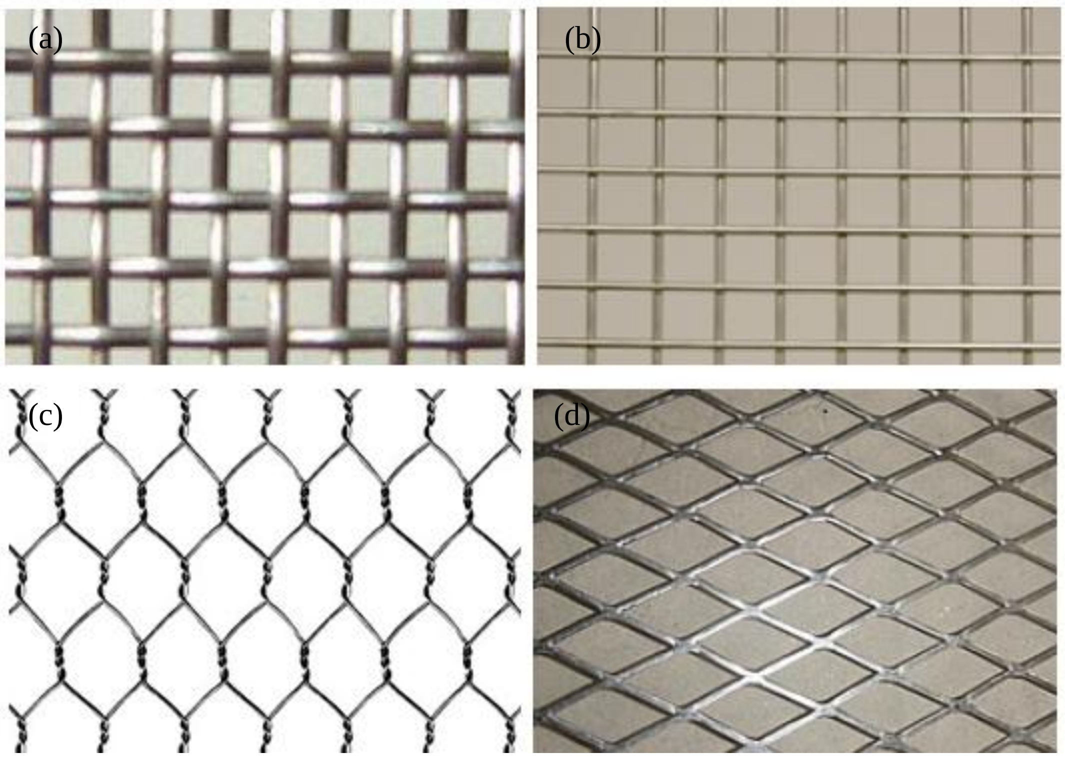

Figure 2-3: Typical types of mesh, (a): (Woven-mesh), (b): (Welded-mesh) (c): (Hexagonal-mesh) (d): (Expanded-mesh)

Woven mesh: As shown in Figure 2-3(a), woven mesh is made of longitudinal wires woven crossing transverse wires. There is no welding at the intersections. Based on the tightness of the weave, the thickness of woven mesh may be up to three wire diameters.

Welded wire mesh: Produced using longitudinal and transverse wires welded together at the intersections, as illustrated in Figure 2-3(b). It has a higher stiffness than woven mesh, which is why the welded mesh leads to smaller deflections in the elastic stage. Welded mesh is also more durable, more intrinsically resistant to corrosion and more stable in structures than woven mesh.

Hexagonal or chicken wire mesh: This mesh is a type of fencing mesh that has hexagonal holes (see Figure 2-3(c)). It has many different applications, such as animal fencing and fence netting. It is fabricated from cold drawn wire that is woven in hexagonal patterns. As no wires are continuous along any one direction, this type of mesh is more flexible than woven or welded mesh, and is generally easier to fabricate and use, especially for curved structures.

Expanded metal mesh: This is formed by slitting thin-gauge steel sheets and expanding them perpendicularly to the slits as shown in Figure 2-3d. This type of mesh offers approximately equal strength in the normal orientation but is much weaker in the direction in which the expansion took place. It can be used as an alternative to welded mesh, but it is difficult to use in construction involving sharp curves.

2.4 Reinforcement mesh parameters

The unique properties of ferrocement are derived from a relatively large amount of two-way reinforcement. The reinforcement is made up of small elements with a much higher surface area than conventional reinforcement. Therefore, the reinforcement has greater elasticity and cracking resistance together with narrow uniformly spaced cracks. The thickness of the covering matrix varies from 3 mm to 5 mm, which leads to thin sections. Based on the Ferrocement Model Code (IFS, 2001), volume fraction and specific surface are used to describe the amount of mesh.

Volume fraction is the volume ratio of the reinforcement to the volume of ferrocement, which is calculated by:

$$V_r = \frac{V_{mesh}}{V_{composite}} \times 100\% \qquad \text{Eq 2-1}$$

Where:

V_r	Volume fraction
V_{mesh}	Total volume of reinforcement mesh
$V_{composite}$	The volume of composite

The specific surface is the bonded surface area of reinforcement per unit volume of the ferrocement, which can be calculated as:

$$S_r = \frac{A_{mesh}}{V_{composite}} \qquad \text{Eq 2-2}$$

Where:

S_r	Specific surface
A_{mesh}	Total surface area of reinforcement mesh

Due to the geometry of the mesh layers, the volume fraction and specific surface in the longitudinal (V_{rl} and S_{rl}) and transverse (V_{rt} and S_{rt}) directions, are calculated separately in some cases.

It has been suggested that the total specific surface of meshes should be greater than or equal to 0.08 mm^2/mm^3 and that the total volume fraction should be greater than 1.8% (ACI, 1988).

It is worth mentioning that the effective area of reinforcement (A_r) is the area in one direction only. It can affect the strength of the ferrocement, especially under uniaxial tensile loading and bending.

$$A_r = \eta V_r A_c \qquad \text{Eq 2-3}$$

Where:

A_c	Gross cross sectional area of the matrix section
η	Global factor of reinforcement mesh in the loading direction

The value of η varies with the mesh orientations. The mesh orientations should be considered in the longitudinal direction (η_l), transverse direction (η_t), or any other angular directions (η_θ). Figure 2-4 shows the direction of reinforcement, and Table 2-1 shows the values of η in longitudinal, transverse and 45° direction for woven square mesh, welded square, hexagonal, expanded metal, and longitudinal bars.

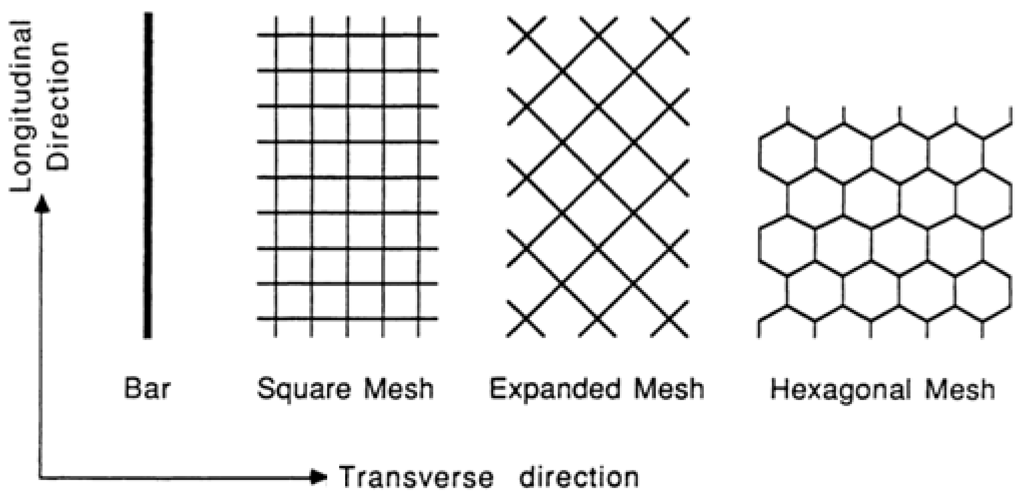

Figure 2-4: Proposed longitudinal and transverse directions of reinforcement mesh (ACI, 1988)

Table 2-1: Global efficiency factor (η) of reinforcement in uniaxial tension or bending (ACI, 1988)

Mesh type	Global efficiency factor (η)		
	Longitudinal (η_l)	Transverse (η_t)	At $\eta_\theta = 45°$
Woven square mesh	0.5	0.5	0.35
Welded square mesh	0.5	0.5	0.35
Hexagonal mesh	0.45	0.3	0.3
Expanded metal mesh	0.65	0.2	0.3
Longitudinal bars	1	0	0.7

2.5 Behaviour of ferrocement

The four major behaviour characteristics of ferrocement elements that should be considered are tension, compression, flexure and shear.

2.5.1 Behaviour under tension

Normally, tensile behaviour of ferrocement can be classified in three stages.

1. Elastic stage (OA in Figure 2-5): The matrix and reinforcement mesh are assumed to be acting as one with linear elasticity. This is similar to the behaviour of reinforced concrete. No cracking occurs in this stage.
2. Elastic-plastic stage (AB in Figure 2-5): Multiple cracks start to form and propagate. In this phase, that ferrocement differs from reinforced concrete as uniform fine cracks (less than 100 micron) form rather than the larger cracks found in reinforced concrete structure.
3. Plastic stage (after point B in Figure 2-5): This is the crack stabilisation and opening phase, and is when the ultimate load occurs.

One interesting part in the elastic-plastic stage is that the primary cracks occur randomly at critical sections when the tensile stress exceeds the matrix tensile strength. As the load rises, new cracks may occur in the matrix due to the tensile stress exceeding the matrix tensile strength. In order to transfer stress between cracks, more cracks will continue to occur at this stage until the stress in the matrix will not exceed the matrix tensile strength again and the number of cracks in the matrix stabilizes.

An advantage of ferrocement is that there is a substantial reserve strength and ductility after the occurrence of visible cracks. One can decide on appropriate repair and strengthening measures based on visual inspections.

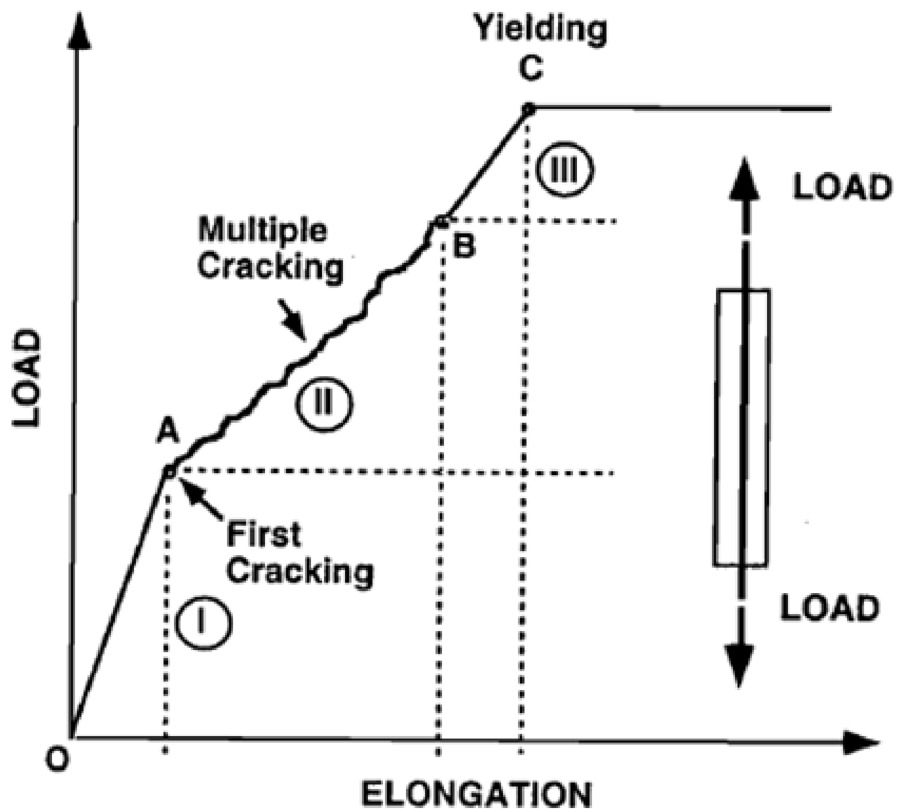

Figure 2-5: Ferrocement under tension (Naaman, 2000)

The peak tensile strength is controlled by the reinforcement characteristics, such as strength, volume fraction, and orientation of the wire. Some researches (Naaman and Shah, 1971, Huq and Pama, 1978, Arif and Kaushik, 1999) carried out several compression and tension experiments on different types of reinforcement meshes. They concluded that in direct tension tests the expanded metal is stronger and stiffer than welded mesh. Arif and Kaushik (1999) performed load-displacement experiments on welded mesh and woven mesh at 0, 15, 30, 45, 60, 75 and 90 degree orientations. The report shows that the ferrocement with 45° orientation mesh has the lowest loading resistance.

Ferrocement tensile failure can be categorized as ductile failure, which means the matrix is cracked long before failure and does not contribute to peak strength; so the load capacity in this case is independent of the thickness of the specimen. Khanzadi and Ramesht (1996) analysed the effect of cover and arrangement of reinforcement on the behaviour of ferrocement in tension. The analysis demonstrates that the load is not affected by the arrangement of reinforcement. The tensile strength of the matrix and thickness of the specimens have a major influence on the first crack strength, but not on the ultimate strength.

2.5.2 Behaviour under compression

Most of the research on the compression behaviour of ferrocement was conducted more than three decades ago. In compression, the load carrying capacity of the matrix strongly influences composite behaviour. Desayi and Joshi (1976) reported that the compressive strength of ferrocement is mainly depending on the matrix and it is possible to control and predict this behaviour within certain limits. A large increase of volume fraction cannot affect the compressive strength.

The orientation of the reinforcement has a relatively minor consequence on direct compressive effect (Nathan and Paramasivam, 1974). A ferrocement column, in which meshes are applied in layers in the same plane as the loading plane, when the longitudinal wire direction is along the loading direction the compressive strength may be higher than for other mesh orientations. It has been found that the strength may be increased by shaping mesh like a closed box and the transverse component of reinforcement has more influence than the longitudinal reinforcement (Johnston and Mattar, 1976).

Shannag and Mourad (2012) reported compression tests of matrix cylinders strengthened with a number of layers mesh, showing the axial load increases as the number of layer increases.

Sufficient ties across the mesh layers are critical for avoiding delaminating due to splitting transverse tensile stress and buckling of the mesh reinforcement in compression.

2.5.3 Behaviour under flexure

Ferrocement behaviour under flexure is combined behaviour in tension and compression, and is influenced by matrix strength, mesh type, mesh properties and mesh orientation. Figure 2-6 shows the flexural behaviour of ferrocement, which is similar to tensile behaviour. It can be categorised into three stages, the elastic stage, the elastic-plastic stage, and the plastic stage (ACI, 1997b).

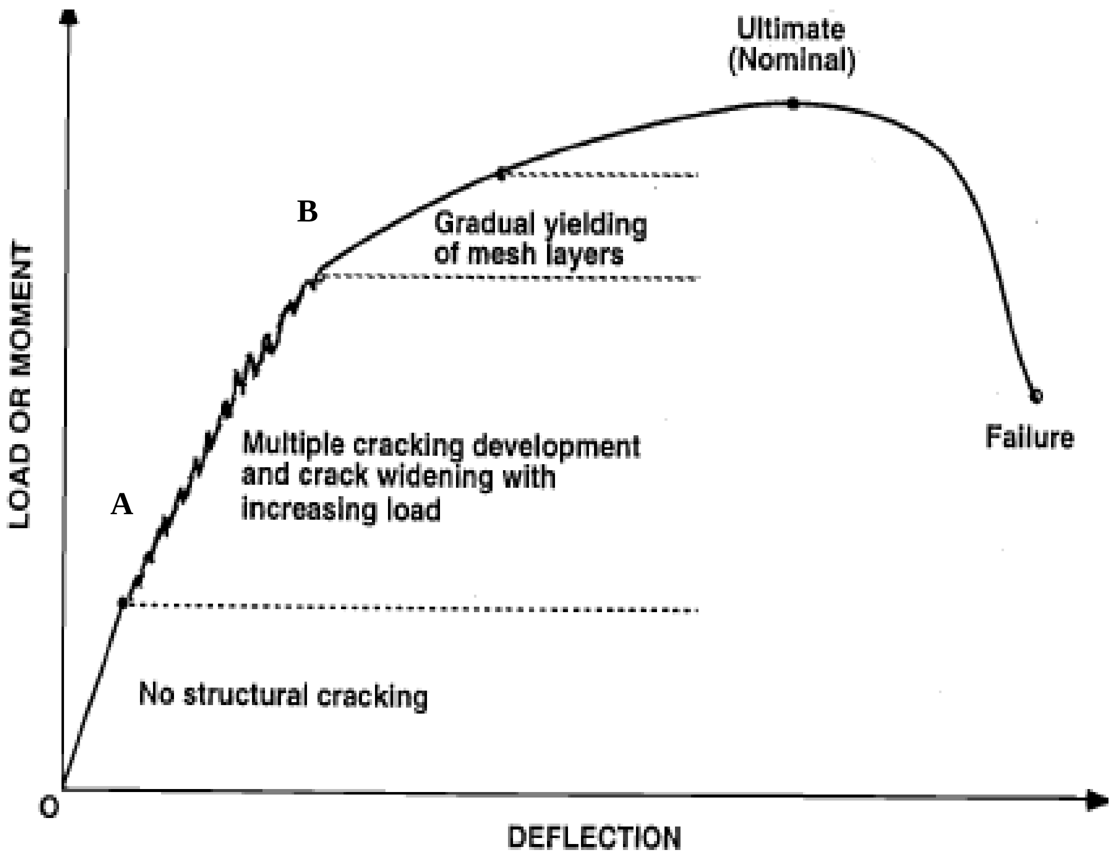

Figure 2-6: Typical load-deflection response of ferrocement (Naaman, 2000)

1) Elastic stage (OA in Figure 2-6): It is the initial portion without structural cracking.
2) Elastic-plastic stage (AB in Figure 2-6): It is also called a multiple cracking stage. This stage sees multiple cracking and crack widening with increasing load.
3) Plastic stage (After point B in Figure 2-6): The ferrocement starts to yield and the mesh layer gradually yields, thus achieving the peak load.

The specific surface has less contribution to flexure. This is because the outer most layers mainly control the flexural cracking.

According to Naaman (2000), the peak flexural strength was proved to be influenced by the volume fraction and the mesh type. It was found that by increasing the volume fraction the flexural resistance had a less than directly proportional increase. This is the result of the position of the neutral axis (N.A) changing. As the neutral axis (N.A) position moves upwards, more mesh is in the tension zone and the peak moment capacity increases. The outer layer has the most influence on the value of the first cracking load.

The orientation of meshes in ferrocement has a considerable effect on the maximum strength. ACI 549 (ACI, 1988) has reported the weakness of the ferrocement under flexure in different directions, therefore orientation is important. When the mesh wire direction is along the principal stress direction, the peak flexural strength may achieve a maximum value.

2.5.4 Behaviour under shear

Research on the behaviour and strength of ferrocement under shear is rather scarce. The lack of research in this area is probably due to ferrocement having been traditional used as thin panels where the shear span-to-depth ratio is large enough to preclude shearing distress. Mansur and Ong (1987) investigated the behaviour and strength of ferrocement in transverse shear by conducting flexure tests under two symmetrical point loads on simply supported rectangular beams (100 × 40 mm) with three different lengths. They reported that ferrocement beams were susceptible to shear failure at small shear span-to-depth ratios when the volume fraction of reinforcement and the strength of the matrix were relatively high.

Al-Kubaisy and Nedwell (1999) investigated the shear behaviour of rectangular ferrocement beams (100 × 40 mm). Their results were compared with the ACI code and empirical formulae were proposed. However, their formulae have not yet been approved by ACI Working Committee 549.

Recently, Tian (2013) studied the shear strength of ferrocement U and I shape of beams, with varying matrix properties and volume fractions. A formula for shear resistance changing with the shear span-to-depth ratio was proposed.

2.6 Ferrocement as repair or strengthening material

Repairing and strengthening of existing concrete structures has become more common during the last decade due to increasing knowledge and confidence in the use of advanced repairing materials, as well as the economical and environmental benefits of repairing or strengthening structures compared to demolition and rebuilding. The renaissance of ferrocement in recent decades has led to ACI 549 (ACI, 1988) design guidelines, with steel meshes being the primary reinforcement for ferrocement.

ACI Committee 546 (ACI, 1997a) have published some useful information on bridge deck repair (Guide for Repair of Concrete Bridge Superstructures). However, ferrocement structures are seldom exposed to the severe conditions encountered by bridge decks. Some research based on restoration of deteriorated concrete provides a basis for understanding many repair methods that are applicable to ferrocement.

Nedwell et al. (1994) investigated the repair of eight short square columns (155 × 155 × 1000 mm) using ferrocement jackets, with two U shape welded meshes jacketing the damaged column. Nedwell et al. (1994) found that the ferrocement retrofit coating on damaged columns increases the apparent stiffness of the column and significantly improves the ultimate loading capacity. Besides, in his investigation, the amount of steel surrounding the column increased both the stiffness and the ultimate stress.

Ahmed et al. (1994) studied the use of ferrocement as a retrofit material for masonry columns, the application of ferrocement coating on bare masonry columns enhances the compressive strength quite significantly, the ferrocement coating increasing the cracking resistance. The greater cover of ferrocement did not increase the load carrying capacity of brick masonry column appreciably.

Yaqub et al. (2013) investigated repaired fire damaged square and circular columns using ferrocement jacket, and reported that the ferrocement jackets increase both the strength and stiffness of post-heated reinforced concrete columns significantly.

2.7 Theoretical study of reinforced concrete under combined uniaxial bending and axial load

This literature review presents a theoretical plastic analysis study of reinforced concrete under combined bending and axial loading. For the combined forces, the interaction diagram shows the combination of applied moment and axial force that fall inside this curve, and therefore, suggest that it is safe against failure.

By using plastic analysis to determine the neutral axis (N.A) and moment at yield point and failure, the behaviour of reinforced concrete, ferrocement column and reinforced concrete column strengthened using a ferrocement jacket was investigated. The tensile strength of concrete is assumed to be zero, as shown in Figure 2-7.

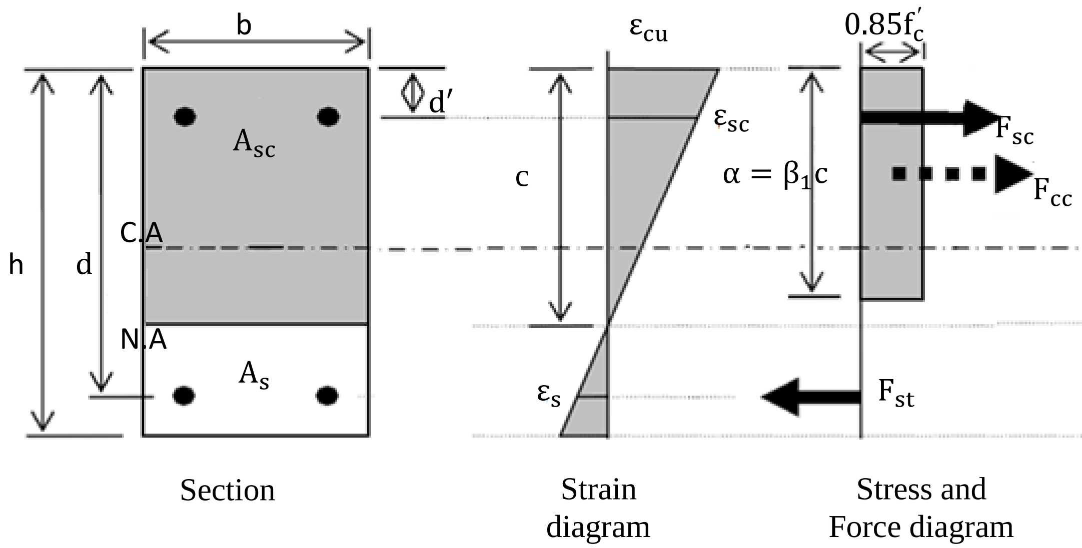

Figure 2-7: The beam section, strain diagram and stress/force diagram with neutral axis in section (after ACI 318)

Where:

h	Height of concrete section
b	Width of concrete section
c	Distance from top surface to neutral axis (N.A)
α	Depth of equivalent rectangular stress block
β_1	Factor relating depth of equivalent rectangular compressive stress block to neutral axis (N.A) depth
d	Distance from top surface to tension steel
d'	Distance from top surface to compression steel
A_{sc}	Cross section area of compression steel
A_s	Cross section area of tension steel
ε_{cu}	Ultimate strain of concrete
ε_{sc}	Strain of compression steel bar
ε_s	Strain of tension steel bar
F_{cc}	Force of compression concrete
F_{sc}	Force of compression steel bar

F_{st} Force of tension steel bar

f'_c Specified compressive strength of concrete

As the force equilibrium, $\sum F = 0$, and moment equilibrium, $\sum M$ about the central axis (C.A) equal zero, then two basic equations are presented in Eq 2-4 and Eq 2-5.

$$P = F_{cc} + F_{sc} + F_{st} \qquad \text{Eq 2-4}$$

$$M = F_{cc}\left(\frac{h}{2} - \frac{\alpha}{2}\right) + F_{sc}\left(\frac{h}{2} - d'\right) + F_{st}\left(\frac{h}{2} - d\right) \qquad \text{Eq 2-5}$$

Where:

P Axial load

M Bending moment

The same method is used for ferrocement and strengthened reinforced concrete calculations.

The performance based design approach for moment-resistant reinforced concrete framed structures demands a thorough understanding of the interaction diagram (P-M diagram), particularly when the structure is subjected to seismic loads.

For a range of values of c (position of N.A) that are defined in Figure 2-7, a set of points result, each representing a combination of axial force and moment. Any combination of applied moment and axial force that fall inside this curve is therefore safe against failure. A number of important points can be identified on a typical interaction diagram as indicated in Figure 2-8.

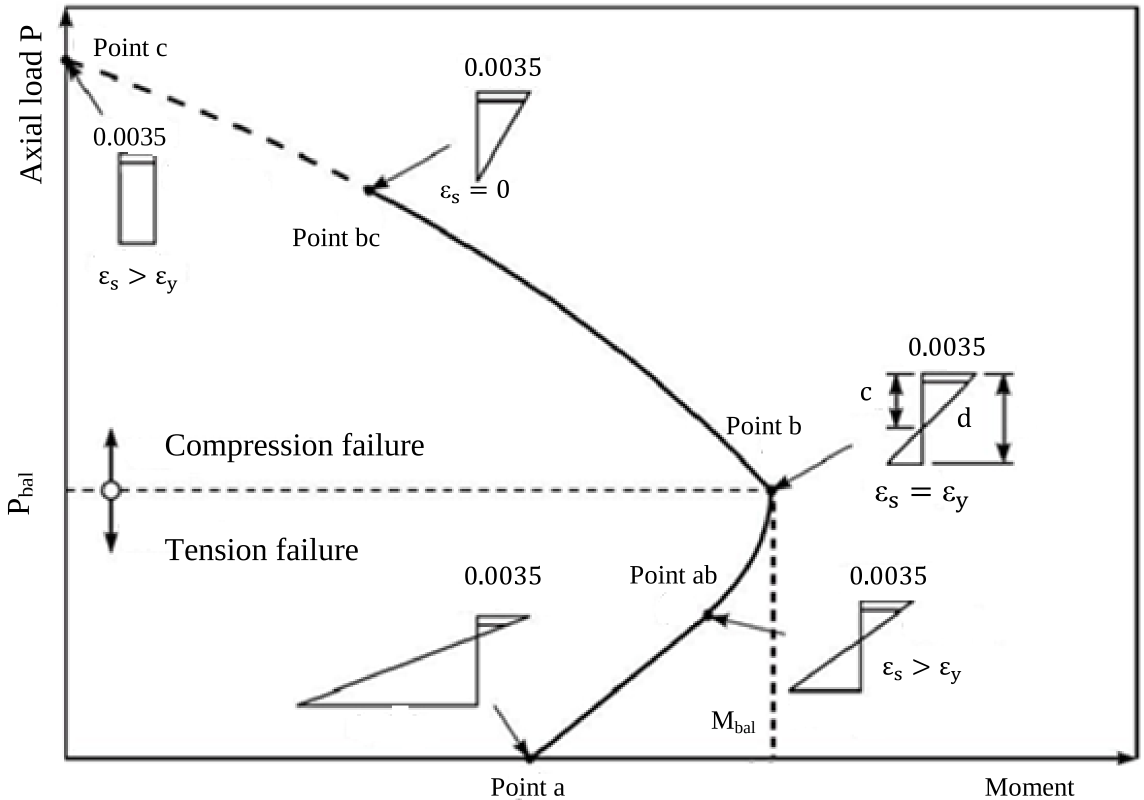

Figure 2-8: The interaction diagram for the element under bending and axial loading (Caprani, 2006)

Where:

P_{bal}	Axial load at balance
ε_{sc}	Strain of compression steel
ε_{yc}	Strain of steel at yield
ε_s	Strain of tension steel
c	Distance from top surface to neutral axis (N.A)

Pure bending (point (a) in Figure 2-8**)**: this point represents that of a beam in pure bending. The presence of a small axial force will generally increase the moment capacity of the beam.

Balanced position (point (b) in Figure 2-8): this is a point where the concrete reaches its ultimate strain, and the tension reinforcement yields simultaneously. For combinations of P and M that fall below the balance point, the failure mode is tension mode which ductile with the reinforcement yielding before the concrete fails in compression.

Pure axial compression (point (c) in Figure 2-8): at this point, the column is subjected to an axial force only with $M = 0$. The capacity of the section is equal to P.

Zero strain in the tension reinforcement (point (bc) in Figure 2-8): moving from the point (b) to point (c), it can be seen that the neutral axis (N.A) increases to infinity as P increases. The strain in the tension reinforcement changes from yielding in tension to yielding in compression, passing through zero at the point (bc). Moving from points (bc) to (c) the neutral axis (N.A) will fall outside the section and the strain distribution will eventually change from triangular to uniform. Between points (b) and (c), an increase in axial load P will lead to a smaller moment capacity M at failure. Conversely, below the balance point an increase in P will increase the moment capacity of the section.

Yield of the compression reinforcement (point (ab) in Figure 2-8): as the axial force P increases from zero and the neutral axis (N.A) increases (point (ab) is greater than N.A at point (a)), the strain in the compression reinforcement will often change from elastic to yielding. This will clearly be influenced by the strength of the reinforcement and its position within the section. This point will typically correspond to a change in slope of the interaction diagram as shown at the point (ab).

2.8 Experimental studies of columns under bending and axial load

2.8.1 Reinforced concrete columns

Many researchers have investigated reinforced concrete columns under bending and axial loads. For this thesis, which is primarily concerned with ferrocement columns, only two simple reinforced concrete examples will be shown.

Kim and Lee (2000) investigated the stress of the reinforced concrete members under axial load and biaxial bending by both experimental tests and numerical methods. Tests were carried out on 16 tied reinforced concrete columns with 100 × 100 mm square and 200 × 100 mm rectangular sections under various loading conditions. The angles between the direction of bending and the major principal axis of the gross section were 0 °, 30 °, 45 ° for the square section and 0 °, 30 °, 45 °, 60 °, 90 ° for the rectangular section. Kim and Lee (2000) reported the numerical method was in good agreement for the ultimate loads, curve of axial loading against lateral deflections. It was also found that the moment method from ACI is conservative in both uniaxial and biaxial bending conditions.

Barrera et al. (2011) have undertaken 44 experimental tests on reinforced concrete columns subjected to constant axial load and a monotonically increasing lateral force to failure. The aim of this was to gain a greater knowledge of the types of elements and provide data that will be of use in calibrating numerical models and validating simplified methods. The test parameters were concrete strength, axial load level and longitudinal and transversal reinforcement ratios. The strength and deformation of the columns was studied, and an examination of the simplified calculation methods in Eurocode 2 (CEN, 2004a) and ACI 318-08 (ACI, 2008) concluded that both are very conservative.

2.8.2 Ferrocement columns

There have been few analytical studies on the combined bending and axial forces in ferrocement columns.

Mansur and Paramasivam (1985) investigated the interaction behaviour of ferrocement sections under combined axial loading and bending. The results of a test programme on three uniformly reinforced sections, each containing different volume fractions of reinforcement, indicated two distinct modes of failure: primary compression and primary tension. The former type of failure occurs under predominant axial loads, while the latter is caused by a moderate compressive load or tension. For combination of axial load and bending, the number of cracks and the capacity of the section increased with increasing volume fraction of reinforcement mesh.

2.8.3 Reinforced concrete columns strengthened using ferrocement jacket

Repairing and strengthening of existing concrete structures has become more common during the last decade due to the increasing knowledge and confidence in the use of advanced repairing materials. Many researchers found that ferrocement jackets can provide effective confinement for reinforced concrete elements and therefore it has great potential for use as a strengthening material. The skill required for the fabrication of ferrocement is of a low level and its constituents are usually available locally.

Takiguchi (2003) studied the behaviour and strength of reinforced concrete columns strengthened using ferrocement jackets. Six identical reference columns were prepared and tested after being strengthened with circular or square ferrocement jackets. The parameters studied included the jacketing schemes and the number of layers of wire mesh. The results show that the peak strength and ductility is enhanced tremendously.

Mourad and Shannag (2012) investigated a series of 10 one-third scale square reinforced concrete columns strengthen using ferrocement jackets containing two-layers of welded wire mesh. The columns were preloaded with uniaxial compression to various percentages of their ultimate load (0, 60, 80 and 100%). The overall response of the specimens was investigated in terms of load carrying capacity, axial displacement, axial stress, axial strain, lateral displacement and ductility. The test results indicated that jacketed square reinforced concrete columns provided approximately 33% and 26% increases in axial load capacity and axial stiffness.

Kaish et al. (2013) investigated the square reinforced concrete strengthening with ferrocement jacket under compressive load, he reported the ferrocement jacketing improves the ultimate load carrying capacity and increases the ultimate axial deflection of RC column.

Ferrocement can provide an effective confinement jacket for existed concrete columns and has a great potential for use as a strengthening material.

2.9 FEM in ferrocement research

The finite element method (FEM) is popular for civil engineering applications worldwide. With the power of computer hardware improving dramatically over the last 30 years, the simulation speed has increased dramatically and the use of new elements and finer meshes, plus experience and feedback from experiments has improved the accuracy of the results, saving engineers both time and money.

FEM is used by many engineers and researchers for structural design and analysis. However, for ferrocement structures, FEM is still a new territory. This is because there are few people who have conducted simulations on ferrocement, although reinforced concrete structure is a major material in construction. Nevertheless, the author of this thesis believes that FEM (at least the ABAQUS package) is good for ferrocement simulations as do others (Nassif and Najm, 2004, Fahmy et al., 2005, Tian, 2013).

Nassif and Najm (2004) used ABAQUS to model experiments on ferrocement strengthened concrete beams under bending. The load-deflection curves from the models closely correlated with the experimental results. Two-dimensional (2D) and three-dimensional (3D) models were developed for comparison with experimental results. It was found that the 3D non-linear models gave the most reliable predictions. In addition, the interaction between the matrix and mesh layers was reported to be critical in analysing ferrocement behaviour and perfect bond was found to be appropriate.

Fahmy et al. (2005) reported an investigation on flexural behaviour of ferrocement elements using a 3D FEM that was developed to study ferrocement sandwich and cored panels. The results of the ultimate strength determinations from the FEMs were compared with experimental results of phases one and two and showed good agreement.

The previous literature shows that FEM can be used in ferrocement studies and can provide acceptable results. Three-dimensional models were reported satisfactory for behaviour studies of complex ferrocement structure. In addition, the 3D model can make parametric studies, especially the effects of geometry and mesh layer numbers, easy to undertake. Consequently, 3D FEM models were used in the simulation studies in this thesis.

2.10 Ductility

The performance of a structure under seismic load depends on its ductility, which in turn depends on the ductility of each individual member and the structural configuration. Ductility is associated with the post-elastic deformation of the structure; this is important because ductility indicates the capability of the material to absorb energy without significant reduction in strength. It is defined as the ratio of the ultimate deformation over the yield deformation.

In earthquake-resistant design of structures, according to Eurocode 8 (CEN, 2004b), the recommended level of design seismic force is significantly less than the elastic response force that is likely to be induced by severe ground motion. For reinforced concrete structures, ductility is generally associated with under-reinforced sections, because in over-reinforced sections the ultimate strength of concrete is reached before the yielding of the steel reinforcement. Park et al. (1982) suggested that ductility is negligible for over-reinforced sections and cannot be used for any practical purpose.

The term ductility could refer to different entities. According to Gioncu and Mazzolani (2003) the ductility of structures can be considered in five categories:

1) **Deformation ductility or material ductility**: characterizes plastic deformation of material under different types of loading.
2) **Curvature ductility or cross-section ductility**: refers to the ductility of the cross-section, usually estimated from the moment-curvature diagram.
3) **Member ductility**: refers to the ductility of a whole element such as a beam or column. This is also termed as displacement ductility and calculated from load-deflection behaviour.
4) **Structural ductility**: relates to the overall ductility of the structure.
5) **Energy ductility**: this is estimated by considering the energy that is dissipated due to seismic motion.

In this thesis, the author uses deformation ductility because it can be directly obtained from experimental tests. In addition, the position of yield and ultimate capacity can be clearly shown from loading-displacement curves.

Barrera et al. (2012) reported a method for idealization of the response diagrams through an energy balance between the experimental curve and the idealized diagram up to ultimate load (see Figure 2-9).

The area below the experimental curve (the heavy shadow in Figure 2-9) is equal to the area below the ideal elastic-plastic curve (the light shadow in Figure 2-9). The effective yielding deformation is obtained (Δ_{yI}) by matching the two areas. The deformation ductility for the column is:

$$\mu_{\Delta} = \Delta_u / \Delta_{yI} \qquad \text{Eq 2-6}$$

Where:

μ_{Δ}	Deformation ductility
Δ_u	Displacement of the column in the descending branch corresponding to 0.85 of the maximum load
Δ_{yI}	Effective yielding displacement

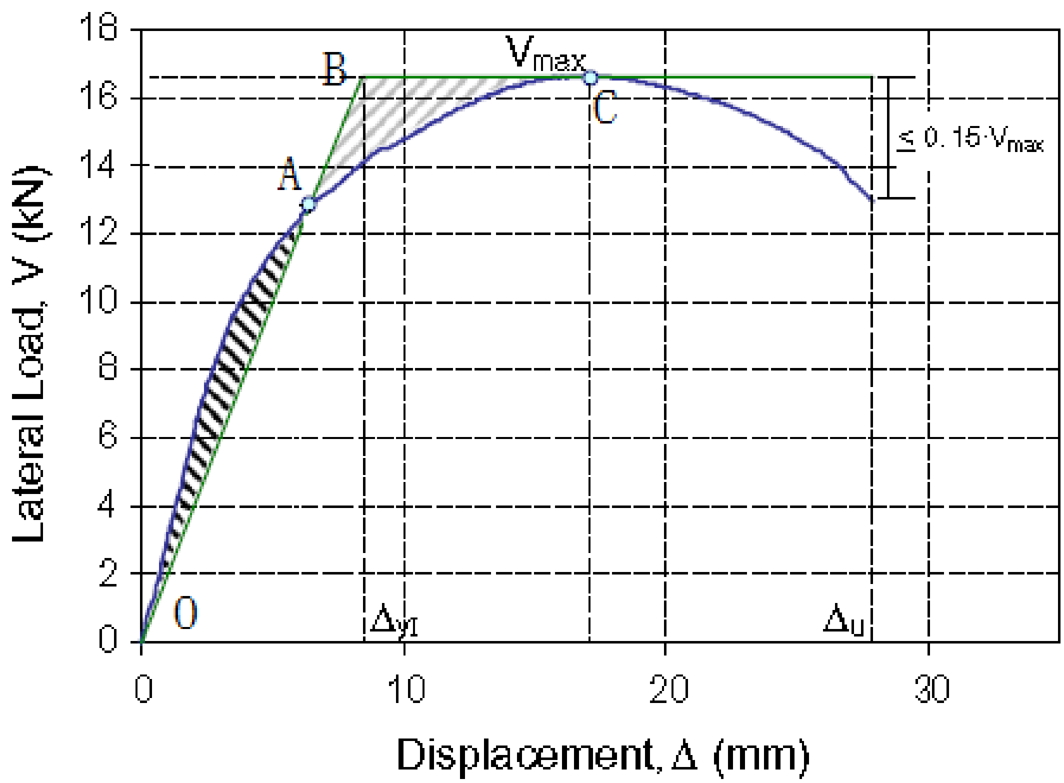

Figure 2-9: Deformation ductility on a general load-displacement curve (Barrera et al., 2012)

2.11 Cyclic load effect on ferrocement structures

In the last 30 years, little research work has been conducted on cyclic load testing of ferrocement structures. However, the behaviour of ferrocement under cyclic load is important, especially in seismic zones.

The cyclic load effect is a process of progressive, permanent internal structural changes in a material subjected to repeated loading. In concrete, these changes are due to progressive growth of cracks. Many reinforced concrete structures including pavements, bridge deck overlays, and offshore structures endure significant cyclic loading during their service life.

Different loading arrangements have been used in cyclic load testing, including compression, tension, bending and combined forces. The most popular method of cyclic testing is via flexural loading, although compressive cyclic tests have also been investigated.

Balaguru et al. (1979) investigated the cyclic characteristics of ferrocement beams. In their experiments, ferrocement beams reinforced with various volume fractions (2% to 6%) and types of square steel meshes were tested. The beams were subjected to flexure with three different levels of loading: 40%, 50%, and 60% of the static yield load. The deflection increased with the applied load and number of loading cycles.

2.12 Summary and conclusions

Based on the literature review in this chapter it can be seen that ferrocement has several advantages when compared with reinforced concrete structures, such as it is lightweight, easy to shape, and has a low carbon foot print and smaller crack width. Due to the closely distributed reinforcement throughout its cross sectional area, ferrocement shows homogenous properties. Because ferrocement structures are not within the main stream of reinforced concrete structures, their development in the last one hundred years has been very slow.

Nevertheless, ferrocement has high potential as a retrofit or strengthening material, for example ferrocement jackets can be used on reinforced concrete columns.

The finite element method (FEM) is popular for civil engineering design and analysis. It can quickly predict structural behaviour thus saving money; but its use with new materials does need to been proven, e.g. for ferrocement.

CHAPTER 3 Experimental tests

3.1 Introduction

This chapter presents details of the experimental tests reported in this thesis. These include:

- **Material property tests**: Five materials/elements were tested: concrete, matrix, 12 mm ribbed steel bar, 3 mm general steel bar and welded mesh. The results are used as input values for the Finite Element Model (FEM)
- **Casting the column specimens**: Eight columns were cast and tested. Five were tested using static loads and three using cyclic load application. All the tests used displacement control.
- **The equipment setup**: The specimens were tested as horizontal cantilevers, with one end fixed, and the load applied to the other end. Linear potentiometers (linpots) were distributed on the bottom surface of each specimen.

3.2 Material property tests: concrete and matrix

3.2.1 Experiment preparation

The experimental programme included casting, curing and testing the specimens. In general, the experiments were based on the concrete test code: BS EN 12350 (BSI, 2009) “Testing fresh concrete” and BS EN 12390 (BSI, 2010) “Testing hardened concrete”.

The concrete and matrix both contain cement, sand, aggregates and water in accordance with code BS EN 12350 (BSI, 2009). The details of the components are given below:

- **Cement:** The cement used was Ordinary Portland Cement (OPC), which was stored under dry conditions, so that the cement used in the experiments was fresh and free of lumps and other foreign matter.
- **Fine aggregates:** Normal-weight natural river sand and uncrushed gravel were used in the matrix. The maximum particle size was 2.36 mm, passing through a No. 7 sieve.
- **Coarse aggregates:** The coarse aggregate used was uncrushed gravel with a maximum particle size of 10 mm.
- **Water:** Clean and fresh potable tap water was used throughout, being free of organic matter and acidic material.
- **Admixtures:** Silica fume and superplasticiser were used to enhance the strength of the matrix.

The mix ratios for concrete and the matrix were constant for all of the experimental tests.

For the concrete: The proportions of the cement, water, fine and coarse aggregate were: 484 kg/m^3, 230 kg/m^3, 616 kg/m^3 and 1050 kg/m^3 respectively, which is based on BS 8500 (BSI, 2006).

For the matrix: The cement and sand were mixed in the ratio of 1:2 by weight, and water cement ratio was 0.4. The admixtures added were 10% of silica-fume by weight of cement and 1.5% of superplasticiser (Paul and Pama, 1978).

3.2.2 Sampling

The concrete and matrix test cylinders were cast in clean moulds lubricated with release oil, in order to make the demoulding easier when the material had hardened. All materials were weighted and well mixed in a blender (see Figure 3-1). Then the mixture was poured into the mould (100 × 200 mm cylinder mould) and mechanical vibration applied. A vibrating table was used to provide expulsion of air voids and compaction, and the material cover controlled using a handheld float.

Figure 3-1: Matrix mix in the blender

The specimens were cured in a cool place and covered by a plastic sheet. After 28 days curing for the matrix, two strain gauges were fixed in the lateral and longitudinal directions for compressive cylinder tests. The capping dental plaster (see Figure 3-2) was placed on top of the compressive cylinder at least 1 day before testing.

Figure 3-2: Horizontal and vertical strain gauges, and the dental plaster

3.2.3 Specimen tests

3.2.3.1 **Compressive test:**

The cylinders were centred on the lower platen of the testing machine. A constant rate of 1 kN/sec loading was selected (BSI, 2010), the load and strain recorded. The compressive strength is:

$$f_{cm} = F_c/A_{cy} \qquad \text{Eq 3-1}$$

Where:

f_{cm}	Compressive strength
F_c	Maximum load at failure
A_{cy}	Cross sectional area of the cylinder

The value of Young’s Modulus (E), and Poisson's ratio (υ) were calculated from the longitudinal and lateral stress-strain curves:

$$\text{Young's Modulus (E)} = \sigma_y/\varepsilon_y \qquad \text{Eq 3-2}$$

Where:

σ_y The yield stress$= 0.4\ f_{cm}$

ε_y The strain at yield stress

$$\text{Poisson's ratio } (\upsilon) = \varepsilon_t/\varepsilon_y \qquad \text{Eq 3-3}$$

Where:

ε_t The lateral strain at yield stress

3.2.3.2 **Split test:**

Based on BS EN 12390 (BSI, 2010), a constant loading rate of 0.05 kN/s was used for the split test. The split test was used to determine the tensile properties of the concrete and the matrix. Figure 3-3(a) is shown the steel jig and Figure 3-3(b) shows a typical cylinder failure in the split test. Eq 3-4 gives the tensile stress formula.

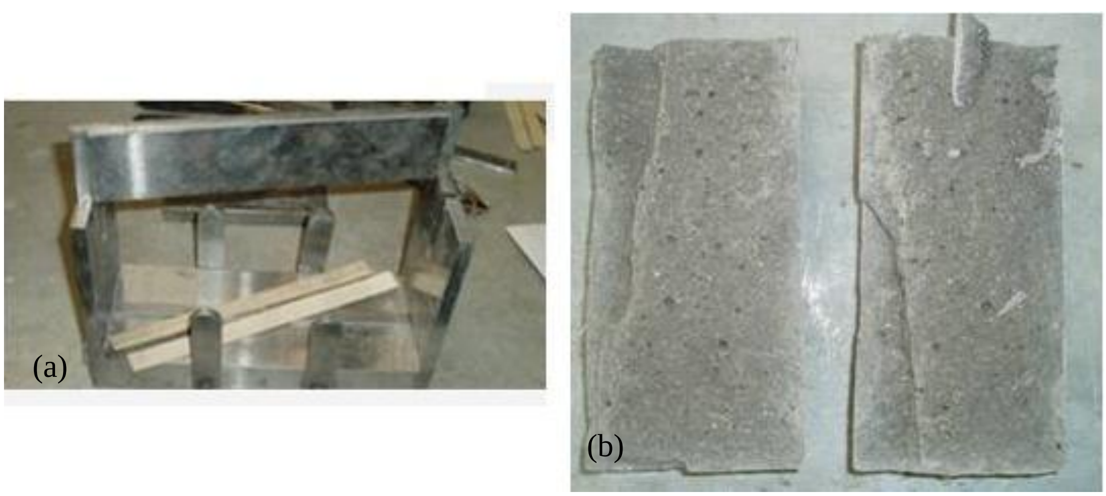

Figure 3-3: The tensile test (a): jig with packing strips, (b): cylinder split test failure

$$\textbf{Tensile strength }(\boldsymbol{\sigma_t}) = \frac{2F_t}{\pi D L_{cy}} \qquad \text{Eq 3-4}$$

Where:

F_t	Maximum loading at failure
D	Diameter of cylinder
L_{cy}	Length of cylinder

3.2.4 The test results

Typical stress-strain curves for concrete and the matrix under compression are shown in Figures 3-4 and 3-5, and results present in Table 3-1. The compressive strength of concrete reached 38 N/mm^2, and compressive strength of matrix reached 62 N/mm^2. The values of Young's Modulus were 27500 N/mm^2 and 21000 N/mm^2 respectively. The result of split test for concrete was 3.74 N/mm^2, for matrix is reached 4.44 M/mm^2.

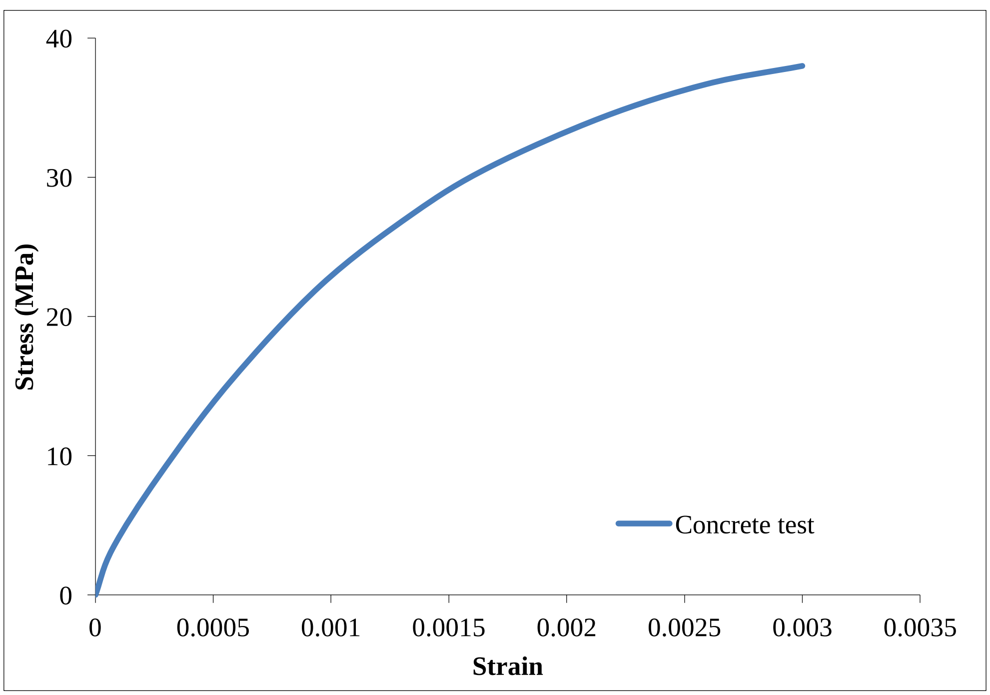

Figure 3-4: Typical concrete cylinder compressive test of stress-strain curve

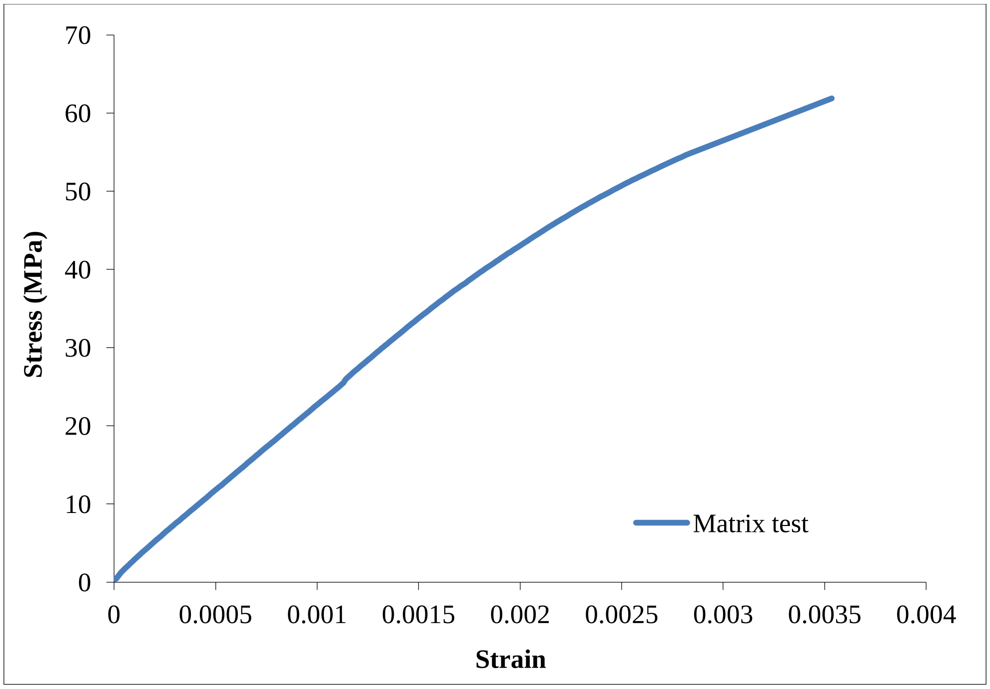

Figure 3-5: Typical matrix cylinder compressive test of stress-strain curve

Table 3-1: The material properties of the concrete and the matrix

Material	Compression strength (N/mm^2)	Young's Modulus (N/mm^2)	Poisson's ratio	Tensile stress (N/mm^2)
Concrete	38	27500	0.22	3.74
Matrix	62	21000	0.22	4.44

3.3 Reinforcing material tests

Three different types of reinforcing material were used for the reinforced concrete and ferrocement specimens.

1) 12 mm diameter ribbed steel bar
2) 3 mm diameter general steel bar
3) Galvanised square welded steel mesh with 1.6 mm wire diameter, 12.6 mm mesh opening

The material properties were measured using tension tests in an INSTRON 4507 test machine with a capacity of 200 kN. The tension tests were performed on each sample with a 50 mm gauge to record the results. The tests were carried out with a displacement ratio: 5 mm/min until the specimens cracked. All the specimens were cut in 150 mm lengths and were clamped into the machine with V shape gripper jaws at both ends (see Figure 3-6). Details of the reinforcement properties are presented in Appendix A.

Figure 3-6 Mesh tensile test set up

The mechanical properties of the reinforcing materials are presented in Table 3-2, and the stress-strain curves are shown in Figure 3-7. The welded mesh had yield strength 380 N/mm^2 with Young's Modulus 175000 N/mm^2.

Table 3-2: The properties of the reinforcing materials

Reinforcement	**Diameter (mm)**	**Yield Strength (N/mm^2)**	**Young's Modulus (N/mm^2)**
Ribbed steel bar	12	480	195000
General steel bar	3	600	190000
Weld mesh	1.6	380	175000

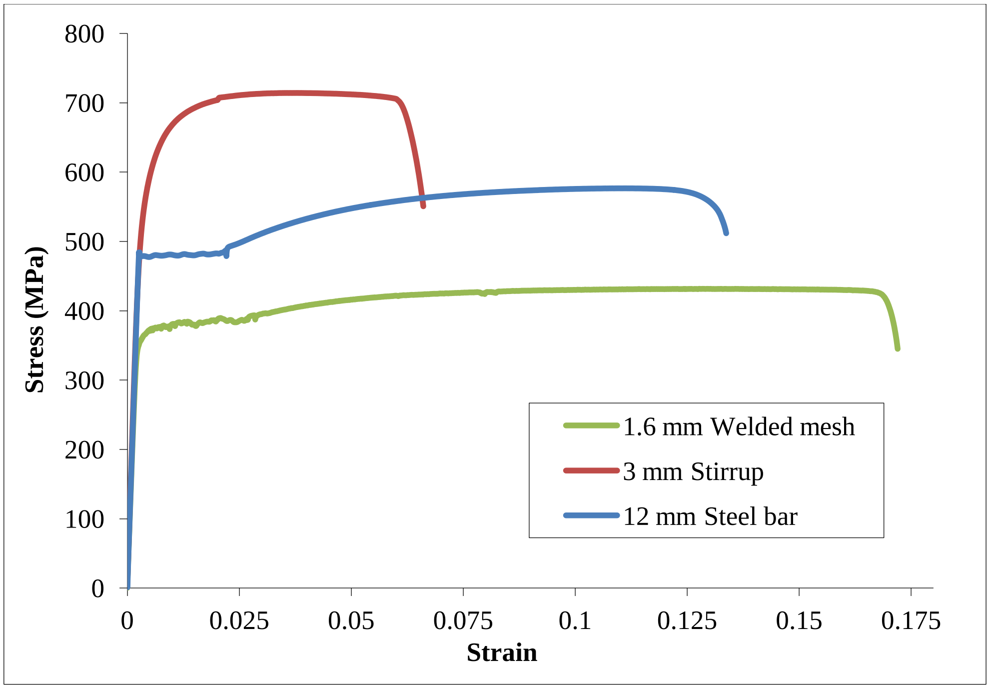

Figure 3-7: Typical reinforcement properties from the experimental tests

3.4 Column Specimens

A sequence of 8 columns was proposed in order to investigate the effects of reinforcement amount on the static and cyclic load behaviour. Table 3-3 below gives the columns and their designation. Control columns of reinforced concrete were provided and compared with ferrocement columns with four layers of mesh (which provides a similar area of longitudinal steel) and two layers of mesh to investigate the effect of steel content. In addition control columns which had been overlain with two and three layers of mesh were used to investigate strengthening. The relationships between the eight specimens are shown in Figure 3-8.

Table 3-3: Specimen nomination

Number	Naming	Description
1	**RC**	Reinforced concrete under static test – Control specimen
2	**RC-C**	Reinforced concrete under cyclic test – Control specimen
3	**FC2**	Ferrocement with 2 layer mesh under static test
4	**FC2-C**	Ferrocement with 2 layer mesh under cyclic test
5	**FC4**	Ferrocement with 4 layer mesh under static test
6	**FC4-C**	Ferrocement with 4 layer mesh under cyclic test
7	**RFC2**	Reinforced concrete strengthened using 2 layer mesh ferrocement under static test
8	**RFC3**	Reinforced concrete strengthened using 3 layer mesh ferrocement under static test

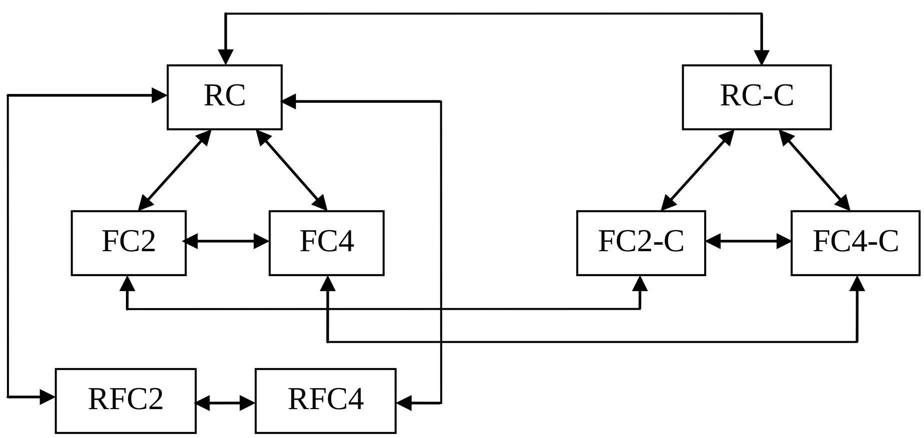

Figure 3-8 Relationship between the eight column specimens

3.5 Casting

3.5.1 The concrete columns (RC)

Four square reinforced concrete columns were cast. The column reinforcement is shown in Figure 3-9, and consisted of four longitudinal 12 mm diameter ribbed steel bars and seven 3 mm diameter steel bar stirrups, with 150 mm spacing in between.

All square columns were cast in a horizontal position using steel moulds for the formwork, as shown in Figure 3-10. The steel moulds were properly oiled on the inner sides for easy removal of the specimens at the time of demoulding. The prepared reinforcement cage was held carefully in the moulds. Concrete spacers of 13 mm size were used to maintain 13 mm concrete cover to the main reinforcement. The concrete was poured in three layers and compaction of each layer was carried out using a vibrating table to remove air voids. Six concrete cylinders cast at the same time.

After 24 hours of casting, all columns and cylinders were demoulded and cured under plastic sheets so that loss of moisture was avoided. Figure 3-11 shows the reinforced concrete and ferrocement columns.

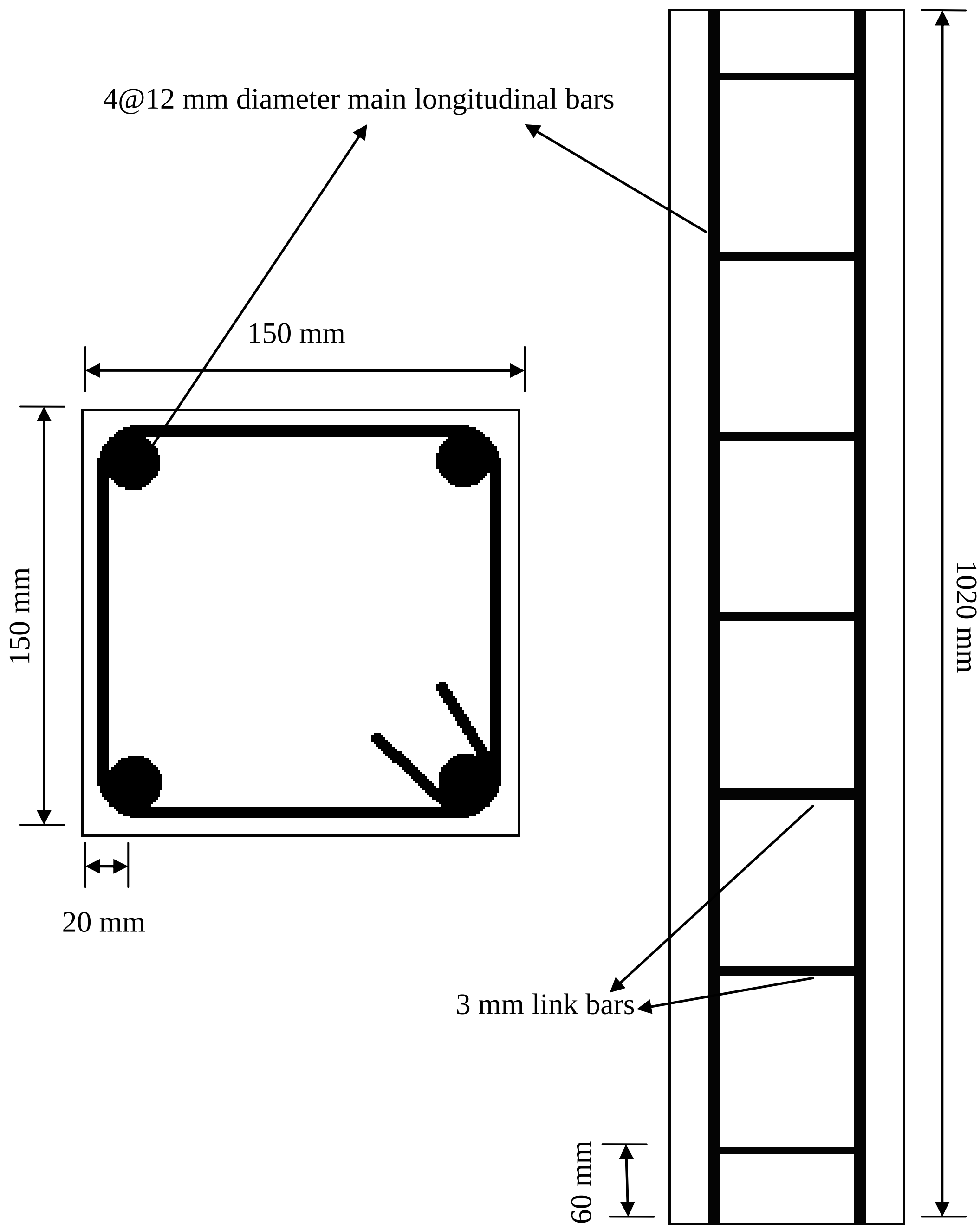

Figure 3-9: Reinforcement arrangement in the concrete column

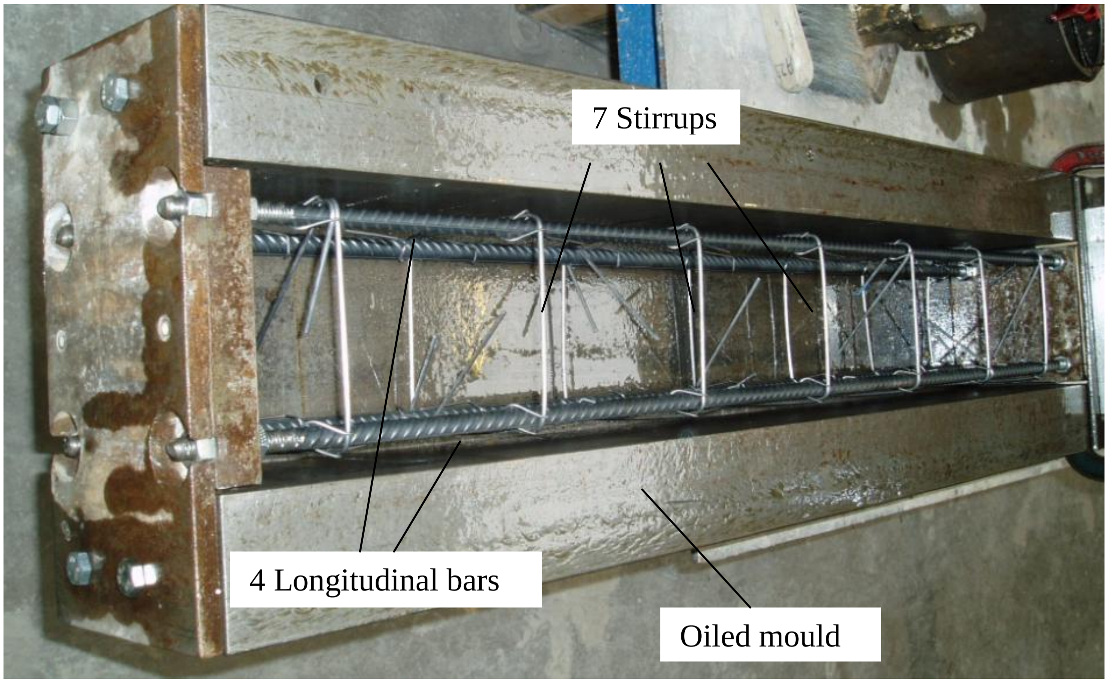

Figure 3-10: Reinforcing steel in a square oiled steel mould

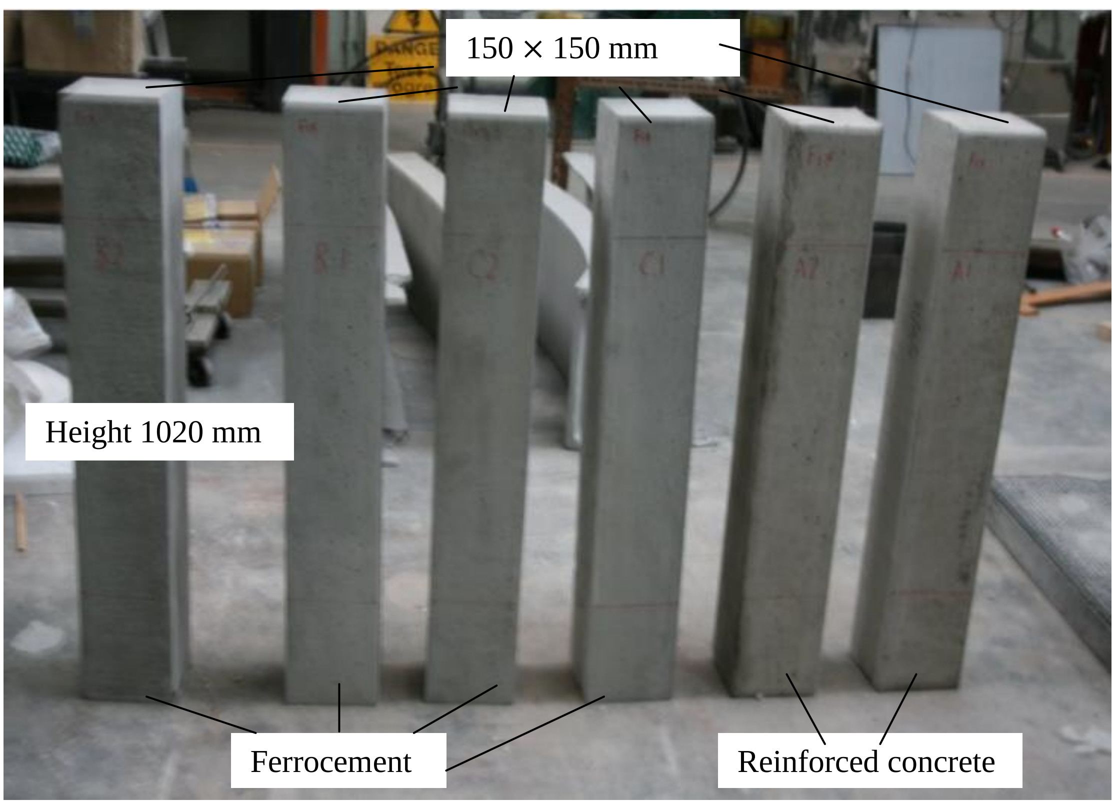

Figure 3-11: The specimens

3.5.2 The ferrocement columns (FC)

Four ferrocement columns were cast; two columns had two-layers of glazed welded mesh, and two had four-layers of mesh. The skeleton of reinforcing mesh is box section, which had 2 or 4 layers enclosed with plastic ties and a 3 mm matrix cover. Figure 3-12 shows the patterns of the 2 layers and 4 layers mesh.

The method and mould used for casting the concrete columns was also used for the ferrocement columns, as shown in Figure 3-13. More vibration sequences were needed to ensure the matrix was evenly distributed through the whole specimen, because the matrix does not easily pass through the layer meshes, especially for four-layer meshes ferrocement. A wooden stop end was added to position the column and to make demoulding easier. Again, the cylinders were cast at the same time, and the columns and cylinders demould after 24 hours casting, then fully covered with plastic sheet for curing.

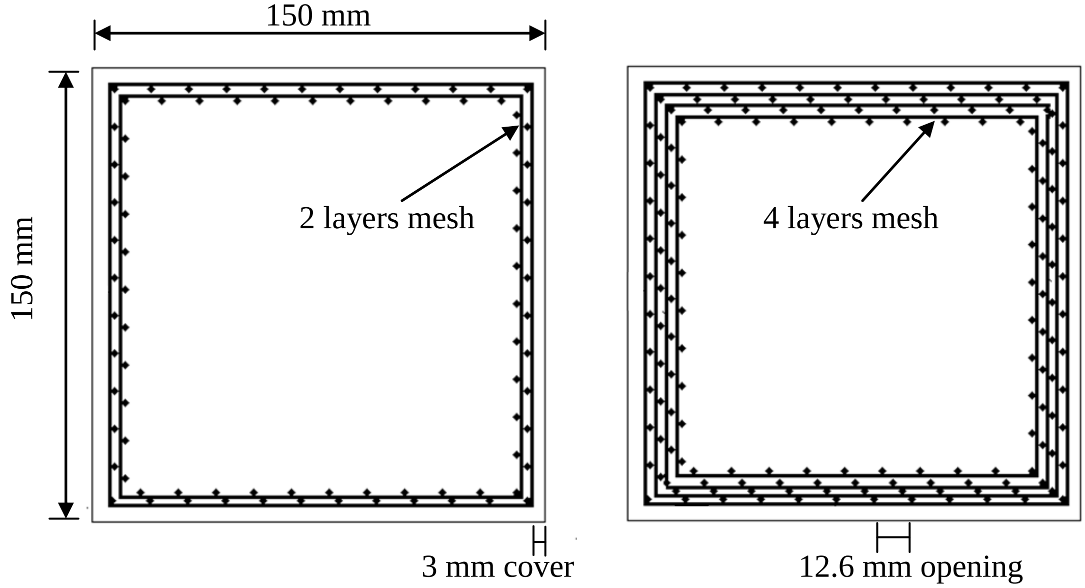

Figure 3-12: The pattern of 2 and 4 layers mesh in the ferrocement columns

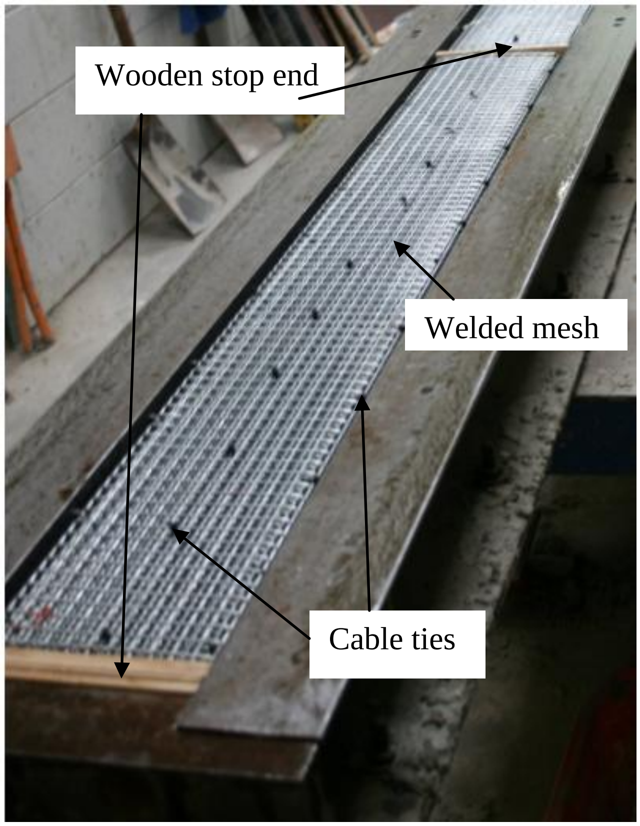

Figure 3-13: The ferrocement column skeleton and mould

The roll of mesh sheet is shown in Figure 3-14. The fabrication method for the mesh skeleton in the ferrocement columns was:

Cutting: After cutting an approximate amount of mesh from the roll using electric shears, it was then trimmed to the required size using a precise cropper, as shown in Figure 3-15.

Bending: These were then bent at right angle, shows in Figure 3-16.

Assembling: In Figure 3-17, for assembly of the square meshes, each layer of the mesh was tied using plastic ties placed with 10 cm spacing. Cable pliers were used to tighten the cable ties to ensure that all layers were fixed together and had a 3 mm cover.

Figure 3-14: Mesh sheet roll

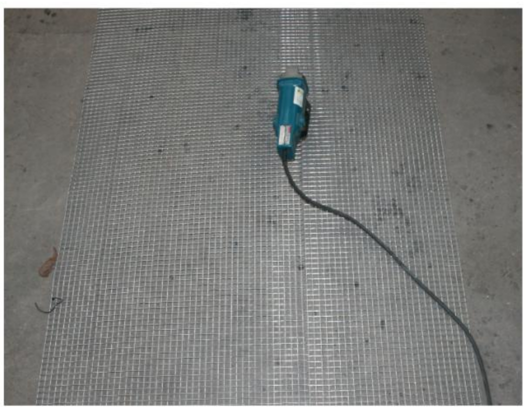

(a): Cutting mesh by shear scissors

(b): The mesh plates

(c): The trim cutting machine

Figure 3-15: Mesh cutting

(a): The bending machine

(b): The square shape meshes

Figure 3-16: Mesh bending

Figure 3-17: The assembly of mesh layers with plastic ties

3.5.3 Reinforced concrete column strengthened using ferrocement jacket (RFC)

After 28 days of the two reinforced concrete columns were strengthened using ferrocement jacket, one with two-layers mesh, the other with three-layers. Figure 3-18 shows the pattern of two and three-layers mesh around the reinforced concrete.

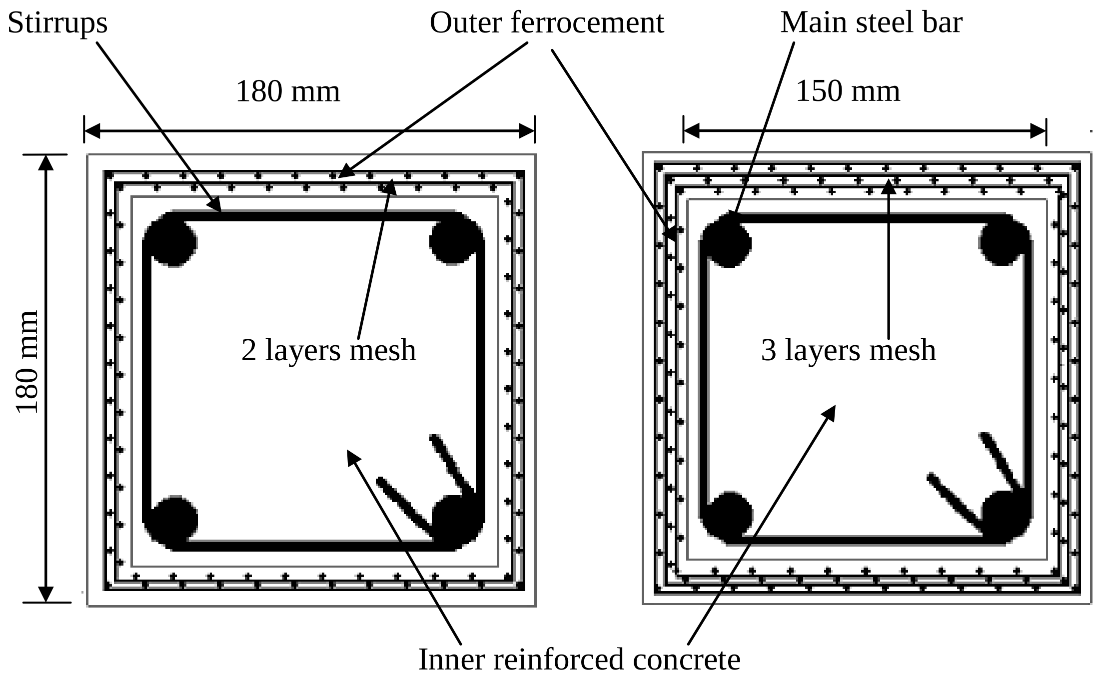

Figure 3-18: The pattern of reinforced concrete strengthened with 2 and 3 layers mesh

The concrete columns were painted twice (see Figure 3-19(a)) with a thin layer of diluted polyvinyl acetate **(**PVA), the proportion of PVA to water being 1:5. This was to fill the micro cracks on the concrete surface and to act as a bonding agent between the concrete and the ferrocement.

The fresh matrix was cast in same manner to the ferrocement columns, where the cement to sand ratio was 1:2 and the water to cement ratio 0.4; with 10% of silica fume by the weight of cement and 1.5% of superplasticizer by the weight of cement added.

After 30 minutes completion of the painting, the enclosed 2 or 3 layers welded mesh were wrapped over the square concrete column (Figure 3-19(b)). Then a steel trowel was used and force applied to ensure full penetration of the matrix into mesh. The final dimensions of the column were 180 × 180 mm. A steel float was used to make the surface of the ferrocement flat. During the plastering process, tape was used to ensure each individual size was close to 180 mm. Figure 3-20 shows the finished strengthened columns. The strengthened reinforced concrete columns after curing are shown in Figure 3-21. The outer ferrocement jacket was not formed in a mould; hence the outer surfaces of the specimens were coarse.

(a): Painting the PVA (b): Put the square mesh on

Figure 3-19: Preparation for strengthening

Figure 3-20: Casting the strengthened concrete column with ferrocement

Figure 3-21: Reinforced concrete columns strengthen with ferrocement jackets

3.6 The experimental rig

3.6.1 The methodology

The specimens were tested under a combination of axial load and bending. Figure 3-22 shows a schematic plot of the experimental programme with the arrow indicating the force P (axial load) and V (lateral load).

For safety, reliability and operability issues, all specimens were tested in a horizontal cantilever position under bi-directional loading, as shown Figure 3-22(b). The static load was applied in the pushing (downward) direction while the cyclic loading was in both pushing and pulling directions. Reversed vertical cyclic loading represents the seismic force, which was applied using a servo controlled hydraulic actuator to the end of the columns. In the test schematic (Figure 3-22(b)), the left shaded area was fixed end while the right shaded area is the loading area of the lateral force (V) applied by the actuator. The setup of the column specimen is shown in Figure 3-23.

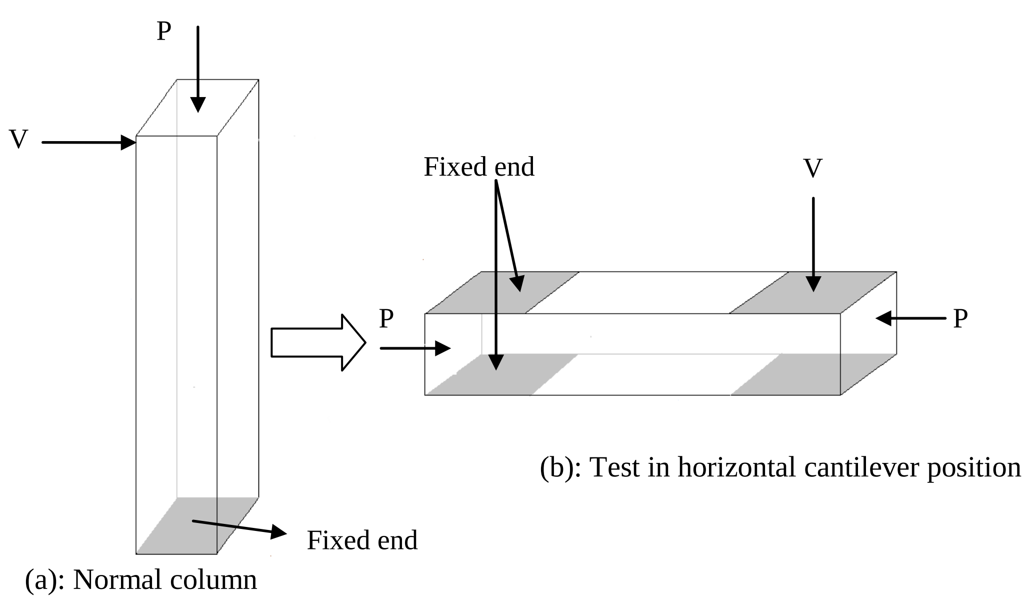

Figure 3-22: The column design layout, and test design layout as a cantilever

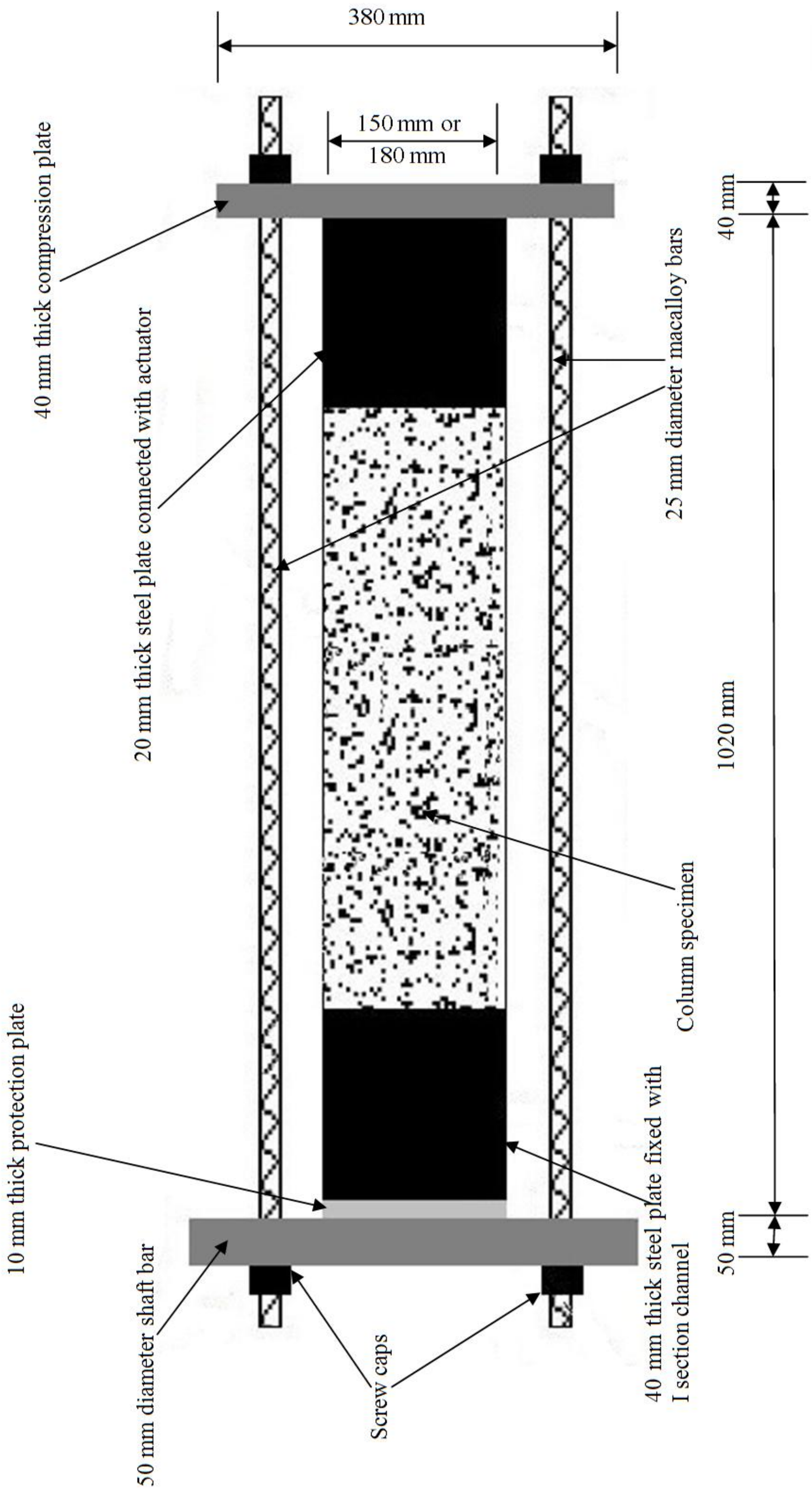

Figure 3-23: Layout of the column setup

Figure 3-23 shows the design layout for the test and provides various dimensions. The axial load (P) was applied to the columns by two high strength calibrated Macalloy bars (25 mm in diameter). The Macalloy bar at the fixed end was tied with a 50 mm diameter shaft-bar and protection-plate. At the actuator end, the bars were connected to a compression-plate. By tightening the nuts at the compression-plate, the axial tensile forces were distributed evenly to the Macalloy bars at 100 kN using a hydraulic jack, and then locked using the nuts (see detailed explanation in §3.7).

The fixed end of column was secured using three (20 mm thick) stiff fixed-end plates with two plates on top and one underneath. The lower steel plate sat on the heavy primary beam of the testing frame (detail see Figure 3-31). Eight steel rods were tied to the plates with high strength bolts to make sure that the end was fixed (see Figure 3-24). Also, the other end of the column was connected to two similar plates (20 mm thick), with one above and the other below and tightened by six high strength steel rods.

The lateral load was applied by a 500 kN capacity hydraulic actuator with a pin frame connector (see Figures 3-25 and 3-26). Four 10 mm diameter high strength screws connected the pin joint and the loading area plate. The pin frame was used to ensure the force applied was always perpendicular to the specimen's top surface.

When the surface of the reinforced concrete column strengthened using ferrocement jacket was not uniform, thick dental plaster was added to both the fixed end area and the load-applied area, to ensure that the contact surface was flat (see Figure 3-27).

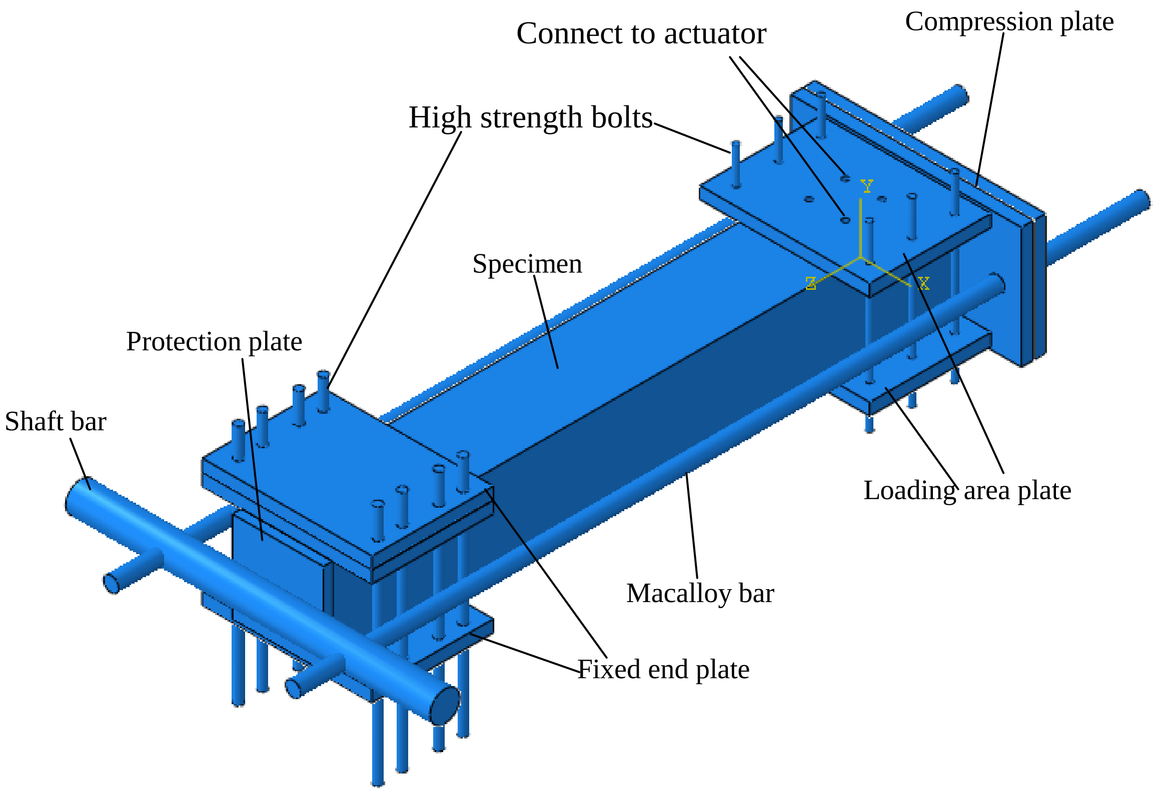

Figure 3-24: The design layout of the test setup (parts detail are shown in Table 3-4)

Table 3-4: Detail of dimension for each parts

Name of part	Description
Fixed end plate	3@200 × 280 ×20 mm with 8@ 13 mm diameter holes
Loading area plate	2@200 × 280 × 20 mm both have 6@ 11 mm diameter holes, and top plate has 4@ 11 mm diameter holes which connect with actuator
Compression plate	2@ 200 × 280 × 20 mm with 2@ 26 mm diameter holes
Protection plate	1@150 × 150 × 10 mm for 150 × 150 mm specimens 1@180 × 180 × 10 mm for 180 × 180 mm specimens
Shaft bar	1@50 mm diameter with 500 mm length
Macalloy bar	2@25 mm diameter with 1500 mm length
High strength bolt	8@12 mm diameter with 400 mm length for support end 6@10 mm diameter with 300 mm length for loading area

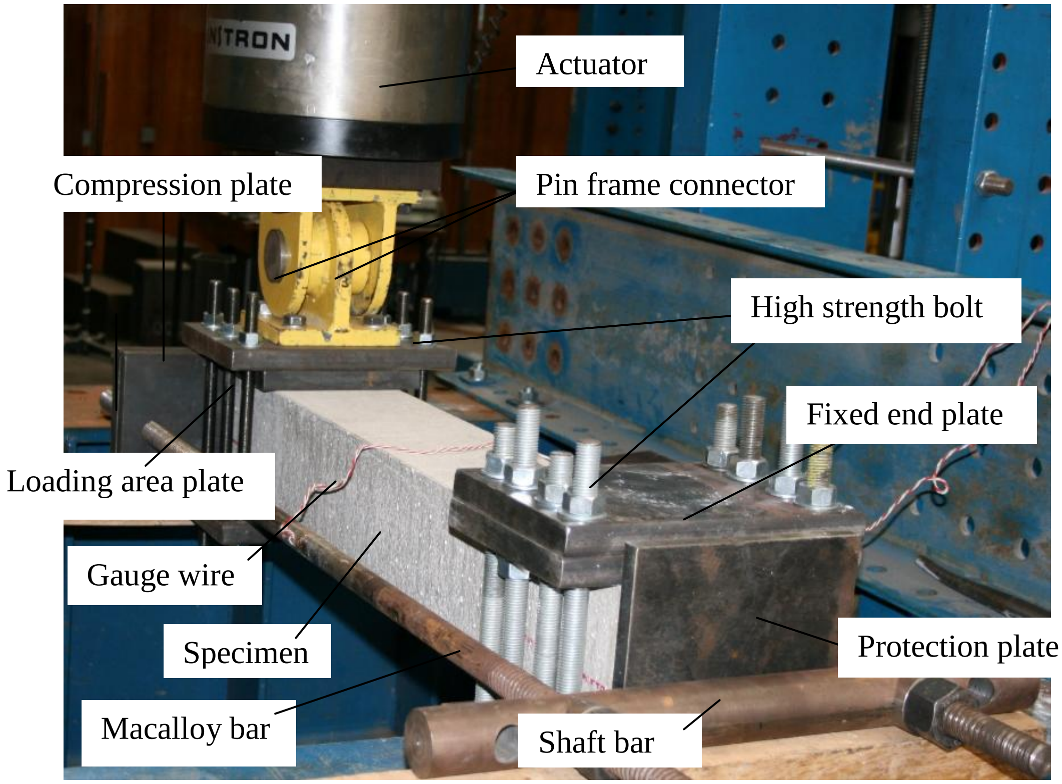

Figure 3-25 A column setup on the equipment before the test

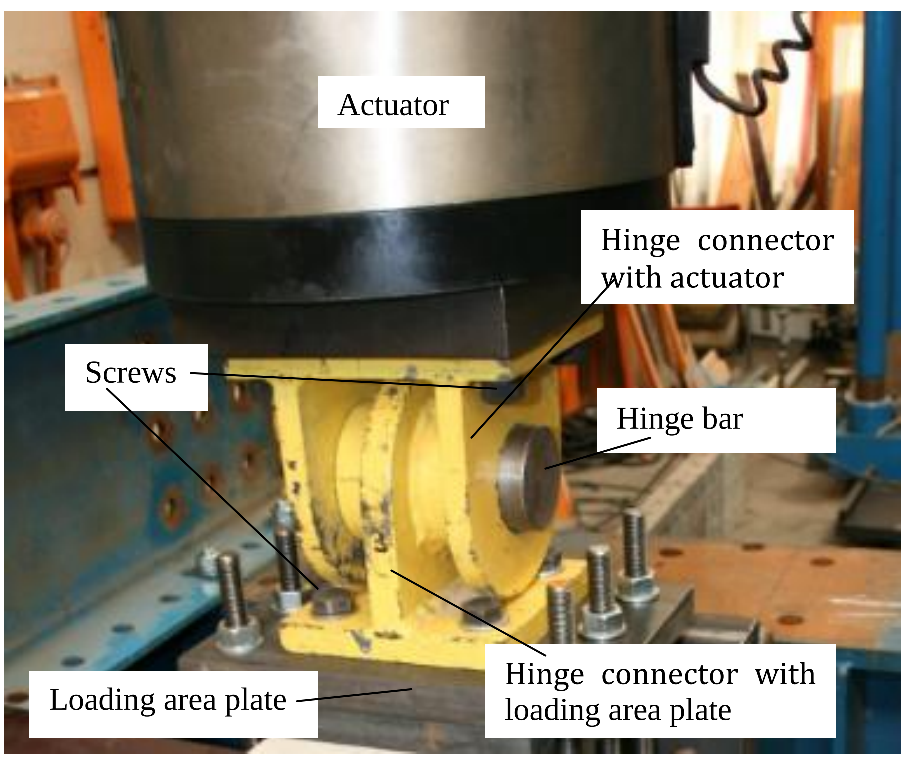

Figure 3-26 The pin joint between actuator and thick steel plate

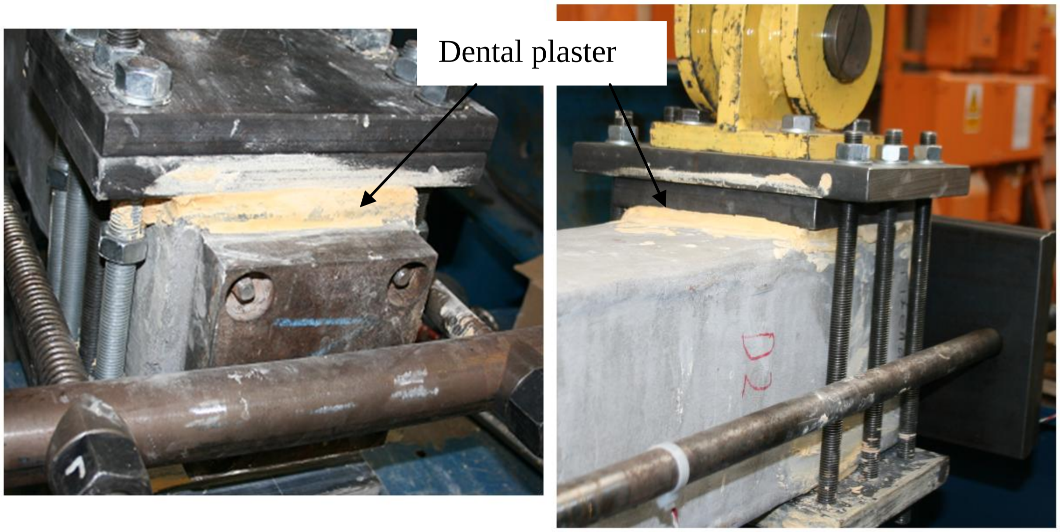

(a): Fixed end area (b): Loading area

Figure 3-27: Dental plaster

3.6.2 The position of the linear potentiometers

Initially, eight linear potentiometers (linpots) were positioned beneath the specimen in two lines, 150 mm apart, to measure the deflection of the specimen during the test (see Figure 3-28(a)). It was proven that the specimen did not twist. After that a new arrangement of linpots was used for the remaining specimens (see Figure 3-28(b)), that one line of linpots at 75 mm spacing.

The selected naming for the linpots (Li) was F or B (Front or Back) and number (1-4 for initial arrangement, 1-7 for final arrangement) along the length between the support and the free-end (for details see Figure 3-28). The Li-A is shown the downward of actuator position.

For accuracy, all the linpots were fixed on a frame lying on the ground. Figure 3-29 shows the final arrangement of linpots beneath the specimen. Notice that the all linpots were independent of the framework. The author made a simple aluminium frame for the linpots, which laid under each specimen when tested. Figure 3-30 shows the two extra linpots at top of fixed-end area to measure the movement the support.

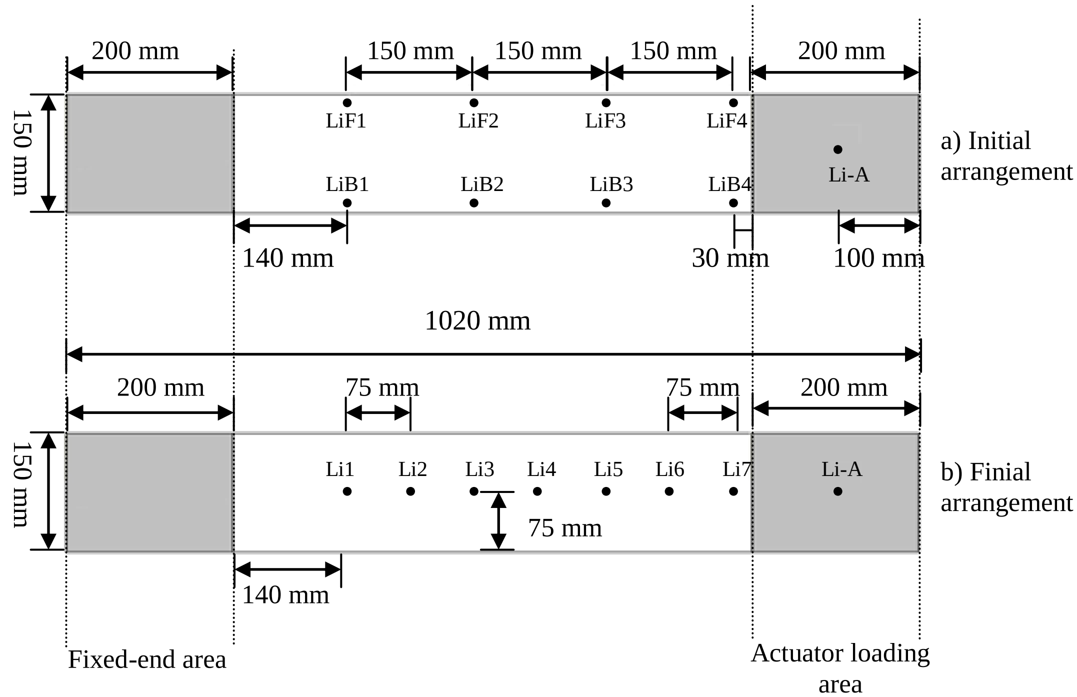

Figure 3-28: Location of linpots under the specimen, (a): initial arrangement, (b): final arrangement

Figure 3-29: Arrangement of linpots on the underside of the specimen

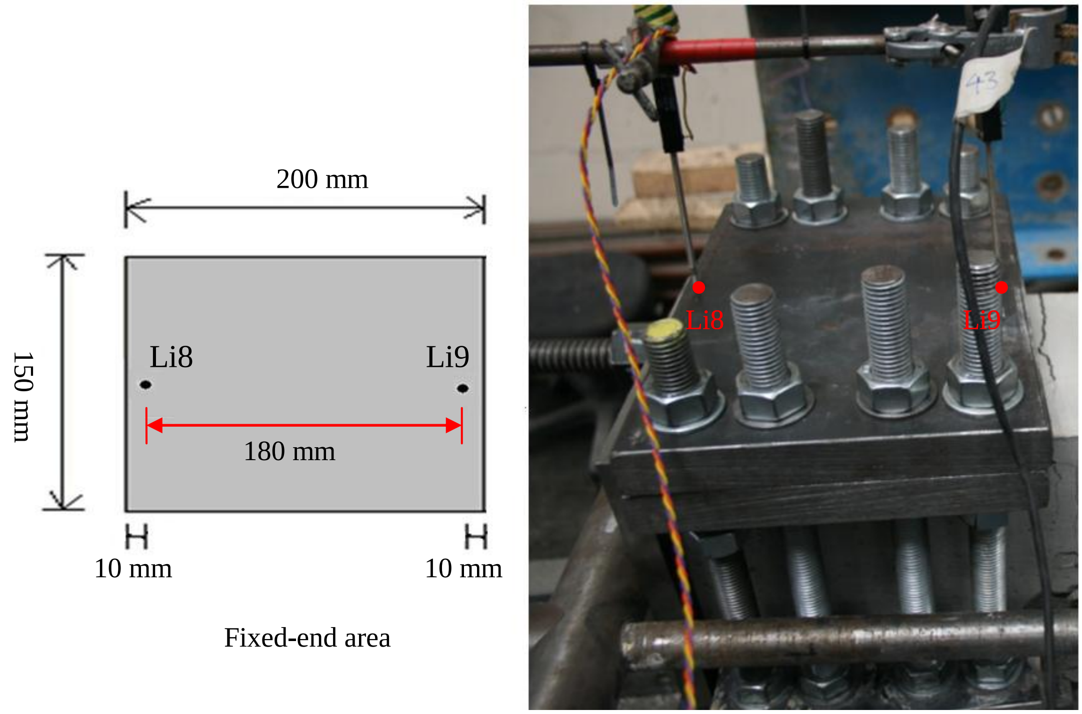

Figure 3-30: The two extra linpots added at the top of the fixed-end area

3.6.3 The loading frame

The testing frame is shown in Figure 3-31 (section along the specimen) and Figure 3-32 (photograph of loading end of specimen). This can be thought to have two major parts: Parallel Flange Channel (PFC) section and Stiffened Universal Beam (UB) section. The frame was bolted to the strong points in the laboratory floor using 25 mm diameter screwed rod. The INSTRON 500 kN servo controlled actuator was fixed at the middle of the Stiffened UB (533 × 312 × 182 UB, see Figure 3-31) and connected to the laboratory hydraulic ring main by way of a Roell Amsler (Zwick) K7500 servo-controller (Figure 3-33).

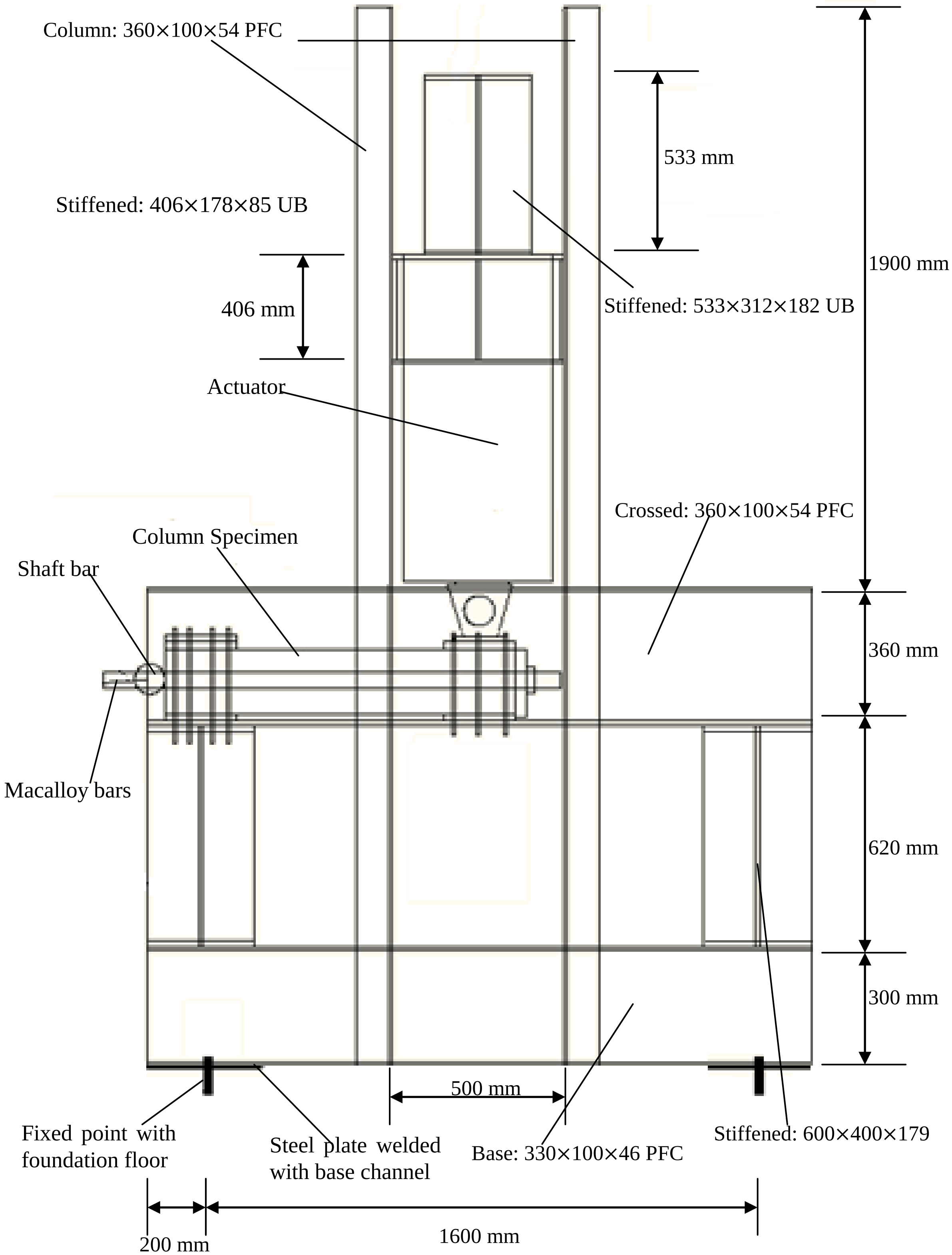

Figure 3-31: Loading frame layout

Figure 3-32: Loading frame

Figure 3-33: The controller for both static and cyclic tests

3.7 Specimen set up and load application

Care was taken when positioning the specimens for each test. Due to the weight of the specimens the overhead crane was used during their installation and removal. The procedure adopted was as follows:

Unclamp both ends of the completed specimen, carefully remove and clean the work area. Lift the new specimen into position, holding horizontally, supported by the crane. Clamp the fixed end and move the actuator so that the pinned end can be clamped whilst the specimen is horizontal. Then remove the crane support and apply the axial load as described below.

Prior to testing a support framework for the displacement gauges (linpots) was placed beneath the specimen.

3.7.1 Axial load application

The axial force was applied to the columns through two high strength (25 mm diameter) calibrated Macalloy bars. At the fixed-end of the specimen was a 50 mm diameter shaft-bar and protection-plate (see Figure 3-25). At the loading end was a compression-plate. An axial tensile force of 100 kN was applied to each Macalloy bar (total axial force is 200 kN). The strain gauge fixed at the middle of each Macalloy bar and the connection with the strain indicator box, as shown in Figure 3-36. For safety and convenience a plywood bar (see Figure 3-34) was used to support the extension bar and prevent the heavy compression-plate moving.

In order to apply the load an extension bar (connected using an extra coupler, see Figure 3-34) is added to the main bar. A hollow support (see Figure 3-35) with access to tighten the main nut was then placed over the extension bar and a hollow bore jack over this. A small spreader was placed over the extension bar and a further nut tightened. The jack was then extended until the bar indicated a load of 100 kN. The main nut was then tightened and the jack released to put the axial force into to the specimen. The operation was repeated on the second bar. The first bar was then checked to ensure that there were no losses, and the force was topped up if necessary. The jacking equipment and extension bar were then removed for the test.

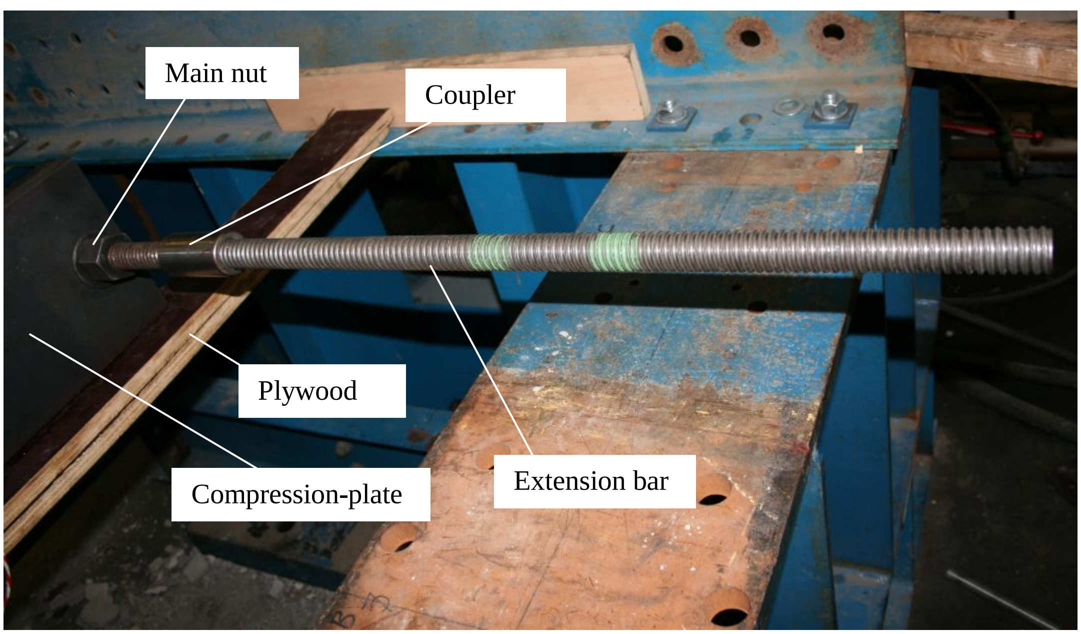

Figure 3-34: Extension bar and coupler

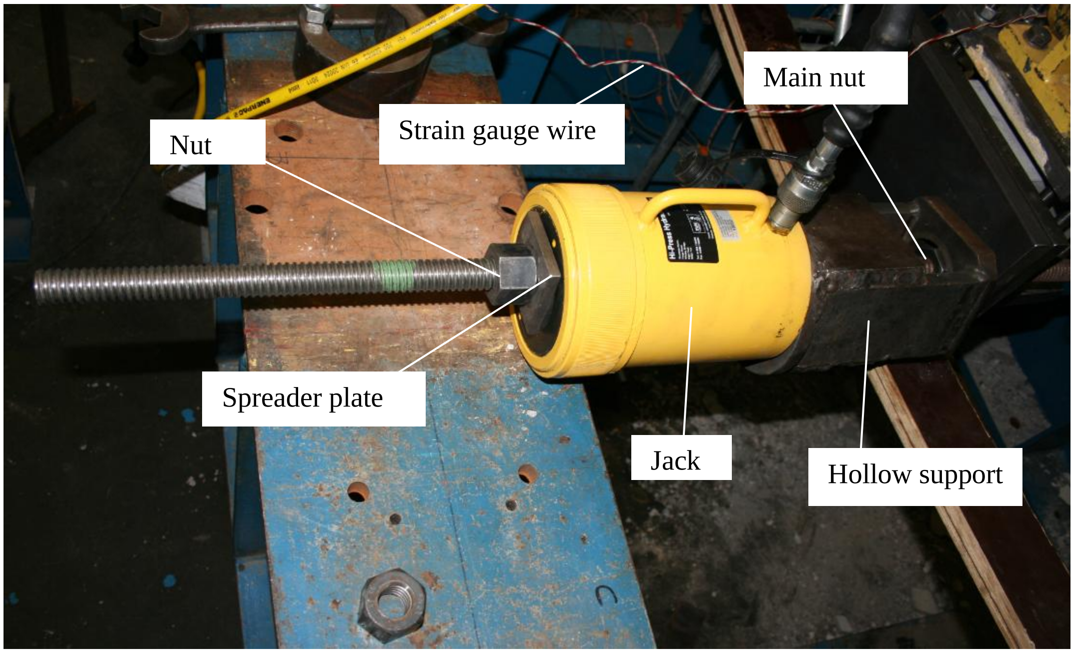

Figure 3-35: The hydraulic jack connection with the end of the Macalloy bar with an extra bar

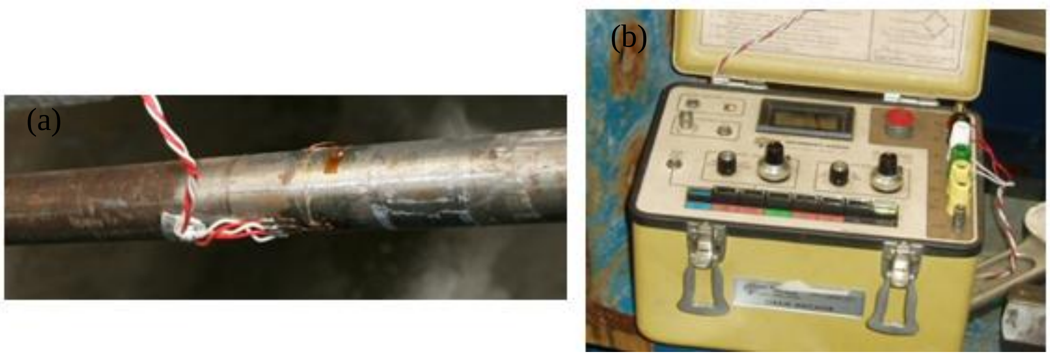

Figure 3-36: The strain gauge fixed at the middle of each Macalloy bar and the connection with the strain indicator box

3.7.2 Lateral load application

Two types of lateral loading were applied: Static and Cyclic. For both loads, the actuator was controlled in its displacement mode. The static tests were carried out first as their results provided the displacement for the cyclic load (detail shown below).

The test sequence was RC, FC2, FC4, RFC2, RFC3, RC-C, FC2-C and FC4-C, As described in Table 3-3.

Static loading test: The actuator was moved uniformly at 0.5 mm/s, which guaranteed sufficient data, with recording scans twice every second.

Cyclic loading test: The amplitude (A) for each test was 60% of the ultimate achieved in the static test, as shown in Eq 3-5.

$$A = 0.6 \times d_{\text{peak load}} \qquad \text{Eq 3-5}$$

Where:

A	Amplitude of test applied
$d_{\text{peak load}}$	The peak load of the specimen under static loading

The test of cyclic load, started with a slow single cycle (0.5 mm/s) to record displacement throughout. Then, the actuator applied high movement speed at 1 Hz. As the data recorder was not able to capture sufficient data at the faster speed it was decided to carry out a low speed cycle at the predetermined intervals of 100, 200, 400 and 600 cycles. Finally, the actuator applied a static load to test the specimen to failure.

3.8 Summary

In this chapter the tests to establish material properties were presented, together with the fabrication method, the equipment design and the testing of the specimens. The following points are emphasized:

a) Material property tests have been conducted, including concrete, matrix, 12 mm diameter steel bar (longitudinal ribbed bar in RC), 3 mm diameter bar (transverse bar in RC) and welded mesh. The concrete and matrix properties were tested, that includes compression and split tests, using 100 × 200 mm cylinders.

b) Eight columns were cast: 2 reinforced concrete columns, 4 ferrocement columns and 2 strengthening reinforced concrete using ferrocement jacket columns.

c) The fabrication of the skeleton ferrocement includes cutting, bending and assembling from a roll of the mesh.

d) For safety, reliability and operability issues, all specimens were tested in a horizontal cantilever position. The two Macalloy bars applied constant axial load and the actuator applied lateral load.

e) The connector between actuator and loading area plate was a pin frame.

f) The linpots were located beneath the specimens.

g) The cyclic load test used a constant frequency (1 Hz), with constant amplitude (A). The amplitude was 60% of the ultimate achieved in the static test.

CHAPTER 4 Experimental results

4.1 Introduction

This chapter presents the results from the static and cyclic loading tests. Eight columns were tested, five subject to static loading (RC, FC2, FC4, RFC2 and RFC3) and three subject to cyclic loading (RC-C, FC2-C and FC4-C). The test specimen nomination is given in Table 3-3. For both loads application, the actuator was controlled in displacement mode. The static tests were conducted first as their results were used for the cyclic load tests. The test sequence was RC, FC2, FC4, RFC2, RFC3, RC-C, FC2-C and FC4-C.

Linear potentiometers (linpots) were used to measure the displacement of each specimen (see §3.6.2). Stiffness and ductility were subsequently calculated and examined.

4.2 Initial displacement results

The first experimental test was on the reinforced concrete (RC) specimen. In order to measure the deflection, two parallel lines of linpots were used to determine rotation as well as deflection (§3.6.2).

Figure 4-1 shows the load-displacement results of RC. No twisting effect was observed during these static loading tests as the LiF1 curve overlapped the LiB1 curve during the loading process. Furthermore, the LiF4 curve follows the LiB4 curve exactly (the nomination of LiF and LiB shows in §3.6.2).

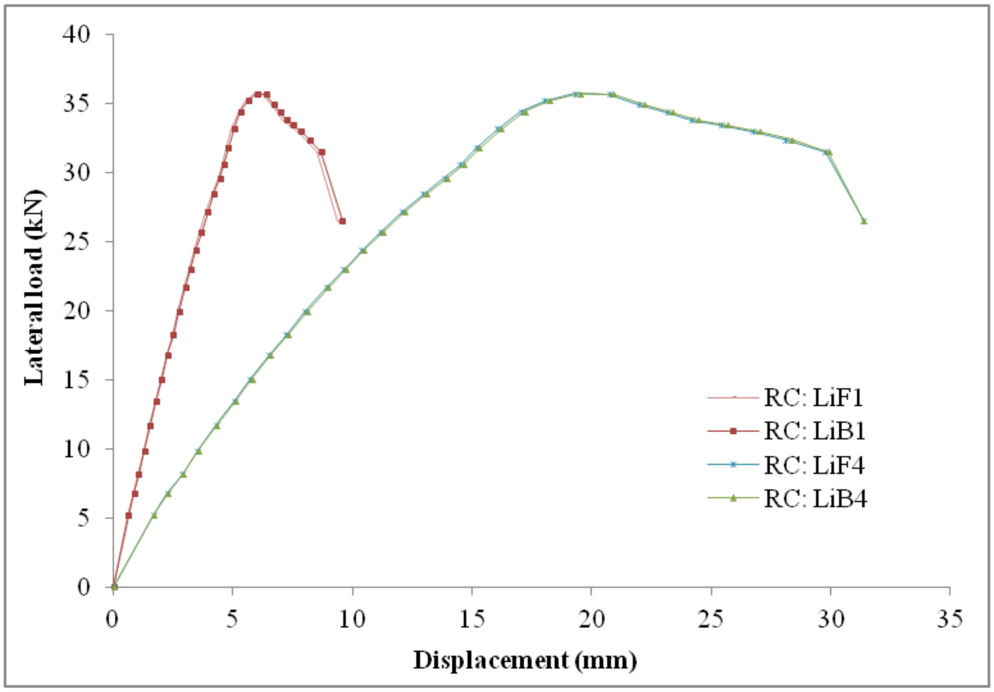

Figure 4-1: Load-displacement relationships for LiF1, LiB1, LiF4 and LiB4 (RC)

After the first column (RC) test, a new arrangement of linpots was used for the remaining column specimens, which is a single line with 75 mm spacing, as shown in Figure 3-28.

4.3 The displacement at the top of the fixed-end plate

During the second test (FC2), the author observed that the fixed-end plate (see Figure 3-25) had a slight movement. Therefore, two extra linpots were added at the fixed-end plate and an additional test was performed (FC4). The two extra linpots (Li8 and Li9) were located at the positions shown in Figure 3-30, where Li8 was located 10 mm from one edge at the top surface of the fixed-end plate and Li9 was located 10 mm from the other edge.

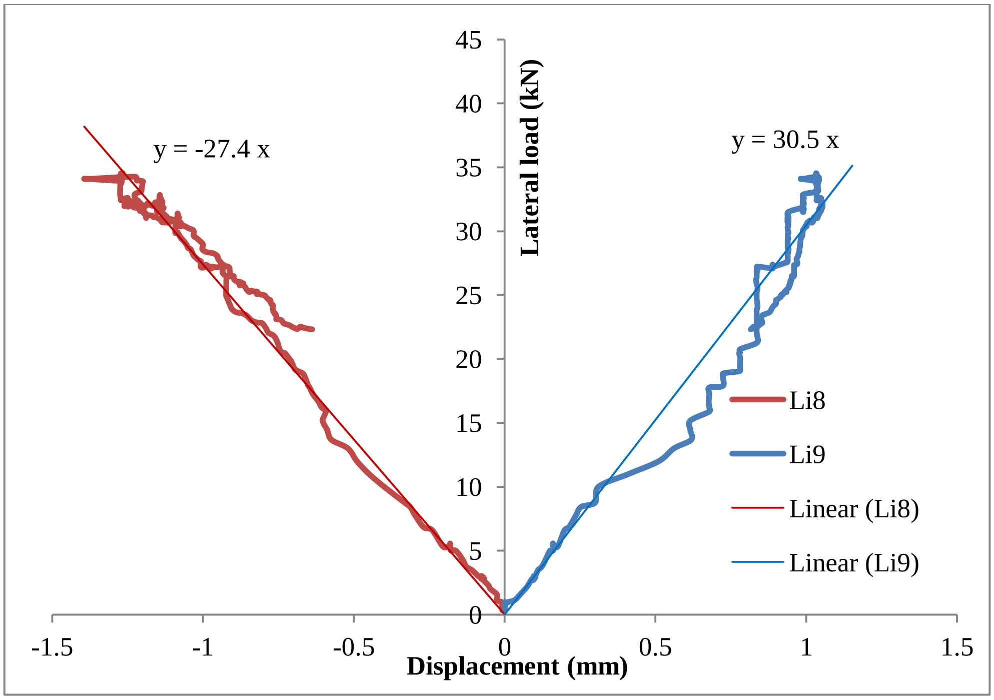

Figure 4-2: Load-displacement relationships for Li8, Li9 and best-fit linear curves

A reasonably linear relationship was observed between lateral load and displacement. Li8 had an upward movement with increasing load and a Li9 had a downward movement. When FC4 reached 34.7 kN (the maximum load), Li8 had 1.3 mm displacement, and Li9 had 1.1 mm displacement. After the peak load, both linpots moved in the reverse direction in a linear manner.

Assumptions of the experimental test shown in Figure 4-3, which the 8 steel bars at support end (see Figure 3-25) assumed connected with 2 linear springs. The forces of the springs are F1 and F2. The top of support end assumed rigid body.

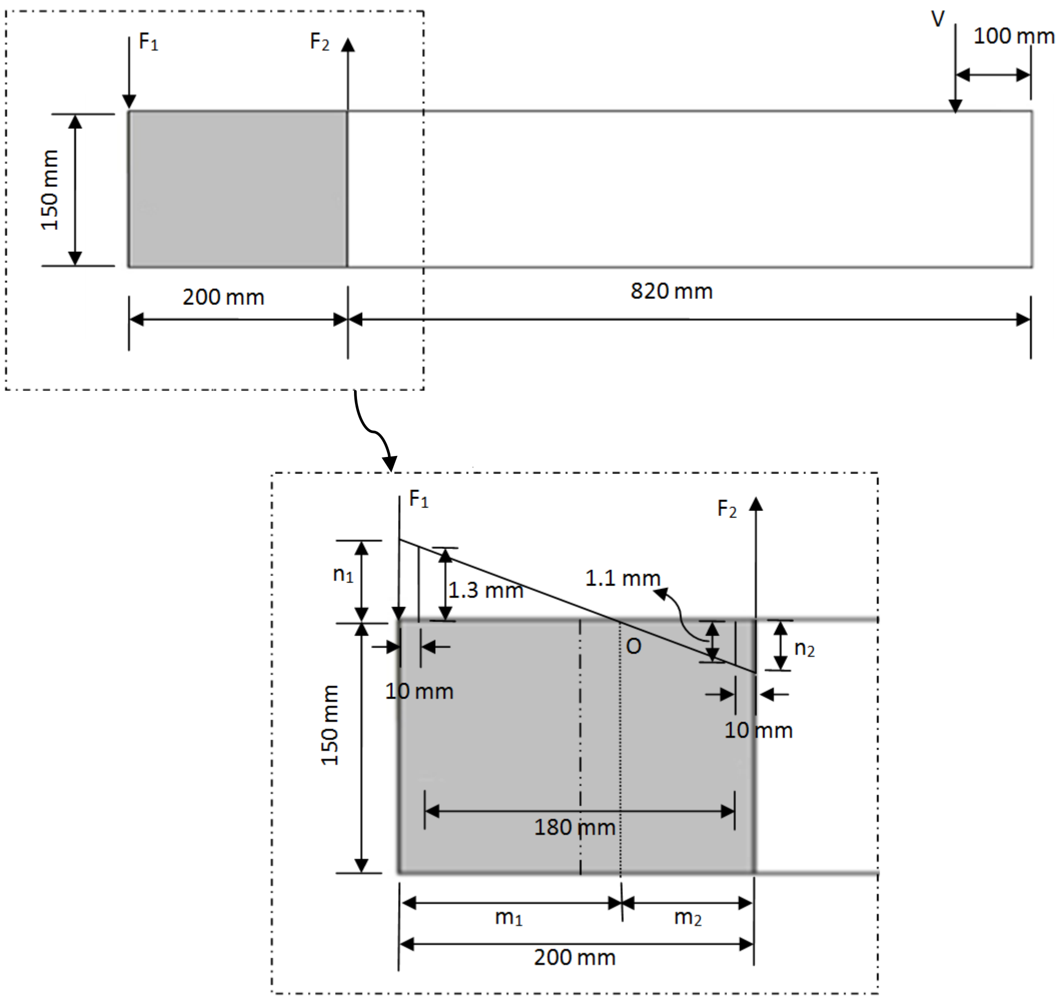

Figure 4-3: Simplified diagram of the specimen at the support end

Where:

V	The lateral load applied by the actuator
F_1, F_2	Assumed forces balancing the lateral forces: F_1 position at the edge of the concrete, F_2 position at 200 mm from the edge
n_1, n_2	The displacements at the edges
m_1, m_2	The distances from point F_1 and F_2 to point O. Point O has zero displacement when lateral load applied

The stiffness of these two points can be calculated considering moment equilibrium as:

$$\mathrm{M} = \mathrm{VL} = \mathrm{F_1 m_1} + \mathrm{F_2 m_2} \qquad \text{Eq 4-1}$$

Where:

L Length from point O to actuator load position

The values of $\mathrm{m_1}$ and $\mathrm{m_2}$ in Eq 4-1 are:

$$\mathrm{m_1} = \frac{180 \times 1.3}{1.3 + 1.1} + 10 = 107.5 \text{ mm}$$

$$\mathrm{m_2} = 200 - 107.5 = 92.5 \text{ mm}$$

Then, value of L is 720 + 92.5 = 812.5 mm

$$\mathrm{n_1} = \frac{1.3 \times 107.5}{97.5} = 1.43 \text{ mm}$$

$$\mathrm{n_2} = \frac{1.1 \times 92.5}{82.5} = 1.23 \text{ mm}$$

By substituting the values of $\mathrm{m_1}$ and $\mathrm{m_2}$ into Eq 4-1 yields:

$$\mathrm{M} = \mathrm{VL} = 34000 \times 812.5 = 27.6 \times 10^6 \text{ Nmm}$$

$$\mathrm{M} = 27.6 \times 10^6 = \mathrm{F_1} \times 107.5 + \mathrm{F_2} \times 92.5$$

The load equilibrium is:

$$34000 = -\mathrm{F_1} + \mathrm{F_2}$$

Then

$$\mathrm{F_1} = 122400 \text{ N}$$

$$\mathrm{F_2} = 156400 \text{ N}$$

Hence, the stiffness for each edge of the fixed-end plate is:

$$\mathrm{k_1} = \mathrm{F_1/d_1} = (122400/1.43) \text{ N/mm} = 85.6 \text{ kN/mm}$$

$$\mathrm{k_2} = \mathrm{F_2/d_2} = (156400/1.23) \text{ N/mm} = 127 \text{ kN/mm}$$

4.4 Reinforced concrete column under static load

Specimen RC had 4 longitudinal bars with 7 stirrups and the load-displacement curves at various positions are shown in Figure 4-4. At the position under the actuator (Li-A), the displacement showed linearity until the lateral load reached approximately 30 kN, with a deflection of 16.5 mm. When the maximum load capacity was reached (35.7 kN), the measured displacement was 23.9 mm. After the peak load, the load reduced.

Observation of RC: The actuator applied force downward on the loading-plate with a speed 0.5 mm/s. Initially, as the displacement increased, the value of lateral load increased. The first crack was observed on the top surface near the fixed end, when the actuator had moved 12 mm and the lateral load was approximately 23 kN. Then more cracks were observed. As the actuator deflection increased, the cracks penetrated from the top surface through to the underside. At an actuator displacement of 23.9 mm, the lateral load reached its maximum, then the load dropped the cracks continued to expand and concrete fragments started to drop from the underside of the specimen at its fixed-end. The column after testing is shown in Appendix C.

Figure 4-5 shows the displacement for each linpot at four different lateral loads together with support rotation effect. The four loads selected, expressed as a multiple of the peak load, were 0.33, 0.66, 1.00 and 0.85 post peak load. The components of displacement at Li-A are shown in Figure 4-6, including total displacement and the two major contributing factors, which are the support rotation effect and the bending-shear effect.

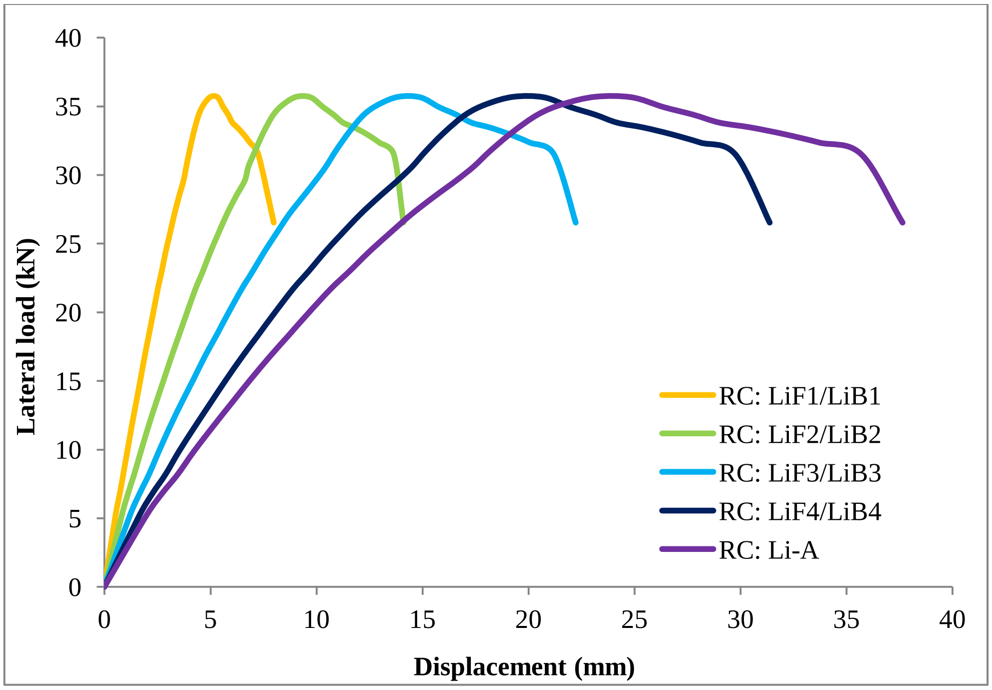

Figure 4-4: Load-displacement curves at different positions (Initial column, RC)

Table 4-1 presents the support rotation effect and bending-shear effect displacement percentage at different loads (33%, 66%, 100% and 85% post peak load).

At 33% peak load (11.9 kN), the support rotation effect provides 67% of the displacement (3.5 mm), which is nearly twice the bending-shear effect. At 66% peak load, the support rotation effect reduced to 57%. At approximately 90% peak load (32.3 kN), the rotation and bending-shear effect were equal. The rotation effect provides 44% at peak load (35.7 kN), after that the bending-shear effect was dominant. At the 85% post peak load (30.3 kN), the percentage of the bending-shear effect on the overall displacement rose to 76%

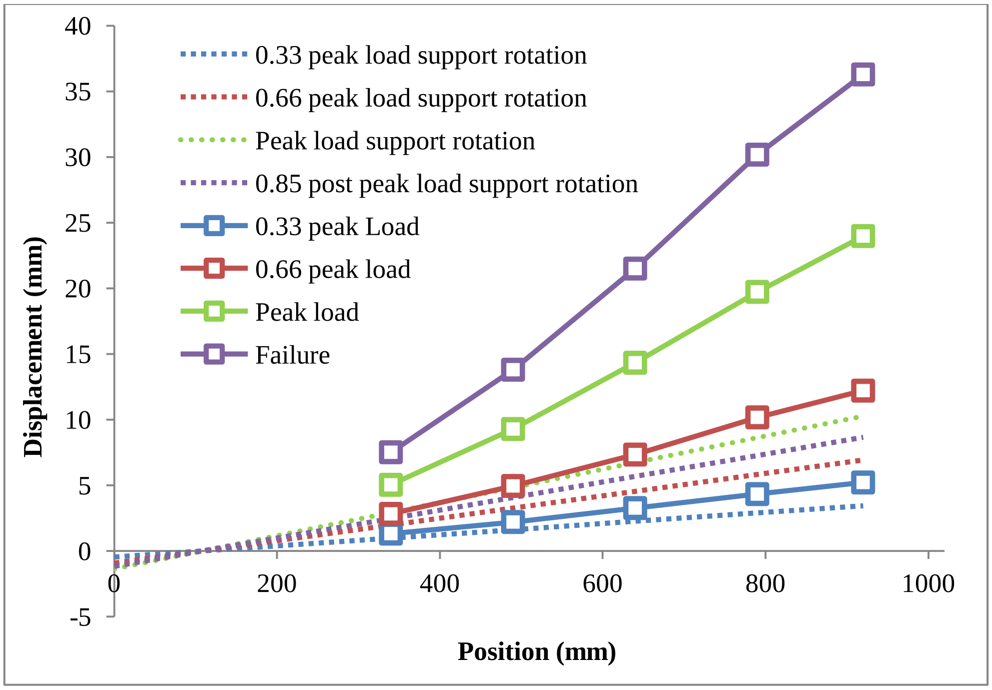

Figure 4-5: Displacement for each linpot at different loads (Initial column, RC)

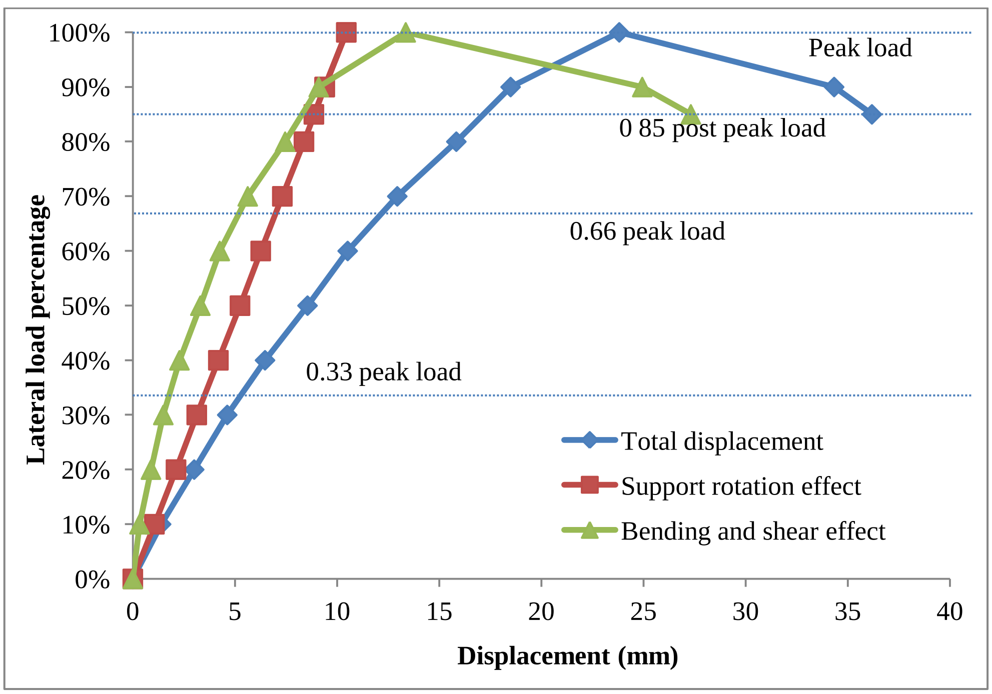

Figure 4-6: Load-displacement curves for the support rotation effect and the bending-shear effect at Li-A (Initial column, RC)

Table 4-1: Results of the support rotation effect and the bending-shear effect (RC)

Specimen	**Lateral load applied**		**Total disp. (mm)**	**Support rotation effect**		**Bending-shear effect**	
	Load (kN)	**Percent (%)**		**Absolute value (mm)**	**Percent (%)**	**Absolute value (mm)**	**Percent (%)**
RC	11.9	33%	5.2	3.5	67%	1.7	33%
	23.8	67%	12.2	7.0	57%	5.2	43%
	32.3	90%	18.8	9.5	50%	9.3	50%
	35.7	100%	23.9	10.5	44%	13.4	56%
	30.3	85%	36.2	8.9	24%	27.3	76%

Checking the result at 33% peak load for the RC specimen (5.2 mm for test, 3.5 mm for rotation effect and 1.7 mm for bending-shear effect), with the load displacement in the linear elastic stage. Using Eq 4-2, assume the specimen was a cantilever.

$$\Delta_A = \frac{VL^3}{3EI}\left[1 + 0.6(1+\upsilon)\frac{h^2}{L^2}\right] \qquad \text{Eq 4-2}$$

Where:

Δ_A	Cantilever deformation one the underside of point Li-A
L	Length of the cantilever
V	Lateral load
E	Young's Modulus of composite
I	Second moment of area
υ	Poisson's ratio
h	Width of column

The result of calculation of Δ_A at 33% peak load is 1.6 mm (detail provided in Appendix D), which is close to the bending-shear effect displacement (1.7 mm)

4.5 Ferrocement column under static load

FC2 and FC4 columns had an inner skeleton which was comprised of a box of welded mesh with 3 mm cover on all sides. Figure 4-7 shows the test results at Li-A (the full set of results are given in Appendix E), the load-displacement curve for both specimens are similar; however, the maximum load capacity and deflection were different.

Observation of FC2 and FC4: Initially, as the actuator deflection increased, the value of lateral load rose. The first crack was observed at the top surface near the fixed end at lateral loads of 16 kN for FC2, and 20 kN for FC4. After that, the first crack grew and more cracks were observed. The observed crack width on FC2 was greater than that on FC4. The cracks of both specimens penetrated from the top surface to bottom surface, and could be observed on the surface at the front and back. After the peak load (29 kN for FC2 and 34.7 kN for FC4), the load dropped and the cracks continued to expand. Under the fixed-ends concrete fragments started to drop from the specimens.

Both FC2 and FC4 had the same stiffness at the start of the test. FC2 reach a peak load of 29 kN at 20.9 mm displacement, and FC4 reached a peak load 34.7 kN at 23.5 mm displacement. The 20% higher load capacity of FC4 is due to its higher reinforcement content.

After the specimens had reached their peak loads, the load dropped. This drop is significant for FC2 (see Figure 4-7); the bond slip occurred at the peak load with the outer layer of mesh yielding. However as FC4 had a denser mesh (higher amount), the bond slip effect was less. After that, in both specimens, the welded mesh carries the load.

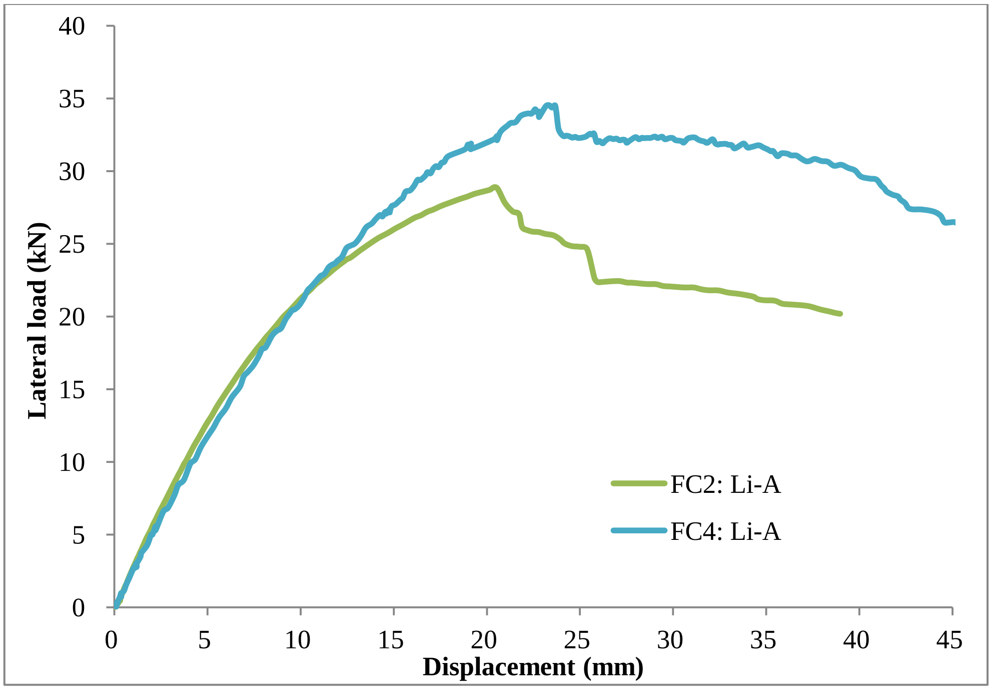

Figure 4-7: Load-displacement curves at Li-A (FC2 and FC4)

Figures 4-8 and 4-9 show load-displacement curves for the support rotation effect and the bending-shear effect for FC2 and FC4 at Li-A, including the total displacement. The support rotation effect and bending-shear effect displacement for FC2 and FC4 at different load levels related to peak load (0.33, 0.66, 1.00 and 0.85 post peak load) are presented in Table 4-2.

With increasing lateral load, the percentage contributions of the support rotation effect were reduced. At 33% peak load, the support rotation effect for both specimens was significant, i.e. providing 65% of the displacement for FC2 and 69% for FC4. The lateral loads, for FC2 was 9.26 kN, which is 10% lower than that for FC4 (11.2 kN).

At 66% peak load, the rotation effect for FC2 had approximately the same percentage (64%) as at 33% peak load, but for FC4, the rotation effect was less important, reducing to 60%. The value of lateral load for each specimen was 18.6 kN for FC2, 23.1 kN for FC4.

At approximately the same percentage of lateral load for both specimens (90% for FC2, 91% for FC4), the bending-shear effect was equal to the support rotation effect.

At the peak load, the bending-shear effect for both specimens has a greater effect than the rotation effect (40% for FC2 and 43% for FC4).

At 85% post peak load, the support rotation effect reduced to 28% for FC2 and 21% for FC4.

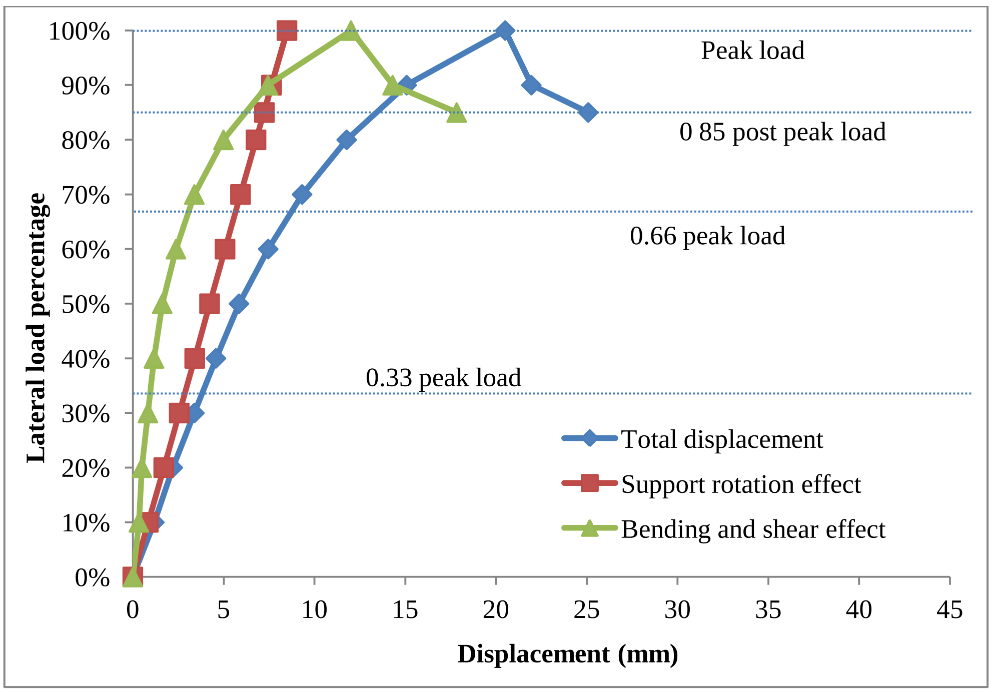

Figure 4-8: Load-displacement curves for the support rotation effect and the bending-shear effect at Li-A (FC2)

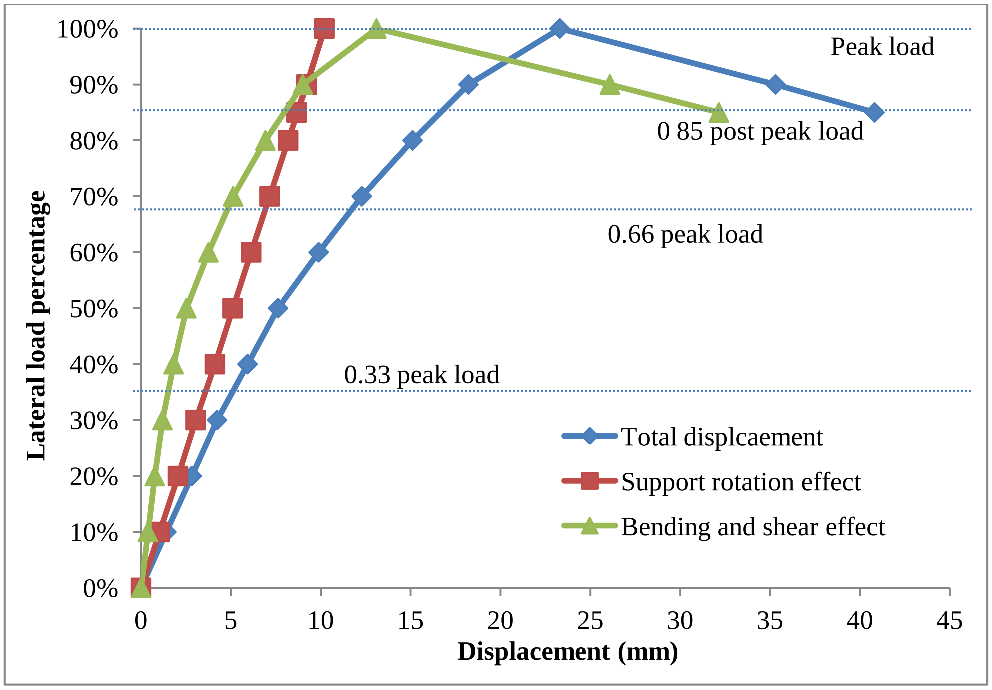

Figure 4-9: Load-displacement curves for the support rotation effect and the bending-shear effect at Li-A (FC4)

Table 4-2: Results of the support rotation effect and the bending-shear effect (FC2 and FC4)

Specimen	Lateral load applied		Total disp. (mm)	Support rotation effect		Bending-shear effect (mm)	
	Load (kN)	Percent (%)		Absolute value (mm)	Percent (%)	Absolute value (mm)	Percent (%)
FC2	9.7	33%	4.4	2.7	65%	1.6	35%
	19.3	67%	8.5	5.4	64%	3.1	36%
	26.1	90%	15.1	7.6	50%	7.5	50%
	29.0	100%	20.9	8.3	40%	12.2	60%
	24.7	85%	24.9	7.0	28%	17.9	72%
FC4	11.6	33%	4.8	3.3	69%	1.5	31%
	23.1	67%	11.2	6.7	60%	4.5	40%
	31.2	91%	18.2	9.1	50%	9.1	50%
	34.7	100%	23.5	10	43%	13.5	57%
	29.5	85%	40.8	8.5	21%	32.3	79%

Checking the deformation result at 33% peak load for FC2 and FC4 using Eq 4-2. For FC2, the result of Δ_A is 1.79 mm and the bending-shear effect is 1.6 mm which shows a 11% difference. For FC4, the result of Δ_A is 1.93 mm and the bending-shear effect is 1.5 mm which shows a 28% difference. This may be because in the simplified sections in the hand calculations, the meshes are merged to form one layer and are uniformly distributed in section. Details of the Δ_A calculations are given in Appendix D.

4.6 Reinforced concrete column strengthened using ferrocement jacket under static load

RFC2 and RFC3 were reinforced concrete columns strengthened using ferrocement jackets and were tested under static loading. The column cross-sections were 180 × 180 mm, the ferrocement was the same as for FC2 and FC4, with a cover of 3 mm. The test results for RFC2 and RFC3 are shown in Figure 4-10, and the behaviour of these two columns was similar. Both columns show a significant increase in load capacity at failure in comparison with RC.

The initial stiffness for both columns was less than RC. This might be due to the possibility that the dental plaster did not provide a perfect contact (see Figure 3-27). The dental plaster was to ensure the specimen support and loading areas were uniform and horizontal. The ultimate load of RC without strengthening is 35.7 kN. The columns strengthened using two-layers and three-layers of mesh achieved 50.9 kN and 57.7 kN respectively, representing nearly 46% and 66% extra capacities.

The outer ferrocement jacket played a confinement role, which provides a significant increase in the load capacity. As the ductility of the welded mesh is high, it produces a smoother descent stage in the load-displacement curve.

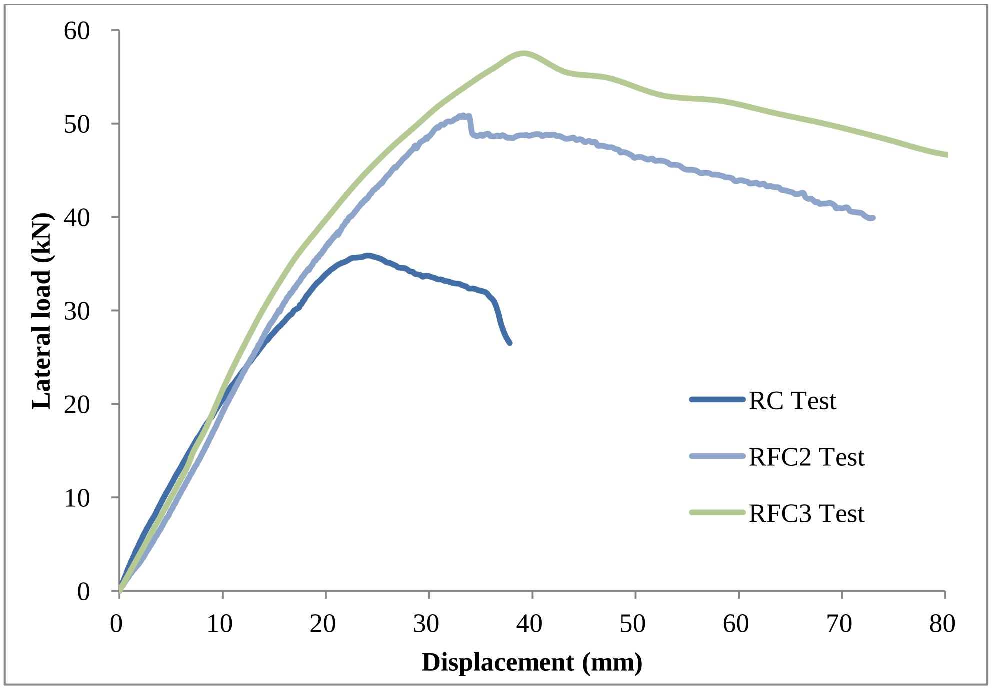

Figure 4-10: Load-displacement curves for the RC and strengthened RC columns under static load at Li-A

Observation of RFC2 and RFC3: The first crack was observed at the top surface near the fixed end, at a lateral load of around 30 kN for RFC2, and 33 kN for RFC3. The observed crack widths for RFC2 and RFC3 were similar, and were small cracks distributed on the top surface. After the peak load (RFC2 reached 50.9 kN and RFC3 reached 57.7 kN), the load dropped.

The support rotation effect and bending-shear effect on displacement of RFC2 and RFC3 at different loads (0.33, 0.66, 1.00 and 0.85 post peak load) are presented in Figures 4-11 and 4-12, the results are presented in Table 4-3. The displacement of RFC2 at peak load was 33.6 mm and at 0.85 post peak load was 62 mm. RFC3 also had a significant displacement difference between peak load and 85% post peak load.

At 33% peak load, the support rotation effect for both specimens was significant, 63% for RFC2, 64% for RFC3. The lateral load for RFC2 was 17 kN and RFC3 was 19.2 kN.

At 66% peak load, the rotation effect for RFC2 was 56%, and for RFC3 was 58%. The value of lateral load for each specimen was, 33.9 kN for RFC2 and 38.5 kN for RFC3.

At approximately similar percentages of lateral load (91% for RFC2, 89% for RFC3) for both specimens, the bending-shear effect equalled the support rotation effect.

At peak load, the bending-shear effect for both specimens had a greater effect than the rotation effect (RFC2 had 45% and RFC3 had 44%).

At 85% post peak load, the bending-shear effect is significantly more important for both specimens, being 79% for both specimens.

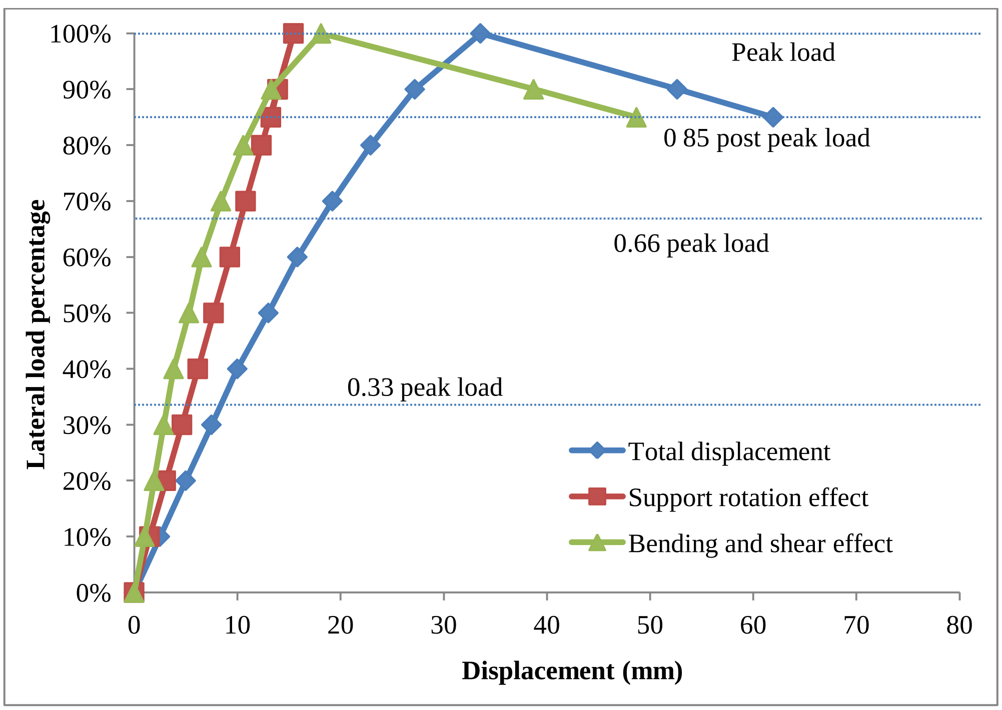

Figure 4-11: Load-displacement curves for support rotation effect and bending-shear effect at Li-A (RFC2)

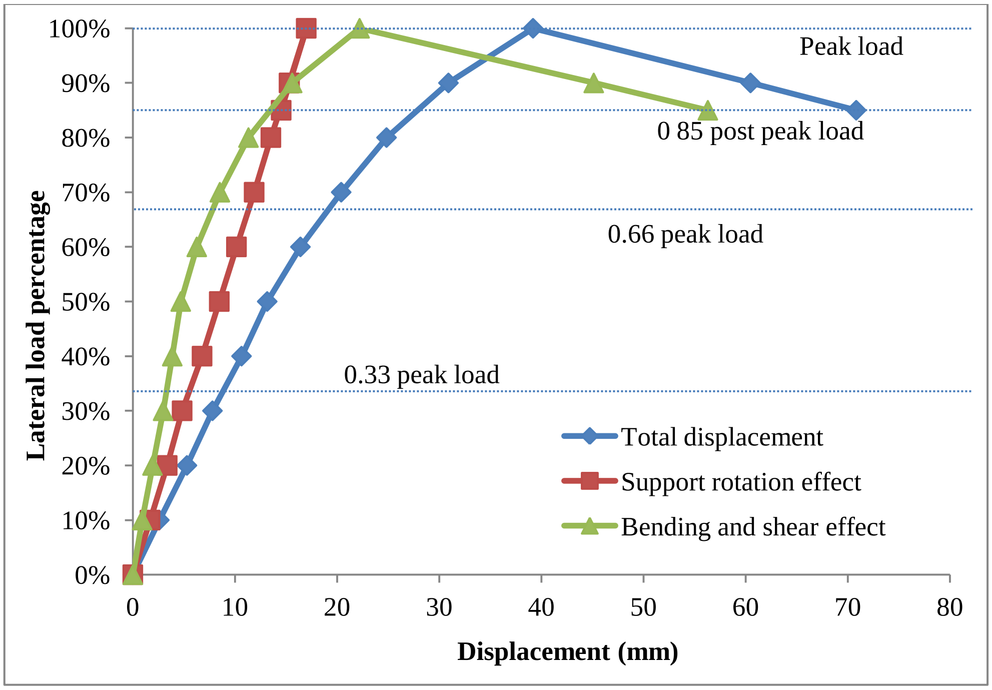

Figure 4-12: Load-displacement curves for support rotation effect and bending-shear effect at Li-A (RFC3)

Table 4-3: Results of support rotation effect and bending-shear effect (RFC2 and RFC3)

Specimen	Lateral load applied		Total disp. (mm)	Support rotation effect		Bending-shear effect (mm)	
	Load (kN)	Percent (%)		Absolute value (mm)	Percent (%)	Absolute value (mm)	Percent (%)
RFC2	17.0	33%	8.0	5.1	63%	2.9	37%
	33.9	67%	18.1	10.1	56%	8.0	44%
	46.3	91%	27.6	13.8	50%	13.8	50%
	50.9	100%	33.6	15.2	45%	18.4	55%
	43.3	85%	62.0	12.9	21%	49.1	79%
RFC3	19.2	33%	9.1	5.7	64%	3.3	36%
	38.5	67%	19.7	11.5	58%	8.2	42%
	51.4	89%	30.8	15.3	50%	15.5	50%
	57.7	100%	39.2	17.2	44%	22.0	56%
	49.0	85%	70.8	14.6	21%	56.2	79%

Checking the deformation result at 33% peak load for RFC2 and RFC3 using Eq 4-2. For RFC2, Δ_A is 1.26 mm, and the bending-shear effect is 2.9 mm. For RFC3, Δ_A is 1.43 mm, and the bending-shear effect is 3.3 mm. There are large differences for these two columns, so the author calculated new second moment area (I) values ignoring the tensile strength of the matrix and concrete. The value of Δ_A is then 2.1 mm for RFC2 and 2.19 mm for RFC3. However, the results are still not good. The reasons for this may be: the restrain cracks inside the concrete or matrix, the imperfect bond between mesh and matrix, the non-uniform section, or the matrix had not perfectly penetrated through the meshes.

4.7 Cyclic loading tests

Three specimens were tested under cyclic loading, RC-C, FC2-C and FC4-C.The three tests followed the same procedure. Before the tests, the amplitude (A) was found for each specimen, the amplitude was 60% of the peak value achieved in the static test as shown in Eq 3-5. The amplitudes for RC, FC2-C and FC4-C were 14.5 mm, 12.5 mm and 14.0 mm.

4.7.1 Load reduction

The experimental test results are shown in Figures 4-13, 4-14 and 4-15. The positive load represents the downward force applied by the actuator. For each specimen, the amplitude was kept constant, so during the cyclic tests the loads showed a clear decreasing trend. The results are presented in Figure 4-16; more detail is given in Appendix E.

During the first cycle, RC-C reached a maximum load (26.6 kN at 14.5 mm), which is higher than that for the another two specimens. The maximum load for FC2-C was 22.2 kN at 12.5 mm and for FC4-C was 25 kN at 14 mm.

After 100 cycles, the maximum load of RC-C reduced to 24.8 kN, which is 7% lower than that for the first cycle. FC2-C was 10% lower (20 kN) and FC4-C was 7% lower (23.2 kN).

After 200 cycles, RC-C reached 23.5 kN, which is 12% lower than that for the first cycle, and after 400 cycles, the load further reduced (22.5 kN, 16% lower than the first cycle), then after 600 cycles, the load reduced to 20.9 kN (21% lower than the first cycle). FC2-C and FC4-C showed a similar trend to RC-C, where with an increasing number of cycles, the maximum load dropped.

However, FC4-C was more stable than either FC2-C or RC-C, in that after 600 cycles, the load reduced by only 11% (see Figure 4-16). Here the dense welded mesh acted as a confinement during the cyclic test and the crack width was much smaller than that for RC-C. FC2-C also had a dense mesh as confinement, but it had less reinforcement than FC4-C.

After 600 cycles, RC-C and FC2-C were pushed to failure, but for FC4-C, the load just reduced by 11% (22.2 kN). Therefore, the author decided to increase the cyclic load to 1000. The load reduced to 16.8 kN, 33% lower than the first cycle.

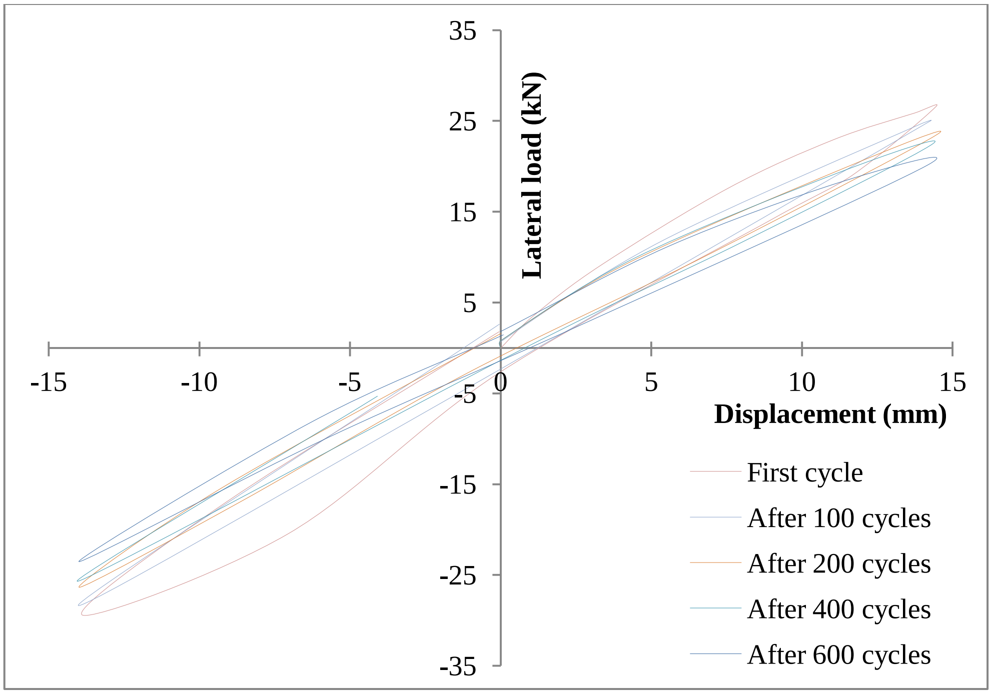

Figure 4-13: Load-displacement curves for RC-C under cyclic load at Li-A

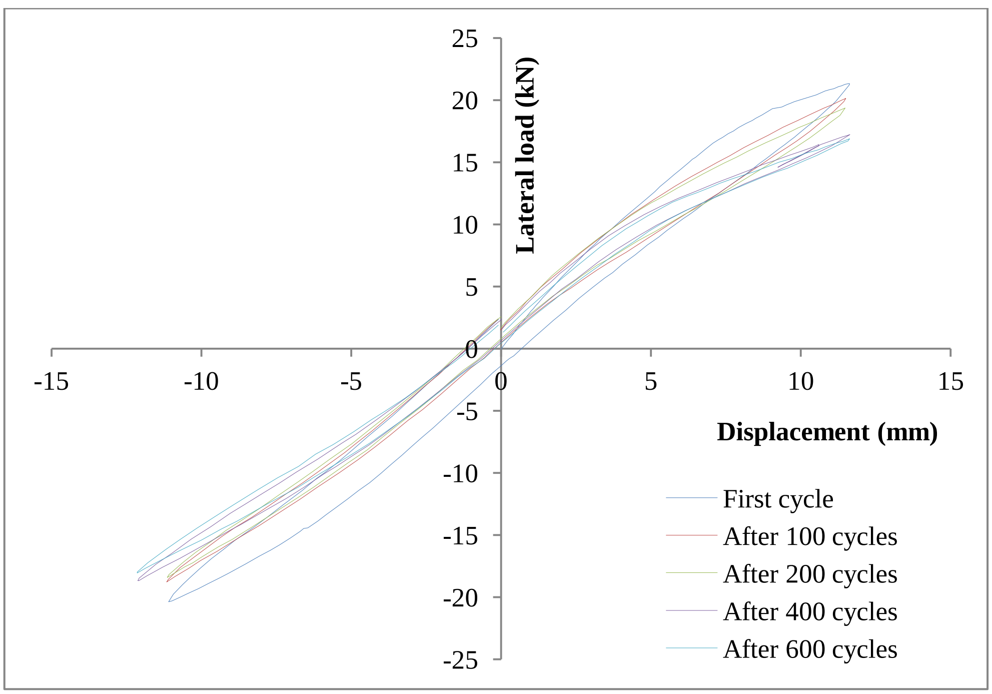

Figure 4-14: Load-displacement curves for FC2-C under cyclic load at Li-A

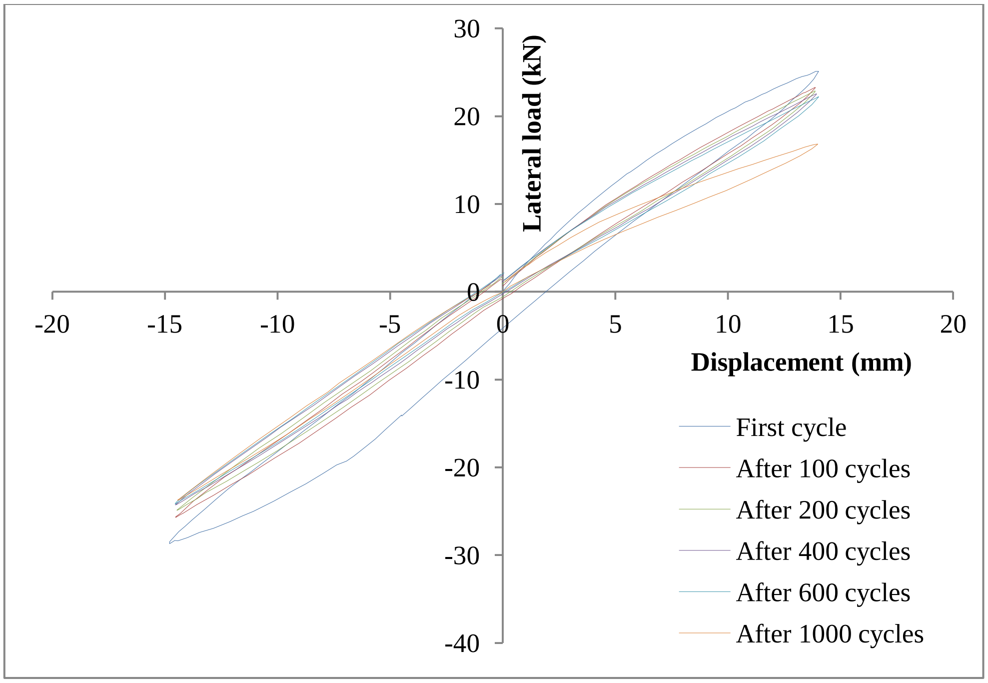

Figure 4-15: Load-displacement curves for FC4-C under cyclic load at Li-A

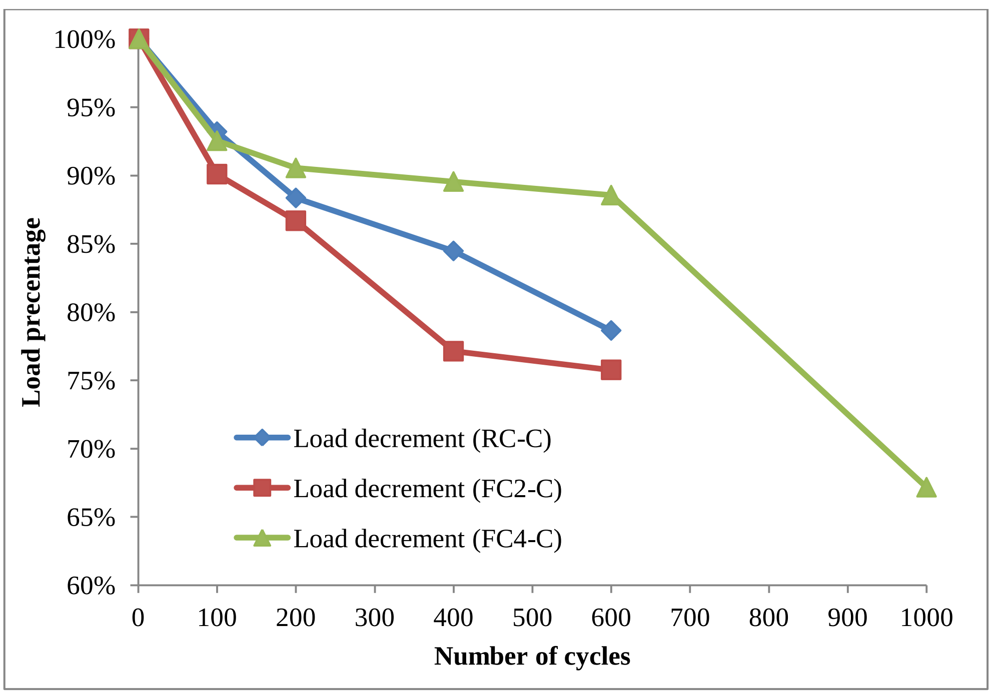

Figure 4-16: Load degradation against number of cycles (for details see Appendix E)

4.7.2 Stiffness degradation

The stiffness of column under cyclic load is degraded during number of cycles increase, it calculated as initial slope of curve lateral load against displacement. The stiffness degradation results are shown in Figure 4-17 and presented in Table 4-4. These three specimens have similar values of stiffness for the first cycle (RC-C had 2.5 kN/mm, FC2-C had 2.59 kN/mm and FC4 had 2.53 kN/mm).

After 100 cycles, the stiffness of RC-C dropped to 2.0 kN/mm, which is 20% lower than the initial value (first cycle), FC2-C and FC4-C were 8% and 9% lower. The reason for this is that the dense weld mesh is providing confinement, and it has stopped the crack width from increasing. That is why it is said that the ferrocement mesh structures have a huge potential for use in seismic zones.

After 200 cycles, the stiffness of RC-C was 1.95 kN/mm, which is 22% lower than the initial stiffness. Then after 400 cycles and 600 cycles, the stiffness of RC-C reduced to 1.84 kN/mm and 1.77 kN/mm. For FC2-C and FC4-C, the stiffness reduced with increasing number of cycles, between 200 and 400 cycles, the stiffness of FC2-C dropped much quicker than FC4-C. After 200 cycles, both specimens had the same stiffness degradation (89% of initial stiffness), but after 400 cycles, the stiffness of FC2-C had reduced to 1.99 kN/mm (23% lower than the initial value), and FC4-C had reduced to 2.07 kN/mm (18% lower than the initial value).

After 600 cycles, the stiffness degradations for RC-C and FC2-C were similar, 71% for RC-C and FC2-C for 72%, but for FC4-C the stiffness degradation was 79%.

The stiffness of FC4-C after 1000 cycles was 60%.

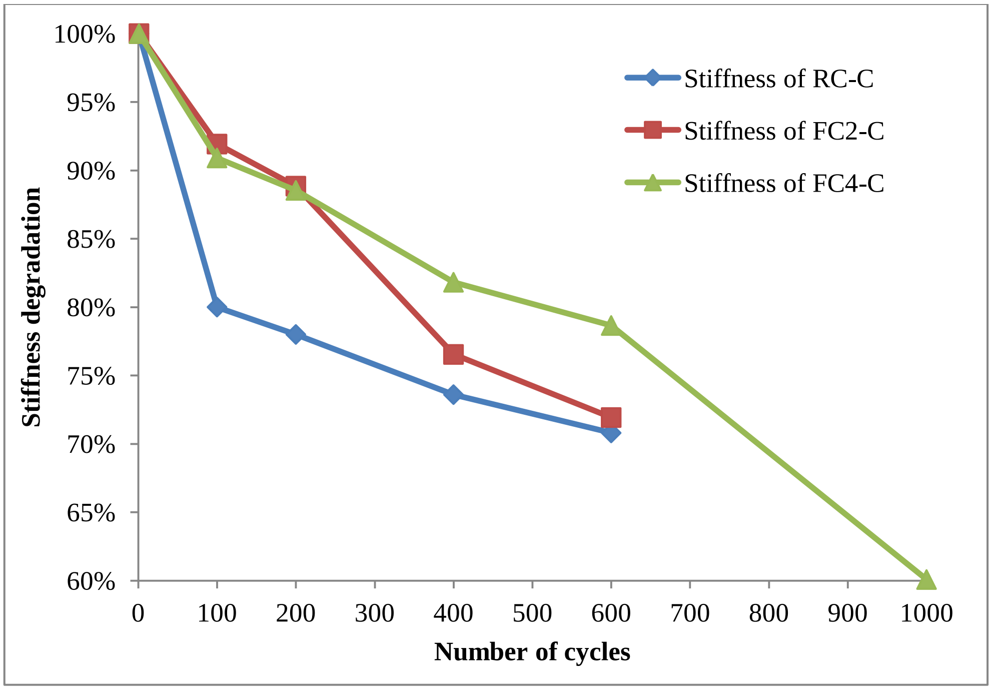

Figure 4-17: Stiffness degradation during number of cycles (for detail see Appendix E)

Table 4-4: Stiffness and degradation of RC-C, FC2-C and FC4-C

No. of cycles	RC-C		FC2-C		FC4-C	
	Stiffness (kN/mm)	**Stiffness degradation**	**Stiffness (kN/mm)**	**Stiffness degradation**	**Stiffness (kN/mm)**	**Stiffness degradation**
First	2.50	100%	2.59	100%	2.53	100%
100	2.00	80%	2.39	92%	2.30	91%
200	1.95	78%	2.31	89%	2.24	89%
400	1.84	74%	1.99	77%	2.07	82%
600	1.77	71%	1.87	72%	1.99	79%
1000					1.52	60%

4.7.3 Failure of the specimens

After cyclic loading, the actuator pushed each specimen to failure. The results of RC-C, FC2-C and FC4-C are shown in Figures 4-18, 4-19 and 4-20. Table 4-5 presents peak loads and displacements of specimens after cyclic loads.

After 600 cycles of RC-C (Figure 4-18), the peak load was 25 kN, which is 70% of its peak load under static testing. The displacement at peak load of was 20.8 mm.

For FC2-C, after 600 cycles, the peak load reached 20.7 kN, which was about 74% of the peak load under static test (FC2), as shown in Figure 4-19. At a lateral load of around 19 kN, FC2-C had an obvious drop and then the specimen continued to take the force by the welded mesh. The displacement at peak load was 28 mm. One possible explanation for the drop, which occurred at about 19 kN, is that there was bond slip between welded mesh and matrix.

For FC4-C, after 600 cycles, the peak load capacity reduced to 20 kN, which is 59% of the peak load in the static test (34.7 kN for FC4), as shown in Figure 4-20. After 1000 circles, the curve for FC4-C is smoother than FC4, and it does not show a clear drop like FC2-C, probably because the four-layers mesh have a higher amount of steel. The displacement at peak load is 24 mm for FC4-C.

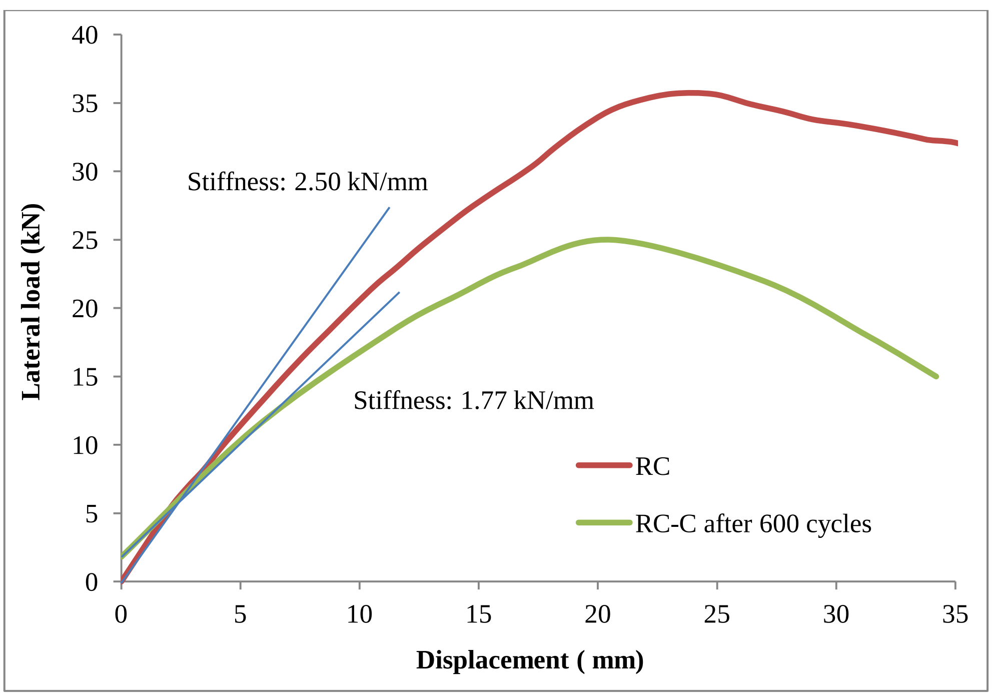

Figure 4-18: Load-displacement curves for RC-C after 600 cycles and RC at Li-A

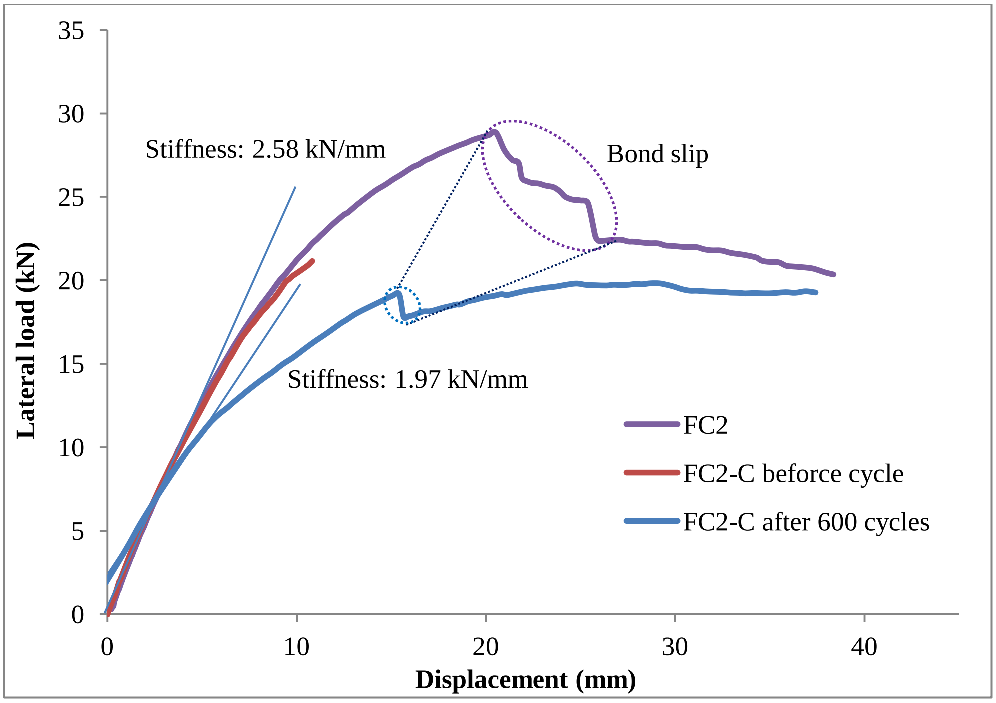

Figure 4-19: Load-displacement curves for FC2-C after 600 cycles and static test at Li-A

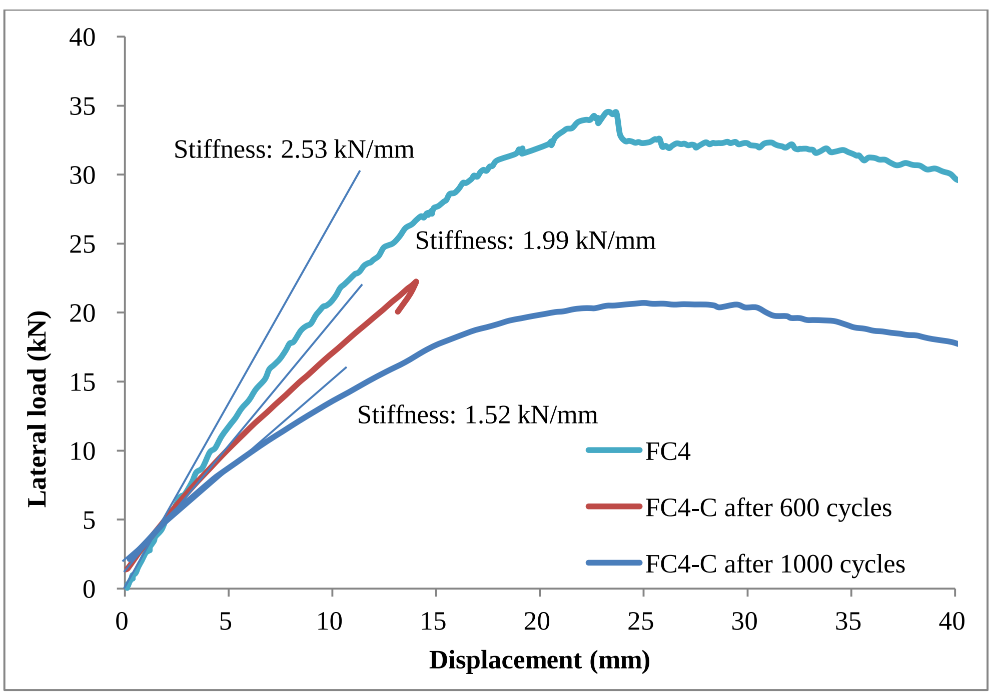

Figure 4-20: Load-displacement curves for FC4-C after 1000 cycles and static test at Li-A

Table 4-5: Peak load and displacement of specimens after cyclic load

Specimen	Peak load (kN)	Peak load degradation	Disp. at peak load (mm)
RC	35.7		23.9
RC-C after 600 cycles	25	70%	20.8
FC2	29		20.9
FC2-C after 600 cycles	20.7	74%	28
FC4	34.7		22.7
FC4-C after 1000 cycles	20	59%	24

4.8 Deformation ductility results

The value of column deformation ductility is calculated as the ratio of deformation at failure to deformation at yield. The energy balance method was used to create an idealised bi-linear curve, the effective yield being at the turning point of the bi-linear curve. The load-displacement diagram in Figure 4-21 shows the definition of the deformation ductility, and this is given in Eq 4-3.

$$\text{The deformation ductility } (\mu_\Delta) = \Delta_u/\Delta_{yI} \qquad \text{Eq 4-3}$$

Where:

μ_Δ Deformation ductility

Δ_u Displacement of the column in the descending branch corresponding to 0.85 of the maximum load

Δ_{yI} Effective yielding displacement

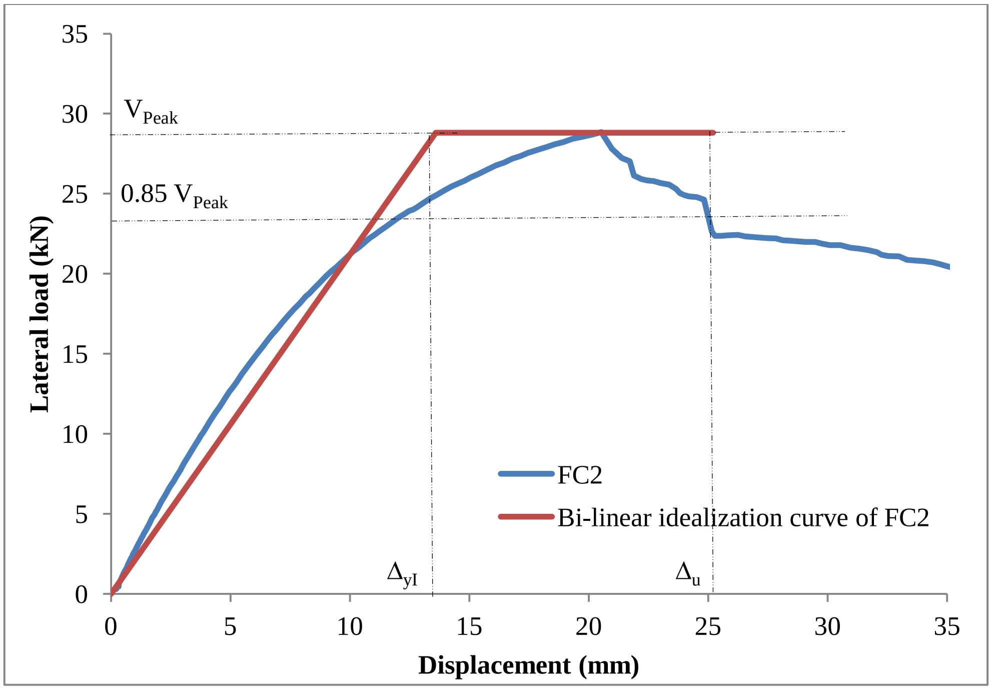

Figure 4-21: The bi-linear idealization curve (FC2)

Figure 4-22 gives an example (FC2) of estimating the position of Δ_{yI}, which is calculated using the area balance method (Barrera et al., 2012). The value of peak load is 29 kN at 20.9 mm displacement (Δ_p). Using a three-degree polynomial equation shows the specimen ascent stage (see Figure 4-22), as:

$$y = 0.0016x^3 - 0.1184x^2 + 3.1789x - 0.4106$$

Where:

x Displacement

y Lateral load

So the area above the x-axis equals:

$$\text{Area} = \int_0^{\Delta_p} (0.0016x^3 - 0.1184x^3 + 3.1789x - 0.4106)\, dx$$

Put the value Δ_p= 20.9 mm in equation, then:

$$\text{Area} = 381.6$$

So, this area equals to the area for the bi-linear representation at $\Delta_p = 20.9$ mm, then:

$$381.6 \times \Delta_{yI} \times V_{Peak} + (\Delta_p - \Delta_{yI}) \times V_{Peak}$$

Finally the value at Δ_{yI} is calculated and is 13.5 mm.

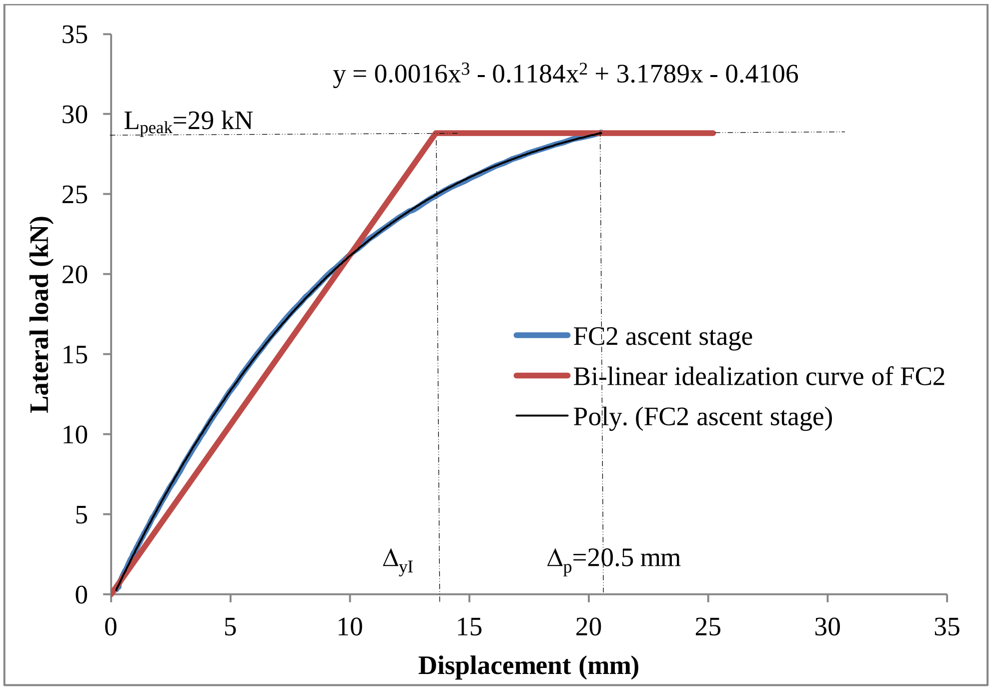

Figure 4-22: Calculating the value of Δ_{yI} example (FC2)

The deformation ductility is calculated as:

$$\mu_\Delta = \Delta_u / \Delta_{yI} = 25.1/13.5 = 1.86$$

Using the same method to measure the ductility of other the specimens yields the results shown in Table 4-6 (more details are shown in Appendix F).

Table 4-6: The deformation ductility results

Specimen	Peak load (kN)	Effective disp. (mm)	Ultimate disp. (mm)	Deformation ductility
RC	35.7	18.6	36.2	**1.95**
FC2	29	13.5	25.2	**1.86**
FC4	34.7	17.9	41	**2.29**
RFC2	50.9	28.6	62	**2.17**
RFC3	57.7	31.1	70.8	**2.28**

The deformation ductility of FC2 is 1.86, which is the lowest for these specimens; that for FC4 is 2.29, 22% higher than FC2. The deformation ductility of RC is 1.95 with peak load 35.7 kN; RFC2 has 11% greater deformation ductility and RFC3 has 17% higher ductility.

Both RFC2 and RFC3 had higher peak lateral loads and their deformation ductilities were also greater than that for RC. So it can be said that, the ferrocement jacket strengthened the RC, increased the load capacity and provided higher ductility which are both significant advantages.

With increasing mesh numbers the ductility rises.

4.9 Summary and conclusion

In this chapter, the results of the tests have been presented. These include static and cyclic tests. The following points are emphasized:

- The initial arrangement of linpots was two parallel lines used for the test on RC. This showed that the specimen did not twist during the loading.

- The displacement at top of the fixed-end plate was measured using two extra linpots. The stiffness for each end of the fixed-end plate was calculated, and it will be used in the ABAQUS modelling.
- The peak load for the ferrocement and the deformation ductility depends on the number of layers of mesh. More layers of mesh lead to higher peak loads and greater values of deformation ductility.
- The peak load for reinforced concrete strengthened using ferrocement jacket was increased significantly.
- During cyclic loading, the columns exhibit reduced load capacity for constant deformation. After cyclic loading, the peak load reduced significantly.
- With higher amounts of mesh (FC4-C) the specimens showed lower load reduction percentages for the same number of cycles.
- The stiffness of RC-C dropped much quicker than that of the ferrocement specimens.
- The deformation ductility was calculated using the energy balanced method. RFC3 had the highest ductility, and FC2 had the lowest.

CHAPTER 5 Finite element modelling

5.1 Introduction

Conducting column tests on ferrocement structures is time-consuming and expensive. To avoid these problems, ABAQUS, a commercial FEM package, has been used by researchers to study the behaviour of reinforced concrete structures. Due to the similarity of ferrocement and reinforced concrete, and based on available literature, ABAQUS has been used by the author in the present study.

ABAQUS has the ability to simulate complex structural behaviour under different loading conditions, such as tension, compression, shear, etc. Complex detailed models require significant computational resources. Ideally, the finite element model needs to be kept as simple as possible. Because of the nature of the reinforcement in ferrocement, a large amount of ferro-mesh including connections needs to be built into each model. If a complete three-dimensional (3D) solid model is chosen for the ferro-mesh, the model sizes and computational time will increase dramatically, which is undesirable for research purposes. Also a 3D-solid detailed model is not needed to capture the behaviour that is required in this study. Hence, a 3D non-linear FE truss model was chosen for the ferro-mesh.

Compared to the welded mesh, the matrix requires less element refinement. Also in ferrocement structures, the performance of the matrix influences the initial cracking and ultimate strength in compression. So a 3D non-linear finite element analysis approach is adopted for the ferro-matrix to provide a simulation that is more detailed and to provide results that are more accurate. The type of elements selected for matrix and ferro-mesh affect both the accuracy and the time taken for the computation.

5.2 Element type

5.2.1 Solid element: concrete and matrix

In the ABAQUS (2009) element library there are different types of element, for example hexahedron (brick), shell, triangular prism. etc. The most commonly used element for concrete studies is the three dimensional brick elements, is shown in Figure 5-1. C3D8 and C3D8R are the two main types of brick element.

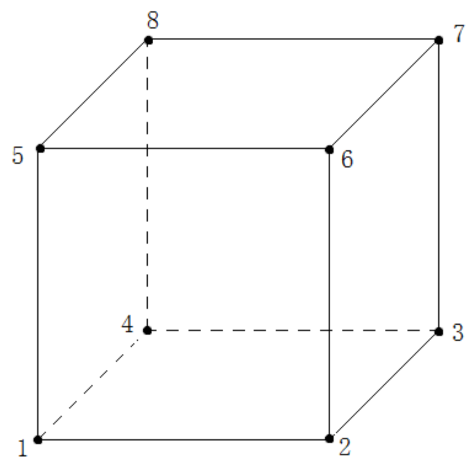

Figure 5-1: The three dimensional brick elements

C3D8: is a fully integrated linear hexahedral element, which contains eight Gauss points. The main advantage of this element type is its accuracy. The disadvantage is for flexural dominated structures. Shear locking phenomenon is commonly associated with this element type, especially for the elements bended, the finer element mesh could be solve this problem with longer time to simulate.

C3D8R: is an eight-node reduced-integration brick element, which has one Gauss point at the centre. Due to insufficient stiffness, spurious singularity (call the hourglass effect) may occur. It is possible for the elements to be distorted, so that the strains calculated at the integration point are all zero, which leads to uncontrolled distortion of the mesh. In order to control this, an artificial stiffness method and artificial damping method in the ABAQUS code is proposed.

For this thesis, the element used for concrete and the matrix was C3D8R. Using C3D8R underestimates the failure load slightly, but it is less time consuming, shear lock problems can be avoided and good results are obtained by adopting fine meshes.

5.2.2 Truss element: steel bar, stirrup and welded mesh

The reinforcement materials, including ribbed bars, stirrups and the welded mesh, are modelled using the T3D2 truss elements. These are two-node three dimensional straight truss elements.

5.3 Concrete damaged plasticity model

The concrete damaged plasticity (CDP) model is capable of capturing the behaviour of concrete and quasi-brittle materials. The inelastic behaviour of concrete can be incorporated using isotropic damage elasticity in combination with the isotropic tension and the compression plasticity. The model considers the degradation of the elastic stiffness due to tensile and compressive plastic straining.

The material property input in ABAQUS is in two groups, uniaxial stress-strain curves and plasticity parameters. These are shown in the following sections:

5.3.1 Concrete under uniaxial compression

Figure 5-2 shows the response of concrete under uniaxial compressive loading. The concrete will behave linearly until its stress reaches initial yield (σ_{c0}). Beyond σ_{c0}

hardening is developed in the concrete and then, after reaching the ultimate stress (σ_{cu}), strain softening is observed.

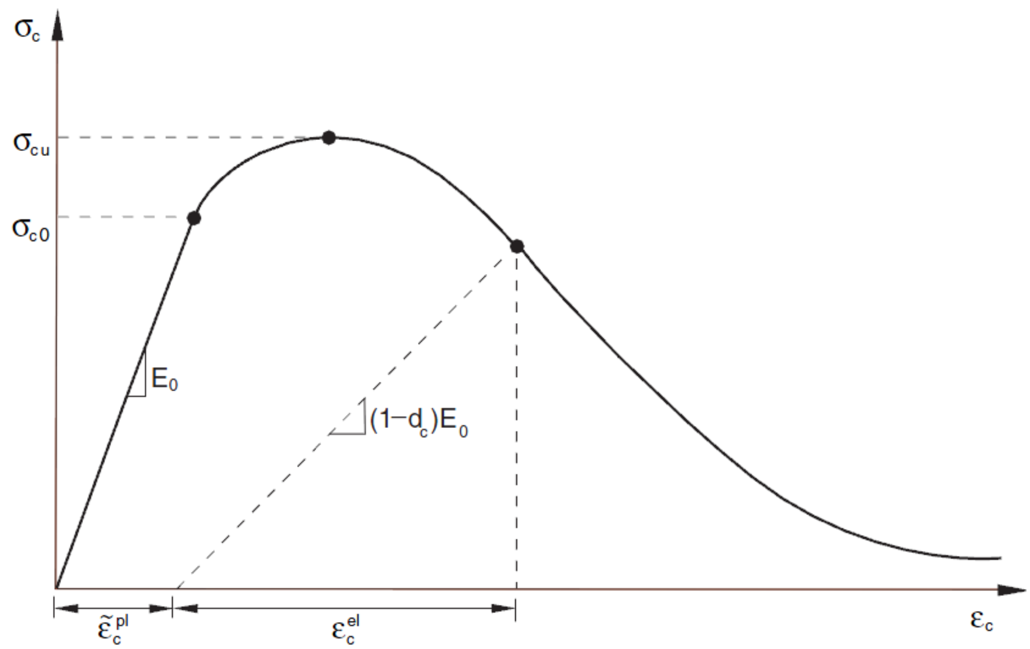

Figure 5-2: Stress-strain curve for plain unconfined concrete under uniaxial loading in compression (ABAQUS, 2009)

Where:

σ_c	Compression stress of concrete
σ_{c0}	Compression yield stress
σ_{cu}	Ultimate compression stress
ε_c	Compression strain
ε_c^{el}	Elastic compressive strain
$\tilde{\varepsilon}_c^{pl}$	Plastic compressive strain
d_c	Compressive damage variable

The damaged variables (d_c) help describe the effect of stiffness recovery during cyclic loading and degradation in the elastic stiffness of concrete. The damaged variables correlate with the plastic strains ($\tilde{\varepsilon}_c^{pl}$). The magnitude of the damage variables range from 0 to 1; with 0 representing the undamaged material and 1 meaning the total loss of material strength.

Therefore, to interpret the concrete damaged plasticity (CDP) model accurately, the compressive behaviour, tensile behaviour and plasticity, need to be considered.

5.3.2 Compressive behaviour for CDP

Compressive behaviour is defined as: the uniaxial compressive response of plain material beyond its elastic range. The inelastic strain is shown in ABAQUS (2009) documentation and is calculated as Eq 5-1:

$$\tilde{\varepsilon}_c^{in} = \varepsilon_c - \varepsilon_{0c}^{el} \qquad \text{Eq 5-1}$$

Where:

$\tilde{\varepsilon}_c^{in}$	Inelastic compressive strain of concrete
ε_{0c}^{el}	Elastic compressive strain of concrete at yield, σ_c/E_0

Two uniaxial compressive stress-strain models have been used in this thesis: Eurocode 2 (CEN, 2004a) and Popovics (1973).

5.3.2.1 **Eurocode 2 concrete material model:**

Figure 5-3 shows the relationship between stress and strain for concrete under uniaxial compression; the mathematical expression of which is given in Eq 5-2.

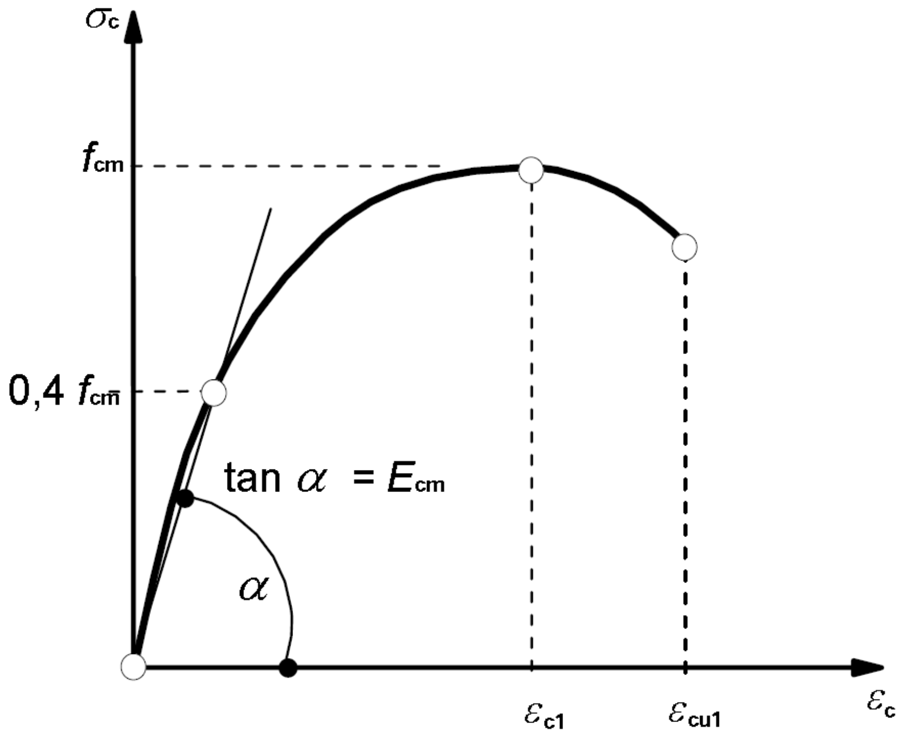

Figure 5-3: The stress-strain curve for concrete under uniaxial compression for Eurocode 2 (CEN, 2004a)

Where:

f_{cm}	Concrete cylinder compressive strength
ε_{c1}	Compressive strain at peak stress, $0.0007f_{cm}^{0.31} < 0.0028$
ε_{cu1}	Ultimate strain, 0.0035 for $f_{cm} < 58$ MPa
E_{cm}	Young's modulus of concrete, $22(0.1f_{cm})^{0.3}$

The equation of this curve is:

$$\frac{\sigma_c}{f_{cm}} = \frac{k\eta - \eta^2}{1 + (k-2)\eta} \qquad \text{Eq 5-2}$$

Where:

η	Ratio of compression strain with strain at peak load, $\varepsilon_c/\varepsilon_{c1}$
k	$=1.05\frac{E_{cm}\lvert\varepsilon_{c1}\rvert}{f_{cm}}$

Figure 5-4 shows the use of the previous equation (Eq 5-2) to simulate the experimental data, which predicted the property of concrete.

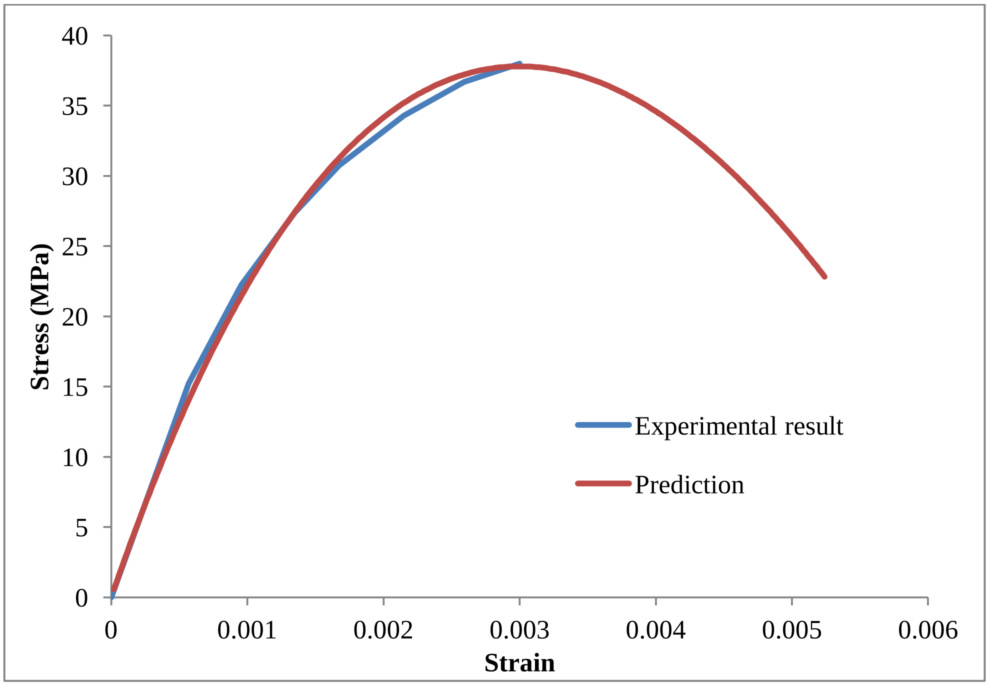

Figure 5-4: Comparison of prediction (Eq 5-2) and experimental results (Eurocode 2 model for compressive concrete property)

5.3.2.2 **Popovics model for matrix material:**

For the matrix cylinder compressive stress-strain relationship, the equation proposed by Popovics (1973) is shown in Eq 5-3. Experimental values of peak stress (f_{cm}) and the related strain (ε_{c1}) were used in this equation, and it was found that the matrix property curve was close to the experimental result, as shown in Figure 5-5. The post peak stage is important for the property of the confined matrix input in ABAQUS, and it will affect the accuracy of the FEM.

$$\sigma = f_{cm}(\varepsilon/\varepsilon_{c1})\frac{n}{n-1+(\varepsilon/\varepsilon_{c1})^n} \qquad \text{Eq 5-3}$$

Where:

σ	Compressive strength
f_{cm}	Peak compressive strength
ε	Compressive strain
ε_{c1}	Compressive strain at peak stress
n	Approximate function of compressive strength of matrix, $n = 0.4 \times 10^{-3} \times 150\, f_{cm} + 1.0$

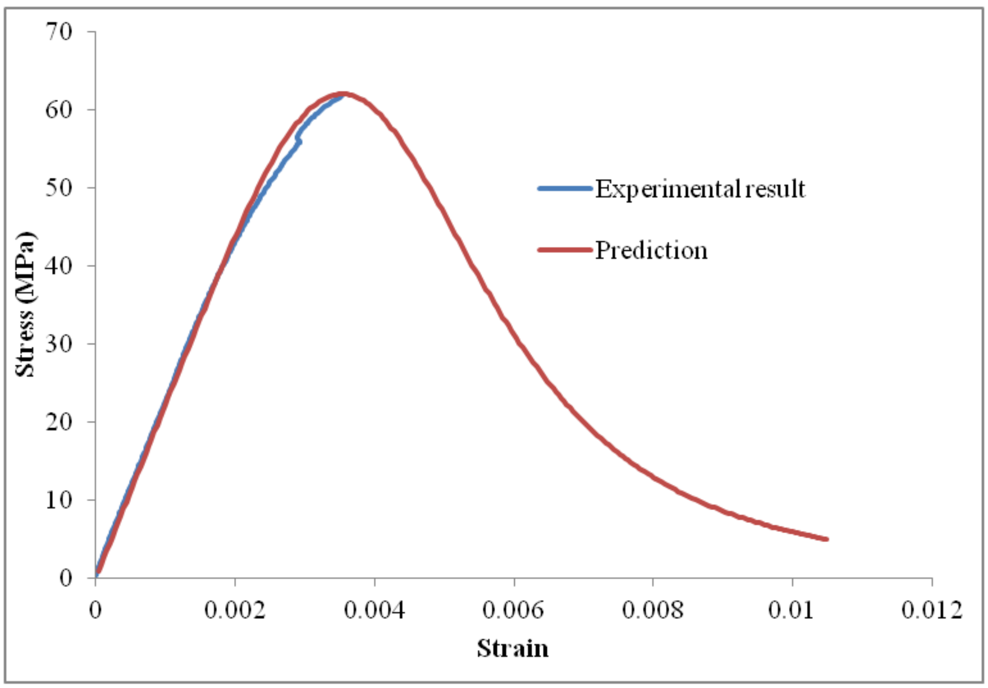

Figure 5-5: Comparison of prediction (Eq 5-3) and experimental results (Popovics model for compressive matrix property)

Therefore, Eq 5-3 is adopted for the parametric studies. To use this formula, two variables need to be selected: peak stress (f_{cm}) and its relative strain (ε_{c1}), a statistical approach based on experimental results was made as shown in Figure 5-6 (Tian, 2013). The resulting expression is given in Eq 5-4.

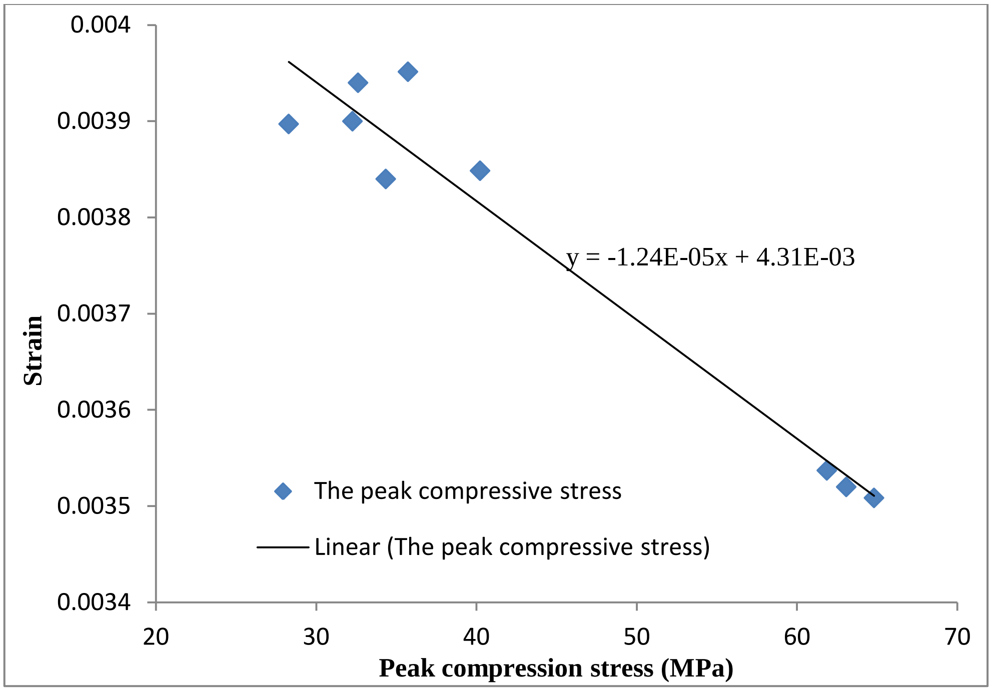

Figure 5-6: The curve fit for peak compressive stress and strain of matrix (Tian, 2013)

Note: Author and Tian cast and test the cylinders together, but Tian analysed the results.

Therefore, the equation as shown:

$$\varepsilon_{c1} = -1.20 \times 10^{-5} f_{cm} + 4.31 \times 10^{-3}$$
$$(30\ \text{MPa} \leq f_{cm} \leq 65\ \text{MPa}) \qquad \text{Eq 5-4}$$

5.3.3 Concrete under uniaxial tension

The stress-strain curve for concrete under uniaxial tension is shown in Figure 5-7. In the first stage of loading concrete will experience linear elastic behaviour until the failure stress (σ_{t0}) is reached. The failure stress corresponds to micro-cracking that occurs in the concrete. Beyond σ_{t0} (second stage), the micro cracks continue to increase and this can be denoted as the softening the response of stress-strain relationship.

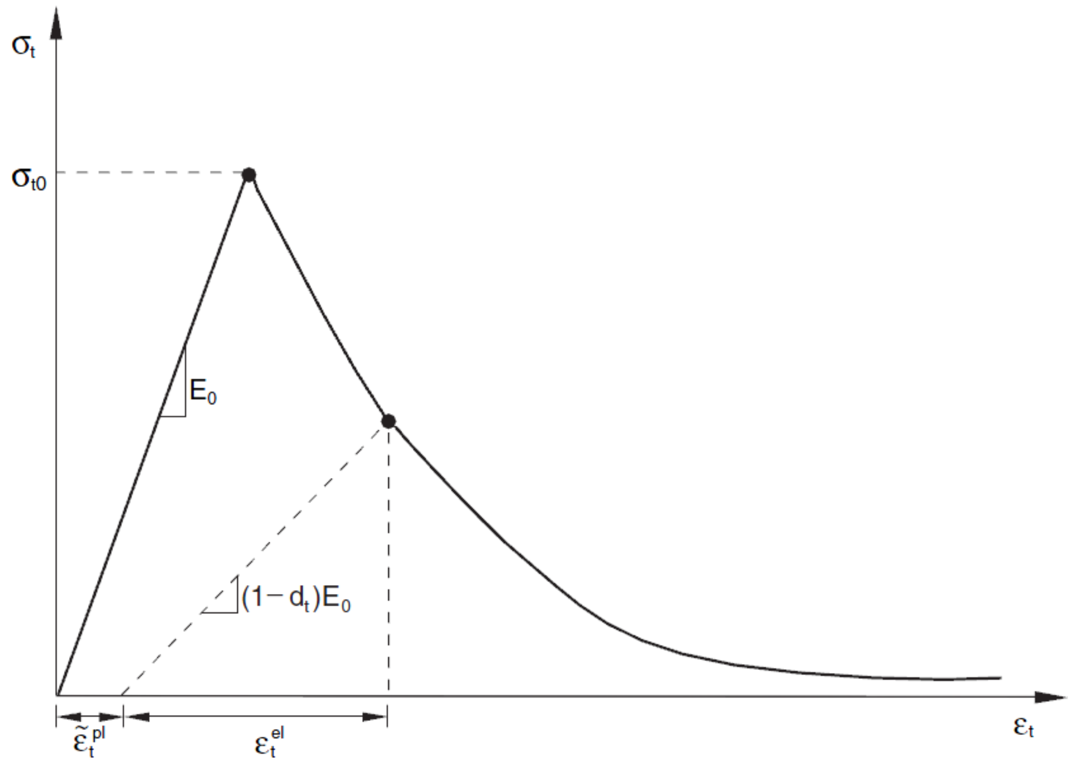

Figure 5-7: Stress-strain curve for plain unconfined concrete under uniaxial loading in tension (ABAQUS, 2009)

Where:

E_0	Initial elastic stiffness
σ_t	Tensile stress of concrete
σ_{t0}	Tensile failure stress
ε_t	Tensile strain
ε_t^{el}	Elastic tensile strain
$\tilde{\varepsilon}_t^{pl}$	Plastic tensile strain
d_t	Tensile damage variable

5.3.4 Tensile behaviour for CDP

The tensile behaviour of concrete or the matrix is defined as the uniaxial tensile response of the material in its post-failure range. The cracking strain is calculated shows in Eq 5-5.

$$\tilde{\varepsilon}_t^{ck} = \varepsilon_t - \varepsilon_{0t}^{el} \qquad \text{Eq 5-5}$$

Where:

$\tilde{\varepsilon}_t^{ck}$ Cracking strain of concrete

ε_{0t}^{el} Elastic tensile strain of concrete at yield, σ_t/E_0

Wang and Hsu (2001) reported a uniaxial tensile stress-strain curve. This value was used for input to ABAQUS for both the tensile property of concrete and the matrix. Eq 5-6 shows the relationship between the cracking strain and stress.

The split tests of cylinder results are shown in §3.2.3, the ultimate stress for concrete reached 3.74 N/mm^2, for matrix reached 4.44 N/mm^2, the stress-strain curves of tensile concrete and matrix properties is shown in Figures 5-8 and 5-9 respectively.

$$\sigma_t = f_{ctm}(\varepsilon_{cr}/\varepsilon_t)^{0.8} \qquad \text{Eq 5-6}$$

Where:

f_{ctm} Tensile stress of concrete

ε_{cr} Strain at cracking, f_{ctm}/E_0

The relationship between the ultimate tensile stress (f_{ctm}) and compressive stress (f_{cm}) is shown in Figure 5-10, where the curve fitting approach is based on experimental results (Tian, 2013). The equation used is shown in Eq 5-7.

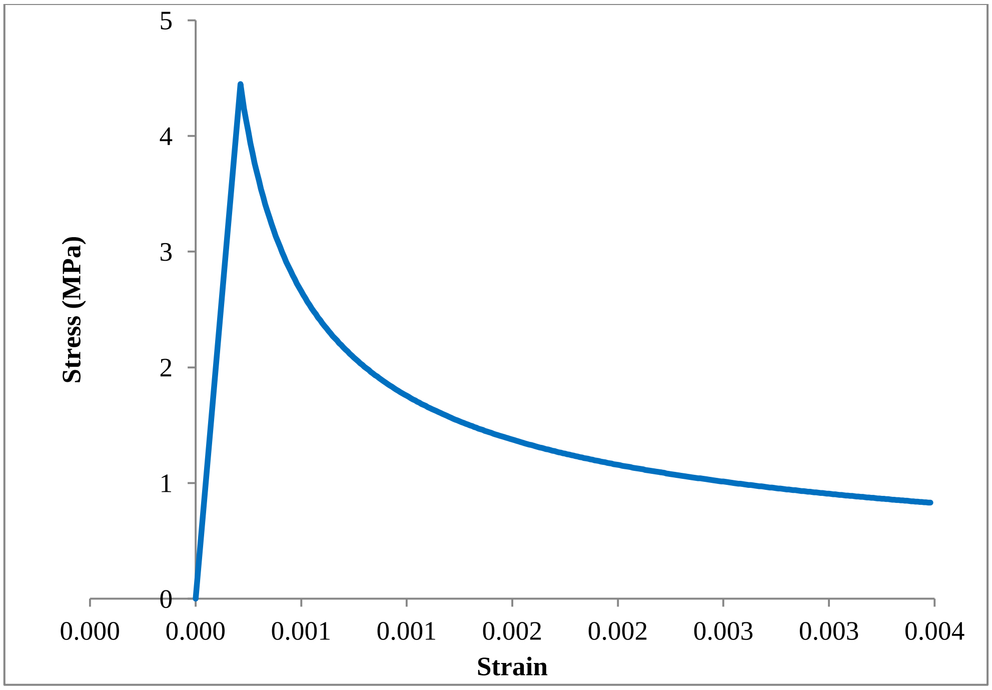

Figure 5-8: Tensile stress-strain curve of concrete based on Eq 5-6 (3.74 N/mm^2 for concrete tensile stress)

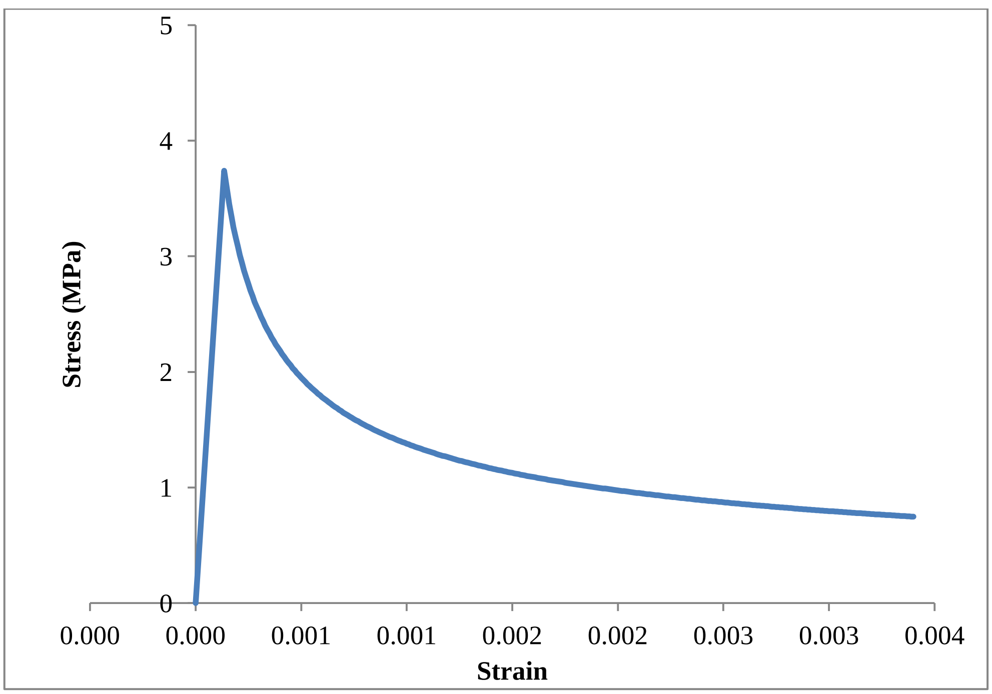

Figure 5-9: Tensile stress-strain curve of matrix based on Eq 5-6 (4.44 N/mm^2 for matrix tensile stress)

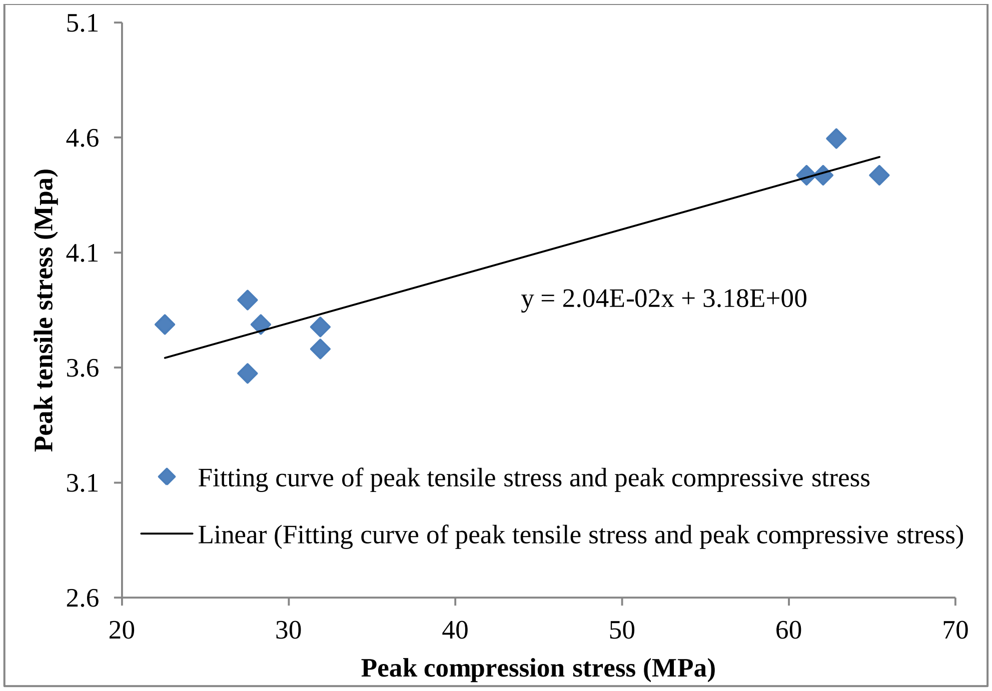

Figure 5-10: Fitting curve of peak tensile stress and peak compressive stress of matrix (Tian, 2013)

Note: Author and Tian cast and test the cylinders together, but Tian analysed the results.

$$f_{ctm} = 2.04 \times 10^{-2} f_{cm} + 3.18 \quad (30\ \text{MPa} \leq f_{cm} \leq 65\ \text{MPa}) \qquad \text{Eq 5-7}$$

5.3.5 Plasticity parameters for CDP model

There are five parameters used in ABAQUS for defining the plasticity of CDP model, include: i) dilation angle (ψ), ii) eccentricity (ϵ), iii) σ_{b0}/σ_{c0}, iv) K_c and v) viscosity parameter. These are explained in subsequent sections.

The ferrocement column with two mesh layers (FC2) is shown in the following section. The FC2 simulations took a shorter time than those for the other specimens FEMs (FC4, RFC2 and RFC3). Through the sensitivity studies, the proposed FEM is determined according to the comparison of the test and simulation results in respect of the peak load, initial stiffness and displacement.

In ABAQUS, the Drucker-Prager hyperbolic function (Drucker and Prager, 2013) is used to define non-associated (not identical with the yield surface) potential plastic flow for concrete damage plasticity (CDP). The potential plastic flow (G), which is continuous and smooth, is shown in Figure 5-11. The equation of the curve is presented in Eq 5-8.

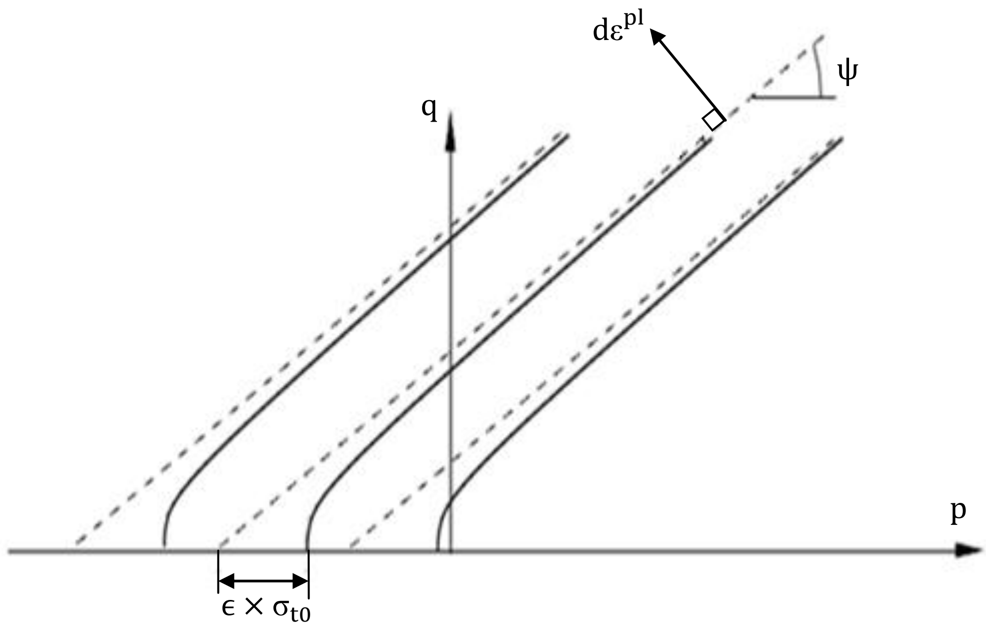

Figure 5-11: The hyperbolic potentials in the meridional stress plane

$$G = \sqrt{(\epsilon \times \sigma_{t0} \times \tan\psi)^2 + q^2} - p \times \tan\psi \qquad \text{Eq 5-8}$$

Where:

ψ	The dilation angle measured in the p–q plane at high confining pressure
ϵ	Eccentricity, defined as the rate of plastic potential function approaches at the asymptote line. The default is $\epsilon = 0.1$
σ_{t0}	The uniaxial tensile stress at failure, taken from the user-specified tension stiffening data
G	The potential plastic flow
p	The effective hydrostatic stress
q	The Von Mises equivalent effective stress

5.3.5.1 **Dilation angle (ψ)**

The dilation angle **(**ψ) measures the inclination of the plastic strain at a high confining pressure. A material with a low value of this angle experiences brittle behaviour, whereas high values indicate that the material has a high ductile behaviour. To decide on the value of ψ, a sensitivity test was carried out and the results were compared with the experimental results. This is shown in Figure 5-12. From this, a dilation angle of 49° is the best fit for the test results, as the load-displacement curve was found to be closest to experimental result.

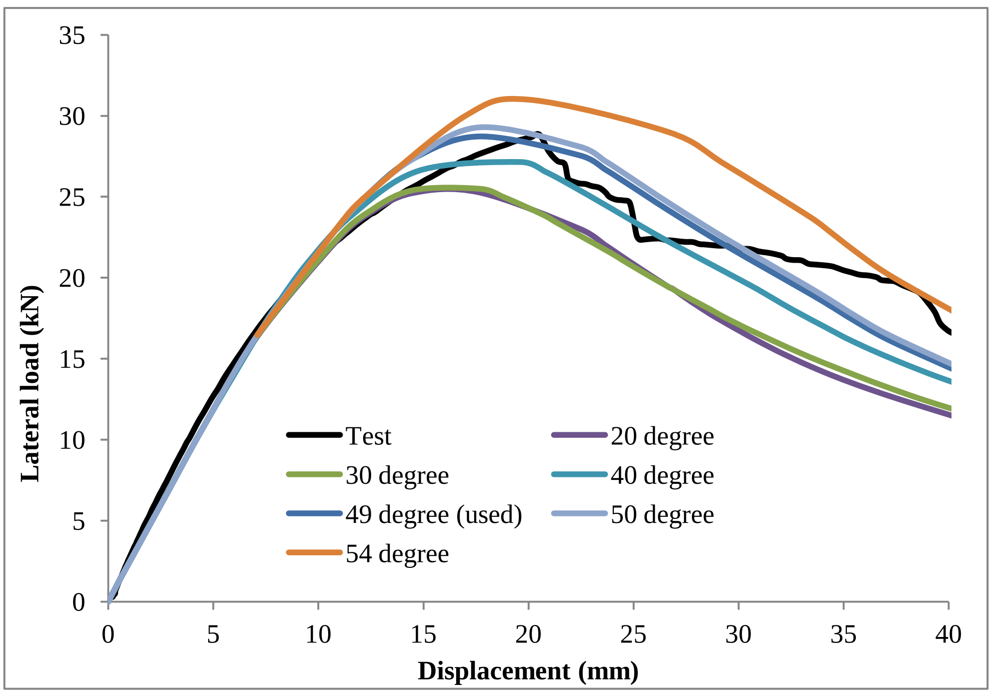

Figure 5-12: Comparison of FEM load-displacement curves using different dilation angles and the experimental result (FC2)

5.3.5.2 **Eccentricity (ϵ)**

Eccentricity (ϵ) is a parameter, that defines the rate at which the function approaches the asymptote (the flow potential tends to a straight line as the eccentricity tends to zero). By decreasing the value, this may lead to convergence problems. The default is ϵ = 0.1. From Figure 5-13, it may be seemed that the results at different values of eccentricity that were studied overlapped. Therefore, the default value was chosen.

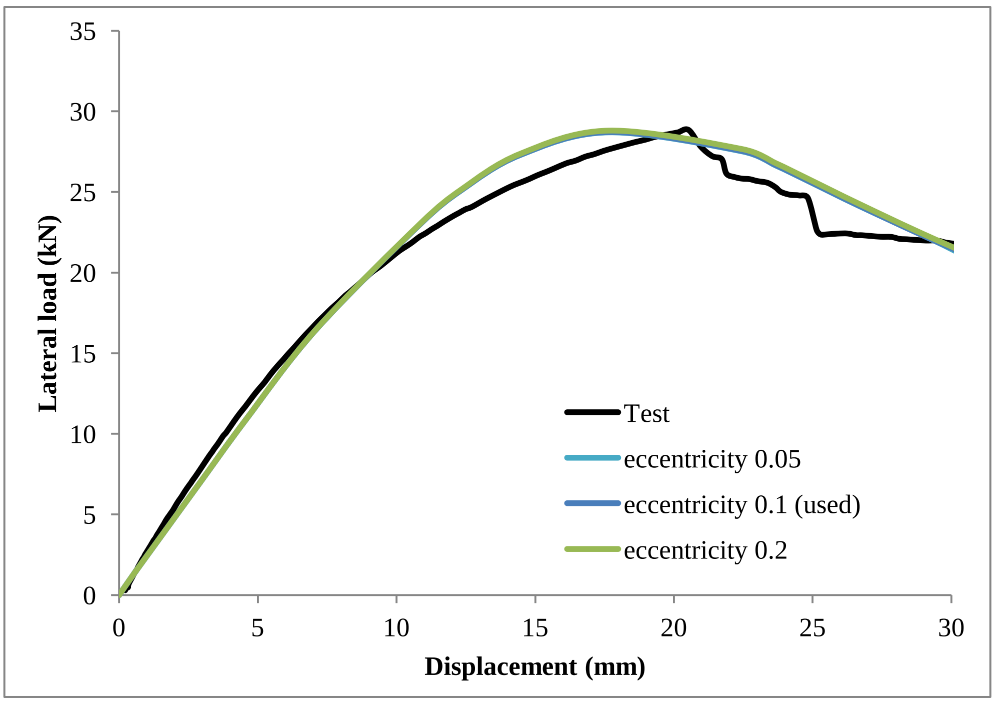

Figure 5-13: Comparison of FEM load-displacement curves using different eccentricities and the experimental result (FC2)

5.3.5.3 σ_{bo}/σ_{co}

The ratio of initial equi-biaxial compressive yield stress to initial uniaxial compression yield stress is required as an input to ABAQUS. Figure 5-14 shows the effect of changing the value of σ_{b0}/σ_{c0}. Again, the results show negligible differences, hence the default input value of 1.16 was chosen.

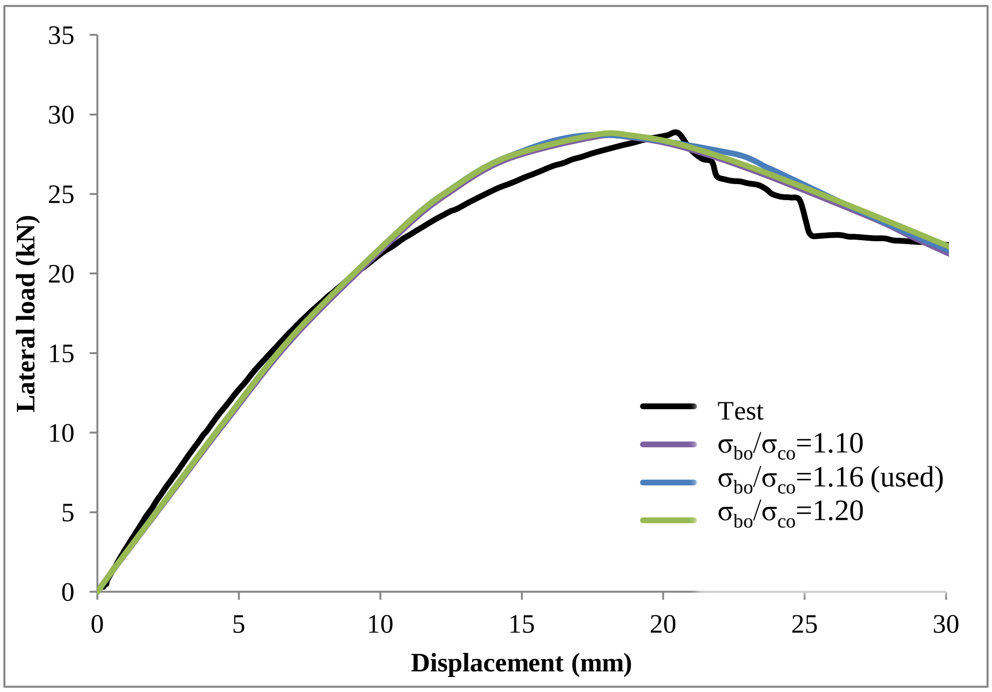

Figure 5-14: Comparison of FEM load-displacement curves using different σ_{bo}/σ_{co} values and experimental result (FC2)

5.3.5.4 **K_c**

The ratio of the second stress invariant on the tensile meridian, q (TM), to the compressive meridian, q (CM), adopted for different evolutions of strength under tension and compression. At the initial yield, for any given value of the pressure invariant p such that the maximum principal stress is negative, $\sigma_{max}<0$. It must satisfy the condition $0.5<K_c<1.0$, the default value being 0.667. Figure 5-15 shows the effect of changing the value K_c, The default value was chosen.

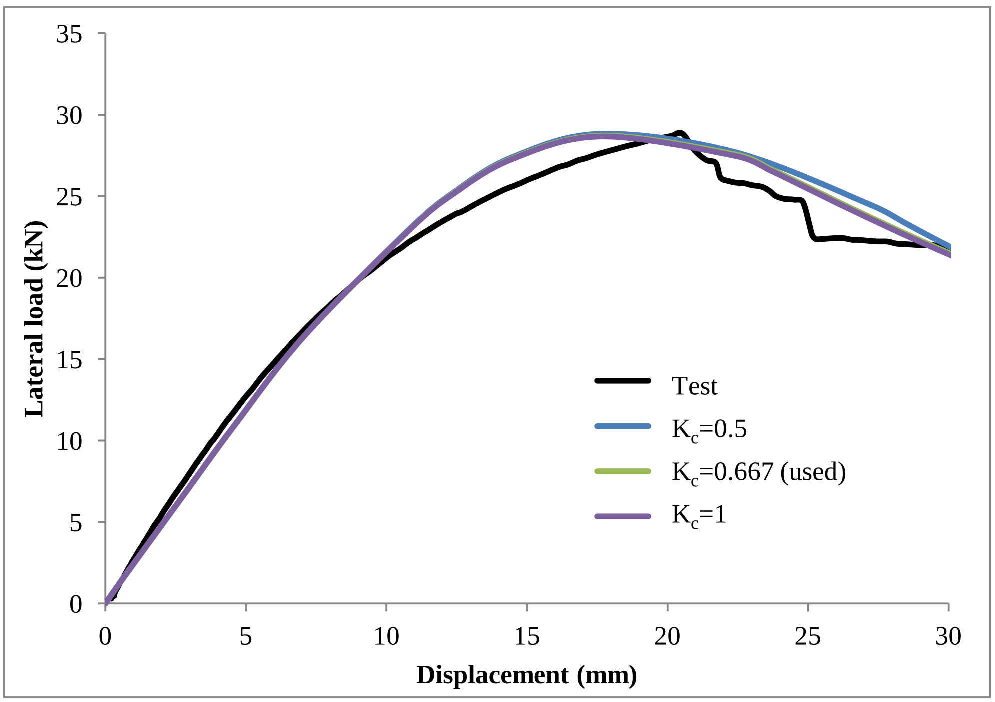

Figure 5-15: Comparison of FEM load-displacement curves using different K_c values and the experimental result (FC2)

5.3.5.5 **Viscosity parameter**

The viscosity parameter (μ) is defined in ABAQUS to represent the relaxation time of the visco-plastic system. By changing this value, the length of the experimental simulation time for each step may be influenced. Moreover, the softening behaviour and stiffness degradation behaviour of the material models may be influenced. Instead of changing the viscosity parameter and step time simultaneously, the step time was set as a constant value and the viscosity parameter was varied. Also by defining a small number μ in ABAQUS, convergence difficulties were overcome.

As shown in Figure 5-16, a viscosity parameter of 0.055 gives the best-fit curve to the experimental curve, so 0.055 was chosen in this study.

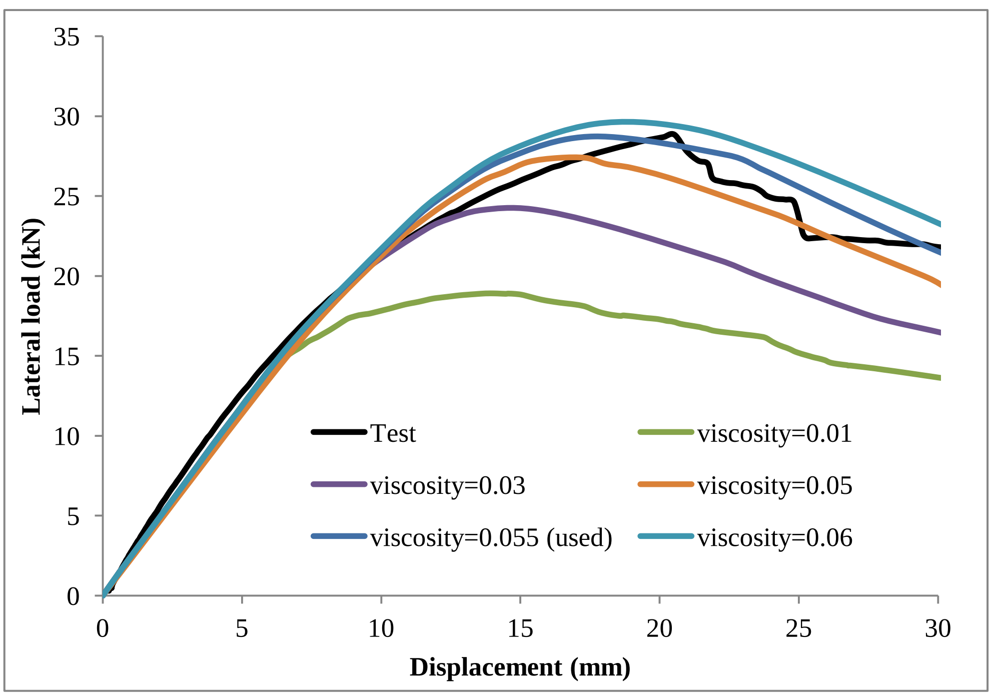

Figure 5-16: Comparison of FEM load-displacement curves using different viscosity parameters and the experimental result (FC2)

In summary, the five coefficients used for modelling the plasticity of the matrix and concrete are tabulated in Table 5-1. For the concrete parameters, the default values shown in Table 5-1 are used, except the viscosity parameter value. The results vary with the viscosity parameter value as shown in Figure 5-17. The best-fit curve is when the viscosity equals 0.015.

Table 5-1: Coefficients for ferrocement and concrete column

Material	Dilation Angle (ψ)	Eccentricity (ϵ)	σ_{b0}/σ_{c0}	K_c	Viscosity parameter (μ)
Matrix	49	0.1	1.16	0.667	0.055
Concrete	30	0.1	1.16	0.667	0.015

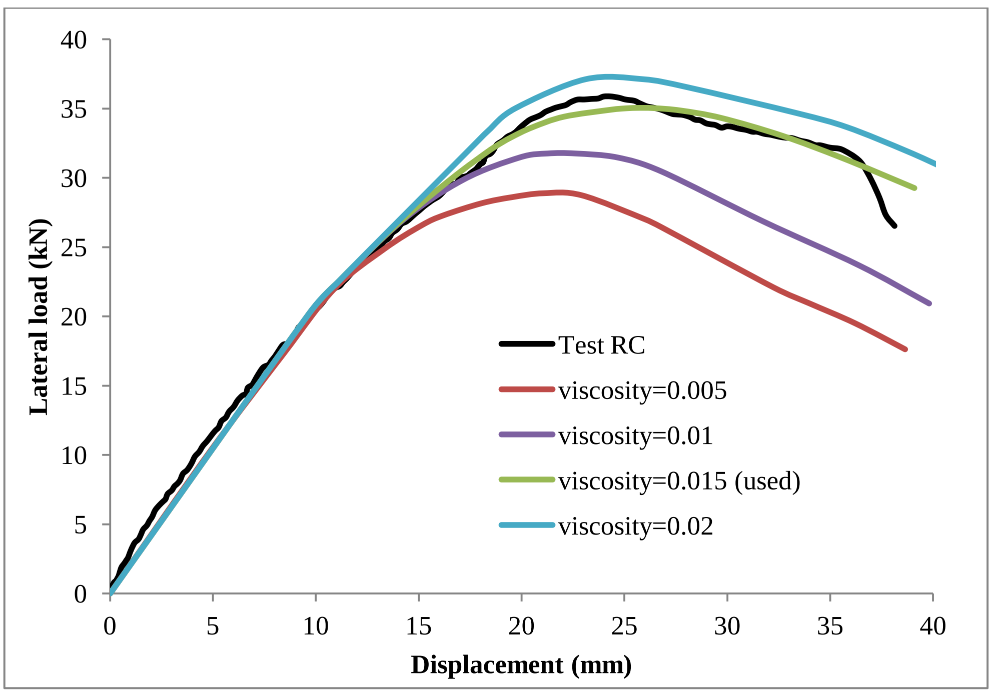

Figure 5-17: Comparison of FEM load-displacement curves using different viscosity parameters and the experimental result (RC)

5.4 Contact

When considering reinforced materials to ensure physical contact, different linking methods are available. Two types of constraint were selected in this thesis; the embedded region constraint and the “Tie” constraint.

5.4.1 Embedded region

Reinforcement in concrete structures is typically provided by rebar. Normally the rebars are defined as one-dimensional wire truss elements and the reinforcement can be defined in ABAQUS using a single wire. In this thesis, a metal plasticity model was used, which presents elastic-perfectly plastic behaviour for reinforcement.

The concrete behaviour is independent of the reinforcement behaviour, so the interaction between concrete and reinforcement, the embedded bond (perfect bond), was defined in this studies to simulate load transfer between concrete and reinforcement. In addition, the welded mesh was also embedded in the matrix structure.

5.4.2 Tie constraint

When concrete columns are strengthened using ferrocement material, the constraint between the concrete surface and the matrix surface was chosen to be a “Tie” constraint in ABAQUS. To use this constraint, some basic rules must be followed. In principle, the master surface should be applied to the stronger material compared with the material using the slave surface. Therefore, the concrete surface can be defined as the master face, whereas the matrix surface should be the slave face during the whole simulation.

5.5 Boundary conditions and load application

The boundary conditions and load application used in the numerical simulations were identical to those used in the experiments in Chapter 3. The columns were modelled as being horizontal, with one side having a fixed-end condition and the other experiencing the applied load.

The fixed-end plate was located on the stiffened support beam using high strength rods (see §3.6.3). For the experiment, the fixed-end was not totally restrained. The rotation was recorded by two extra linpots on the top of the fixed-end plate. This support flexibility was simulated in ABAQUS using two linear spring supports at the fixed end.

The boundary and loading conditions are shown in Figure 5-18. Reference Points (RP) were introduced in the simulations from the ABAQUS toolset, which defines reference points that are used in constraints and connectors. The coupling interactions provide a constraint between a reference node and the nodes on a surface. The following shows the detail.

a) RP-1 and RP-2 are load application points.
b) RP-3 is coupled on the surface of protection plate.
c) RP-4 and RP-5 are totally restrained, and these points are one end of springs connected with RP-6 and RP-7, respectively.
d) RP-6 and RP-7 are coupled with the edge line and are 200 mm from the edge.
e) A pinned condition was applied to the underside of the specimens, 107.5 mm from the fixed-end (see §4.3). As lateral load is applied the whole structure will rotation about this line.

There are two steps for the load application during simulation: first axial load and then lateral load. The axial load for the experiments was applied by two Macalloy bars, each bar given a 100 kN force. So 200 kN is applied at RP-2 for step 1. The lateral load was applied by the actuator, under displacement control, so for the simulation, displacement was applied at RP-1 for step 2.

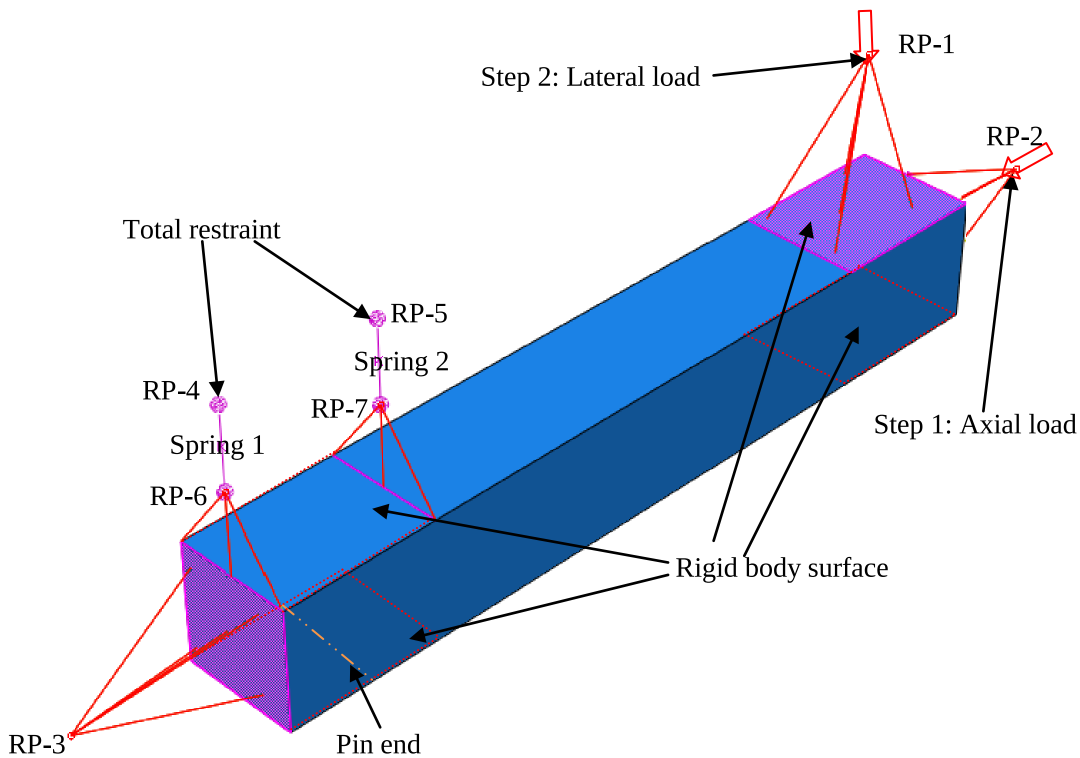

Figure 5-18: The boundary conditions and loading applications

Two linear springs were added at the fixed-end to simulate the rotations observed for the whole specimen (see §4.3). The value of spring stiffnesses by hand calculation are: $k_1 = 85.6$ kN/mm and $k_2 = 127$ kN/mm (see §4.3).

5.6 Detail description of reinforcement in ABAQUS

The reinforcement of RC, FC and RFC in ABAQUS simulation is exactly same position and amount as experimental specimens, shown in Figures 5-19, 5-20 and 5-21.

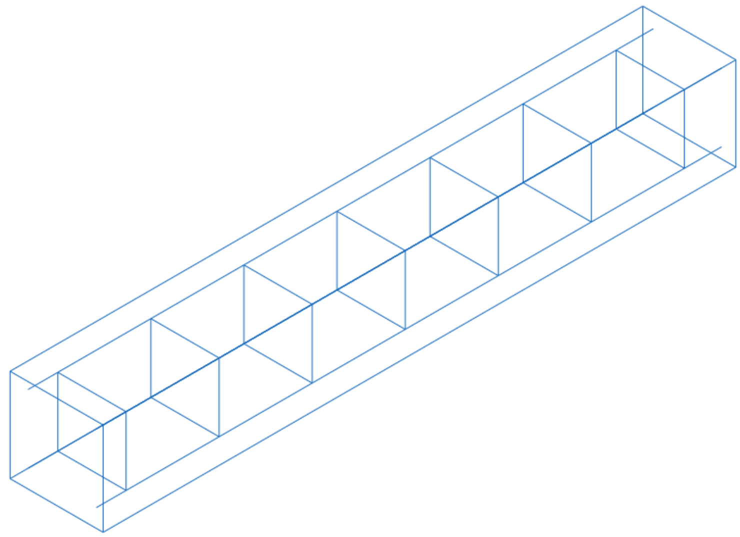

Figure 5-19: The reinforcement of RC

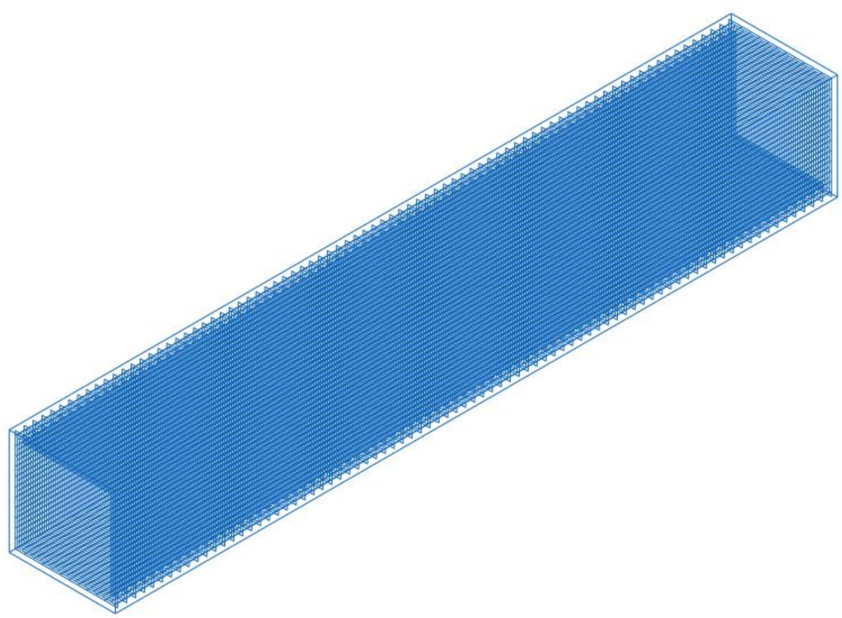

Figure 5-20: The reinforcement of FC

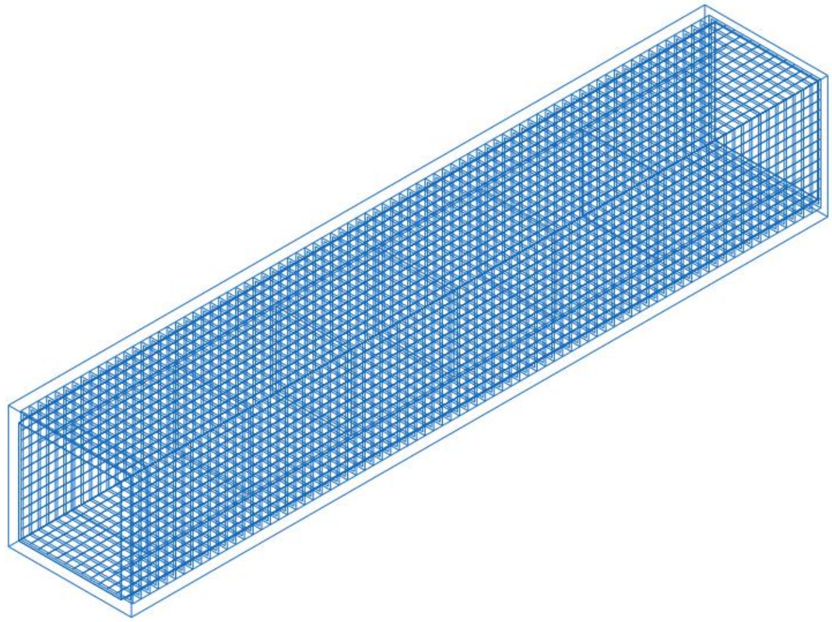

Figure 5-21: The reinforcement of RFC

5.7 Finite element mesh size

The size of mesh used in finite element method (FEM) can affect the results. Although using a finer-mesh can produce more accurate results, a major disadvantage is that a large amount of computational resource is required. In order to find the most efficient mesh size, a sensitivity study was carried out and this is explained in this section. Figure 5-22 shows the mesh size for the matrix structure.

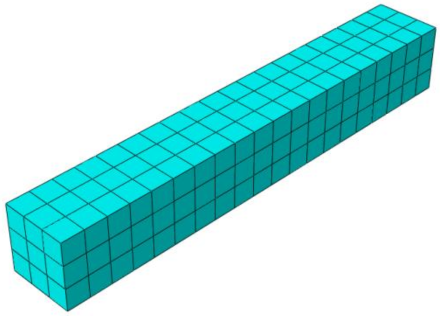

(a): mesh size 50 mm

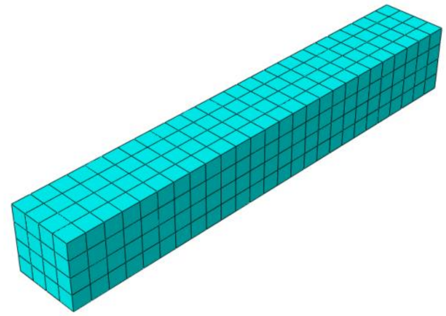

(b): mesh size 40 mm

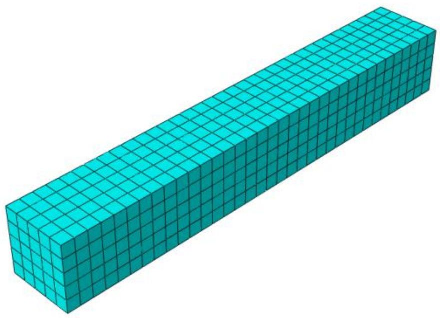

(c): mesh size 30 mm

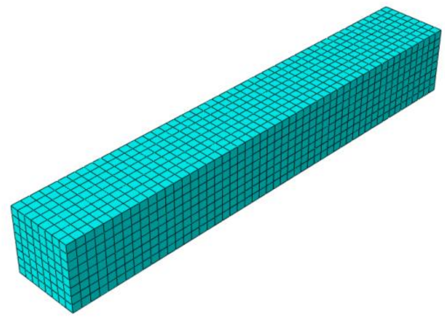

(d): mesh size 20 mm

Figure 5-22: The mesh size for the matrix

Figure 5-23 shows the simulation results for FC2 using different mesh sizes for the matrix. It is clear that the four different mesh sizes produce the same initial stiffness, however, the 20 mm mesh size generated the closest results to the test results on the descent part, with a computational CPU time of 523 minutes. In comparison with this, using 30 mm mesh size produces similar results, but the calculation time reduced to 143 minutes. Therefore, the 30 mm mesh size for the matrix was selected.

Table 5-2 presented the effects of different element sizes of matrix on the numerical simulation for FC2.

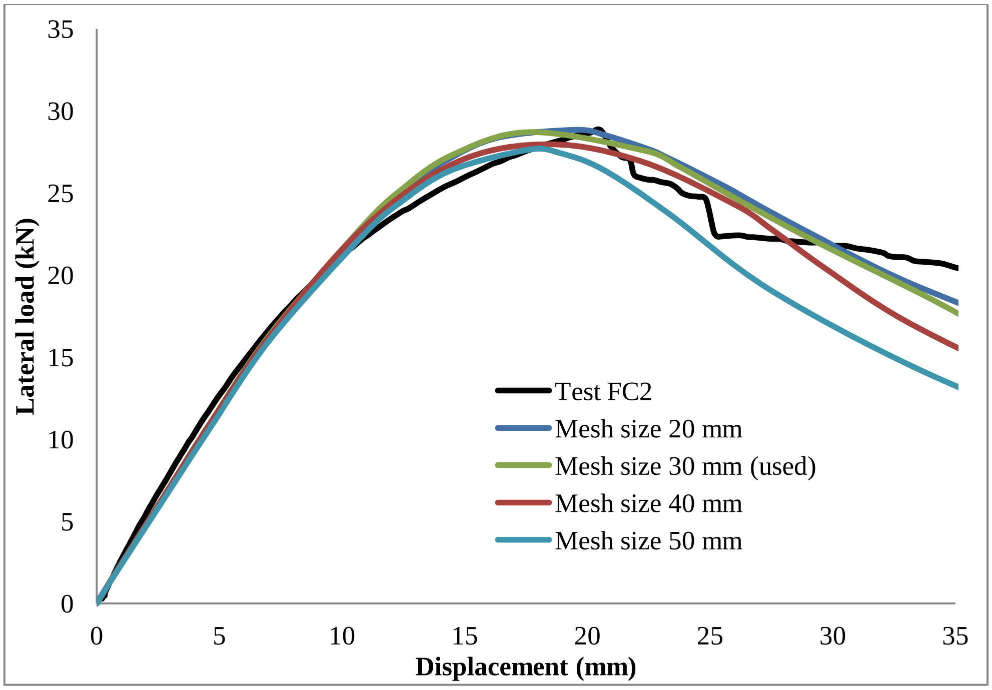

Figure 5-23: The mesh size for the matrix (FC2)

Table 5-2: Mesh sensitivity study for matrix mesh size

Matrix mesh size(mm)	Number of elements	Simulation time (CPU mins)	Test load (kN)	Simulation load (kN)
20	3264	523	29.5	29.4
30	875	143		29.1
40	416	85		28.0
50	180	58		27.6

Then, the author simulated varying with the mesh size of reinforcing mesh, shows in Figure 5-24, and results presents in Table 5-3. The results show the 12.6 mm mesh size have same value with the mesh size equal 6.3 mm. So finally, the 12.6 mm mesh size for mesh reinforcement was selected.

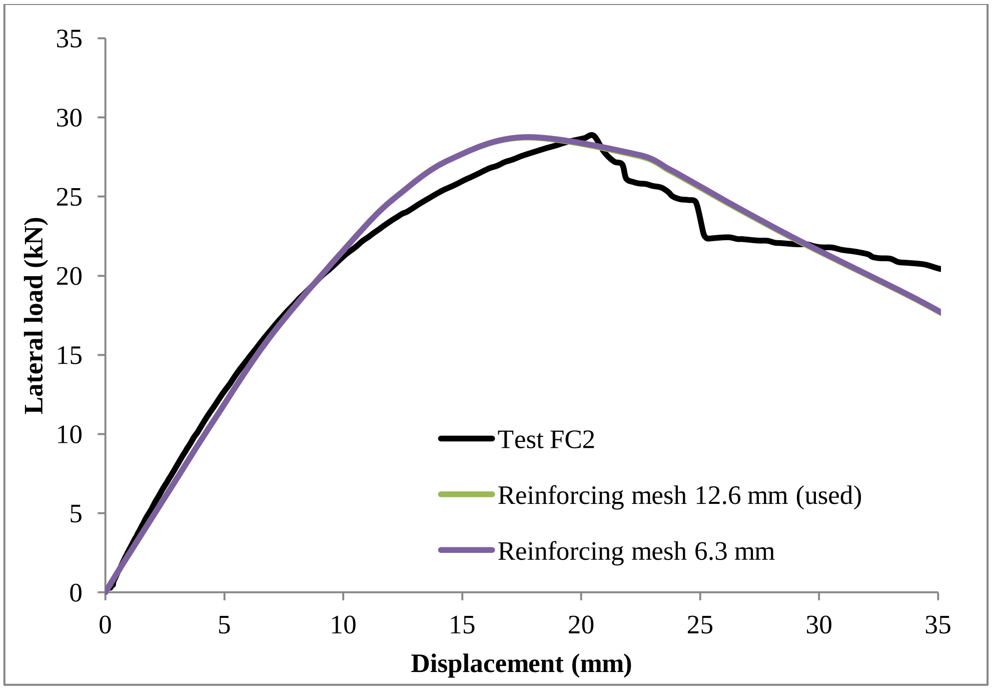

Figure 5-24: The mesh size of reinforcement (FC2)

Table 5-3: Mesh sensitivities for reinforcing mesh size with concrete size 30 mm

Welded mesh size (mm)	Number of elements	Simulation time (CPU mins)	Test load (kN)	Simulation load (kN)
12.6	14976	143	29.5	29.1
6.3	29952	501		29.0

5.8 Verification of FEM with experiments

Verification of the FEM results using the experimental results is given in the following sections. The load-deflection response of the columns under combination of axial load and bending were shown in Chapter 3. A good agreement was found between the FEM results and the experimental results as described in the following sections, especially in the ascending stages and peak loads for all numerical simulations, but with slight differences on the descending part. Three groups of FEM results are compared with the experiment results:

a) Reinforced concrete column (RC)
b) Ferrocement columns (FC)
c) Reinforced concrete columns strengthened using a ferrocement jacket (RFC)

5.8.1 Reinforced concrete column

A comparison between the FEM analysis results and the experimental results for RC is shown in Figure 5-26. The values and deviations are presented in Table 5-4. The deviation is calculated using Eq 5-1; notice that the deviations of initial stiffness for all specimens are calculated at a lateral applied load of 10 kN. The deviation of peak load was 3% lower and displacement at peak load was 6% higher.

$$\text{Deviation} = \frac{\text{FEM} - \text{Test}}{\text{Test}} \times 100\% \qquad \text{Eq 5-1}$$

In Figure 5-26, it may be seen that the simulation results are close to the test results despite the maximum load obtained from FEM being smaller. It is worth mentioning that the test load dropped suddenly when the column deflection reached 39 mm, however the curve in the simulation gradually decreased. There are two loads of particular interest, namely the peak load and 85% post peak.

The FEM details of FC column at peak load and 85% post peak load are shown in Figure 5-27.

Figure 5-25 is the display and describe of the Figures 5-27, 5-30, 5-31, 5-34 and 5-35.

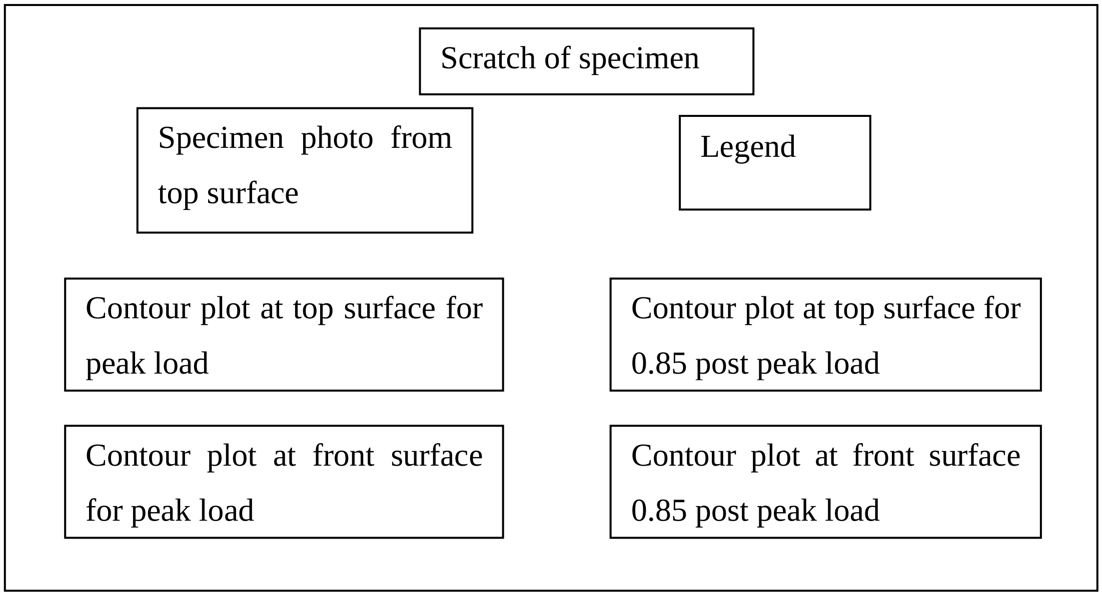

Figure 5-25: The display of each following figures (Figures 5-27, 5-30, 5-31, 5-34 and 5-35)

Note: Figures 5-34 and 5-35 (RFC2 and RFC3) have showed the both concrete and matrix

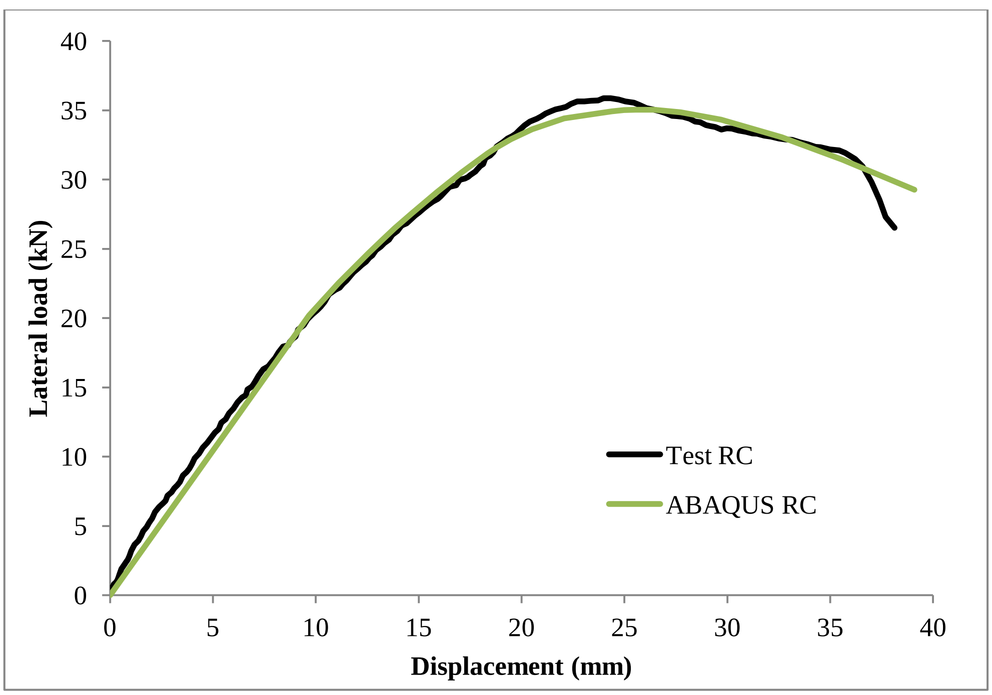

Figure 5-26: The comparison between the simulation and experiential results for the load-deflection response of RC

Table 5-4: Comparison of test and FEM (RC)

Specimen	RC		
	Test	**FEM**	**Deviation**
Peak load (kN)	35.7	34.6	-3%
Displacement at peak load (mm)	23.9	25.3	6%
Stiffness (kN/mm)	2.50	2.13	-12%

At the peak load, the maximum principal strain occurs on the top surface and reached 0.009. This produced cracks round the top surface. After the peak load, the strain of the concrete significantly increases, and at 85% post peak load it reached 0.0186.

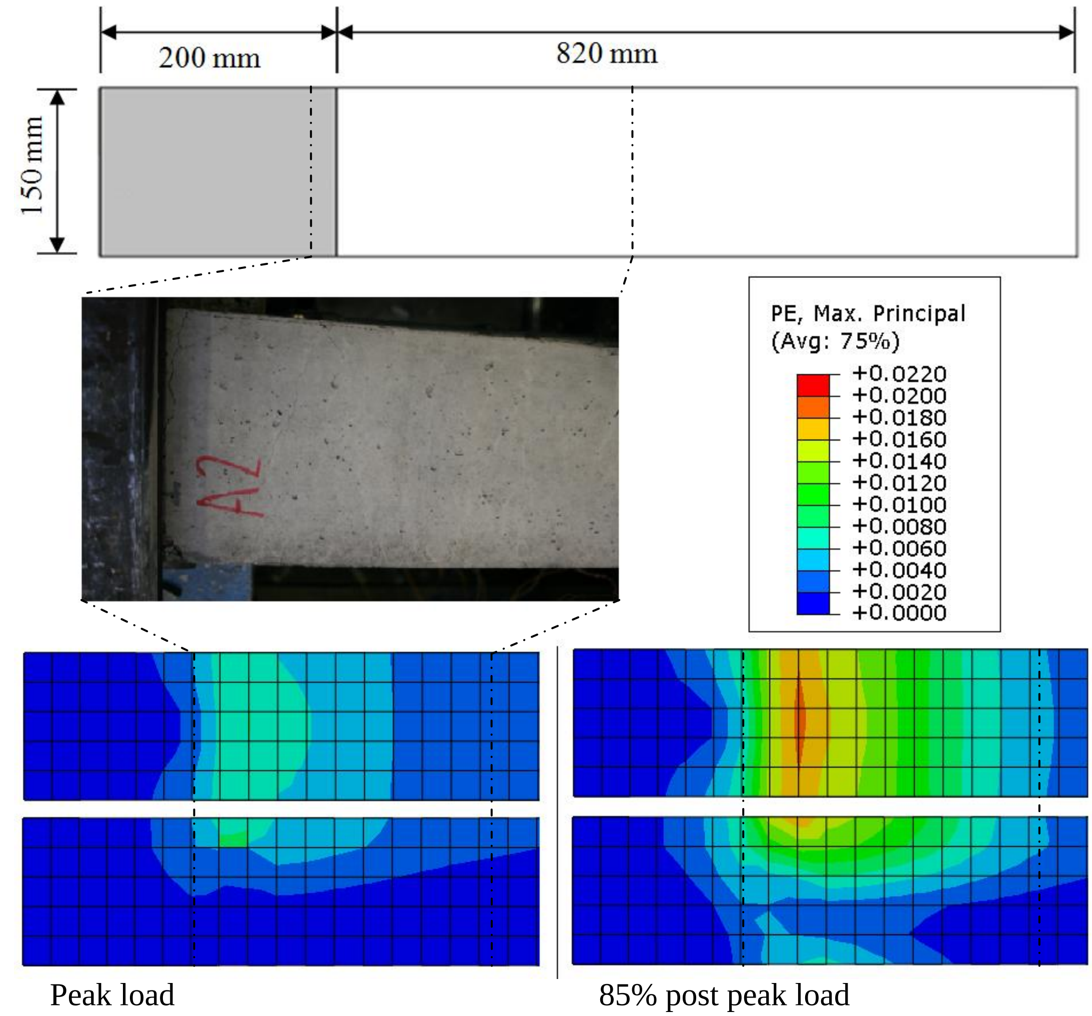

Figure 5-27: The PE, Max. Principal at peak load of FEM, 0.009 at peak load, 0.0186 for 0.85 post peak load (RC)

Note: Test picture is taken approximately before the lateral peak load has been reached

5.8.2 Ferrocement columns

FEM results for the ferrocement columns are in good agreement with experiments as seen in Figures 5-28 and 5-29. Table 5-5 presents the difference between the FEM results and the test results.

In Figure 5-28, the linear part of the FEM result is slightly softer than that from the experiment; the initial stiffness for the FEM is 2.35 with a deviation that is 9.6%

lower than the experimental results (see Table 5-5). This might be because the embedded interaction used in the FEM, between the matrix and reinforcement, is perfect, whereas bond slip may lead to a smaller deformation during the experimental test. The maximum load obtained was almost identical for the FEM and experimental tests (deviation is 1% lower), but the descending part shows that the FEM results are smoother.

In Figure 5-29, the ascending part of the FEM overlaps the experimental curve whilst the descending part has the same effect as FC2, in that it is smoother than the experimental test. The deviation of initial stiffness is 1.2% lower.

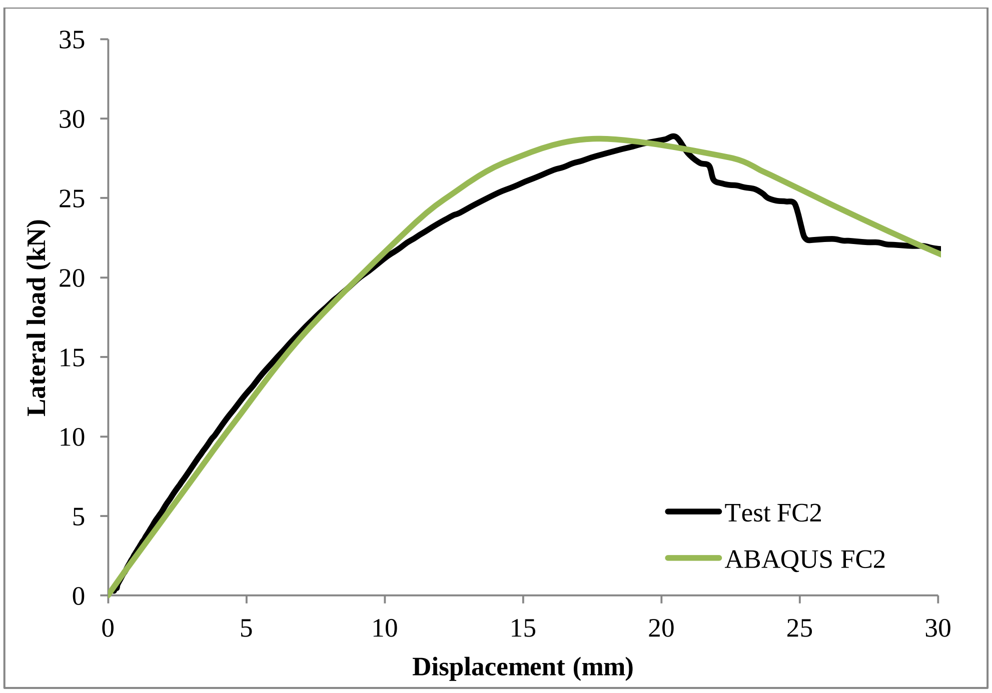

Figure 5-28: The comparison between the simulation and experiential results for the load-deflection response of FC2

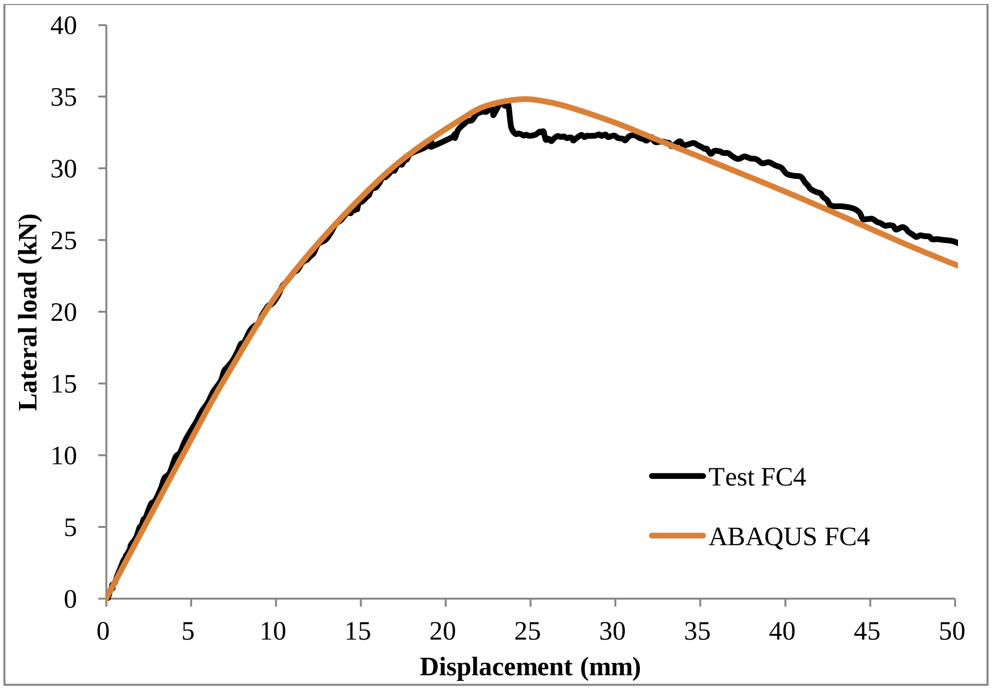

Figure 5-29: The comparison between the simulation and experiential results for the load-deflection response of FC4

Table 5-5: Comparison of test and FEM (FC2 and FC4)

Specimen	**FC2**			**FC4**		
	Test	**FEM**	**Deviation**	**Test**	**FEM**	**Deviation**
Peak load (kN)	29	28.7	-1%	34.7	35	1%
Displacement at peak load (mm)	20.9	19.6	-4%	23.5	24.8	-5.5%
Initial stiffness (kN/mm)	2.58	2.35	-9.6%	2.53	2.5	-1.2%

Figures 5-30 and 5-31 show the FEM of FC2 and FC4 at peak load and 85% post peak load.

The strain of FC2 at peak load is 0.01, and for FC4 is 0.011. The values of strain for both specimens are similar, but FC4 had two extra mesh layers, which enabled the specimen to attain a higher bending moment and higher displacement.

At 85% post peak load, the strain of FC2 reached 0.0202, and for FC4 was 0.0225. In addition, the peak strains for each FEM are shown at the top surface, where cracks were observed.

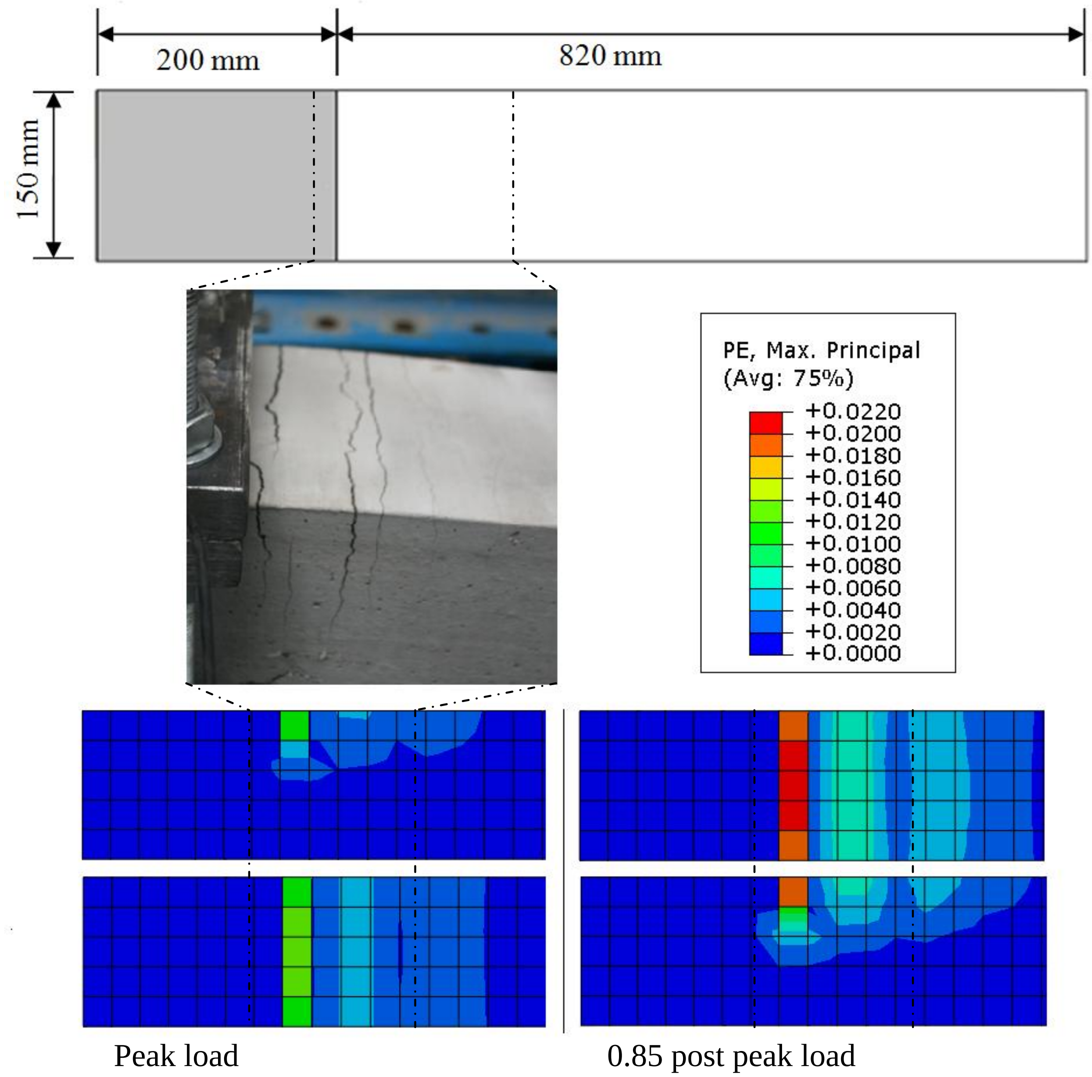

Figure 5-30: The PE, Max. Principal at peak load of FEM, 0.01 at peak load, 0.0202 for 0.85 post peak load (FC2)

Note: Test picture is taken approximately after the lateral peak load has been reached

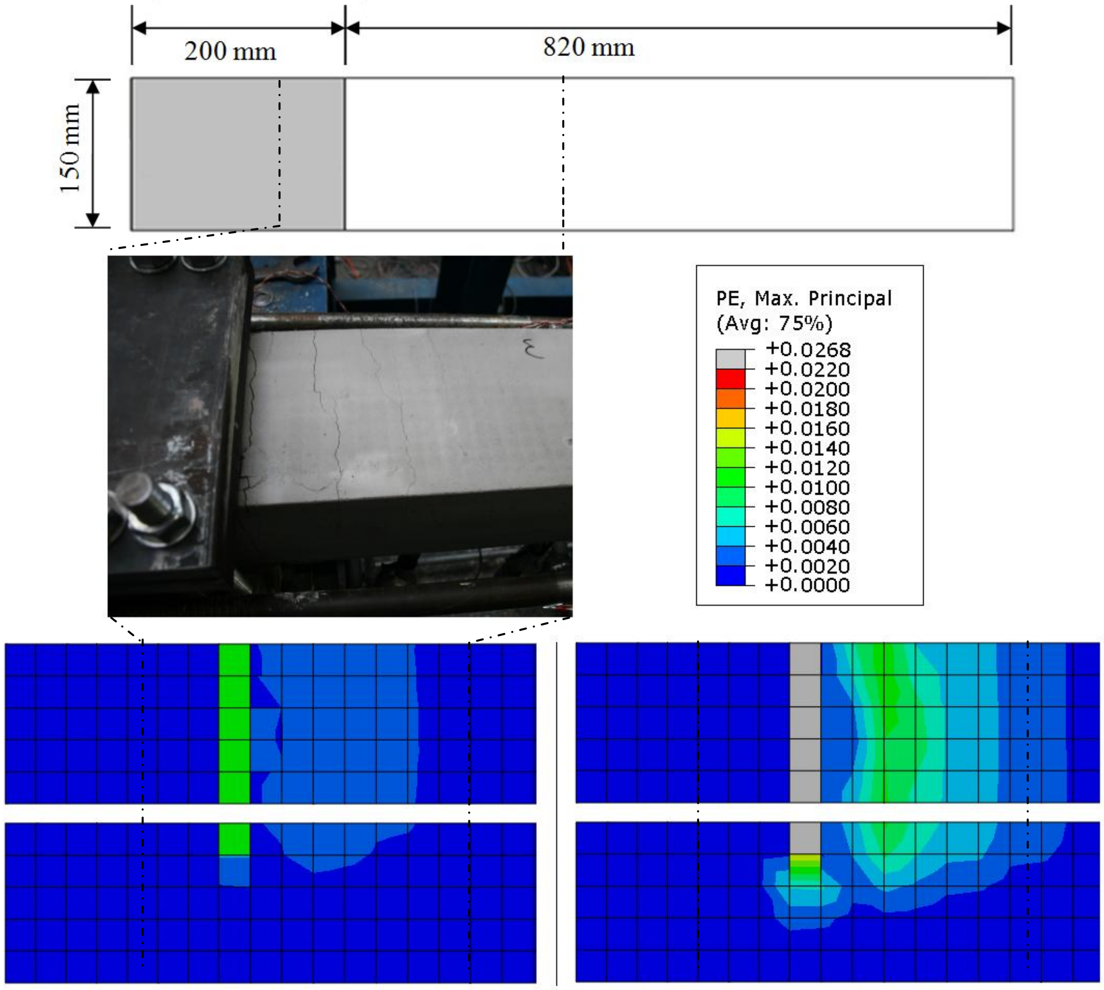

Figure 5-31: The PE, Max. Principal at peak load of FEM, 0.011 at peak load, 0.0268 for 0.85 post peak load (FC4)

Note: Test picture is taken approximately before the lateral peak load has been reached

5.8.3 Reinforced concrete columns strengthened using ferrocement jackets

The good agreement of the FEM results and the experimental results for both columns (RFC2 and RFC3) is shown in Figures 5-32 and 5-33. The deviations are shown in Table 5-6. The initial ascending part of the FEMs had slightly higher initial stiffness (deviation for RFC2 is 22% higher and for RFC3 is 20% higher), but after peak load the curves of the FEMs gradually reduced. The lower initial stiffness of the experimental tests may be because:

1) The matrix had not perfectly penetrated the mesh, as it was applied manually rather than vibrated (see Figure 3-20).
2) The imperfect cover of the dental plaster (see Figure 3-27).
3) The outer ferrocement jacket dimensions were not uniform (see Figure 3-21).

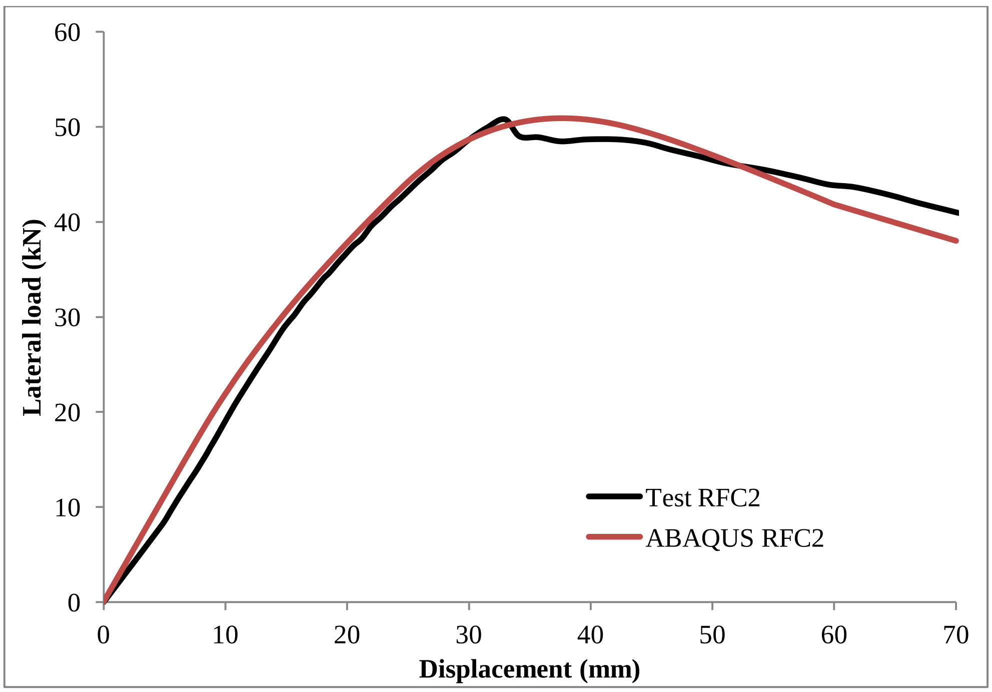

Figure 5-32: The comparison between the simulation and experiential results for the load-deflection response of RFC2

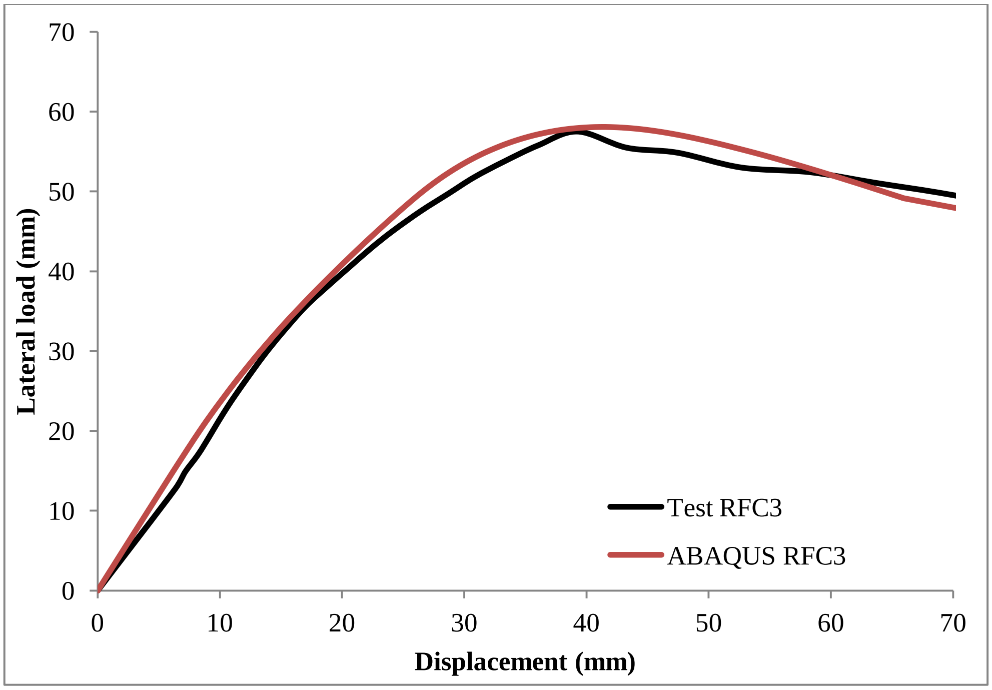

Figure 5-33: The comparison between the simulation and experiential results for the load-deflection response of RFC3

Table 5-6: Comparison of test and FEM (RFC2 and RFC3)

Specimen	RFC2			RFC3		
	Test	FEM	Deviation	Test	FEM	Deviation
Peak load (kN)	50.8	51	0%	57.5	58.1	1%
Displacement at peak load (mm)	33.6	37.5	12%	39.2	42.5	8%
Initial stiffness (kN/mm)	1.7	2.1	22%	2.0	2.4	20%

Figures 5-34 and 5-35 show the RFC2 and RFC3 FEM at peak load and 85% post peak load. Each simulation represents the inner reinforced concrete and the outer ferrocement.

RFC2: At the peak load, the strain of reinforced concrete reached 0.0093, and outer ferrocement 0.0288, the ferrocement layer acted as confinement. At 85% post peak load, the ferrocement strain reached 0.0651, many cracks were present on the top surface, and front and back surfaces.

RFC3: The behaviour of RFC3 was similar to RFC2, at peak load, the strain of inner reinforced concrete was 0.0099, and outer ferrocement 0.0305. At 85% post peak load, the ferrocement strain reached 0.0544, which is lower than that for RFC2.

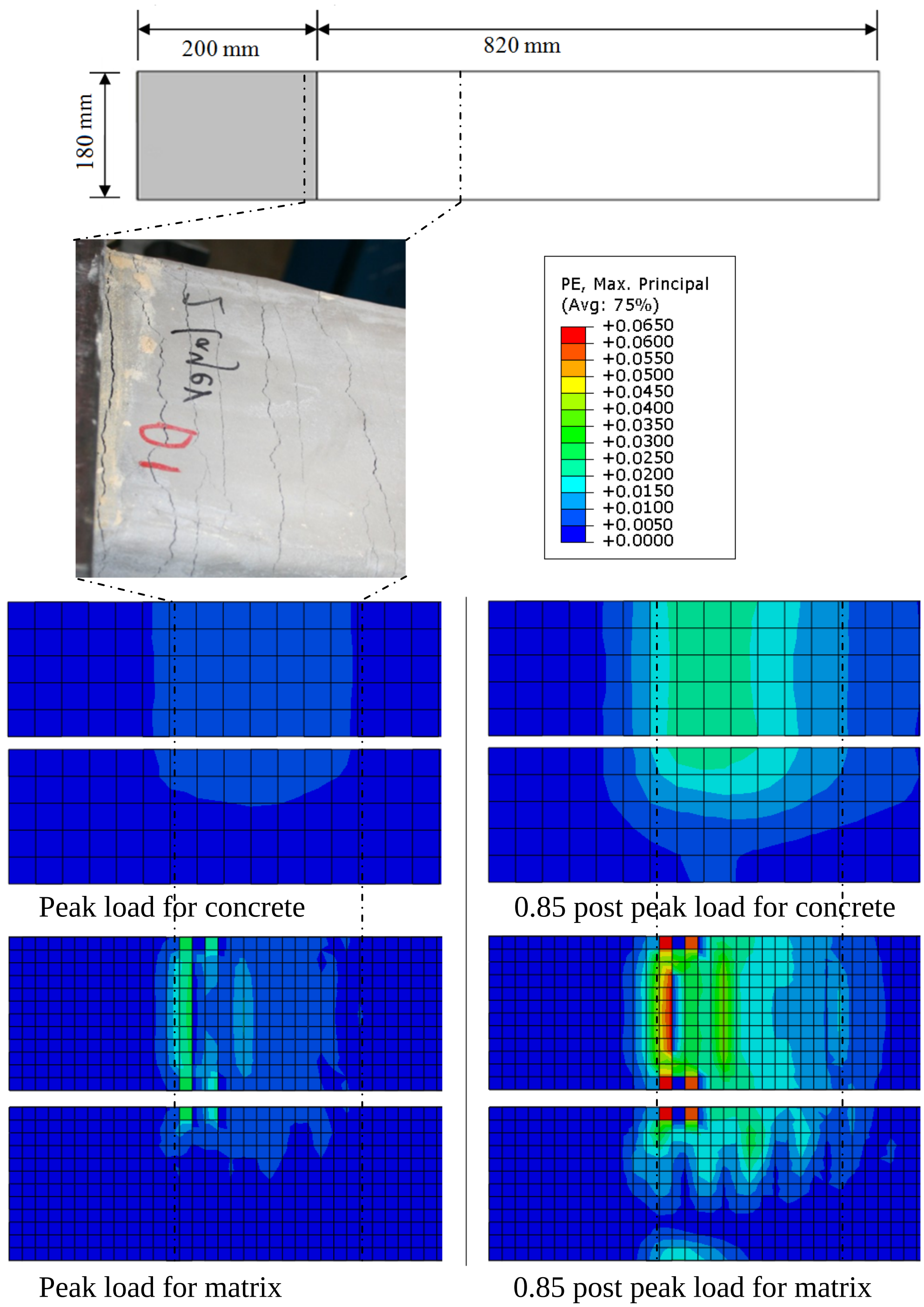

Figure 5-34: The PE, Max. Principal at peak load of FEM, 0.011 at peak load, 0.0268 for 0.85 post peak load (RFC2)

Note: Test picture is taken approximately after the lateral peak load has been reached

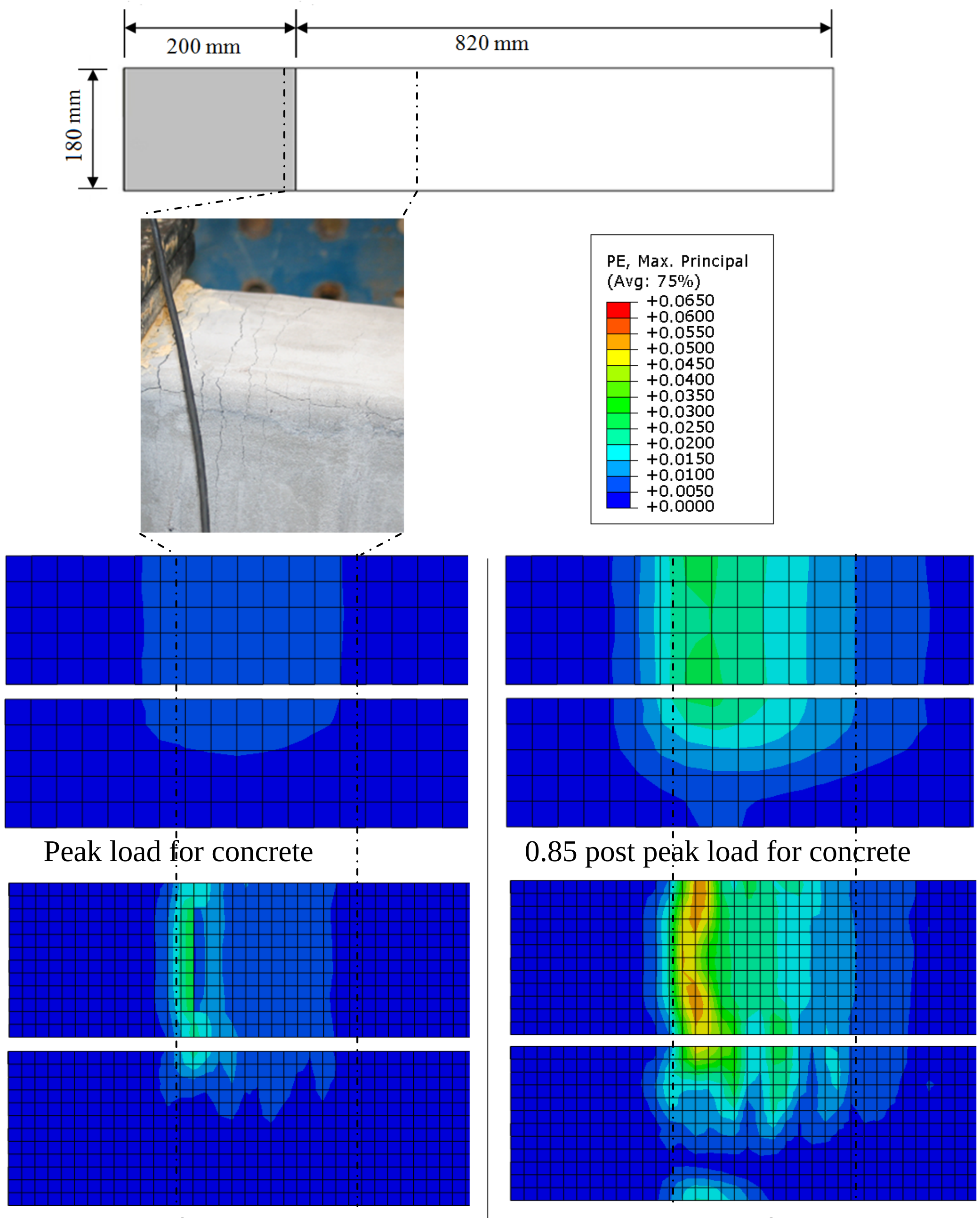

Figure 5-35: The PE, Max. Principal at peak load of FEM, 0.011 at peak load, 0.0268 for 0.85 post peak load (RFC3)

Note: Test picture is taken approximately before the lateral peak load has been reached

5.9 Ductility of FEM compared with experimental tests

The deformation ductility of each simulation is shown in Table 5-7. RFC2 has the same value as the experimental test (2.20). FC2 had quite a different value from the experimental test. For FC2: after the peak load, the load of the experimental test drops quickly, but the simulation could not properly represent the descent stage, as the simulation had a smooth decrease load after peak load.

Table 5-7: Deformation ductility comparison of test results and FEM

Name	Type	Peak load (kN)	Effective displacement (mm)	Ultimate displacement (mm)	Deformation ductility
RC	**Test**	35.7	21.6	37.5	1.74
	FEM	35.0	20.9	38.5	1.83
FC2	**Test**	28.0	13.5	25.1	1.74
	FEM	28.7	14.0	28.8	2.05
FC4	**Test**	34.7	16.8	41.0	2.44
	FEM	35.0	16.5	39.5	2.40
RFC2	**Test**	50.8	28.6	62.7	2.19
	FEM	51.0	27.0	59.2	2.20
RFC3	**Test**	57.5	29.5	75.4	2.56
	FEM	58.4	28.1	67.0	2.38

5.10 Conclusion

In this study, a finite element model, using the commercial package ABAQUS, was used to simulate the behaviour of ferrocement columns. The results from the experimental work were validated using the FEM, and the behaviour of ferrocement or the strengthened columns were predicted. The concrete damaged plasticity model was used for this thesis.

The FEM predicted the load-deflection curve with a high degree of correlation (less than 10% differences). The deformation ductilities of the simulations had similar values to those in the experimental tests. There are several reasons for the differences between the experimental data and the finite element analysis.

- The embedded interaction used for the FEM is too perfect to simulate the realistic cases as bond-slip may occur.
- The material properties cannot be perfectly input in ABAQUS, especially for the tensile property of the concrete or matrix.
- The spring setting in ABAQUS may not totally describe the experimental tests.

CHAPTER 6 Parametric studies

6.1 Introduction

In the experimental tests, it is hard to measure the strain variation. Hence, using strain failure as a damage criterion for a structure is extremely difficult. However, the finite element model can clearly show the strain variation of the structure under loading. Moreover, in addition to their high cost, the tests are extremely time consuming since the concrete or ferrocement needs at least 28 days to dry. Therefore, it is very difficult to conduct a large range of experiments.

The following section represents the parametric FEM studies performed on the reinforced concrete column (RC), ferrocement column (FC) and reinforced concrete column strengthened using a ferrocement jacket (RFC).

6.2 Parameters

A large number of numerical simulations have been conducted. The investigated parameters are given in Table 6-1. Six parameters were investigated namely: the column condition, concrete property, matrix property, main reinforcing bar, stirrup and welded mesh. The details of the parameter changes for individual FEMs are given in Appendix G.

Table 6-1: List of parameters studied in this chapter

Number	Parameter		RC	FC	RFC
1	Column	End condition		√	
		Axial load	√	√	
		Length		√	
2	Concrete strength		√		
3	Matrix strength			√	√
4	Main reinforcing bar	Strength	√		
		Diameter	√		
		Number of bars	√		
5	Stirrup	Strength	√		
		Size	√		
6	Welded mesh	Strength		√	√
		Diameter		√	√
		Number of layers		√	√

6.3 Columns

6.3.1 End conditions

Although all the boundary conditions of the tested columns are semi-rigid, fixed-end boundary conditions are more realistic. Therefore, all the parametric studies are carried out assuming fixed-end boundary conditions (fully restrained). In order to investigate the effect of the boundary conditions on the structural behaviour of columns, the results of one numerical simulation model, utilizing FC4 with total end fixed boundary conditions, are compared with the results from the test and the validation model as shown in Figure 6-1.

Figure 6-1 clearly shows that the model using fixed-end boundary conditions gives a larger initial stiffness and higher peak load than the test and the validation model results. Also, the stiffness of the simulation under rigid condition has the same stiffness as the experimental test bending-shear effect curve (for details see §4.5 and Figure 4-9).

This result indicates that the more rigid boundary condition can achieve a smaller deflection with a higher load capacity.

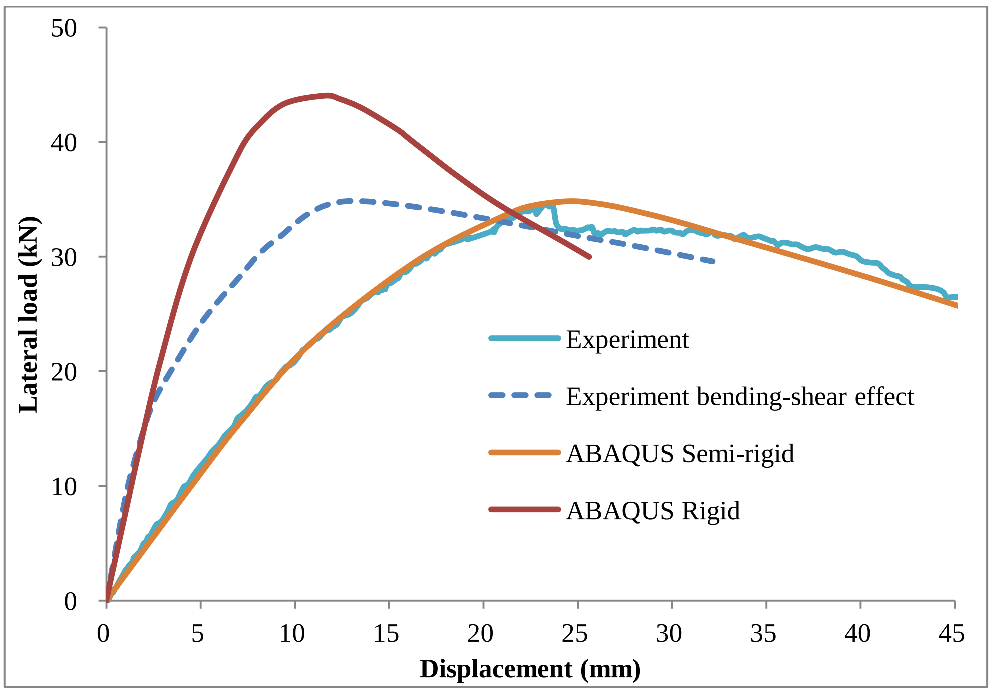

Figure 6-1: Load-displacement curve for total restrained support conditions (FC4)

6.3.2 Axial load

Figure 6-2 demonstrates the effect of changing axial load on structural behaviour of the reinforced concrete column (RC) as shown by the load-deflection relationships. The axial load increment is 100 kN. The interaction relationship of the axial load capacities and the lateral load capacities of the column is presented in Figure 6-3.

At the axial load is zero, the column can bear a pure bending moment with the maximum lateral load reaching 36.4 kN. When the axial load increases to 400 kN, the lateral load capacity increases to 45.0 kN, this point is the balanced point (see §2.7). However, when the axial load exceeds the balanced point, the interaction relationship shows a reverse trend. For example, if the column is subjected to 800 kN axial load, the lateral load capacity reduces to 33.2 kN. The ultimate axial load capacity of the column is 1220 kN when there is no bending moment.

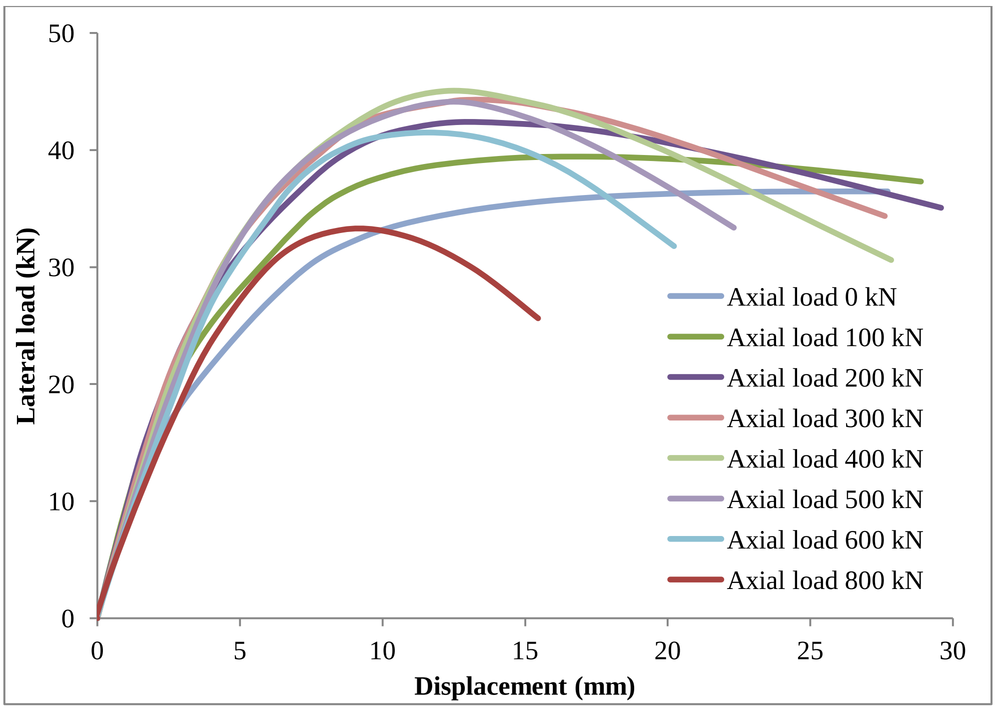

Figure 6-2: Load-deflection curves for different axial loads (RC)

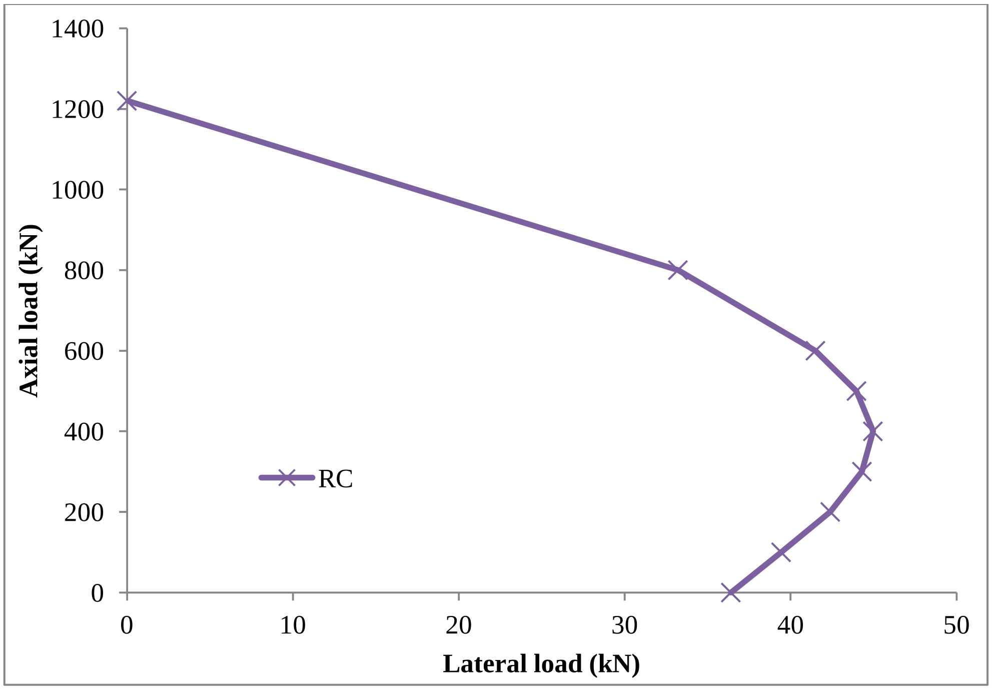

Figure 6-3: Interaction diagram for RC

Similar structural behaviour is found in the numerical simulations of FC2, FC4, in respect to axial load against lateral load curves, as shown in Figure 6-4 (for details see Appendix H).

At zero axial load, the lateral load capacity of FC2 is 25.6 kN, and FC4 is 41% greater than FC2 (36.2 kN), as presented in Table 6-2.

At the balanced point, the lateral load capacities of FC2 and FC4 rise to 45.8 kN and 50.8 kN respectively; FC4 being approximately 11% higher than FC2.

When only the axial loads are applied to FC2 and FC4, without any bending moment, the maximum axial load capacities reach 1523 kN and 1605 kN respectively. These results show that the higher the amount of welded mesh the greater the lateral load that can be resisted.

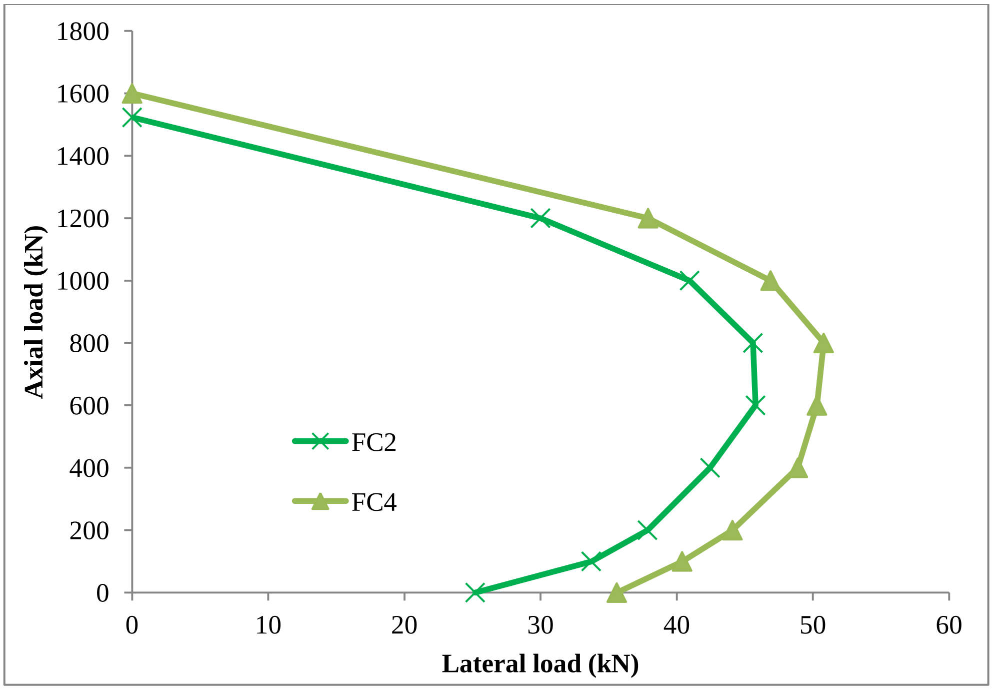

Figure 6-4: Interaction diagram from ABAQUS simulation for FC2 and FC4

Table 6-2: Result of maximum lateral loads for different axial loads for FC2 and FC4

Axial load (kN)	**Lateral load (kN)**		**Difference (%)**
	FC2	**FC4**	
0	25.2	35.6	41%
100	33.7	40.4	20%
200	37.9	44.1	16%
400	42.5	48.9	15%
600	45.8	50.3	10%
800	45.6	50.8	11%
1000	41.0	46.9	15%
1200	30.0	37.9	26%
1523	0		
1605		0	

6.3.3 Length

The length of the column affects the value of the maximum lateral load and the stiffness of the column. Figure 6-5 shows column FC4 with different lengths, 1020 mm, 1275 mm (25% higher length than 1020 mm) and 1530 mm (50% higher length than 1020 mm).

The 1020 mm length column has a maximum capacity 44.1 kN, and the 1275 mm reached a peak load of 23.9 kN, which is 54% of the load capacity of the 1020 mm column. For the 1530 mm column, the maximum lateral load was just 35% of the load capacity of the 1020 mm column. The initial stiffness also significantly reduced, the stiffness of 1020 mm column had 7.4 kN/mm, stiffness of 1275 mm column reached to 3.1 kN/mm which had 42% of the stiffness of the 1020 mm column. For 1530 mm column, the initial stiffness reduced to 1.4 kN/mm. The longer column has lower peak lateral load and lower initial stiffness.

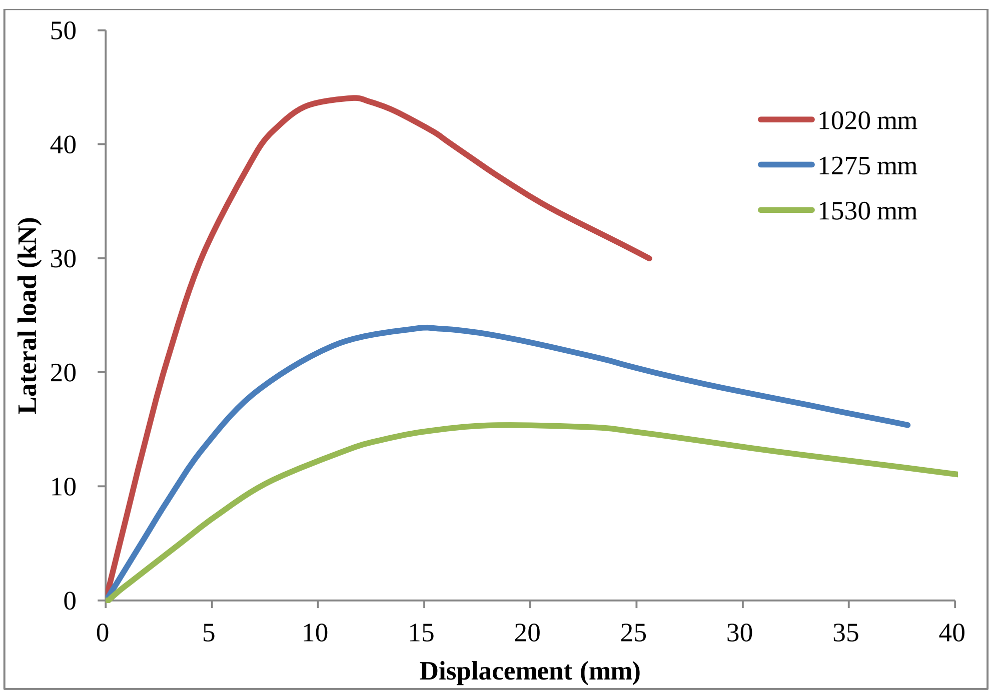

Figure 6-5: Load-deflection curves for different lengths of column (FC4)

Table 6-3: Result of lateral load with varying column lengths (FC4)

Length of column (mm)	Lateral load		Stiffness	
	Value (kN)	Degradation (%)	Value (kN/mm)	Degradation (%)
1020	44.1		7.4	
1275	23.9	54%	3.1	42%
1530	15.3	35%	1.4	19%

6.4 Concrete strength

In this section, three concrete compressive strengths are used, which are 30, 40 and 50 MPa (C30, C40 and C50) based on the Eurocode 2 (CEN, 2004a) concrete material model (see §5.3.2.1). The corresponding results are shown in Figure 6-6. These results illustrate that the maximum lateral load capacity can be increased by increasing the strength of the concrete. As shown in Figure 6-6, the lateral load capacity of the column increases from 38.3 kN to 46.8 kN as the concrete compressive strength is increased from C30 to C50. In addition, the initial stiffness of the column can be increased when the concrete compressive strength arises.

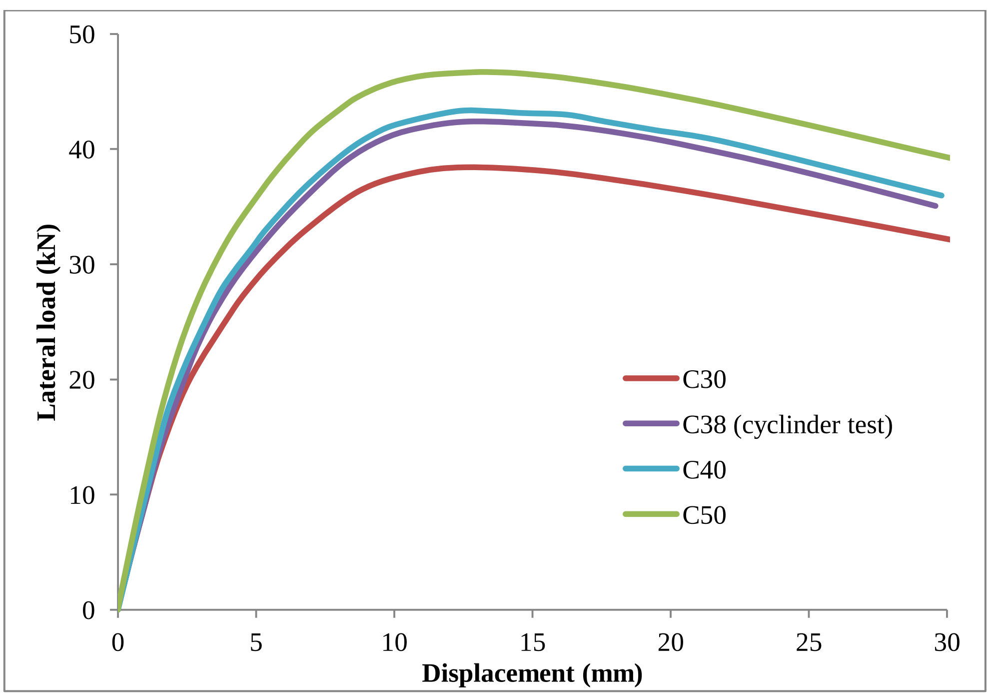

Figure 6-6: Load-deflection curves for different concrete strengths (RC)

6.5 Matrix strength

Based on Popovics (1973) material model (see §5.3.2.2), various compressive strengths for the matrix were used in this parametric study for the FC4 and RFC2 columns. They are 40, 50 and 60 MPa (M40, M50 and M60). The numerical simulation results are shown in Figures 6-7 and 6-8. It can be seen that the lateral load capacity and initial stiffness can be increased if the matrix strength is increased for these two sets of simulations.

For FC4, the lateral load capacity of the column using a M50 matrix is 39.4 kN, which is 12.5% higher than that using a M40 matrix. However, using a M60 matrix only increases this by a slight amount compared with the column using a M50 matrix. These comparisons indicate that the use of a very high grade of matrix cannot give significant benefits for the lateral load capacity of the column. From the numerical simulations of RFC2, the same conclusion can be drawn.

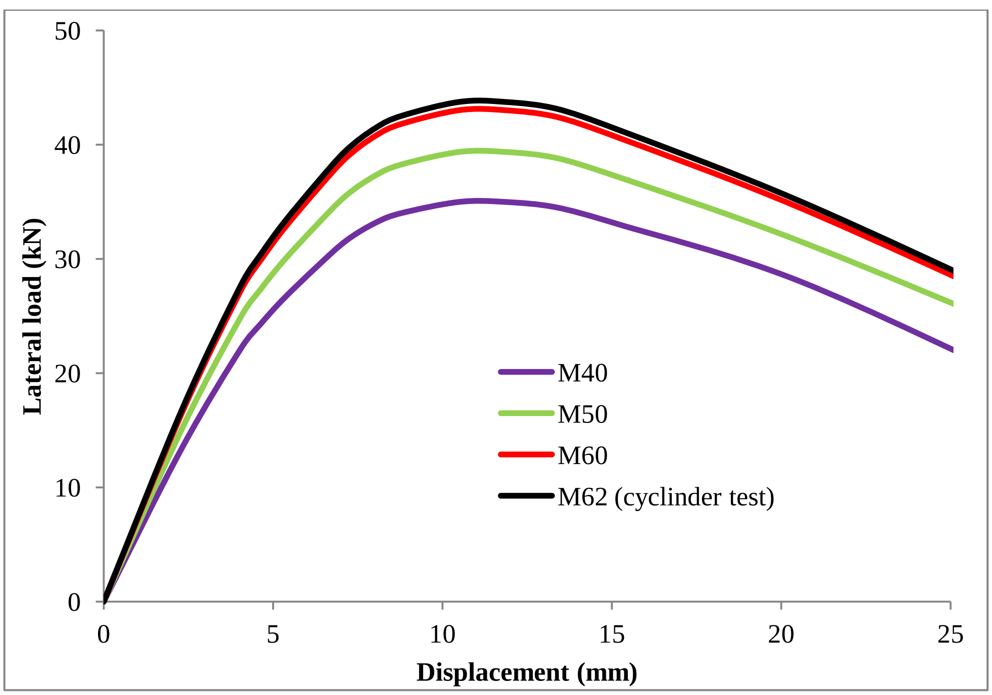

Figure 6-7: Load-deflection curves for different matrix strengths (FC4)

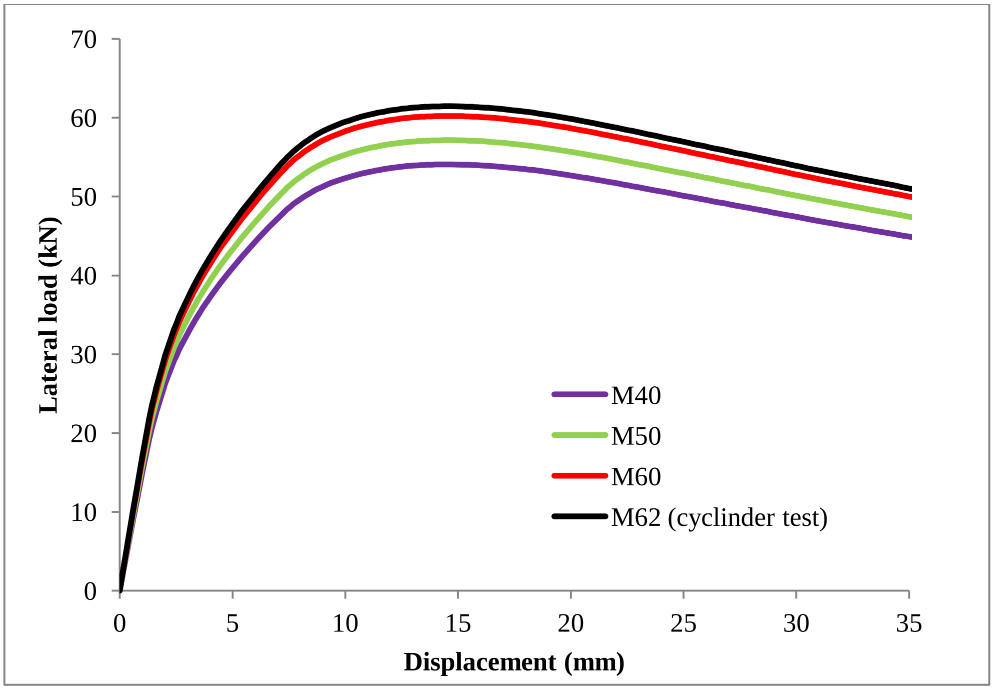

Figure 6-8: Load-deflection curves for different matrix strengths (RFC2)

6.6 Main reinforcing bar

The properties of the reinforcing bars are parameters that may drastically affect the structural behaviour of the column. This section will investigate the effect of reinforcing bars in terms of strength, diameter and number. Only RC column is used to examine the main effect of the reinforcing bars.

6.6.1 Strength

Figure 6-9 shows that the lateral load capacity of the RC column increases proportionally with the increasing strength of the steel bar. However, the initial stiffness of the column remains unchanged, because the Young's Modulus of the steel bar whatever S275, S355, S480 and S525 have similar value (CEN, 2004a).

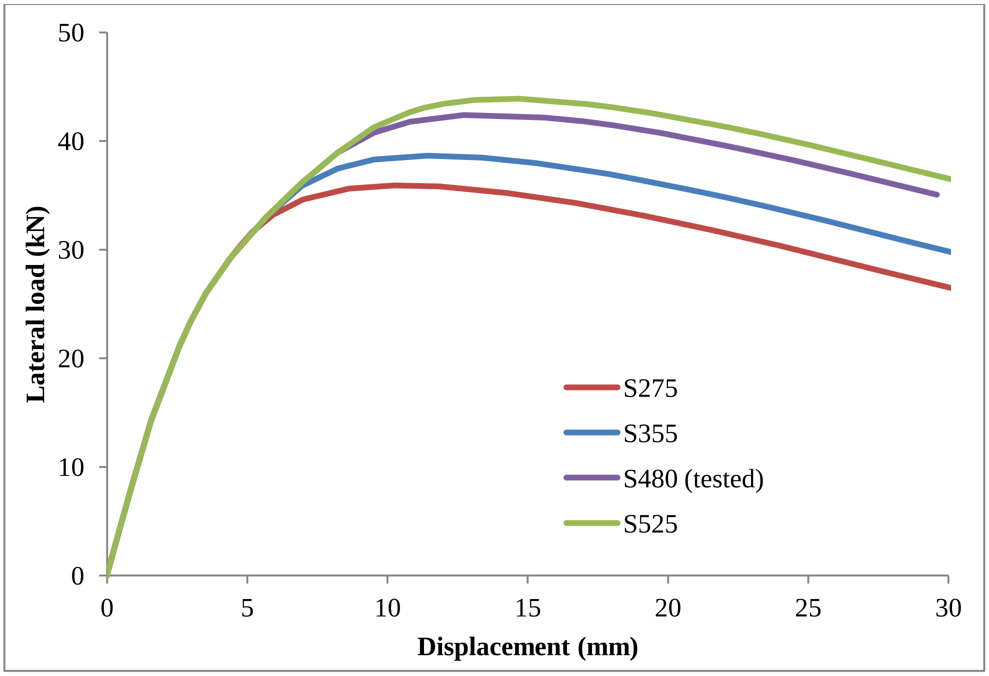

Figure 6-9: Load-deflection curves for different steel bar strengths (RC)

6.6.2 Diameter and number of bars

If the diameter of steel bar is enlarged, the lateral load capacity arises significantly as shown in Figure 6-10. For example, the lateral load capacity of the column is increased by 42% by using the steel bars having 905 mm^2 cross-section area compared with 452 mm^2. The reason is the increased diameter of the steel bar can strengthen both tension and compression resistances. Therefore, the bending moment capacity of the column is increased.

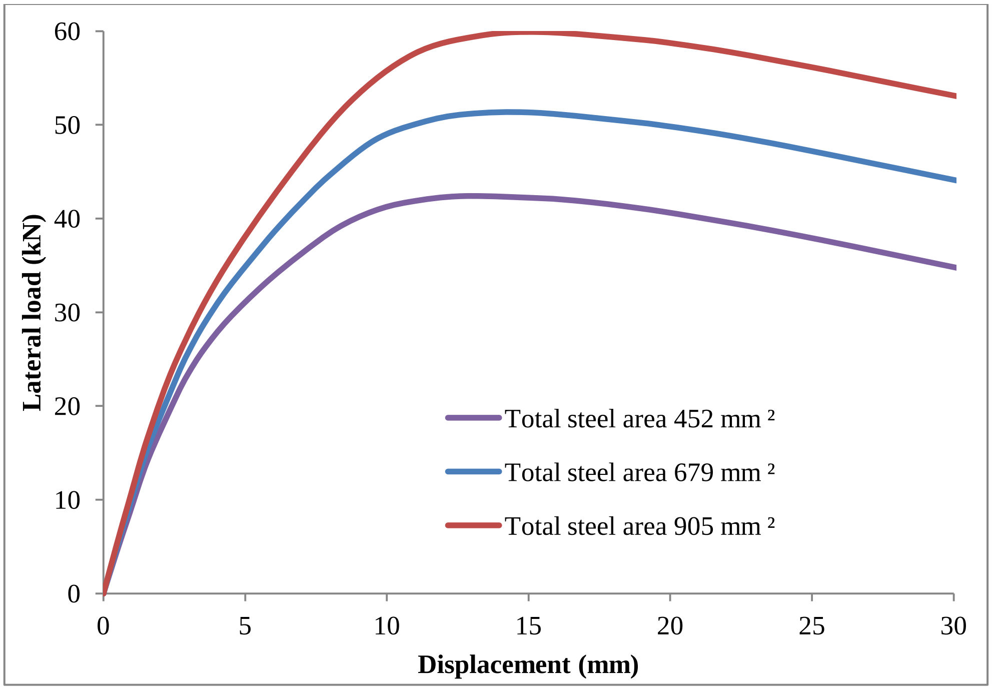

Figure 6-10: Load-deflection curves for different cross-section areas of steel bars (RC)

Compared with the original RC column (four steel bars at corner, detail in Figure 3-9), there are eight steel bars which are embedded in the reinforcement concrete for the modified column as shown in Figure 6-11 (four extra bars added). Number 1, 2, 3 and 4 bars are original arrangement, Number 5, 6, 7 and 8 bars are located at the middle point of each side. However, the total area (905 mm^2) of steel bars in the two columns is the same. Figure 6-12 shows the lateral load-deflection curves for 4 bars column and 8 bars column, which the 4 bars gave a higher lateral load capacity. The 4 bars column had peak lateral load capacity of 59.5 kN, which is 11% higher than the column using 8 bars arrangement (52.8 kN for 8 bars).

The reason is that bars 6 and 7, which are located at the neutral axial in the modified RC column, cannot provide any bending moment resistance. Therefore, the column using the 8 bars arrangement uses less steel for bending moment resistance.

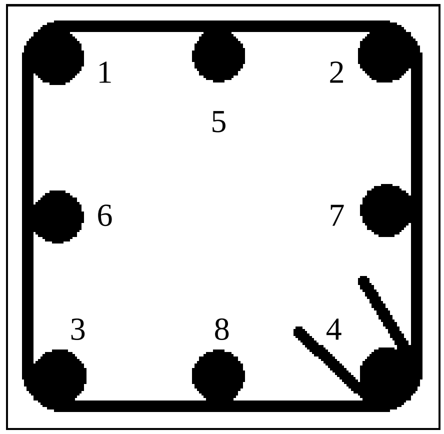

Figure 6-11: The eight steel bar arrangement

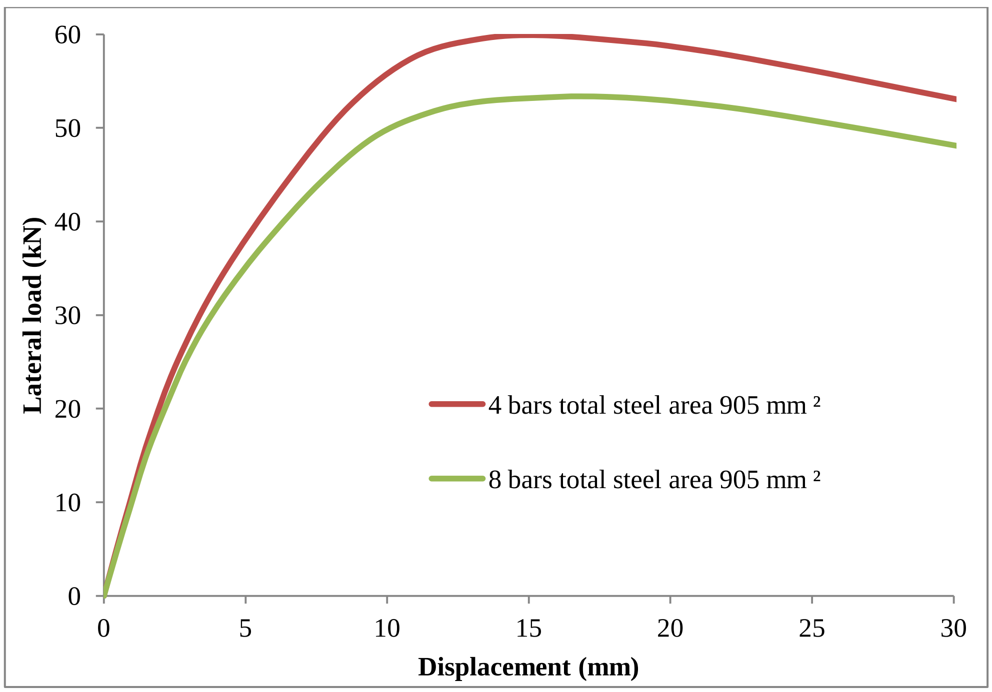

Figure 6-12: Load-deflection curves for the same area of steel with different bar arrangements (RC)

6.7 Stirrups

This section analyzes the influence of the stirrups on the structural behaviour of the column. Two aspects of the stirrups are considered: strength and size.

6.7.1 Strength

The stirrups only play a confinement role in reinforced concrete. Hence, Figure 6-13 shows that varying the strength of the stirrup cannot change the column relationship between lateral load and deflection.

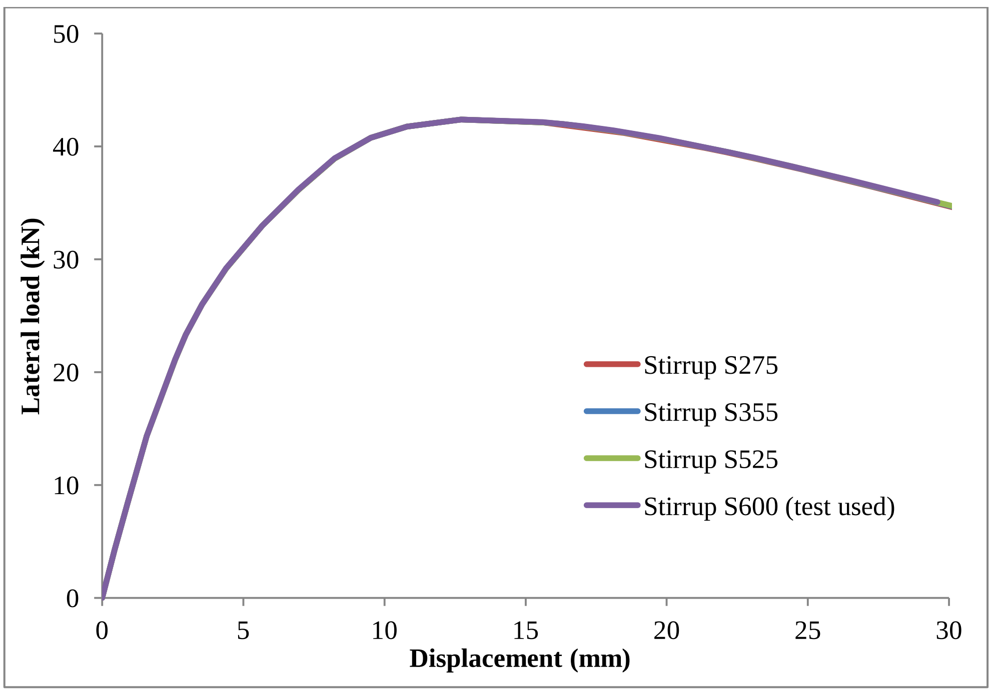

Figure 6-13: Load-deflection curves for different stirrup strengths (RC)

6.7.2 Size

Again, Figure 6-14 shows that the size of the stirrups has no effect on the column structural behaviour in terms of the load-deflection relationship. This further demonstrates the confinement role of the stirrups.

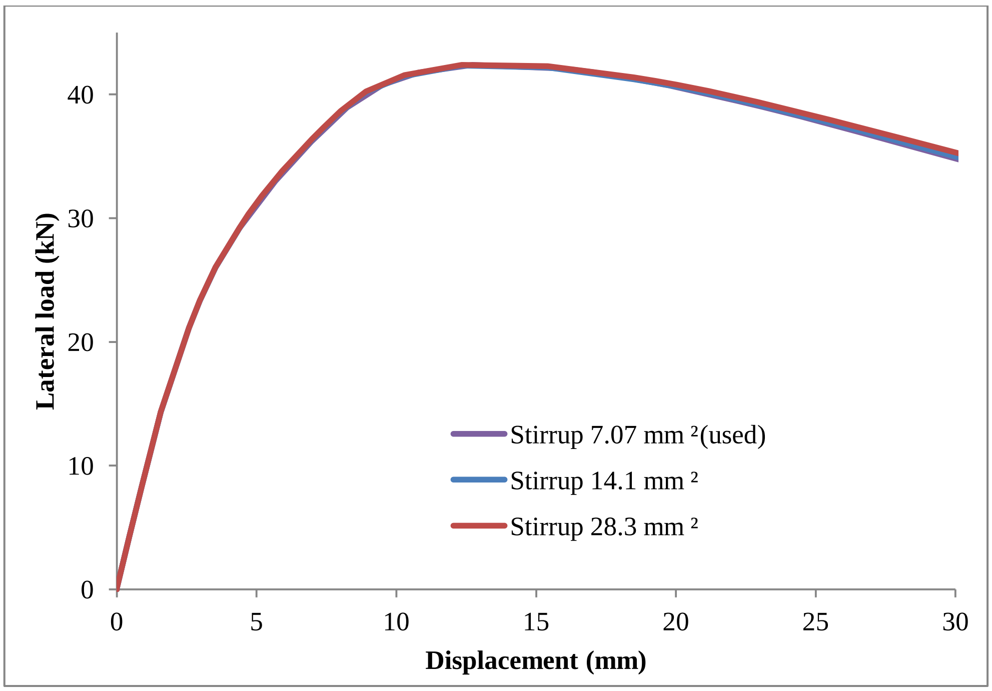

Figure 6-14: Load-deflection curves for different cross-section areas of stirrups (RC)

Whatever varying with the grade of stirrups and cross-section of stirrups, the value of lateral load had not significant change. The main contribution of the stirrups is to provided confined effect to the column, however, the stirrups has negligible effect on the bending moment capacity of the column.

6.8 Welded mesh

Welded mesh is a very important element in the construction and workability of the column. Therefore, the effects of the mesh strength, diameter and number of layer on the column behaviour are investigated. Columns FC4 and RFC2 are examined here.

6.8.1 Strength

Three different welded mesh grades were analyzed, which are 275, 355 and 525 MPa (S275, S355 and S525). Figures 6-15 and 6-16 present that lateral load capacity-deflection curves of FC4 and RFC2 column respectively, for both group of column, the strength of the welded mesh can influence the lateral load capacity rather than the initial stiffness. The higher strength of welded mesh produces a larger lateral load capacity.

The ferrocement column (FC4), using the S525 welded mesh can provide 24% higher lateral load capacity in comparison with a low-grade S275 welded mesh. The lateral load capacity of the S525 is 47 kN. The same conclusion was reached studying the reinforced concrete column strengthened using a ferrocement jacket (RFC2).

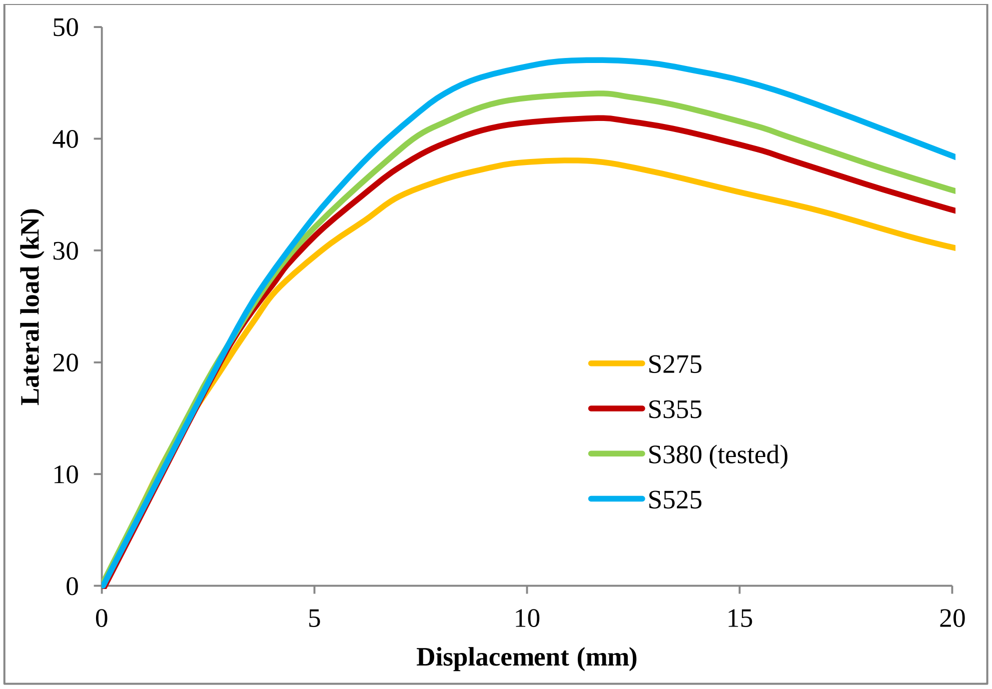

Figure 6-15: Load-deflection curves for different mesh strengths (FC4)

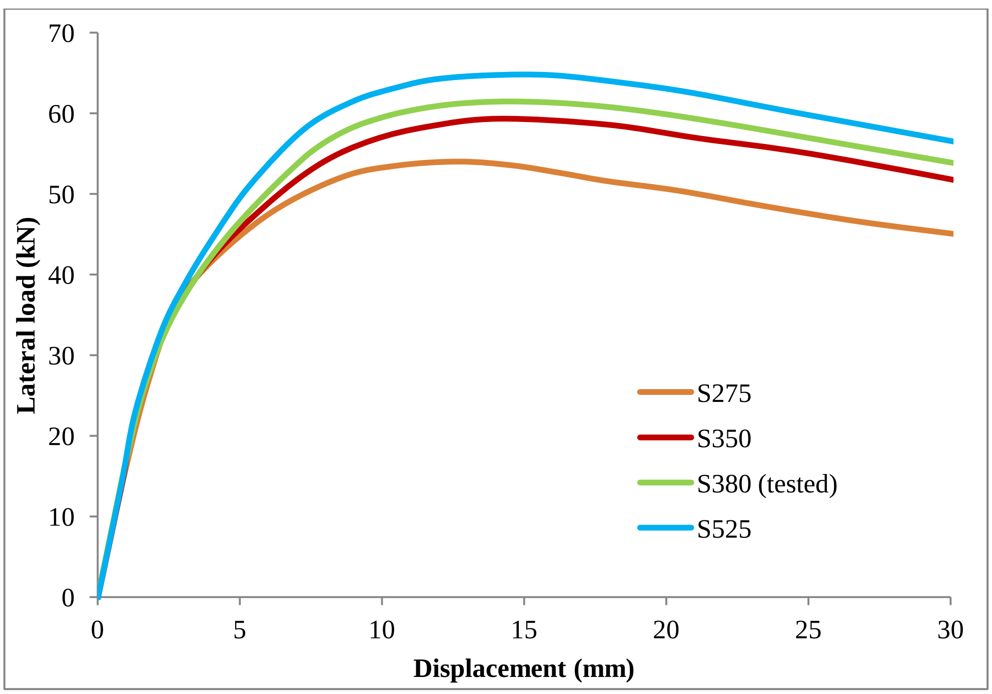

Figure 6-16: Load-deflection curves for different mesh strengths (RFC2)

Table 6-4: Peak load for different mesh strengths for FC4 and RFC2

Strength of mesh	**Ferrocement**		**Strengthened reinforced concrete**	
	Lateral peak load (kN)	**Increment (%)**	**Lateral peak load (kN)**	**Increment (%)**
S275	37.9		53.5	
S355	41.9	11%	59.1	10%
S380	44	16%	61.3	15%
S525	47	24%	64.7	21%

6.8.2 Diameter

In these parametric studies, three different welded mesh diameters were investigated. They are 1, 2 and 4 mm^2. Figures 6-17 and 6-18 show that the relationship of the load-displacement curves varies due to changing the cross-sectional area of the welded mesh in both columns, results are presented in Table 6-5.

For FC4, the lateral load capacity of the column using 4 mm^2 mesh reached 49.8 kN, which is 22% higher than the column using 1 mm^2 mesh, for the column using 2 mm^2 mesh has 13% higher than 1 mm^2 mesh column.

However, increasing the mesh diameter to increase the lateral load capacity for RFC2 column is not as significant as for the FC4 column. The RFC2 column using 4 mm^2 mesh can increase the lateral load capacity to 65 kN. This is 14% higher than the column using 1 mm^2 mesh.

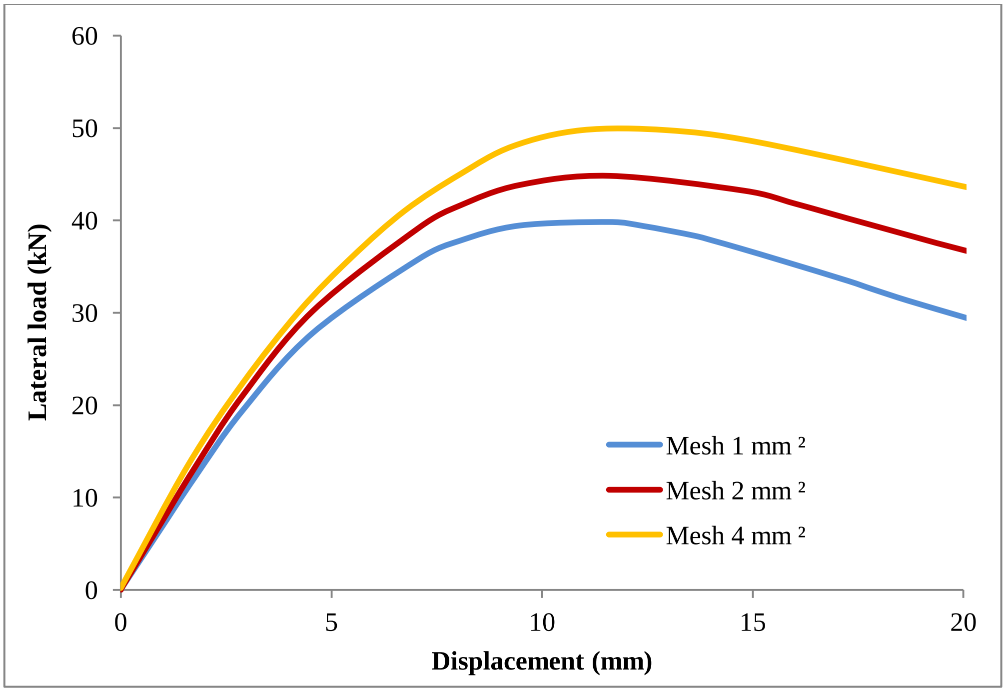

Figure 6-17: Load-deflection curves for different mesh sizes (FC4)

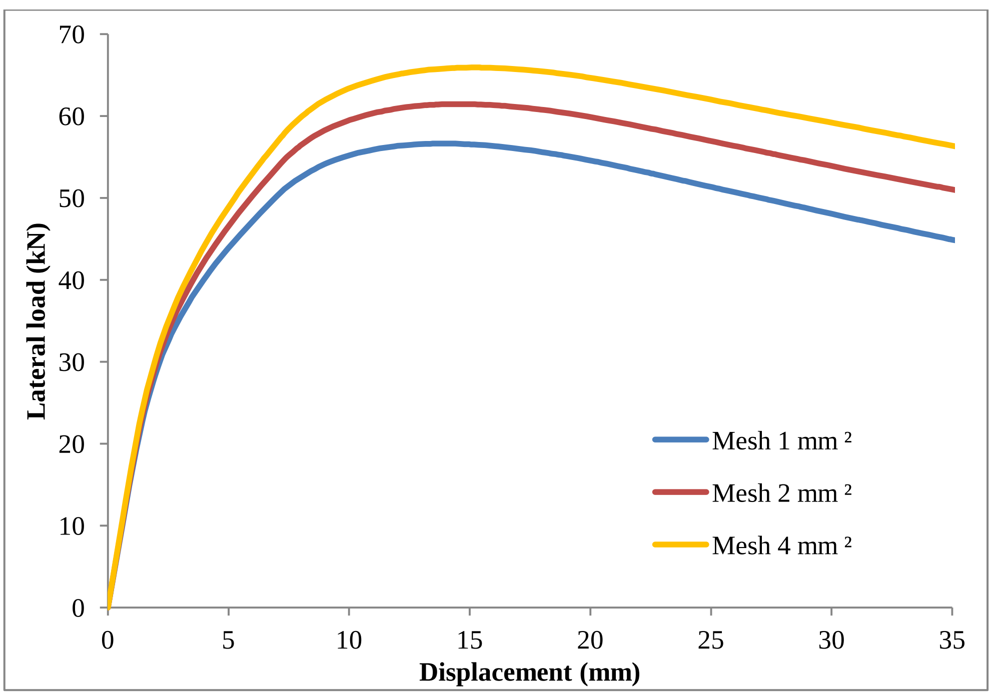

Figure 6-18: Load-deflection curves for different mesh sizes (RFC2)

Table 6-5: Peak load for various cross-sectional areas of mesh for FC2 and RFC2

Cross-section of mesh (mm^2)	FC4		RFC2	
	Lateral peak load (kN)	Increment (%)	Lateral peak load (kN)	Increment (%)
1	39.8		56.6	
2	44.9	13%	61.5	9%
4	49.8	22%	65	14%

6.8.3 Number of layers

The load-displacement curves for FC columns and RFC with varying numbers of layers mesh are shown in Figures 6-19 and 6-20, respectively. Obviously, increasing the number of layers for both group arise the maximum lateral load capacity. The stiffness of the ferrocement also increased as the number of layer increased, but for RFC this is not distinct.

Table 6-6 shows the peak lateral load for increasing numbers of mesh layers and the percentage load increase both for FC and RFC. The one-layer mesh FC (FC1) had a peak load of 37 kN. For the two-layer mesh column, the lateral load rose to 40.8 kN, which is 10% higher; and for FC5 it reached 46.8 kN (26% higher).

For RFC, the one-layer mesh column had a peak lateral load of 57.6 kN. For the two-layers mesh, it was 61.8 kN, which is 7% greater, and for the four-layer mesh (RFC4) it increased to 72.7 kN (26% greater).

The higher amount of mesh can strengthen both tension and compression resistances, so the bending moment capacity of the column is increased.

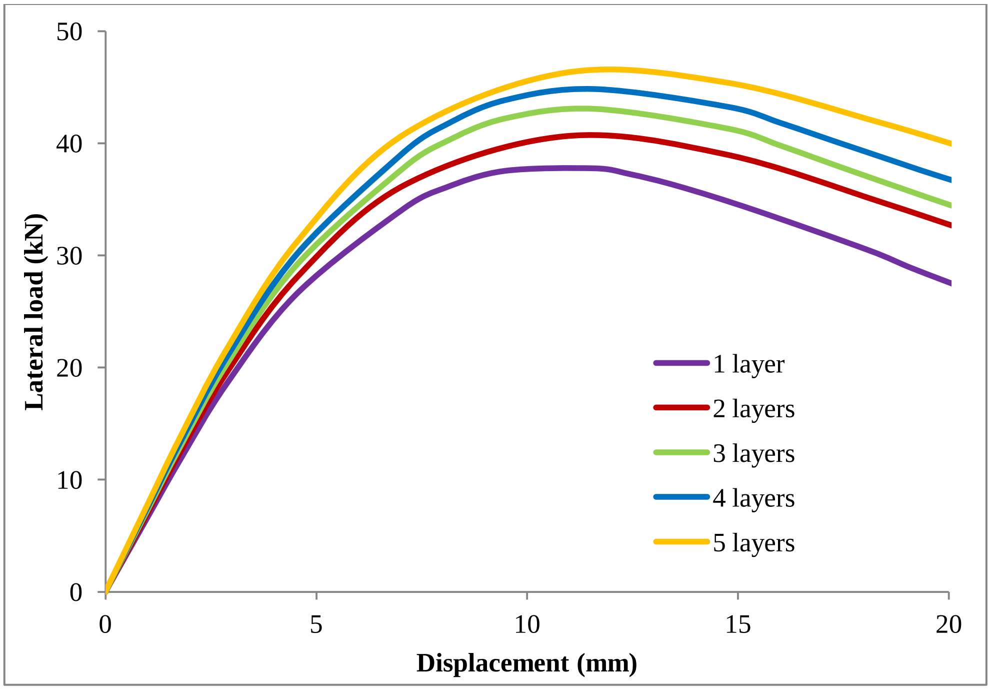

Figure 6-19: Load-deflection curves for different numbers of layers of mesh (FC)

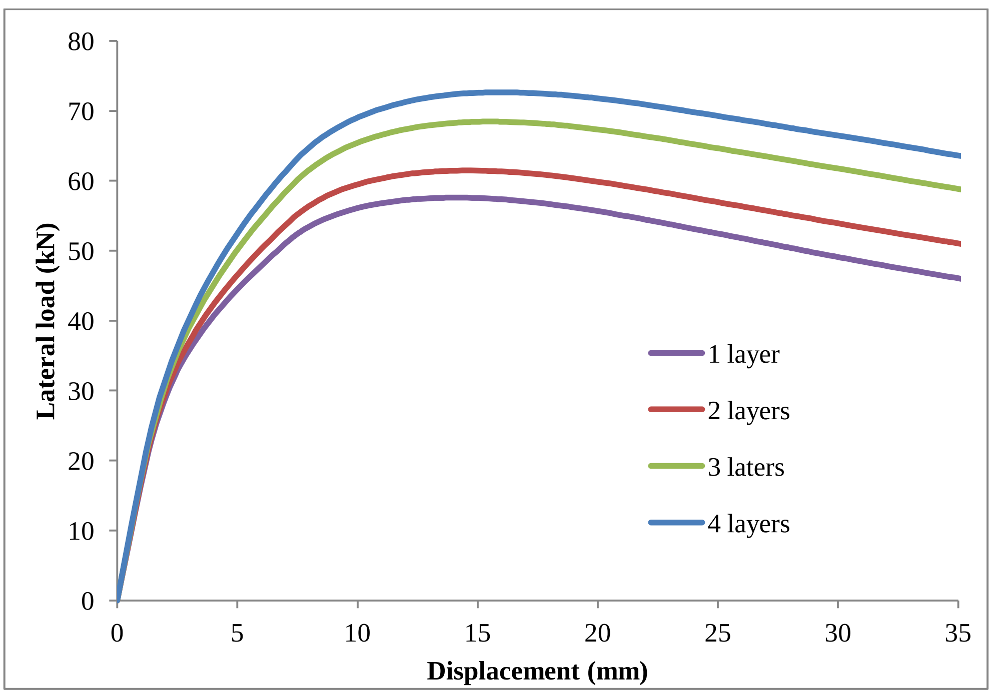

Figure 6-20: Load-deflection curves for different numbers of layers of mesh (RFC)

Table 6-6: Peak load for FC and RFC with different numbers of mesh layer

Number of layers	Ferrocement		Strengthened reinforced concrete	
	Lateral peak load (kN)	Increment (%)	Lateral peak load (kN)	Increment (%)
1	37		57.6	
2	40.8	10%	61.8	7%
3	43.1	16%	68.5	19%
4	44.9	21%	72.7	26%
5	46.8	26%		

6.9 Summary

In this chapter details of the parametric studies results have been presented. The following points are emphasized:

- Several parameters were examined using the ABAQUS simulation. These include end conditions, axial load, length of column, properties of the material and diameter of the reinforcement.
- The end condition and axial load have a significant effect on the peak lateral load. It has the same initial stiffness as the experiment bending-shear effect (detail in Chapter 4 and §6.3.1).
- With increasing grade of concrete or matrix, the peak load increases.
- For the stirrups, changes in the strength or cross-section area of the stirrup had negligible effect on the peak load capacity of the column.
- The interaction diagrams for ferrocement are similar; with FC4 having 10% greater lateral load than FC2 at the balanced point.

CHAPTER 7 Design guidelines

7.1 Introduction

The current design of ferrocement structures is usually based on the recommendations of Naaman (2000), IFS code (IFS, 2001) and ACI 549 (ACI, 1997b); however, design guidelines for ferrocement columns and reinforced concrete columns strengthened using ferrocement are not yet available. In this chapter, interaction diagrams for both FC and RFC columns are presented and design guidelines for columns are given.

For the design guidelines, the matrix properties are based on ACI 318 (ACI, 2008) and a simplification of Popovics (1973) model is used, as shown in the following section.

7.2 Material property

7.2.1 Welded mesh property

The property of welded mesh is assumed as a bi-linear (idealization) curve for the design guide, as shown in Figure 7-1. The first stage of the idealization curve is from 0 to the yield point $(\sigma_y, \varepsilon_y)$, the slope of this stage is the same as the Young's Modulus for the experimental test curve (175000 N/mm^2). The second stage is after the yield point.

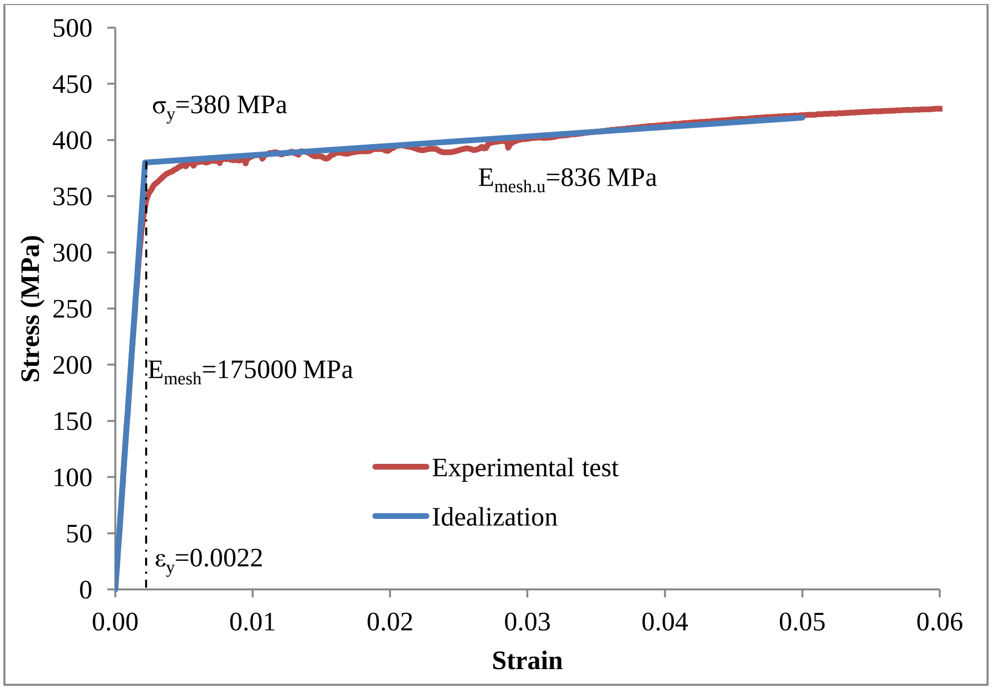

Figure 7-1: Ideal mesh bi-linear curve (S380)

The Young's Modulus of the mesh (E_{mesh}) for S380 (used in experimental test) is 175000 N/mm^2, and slope for second stage ($E_{mesh.u}$) is calculated as:

$$E_{mesh.u} = \frac{\sigma - \sigma_y}{\varepsilon - \varepsilon_y} \qquad \text{Eq 7-1}$$

Selecting a point where stress (σ) at 420 N/mm^2 and strain (ε) is 0.05, then

$$E_{mesh.u} = \frac{420 - 380}{0.05 - 0.0022} = 836\ \mathrm{N/mm^2}$$

$$f_{mesh} = \begin{cases} \varepsilon_{mesh} E_{mesh} & \varepsilon_{mesh} \ll \varepsilon_y \\ f_y + (\varepsilon_{mesh} - \varepsilon_y) E_{mesh.u} & \varepsilon_{mesh} \gg \varepsilon_y \end{cases} \qquad \text{Eq 7-2}$$

7.2.2 Matrix property

The property of the matrix is based on ACI 318 (ACI, 2008) and uses a simplification of Popovics (1973) model, and is shown in Figure 7-2. This curve was obtained in tests in the laboratory. This matrix was used in the FC2, FC4, RFC2 and RFC3 columns. The strength of this matrix is 62 N/mm^2 (called M62).

The "red" colour in Figure 7-2 presents Popovics model. This model is derived from experimental data; the details of which are shown in § 5.3.2.2. The maximum matrix compressive strain is usually between 0.003 and 0.004 (ACI, 2008). For M62, a strain of 0.004 was chosen as the ultimate strain.

The "blue" colour is a rectangular section which is recommended by ACI 318 (ACI, 2008). The stress-block having 0.85 f_m and strain is $\beta_1\varepsilon_{mu}$, where β_1 is a factor of the stress-block length related to the ultimate strain (see Figures 7-2 and 7-3).

The value of β_1 varies with the strength of the matrix and can be calculated using Eq 7-3, which is given by ACI 318 (ACI, 2008)

$$\beta_1 = \begin{cases} 0.85 & f_m \leq 27.6\ \text{MPa} \\ 0.85 - 0.05\left(\dfrac{f_m - 27.6}{6.9}\right) \geq 0.65 & f_m \geq 27.6\ \text{MPa} \end{cases} \qquad \text{Eq 7-3}$$

So for M62, the value of $\beta_1 = 0.85 - 0.05\left(\frac{62-27.6}{6.9}\right) = 0.6 < 0.65$, then $\beta_1 = 0.65$.

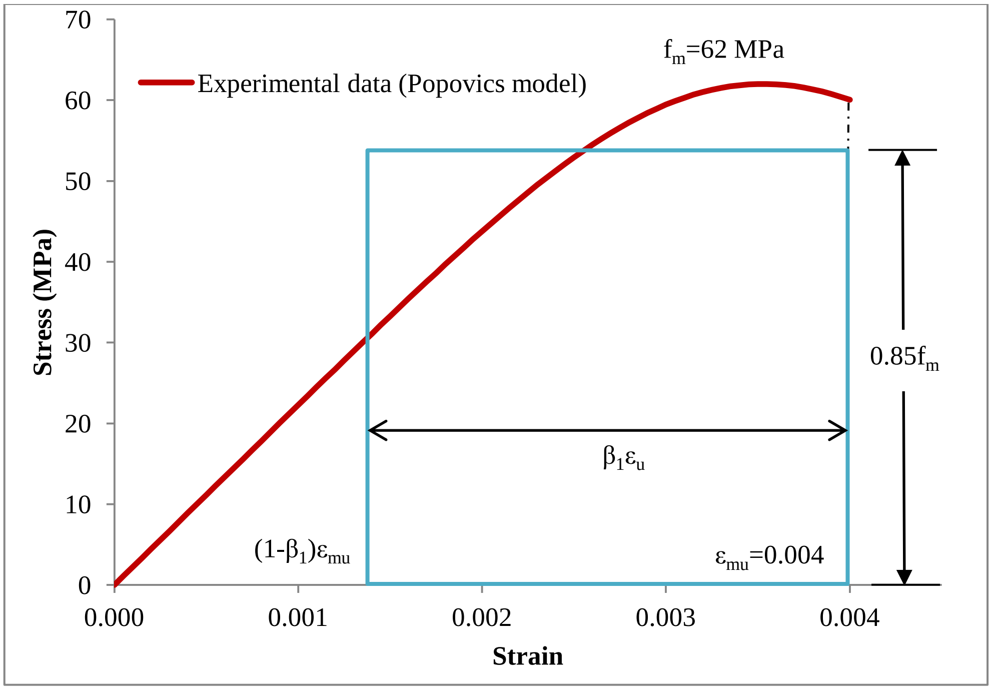

Figure 7-2: Design for matrix stress-block with strength 62 MPa (M62)

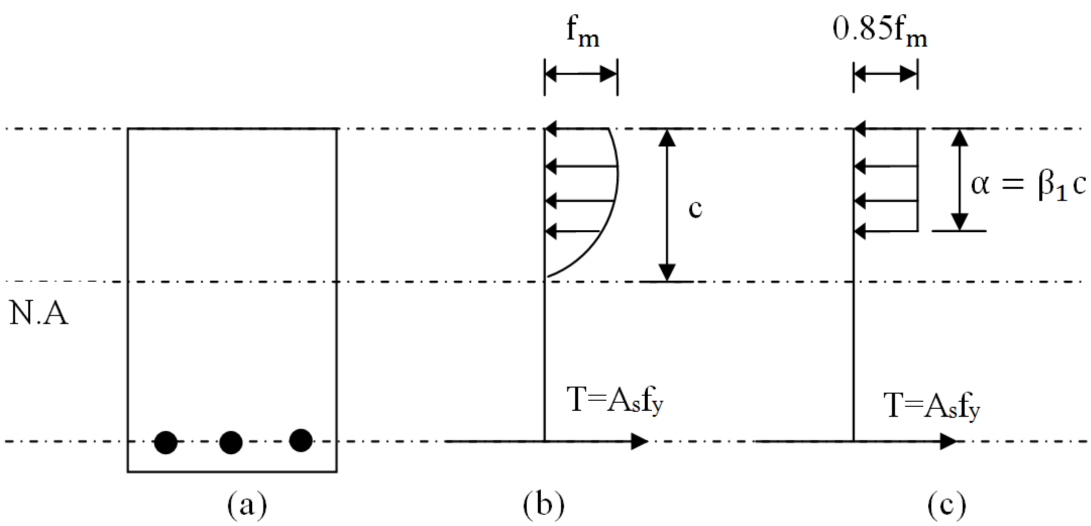

Figure 7-3: Stress-distribution shape, (a): cross-section, (b): the actual stress distribution, (c): the simplified rectangular distribution (after ACI 318)

Where:

f_m	Specified compressive strength of concrete
c	Distance from extreme compression to neutral axis (N.A)
α	Depth of equivalent rectangular stress block
β_1	Factor relating depth of equivalent rectangular compressive stress block to neutral axis (N.A) depth

For design, the tensile strength of the matrix is ignored.

7.3 Theoretical interaction diagrams and FEM results

7.3.1 The simplified strain and stress distribution diagram of FC4

To simplify the problem, assume that the welded mesh is uniformly distributed and the number of layers are merged as one, as shown in Figure 7-4. The next section gives an example (FC4, 150×150 mm) to describe and calculate the important points in the interaction diagram.

Firstly, the author assumed that the welded mesh in the ferrocement column is uniformly distributed with uniform cover thickness (minimum 3 mm) and spacing of 12.6 mm (the welded mesh opening is 12.6 mm). Calculate the number of strands for each side.

$$\text{Number of strands} = \frac{\text{width} - 2 \times \text{cover}}{\text{mesh opening}} + 1 = 12.4$$

Therefore, each side of the section has 12 strands and the cover is 5.5 mm. As the FC4 section is uniform and symmetrical, so the central axis (C.A) is through the middle of the section. The distance "c" (see Figure 7-3) is from the extreme compression surface to the position of the neutral axis (N.A).

As force equilibrium, the compressive and tensile forces must be balanced, which the compressive force include matrix and compressive mesh (C_m and $\sum C_{si}$), and the tensile force from tensile mesh $\sum T_{si}$. Notice that the force balance should consider the value of P, where P is the axial load on the section (see Figure 7-5), and Eq 7-4 shows the theoretical formula.

$$P = C_m + \sum C_{si} + \sum T_{si} \qquad \text{Eq 7-4}$$

Where:

P	Axial force
C_m	Force of matrix under compression
$\sum C_{si}$	Total force of welded mesh under compression
$\sum T_{si}$	Total force of welded mesh under tension
i	The letter "i" is number of meshes level

Define the compressive forces to be positive ($\mathbf{C_m}$ and $\sum \mathbf{C_{si}}$) and tensile forces to be negative ($\sum \mathbf{T_{si}}$). For each part of the Eq 7-4 is shown below:

The value of C_m is calculated in Eq 7-5, and displayed in §7.2.2.

$$C_m = 0.85 f_m(\alpha b) = 0.85 f_m(\beta_1 cb) \qquad \text{Eq 7-5}$$

The value of $\sum C_{si}$ is the sum of the forces at all welded mesh levels in compression, and $\sum T_{si}$ is the sum of forces at all mesh levels in tension. For accuracy, the forces at the mesh levels should be calculated individually. On failure of the section, the peak strain of the matrix (ε_{mu}) is 0.004, so the strain of mesh layer is calculated as shown in Eq 7-6.

$$\varepsilon_{si} = 0.004 \frac{(c - d_{si})}{c} \qquad \text{Eq 7-6}$$

The stress for each mesh level can be found using Eq 7-2, then the forces at the mesh levels can be determined, are shown in Eq 7-7 and Eq 7-8. When the value of ε_{si} is positive, the mesh will be taken compressive force (calculated in Eq 7-7), at value of ε_{si} is negative, the mesh will be taken tensile force (calculated in Eq 7-8).

$$C_{si} = A_{si}(f_{si} - 0.85f_c') \qquad 0 < \varepsilon_{si} \qquad \text{Eq 7-7}$$

$$T_{si} = A_{si}f_{si} \qquad 0 > \varepsilon_{si} \qquad \text{Eq 7-8}$$

At the neutral axis (N.A), the strain of the matrix or mesh is zero, above the N.A, it is in compression (calculated as C_{si}) and below it is in tension (calculated as T_{si}). Figure 7-5 shows the simplified strain and stress distribution diagrams. Note that the matrix stress and mesh stress are not to scale.

The bending moment is calculated about the central axis (C.A) and this is shown in Eq 7-9. All the member calculations are based on the C.A.

$$M = C_m\left(\frac{h}{2} - \frac{\alpha}{2}\right) + \sum C_{si}\left(\frac{h}{2} - d_{si}\right) + \sum T_{si}\left(\frac{h}{2} - d_{si}\right) \qquad \text{Eq 7-9}$$

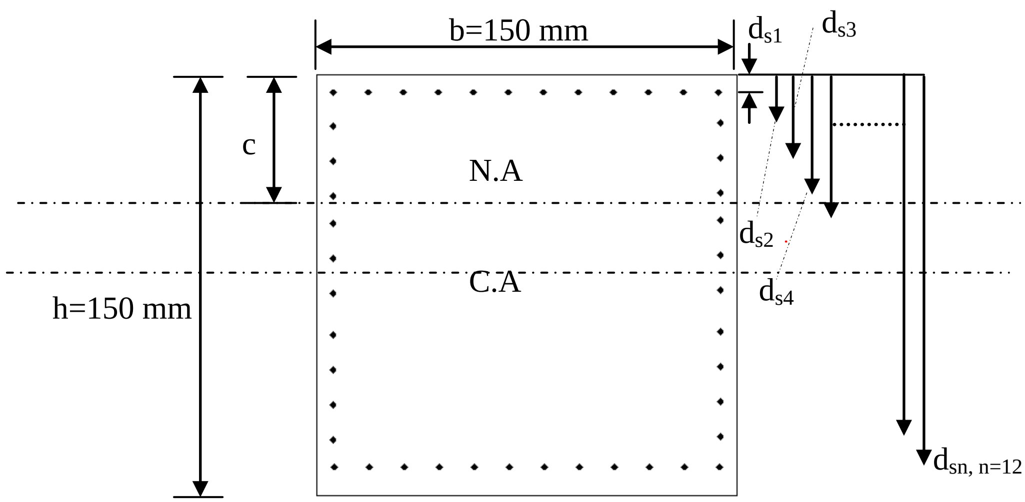

Figure 7-4: Ferrocement section

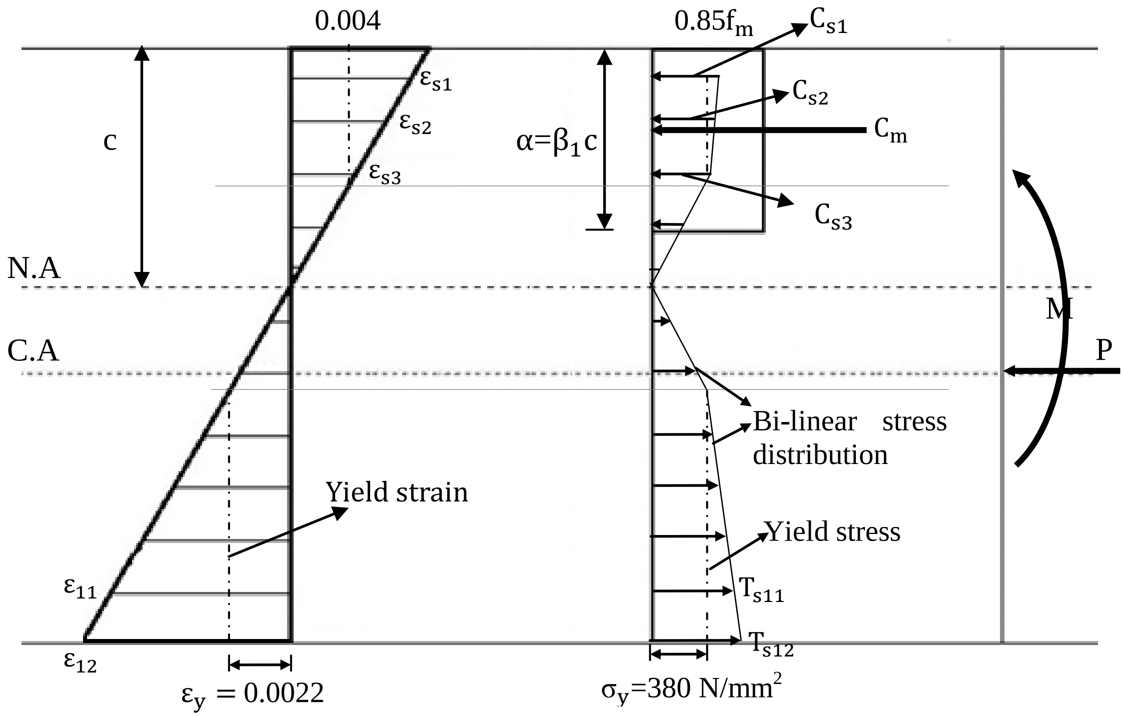

(a): Strain distribution (b): Stress distribution (c): Force and Moment

Figure 7-5: The simplified strain and stress distribution diagram

Note： the matrix stress and mesh stress are not to scale

7.3.2 Interaction diagram (P-M) for the matrix

Figure 7-6 shows the interaction diagram (P-M), through the different values of axial load and positions of the N.A There are four important situations: (i) point a, pure bending moment, (ii) point b, balance position, (iii) point bc, zero strain in the tension mesh, (iv) point c, pure axial load. A detailed description is provided below.

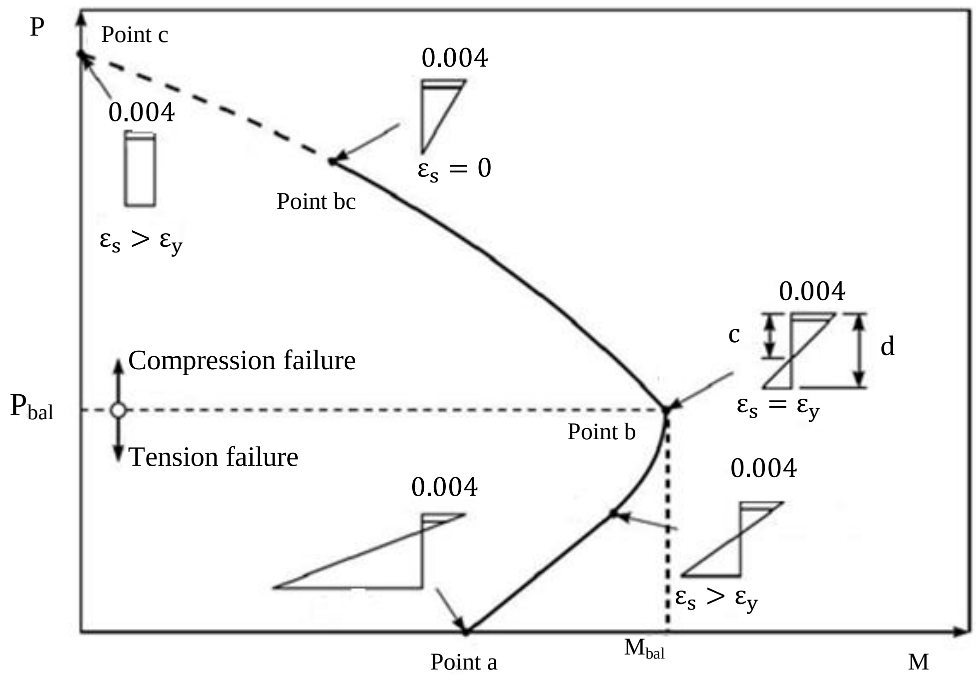

Figure 7-6: The interaction diagram (Caprani, 2006)

Point a: Pure bending:

This point represents the matrix column in pure bending. The surface with the extreme compression reaches its ultimate strain of 0.004. The N.A is close to the top of the compression welded mesh and the section failure is a tension failure.

Point b: Balanced position:

This point represents the matrix column in a balanced position. The surface of extreme compression is reaching its ultimate strain of 0.004, just as ε_{12} is yielding. The value of ε_{12} is calculated as $\sigma_{12}/\ E_{mesh} = 380/175000 = 0.0022$. The value of axial load at point c is critical in that below this value the column will be fail in tension, above this value it will fail in compression (see Figure 7-6).

Point bc: Zero strain for M-d$_{s12}$:

The point bc will occur when the strain of M-ds$_{12}$ at zero. At this point, the N.A is through the M-d$_{s12}$ strands (the distance of N.A is 144.5 mm). Increasing the axial load forms the balanced position (Point b shows in Figure 7-6), then the N.A moves to the tensile zone, until it reached M-d_{s12}. All the mesh takes a compressive force (not including M-d_{s12}, which takes no force).

Point c: Pure axial load

This point represents the matrix column under pure axial load. All the surfaces are taken equally in compression. M is zero and the N.A is at infinity.

7.4 Example calculation using FC4

7.4.1 Information required

The mesh arrangement is exactly as in Figure 7-4. Before the calculation, the dimensions and properties will be presented. Table 7-1 shows the dimension of the matrix and welded mesh section. Table 7-2 shows the properties of the matrix and mesh. Table 7-3 shows the position of each mesh level.

Dimensions:

Table 7-1: Dimensions of the matrix and the welded mesh

Matrix	**h (mm)**	150
	b (mm)	150
	A_g (mm^2)	22500
Welded mesh	**Diameter (mm)**	1.6
	Opening (mm)	12.6
	A_s for single wire (mm^2)	2.01
	A_{s1} and A_{s12} (mm^2)	2.01×4×12=96.5
	A_{s2}, A_{s3}, ..., A_{s11} (mm^2)	2.01×4×2=16.1

Properties:

Table 7-2: The properties of matrix and welded mesh

Matrix	f_m **(N/mm²)**	62
	E_m **(N/mm²)**	21700
	ε_{mu}	0.004
	β_1	0.65
Welded mesh	f_y **(N/mm²)**	380
	E_{mesh} **(N/mm²)**	175000
	$\varepsilon_{mesh.y}$	380/175000=0.0022
	$E_{mesh.u}$ **(N/mm²)**	836

Arrangement:

Table 7-3: The position of each mesh level, d_{si}

Level of mesh	**Each mesh layer area A_s (mm²)**	**Distance from extreme compression d_{si} (mm)**
1	96.5	5.5
2	16.1	18.1
3	16.1	30.8
4	16.1	43.4
5	16.1	56.0
6	16.1	68.7
7	16.1	81.3
8	16.1	94.0
9	16.1	106.6
10	16.1	119.2
11	16.1	131.9
12	96.5	144.5

7.4.2 Point a: Pure moment

In the detailed calculations that follow, the convention that is adopted is that compression is positive and tension is negative. A trial and error method is used in this section, to solve the values of c (position of N.A) at different points. This method uses "EXCEL" and is presented in Tables 7-4 and 7-5.

Input a value of c, the mesh strain, mesh stress, mesh force, mesh moment, matrix force and moment for each member to be calculated using the load equilibrium and moment equilibrium equations (Eq 7-4 and Eq 7-9). Figure 7-7 shows the strain diagram of the N.A for pure moment.

For pure moment, the value of the axial load (P) is zero, as shown:

$$P = C_m + \sum C_{si} + \sum T_{si} = 0 \qquad \text{Eq 7-10}$$

For the trial and error method, set two basic values of "c", say 5.5 mm and 75 mm, when the N.A passes through M-d_{s1} and the central axis. After calculation, the position of N.A (c) is found to be 12.7 mm for a total axial load (P) of zero.

Table 7-4 presents the results for the mesh strain, stress, force and moment. The mesh strain variation from positive 0.0023 (M-d_{s1}) to negative 0.04312 (M-d_{s12}), is calculated as being linear (see Figure 7-5), and the extreme compression matrix surface is 0.004.

The mesh strain for each level of mesh is calculated using Eq 7-2. This equation is a bi-linear curve for mesh strength (see Figure 7-1).

The mesh force is the mesh stress times the cross-section area of each mesh level. M-d_{s12} has taken the highest force which is 39.9 kN. The calculation requires the compressive strength C_{si} (always positive) and the tensile strength T_{si} (always negative).

The mesh moment, Eq 7-9, is calculated as:

Compressive mesh moment: $$C_{si}\left(\frac{h}{2} - d_{si}\right)$$ Eq 7-11

Tensile mesh moment: $$T_{si}\left(\frac{h}{2} - d_{si}\right)$$ Eq 7-12

The value of $(h/2 - d_{si})$ will be positive above the central axis (C.A.), and negative below it. So the mesh moment of M-d_{s1} is 2.55 kNm (only this mesh level has a positive mesh force, which the force is 36.7 kN). The second level mesh has a tensile force (negative 4.82 kN), so the resulting moment is -0.27 kNm. Then, the values of the moment in the mesh are all negative above the C.A.

Below the C.A. the value of $(h/2 - d_{si})$ is negative, so the tensile force in the mesh is negative, but the resulting mesh moment becomes positive (negative times negative). The highest value of the moment is M-d_{s12}, 2.77 kNm, and the lowest value, which is close to the C.A. is 0.04 kNm, for M-d_{s6} is negative value and M-d_{s7} has positive value.

Table 7-4: Force and moment for meshes for the pure moment (c=12.7 mm)

Mesh name	**Mesh strain (ε_{si})**	**Mesh stress f_{si} (MPa)**	**Mesh force (kN)**	**Mesh moment (kNm)**
M-d_{s1}	0.0023	380.1	36.7	2.55
M-d_{s2}	-0.0017	-291.8	-4.82	-0.27
M-d_{s3}	-0.0056	-382.9	-6.16	-0.27
M-d_{s4}	-0.0096	-386.2	-6.21	-0.20
M-d_{s5}	-0.0135	-389.5	-6.27	-0.12
M-d_{s6}	-0.0175	-392.8	-6.32	-0.04
M-d_{s7}	-0.0214	-396.1	-6.37	0.04
M-d_{s8}	-0.0254	-399.4	-6.43	0.12
M-d_{s9}	-0.0293	-402.7	-6.48	0.20
M-d_{s10}	-0.0333	-406.0	-6.53	0.29
M-d_{s11}	-0.0372	-409.3	-6.59	0.37
M-d_{s12}	-0.0412	-412.6	-39.9	2.77

Table 7-5 shows the total mesh force and mesh moment. The total force is zero, which compressive matrix is 65.3 kN, compressive mesh is 36.7 kN and tensile mesh force is negative 102 kN. The moment of the compressive matrix is 4.62 kNm, and the moment of the compressive mesh is 2.55 kNm. The rest of the mesh takes a tensile force, so the moment is 2.90 kNm. The total moment is the sum of the three parts, which gives 10.1 kNm (which calculated as 4.62+2.55+2.90=10.1 kNm).

Table 7-5: Results for total axial load and moment of meshes for the pure moment

Description	**Force (kN)**		**Moment (kNm)**	
Compressive matrix	C_m	65.3	$C_m\left(\frac{h}{2}-\frac{\alpha}{2}\right)$	4.62
Compressive meshes	$\sum C_{si}$	36.7	$\sum C_{si}\left(\frac{h}{2}-d_{si}\right)$	2.55
Tensile meshes	$\sum T_{si}$	-102	$\sum T_{si}\left(\frac{h}{2}-d_{si}\right)$	2.90
Total	P	0	M	10.1

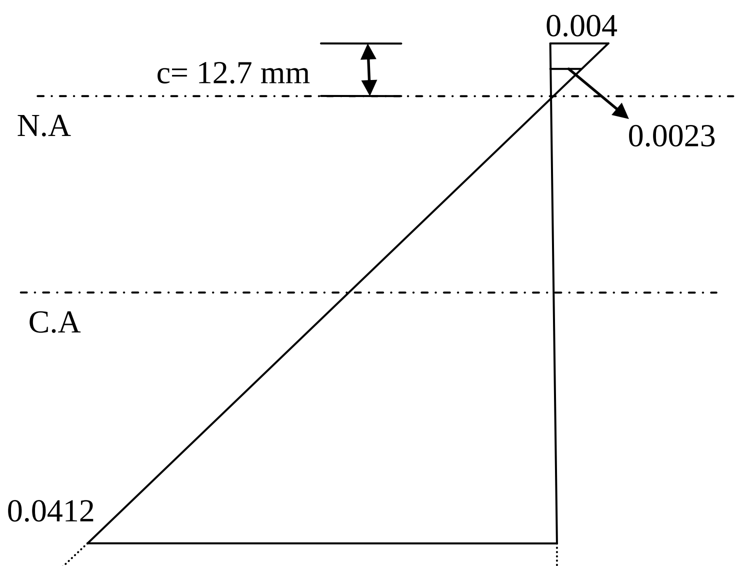

Figure 7-7: Strain diagram of the N.A for a pure moment

7.4.3 Point b: Strength at the balanced condition

Point b is when the compressive matrix reaches its ultimate strain (0.004) and the tension reinforcement, M-d_{s12}, yields (0.0022) simultaneously. The load equilibrium is based on Eq 7-4. As the axial load increases, the compression matrix and reinforcing forces are increased, and the N.A moves in the tensile direction.

Between the pure bending and the balanced position conditions, the strain of the tensile mesh (M-d_{s12}) is greater than the mesh at yielding, which is fail as a tensile failure. After the balanced position the column will fail as a compression failure.

Again, the value of mesh strain, stress, force and moment is calculated using the same method (trial and error method). The position of N.A (c) is equal 93.7 mm. Tables 7-6 and 7-5 show the results.

Table 7-6: Force and moment of meshes at the balanced condition (c=93.7 mm)

Mesh name	**Mesh strain (ε_{si})**	**Mesh stress f_{si} (MPa)**	**Mesh force (kN)**	**Mesh moment (kNm)**
M-d_{s1}	0.0038	381.3	36.8	2.56
M-d_{s2}	0.0032	380.9	6.13	0.35
M-d_{s3}	0.0027	380.4	6.12	0.27
M-d_{s4}	0.0021	375.7	6.04	0.19
M-d_{s5}	0.0016	281.3	4.52	0.09
M-d_{s6}	0.0011	186.9	3.01	0.02
M-d_{s7}	0.0005	92.5	1.49	-0.01
M-d_{s8}	0.0000	-1.9	-0.03	0.00
M-d_{s9}	-0.0006	-96.3	-1.55	0.05
M-d_{s10}	-0.0011	-190.7	-3.07	0.14
M-d_{s11}	-0.0016	-285.1	-4.59	0.26
M-d_{s12}	-0.0022	-379.5	-36.63	2.55

Table 7-7: Results of total axial load and moment of meshes at balanced condition

Description	Force (kN)		Moment (kNm)	
Compressive matrix	C_m	481.4	$C_m\left(\frac{h}{2}-\frac{\alpha}{2}\right)$	21.4
Compressive meshes	$\sum C_{si}$	64.1	$\sum C_{si}\left(\frac{h}{2}-d_{si}\right)$	3.46
Tensile meshes	$\sum T_{si}$	-45.9	$\sum T_{si}\left(\frac{h}{2}-d_{si}\right)$	2.99
Total	P	499.7	M	27.9

When the N.A is at 93.7 mm, nearly two-thirds of the section from the surface, 7 level meshes (M-d_{s1} to M-d_{s7}) takes compression, and M-d_{s1} takes 36.8 kN force. The strain of M-d_{s12} is negative 0.0022 (just yielding), when it has taken 36.7 kN force in tension.

The axial load at the balanced position is 499.7 kN. Most of the axial load is supported by matrix compression (481.4 kN). The moment at balanced position is 27.9 kNm.

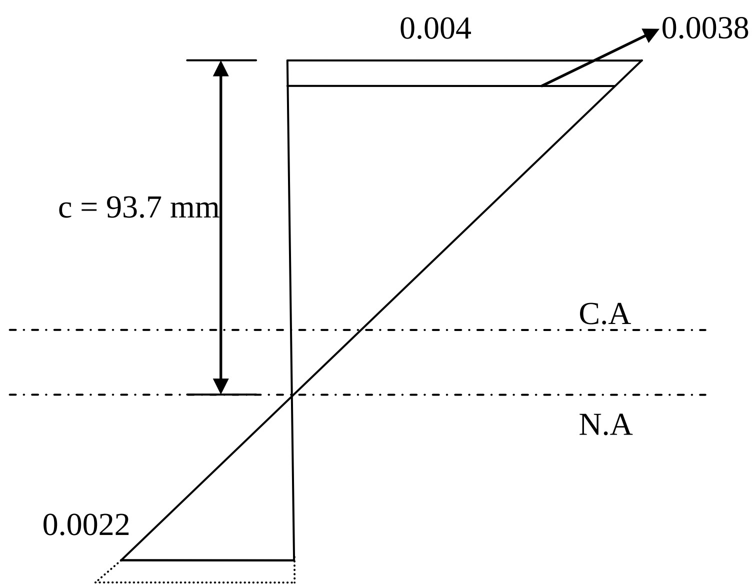

Figure 7-8: Strain diagram of the N.A at the balanced position

7.4.4 Point bc: M-d_{s12} mesh at zero tensile strain

After the axial load exceeds 499.7 kN (the load for the balanced position), the N.A moves further towards the tension surface, and the section will fail as a compression failure. The strain of the matrix surface reaches a peak strain before M-d_{s12} yields. When the N.A moves to M-d_{s12}, the strain of M-d_{s12} is zero, so no mesh takes tension. Tables 7-8 and 7-9 show the results of the N.A at through the first level mesh (M-d_{s1}), the value of "c" is 144.5 mm.

Table 7-8: Force and moment of meshes at point bc (c=144.5 mm)

Mesh name	Mesh strain (ε_{si})	Mesh stress f_{si} (MPa)	Mesh force (kN)	Mesh moment (kNm)
M-d_{s1}	0.0038	381.4	36.81	2.56
M-d_{s2}	0.0035	381.1	6.13	0.35
M-d_{s3}	0.0031	380.8	6.13	0.27
M-d_{s4}	0.0028	380.5	6.12	0.19
M-d_{s5}	0.0024	380.2	6.12	0.12
M-d_{s6}	0.0021	367.3	5.91	0.04
M-d_{s7}	0.0017	306.1	4.92	-0.03
M-d_{s8}	0.0014	244.9	3.94	-0.07
M-d_{s9}	0.0010	183.6	2.95	-0.09
M-d_{s10}	0.0007	122.4	1.97	-0.09
M-d_{s11}	0.0003	61.2	0.98	-0.06
M-d_{s12}	0	0.0	0.00	0.00

Table 7-9: Results of total axial load and moment of meshes at point bc

Description	**Force (kN)**		**Moment (kNm)**	
Compressive matrix	C_m	742.5	$C_m\left(\frac{h}{2}-\frac{\alpha}{2}\right)$	20.8
Compressive meshes	$\sum C_{si}$	82.0	$\sum C_{si}\left(\frac{h}{2}-d_{si}\right)$	3.18
Tensile meshes	$\sum T_{si}$	0.00	$\sum T_{si}\left(\frac{h}{2}-d_{si}\right)$	0.00
Total	P	824.5	M	24.0

The N.A moves to 144.5 mm. At this position, no-one mesh level takes a tension force. The matrix compression supports 742.5 kN, and the value of axial load reaches 824.5 kN. The value of total moment is 24.0 kNm. The moment of mesh is only 3.18 kNm. Figure 7-9 shows the simplified strain diagram with the N.A at M-d_{s12}.

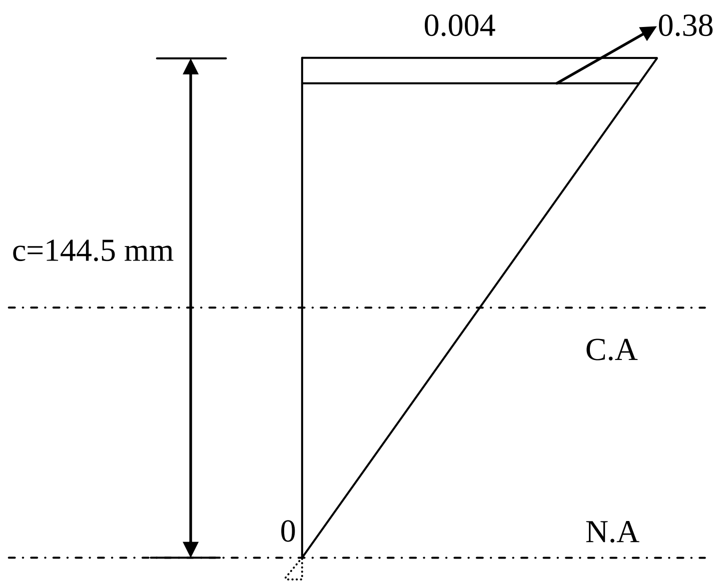

Figure 7-9: Strain diagram for the N.A at the balanced position

7.4.5 Point c: Pure axial load:

When the N.A moves forward from the M-d_{s12} mesh at zero strain, the N.A will fall outside the section and the strain distribution will eventually change from triangular to uniform. An increase in axial load will lead to a smaller moment at failure. The pure axial load of the section creates a uniform strain distribution and can be calculated using Eq 7-13. Moreover, Figure 7-10 shows a simplification of the N.A outside the element and at infinity.

$$P_0 = 0.85f'_c(A_g - A_{st}) + f_yA_{st} \qquad \text{Eq 7-13}$$

The load is then 1302 kN.

Under pure axial load, all cross-sections of the matrix and mesh are calculated, and uniform strain is shown in Figure 7-10.

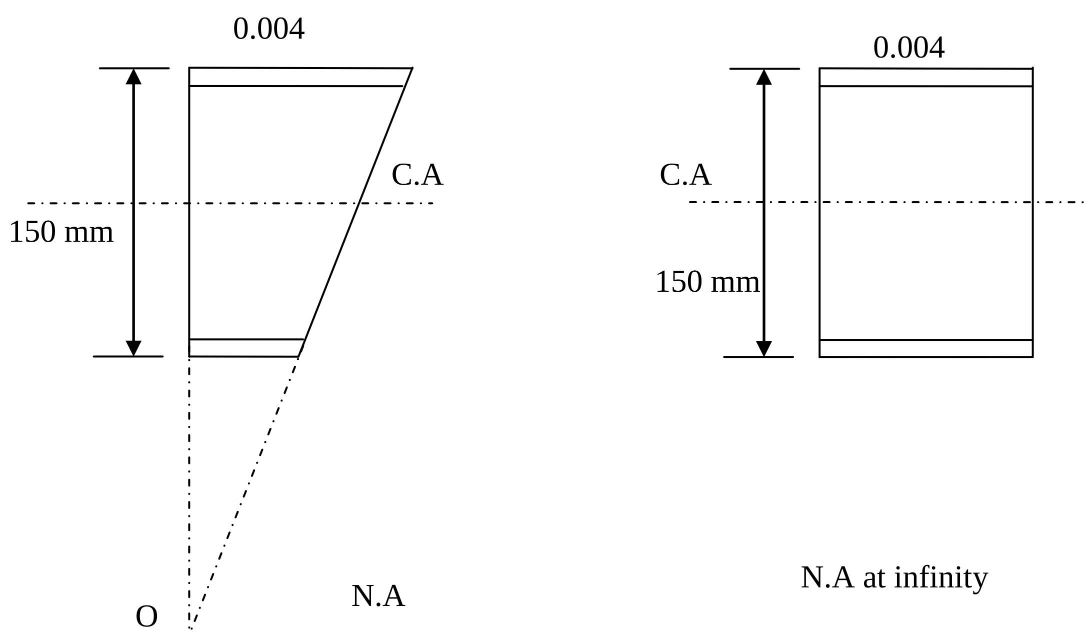

Figure 7-10: Strain diagram for N.A at an outside position and at infinity

7.4.6 The interaction diagram of FC4

The interaction diagram presents the relationship between axial load and bending moment. Table 7-10 and Figure 7-11 show the theoretical calculated result for a ferrocement column using four-layers of mesh under different loads. As the axial load increases, the bending moment increases until a balanced position is achieved and then this reverses.

In Table 7-10 and Figure 7-11, some additional data have been added to make the curve more accurate. An additional point has also been added when the N.A is outside the section. When the N.A is at 187.5 mm (1.25 times width), the axial load and moment are 1072 kN and 18.9 kNm.

Table 7-10: The results from the four-layer mesh column with different axial loads

Position	c (mm)	Axial Load (kN)	Moment (kNm)
Pure Moment	12.7	0	10.1
Quarter	37.5	155.5	18.6
Half	75.0	385	26.3
Balance	94.9	499.9	27.9
Three quarter	112.5	622.9	27.3
f_s=0	144.5	823.0	24.6
Outside	187.5	1072	18.9
Pure load	∞	1301.6	0

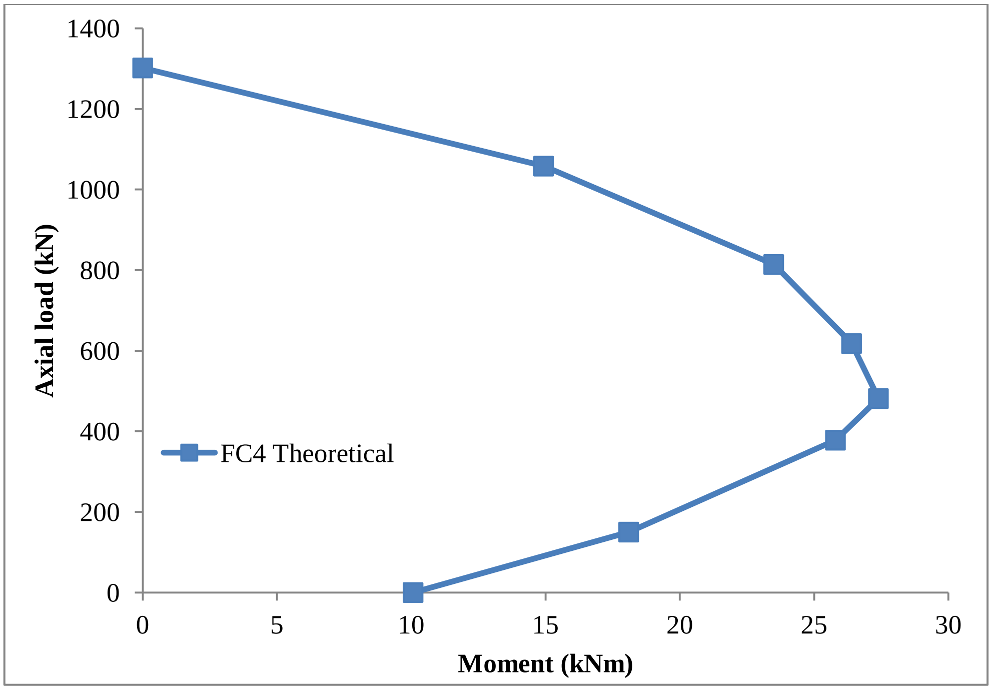

Figure 7-11: The interaction curve for FC4 by theoretical calculation

7.5 Theoretical results

The theoretical results for the interaction diagrams for FC2, FC4, RFC2 and RFC3 are shown in Figures 7-12 and 7-13. The procedure for producing the interaction diagrams has been demonstrated in the previous section. It clearly shows that in both figures, theoretical results present the same trend, when the amount of mesh increases, the axial load or the moment increase. Results are presented in Tables 7-11 and 7-12.

Pure moment condition:

From theory calculation, FC2 has a moment 5.3 kNm, and FC4 has a moment that is 90% higher than FC2, which reached 10.1 kNm. The N.A of FC2 is 8.2 mm and of FC4 is 12.7 mm. For RFC3 at pure moment the moment is 26.3 kNm, which is 15% higher than for RFC2.

Balanced position:

For FC2 and FC4: The balanced position of the N.A is when the welded mesh M-d_{s12} just reaches 0.0022 ($\varepsilon_{mesh.y}$). The moment for FC2 is 24.7 kNm, and for FC4 is 27.9 kNm (13% higher than FC2). Both compression and tension mesh forces for FC4 are greater than FC2, but the total forces for each specimen are almost same (490.6 kN for FC2 and 499.9 kN for FC4). The N.A for both FC2 and FC4 are same, 93.7 mm.

For RFC2 and RFC3: Two possible values of the N.A exist at the balanced position of RFC2 or RFC3, one is when the mesh starts to yield (M-d_{s15}) and one is when the steel bar starts to yield. The results are shown in Table 7-12.

After calculation, the N.A is when the tensile steel bar yields (value of “c” is 91.6 mm). Then the axial loads for RFC2 and RFC3 are almost the same, 400 kN, and the moment for RFC2 is 43.2 kN and that for RFC3 is 45.8 kN.

Pure axial load:

The pure axial for all of the columns with zero bending moment means the position of the N.A is infinity. The value of axial forces is 1243 kN (FC2), 1302 kN (FC4), 1528 kN (RFC2) and 1566 kN (RFC3)

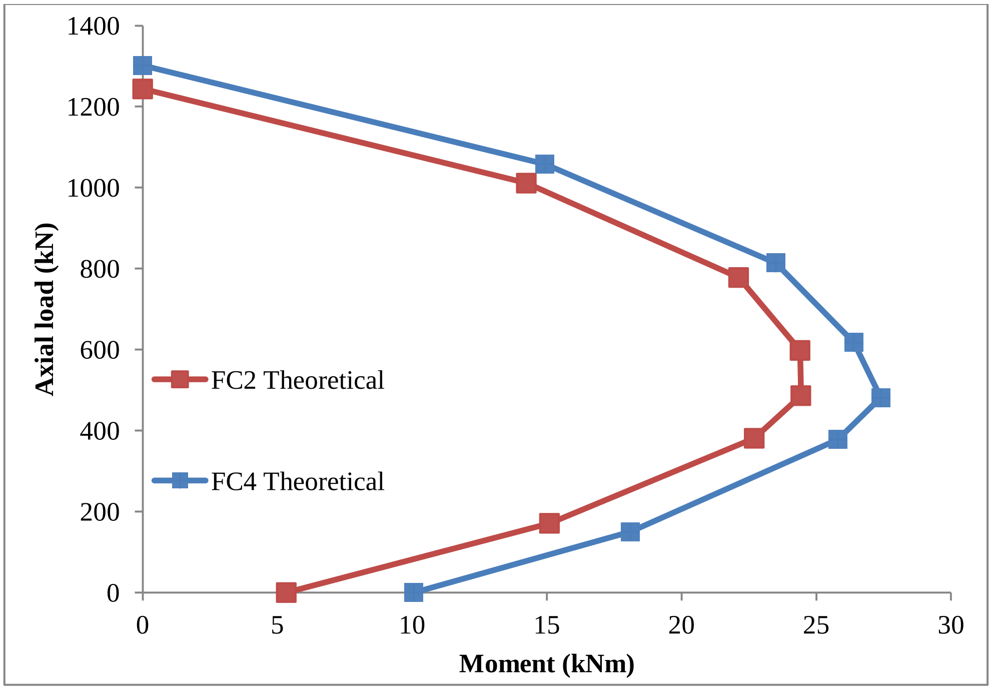

Figure 7-12: The interaction diagram for FC2 and FC4 by theoretical calculation

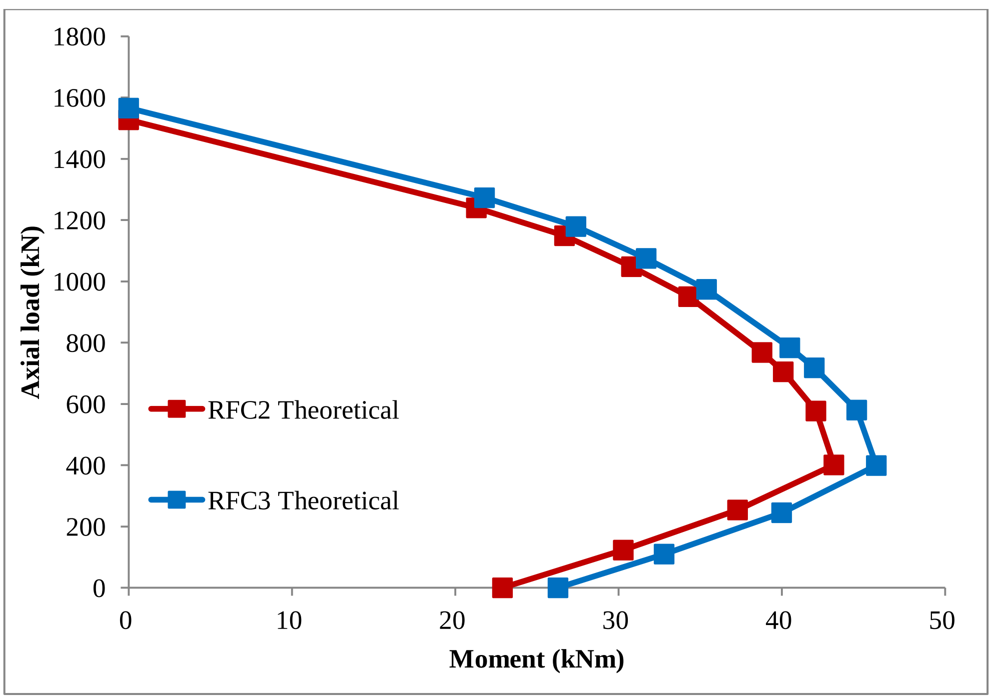

Figure 7-13: The interaction diagram for RFC2 and RFC3 by theoretical calculation

Table 7-11: Theoretical results for FC2 and FC4

N.A		FC2		FC4		Different (%)	
Describe	c (mm)	P (kN)	M (kNm)	P (kN)	M (kNm)	P	M
Pure moment	8.2/12.7	0.0	5.3	0.0	10.1		90%
Balanced	93.70	490.6	24.7	499.9	27.9	2%	13%
f_{mesh}=0	145.00	783.0	22.4	823.0	24.6	5%	10%
Pure axial load	∞	1243.0	0.0	1302.0	0.0	5%	

Note: at position of N.Aunder pure moment, the 8.2 mm for FC2 and 12.7 mm for FC4

Table 7-12: Theoretical results for RFC2 and RFC3

N.A		RFC2		RFC3		Different (%)	
Describe	c (mm)	P (kN)	M (kNm)	P (kN)	M (kNm)	P	M
Pure moment	31.1/32.4	0	22.9	0	26.3		15%
Steel bar balanced	91.6	401	43.2	399	45.8	0%	6%
Mesh balanced	116	577	42.1	580	44.6	1%	6%
$f_{steel\ bar}$=0	145	768	38.8	783	40.5	2%	4%
f_{mesh}=0	176.8	950	34.3	974	35.4	3%	3%
Pure axial load	∞	1528	0	1566	0	5%	

Note: at position of N.Aunder pure moment, the 31.1 mm for RFC2 and 32.4 mm for RFC3

7.6 Comparison of the theoretical interaction diagrams with ABAQUS

The simulated and theoretical interaction diagrams for FC4 and RFC2 are shown in Figures 7-14 and 7-15 respectively, and the results presented in Tables 7-13 and 7-14. It clearly shows that the ABAQUS simulation results are higher than theoretical results.

Pure moment condition:

The theoretical moment for FC4 is 10.1 kNm, which is 40% of the simulation result (25.3 kNm). The theoretical moment for RFC2 is 55% of simulation value. One possible reason is the dense transverse welded mesh acts as confinement, which is not considered in the theoretical calculations.

Balanced position:

The theoretical moment for FC4, at the balanced position, is 27.9 kNm with an axial load of 499.9 kN. The equivalent moment in the ABAQUS simulations 36.5 kNm and the axial load is approximately 700 kN.

For RFC2, the theoretical moment is 43.2 kNm at an axial load 401 kN, whereas from ABAQUS the moment is 64.2 kNm and the axial load is approximately 700 kN.

The theoretical moment for FC4 is 71% of the simulation value, and for RFC2 it is 57%.

Pure axial load:

The theoretical load for FC4 is 1301 kN, which is 81% of the ABAQUS result (1608 kN). The theoretical load for RFC2 is 1528 kN, whereas the simulation gives 1808 kN.

Hence the theoretical calculations are underestimates, because the transverse welded mesh (enclosed box mesh) absorbs extra energy, especially during pure bending.

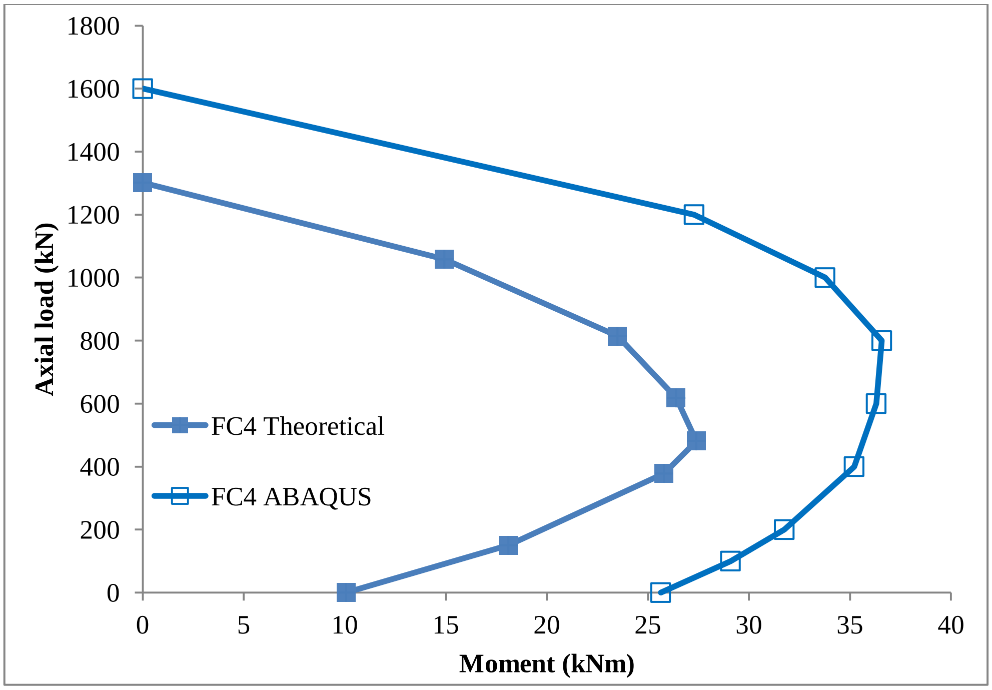

Figure 7-14: The interaction diagram for FC4 by theoretical calculation and ABAQUS simulation

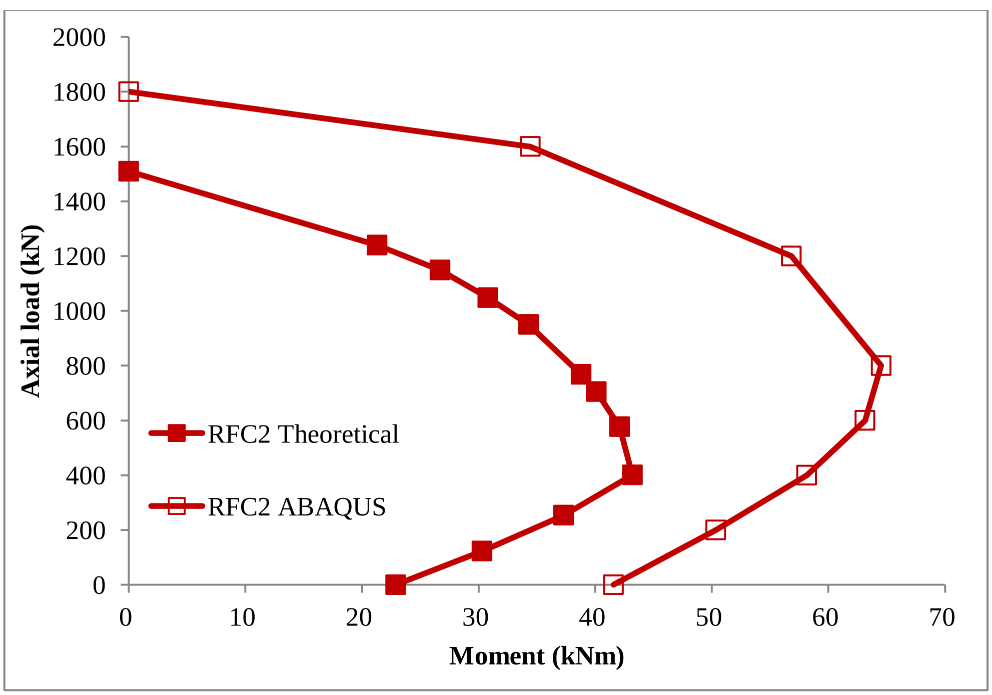

Figure 7-15: The interaction diagram for RFC2 by theoretical calculation and ABAQUS simulation

Table 7-13: Theoretical and simulation results for FC4

FC4	Theoretical		ABAQUS		Contain (%)	
	P (kN)	M (kNm)	P (kN)	M (kNm)	P	M
Pure moment	0	10.1	0	25.3		40%
Balanced	499.9	27.9	700	36.5	71%	76%
Pure axial load	1302	0	1608	0	81%	

Table 7-14: Theoretical and simulation results for RFC2

RFC2	Theoretical		ABAQUS		Contain (%)	
	P (kN)	M (kNm)	P (kN)	M (kNm)	P	M
Pure moment	0	22.9	0	41.4		55%
Balanced	401	43.2	700	64.2	57%	67%
Pure axial load	1528	0	1808	0	85%	

7.7 Non-dimensional interaction diagrams

The non-dimensional interaction diagram is a classical column design chart, which is used for any size of column and any mesh arrangement. Eurocode 2 (CEN, 2004a) and ACI 318 (ACI, 2008) recommend this method and it is becoming more and more popular for the design of beams and columns. However, for ferrocement and strengthened reinforced concrete columns, design charts are not available.

The author gives a simplified interaction diagram for a rectangular ferrocement column with a box-section of meshes. This is shown in Figure 7-16. These show 12 curves with values of $A_s f_y/bhf_m$ ranging from 0 to 0.55, which value of $A_s f_y/bhf_m$ is the ratio of reinforcing force capacity to matrix force capacity.

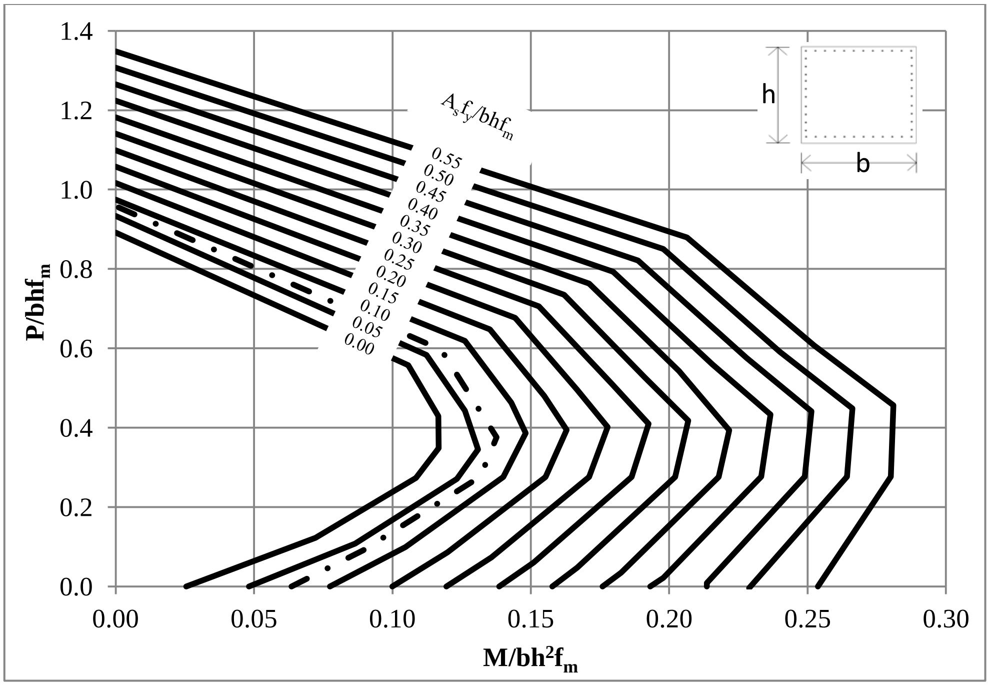

Figure 7-16: The interaction diagram for the ferrocement column (following Eurocode 2)

Note: The dotted line is the lowest requirement volume fraction 1.8% (ACI 549)

Where:

$\frac{P}{bhf_m}$	Non-dimensional axial load
$\frac{M}{bh^2f_m}$	Non-dimensional moment
$\frac{A_sf_y}{bhf_m}$	Ratio of reinforcing force capacity to matrix force capacity

The interaction diagram for reinforced concrete columns strengthened using ferrocement jackets (RFC) is shown in Figure 7-17.

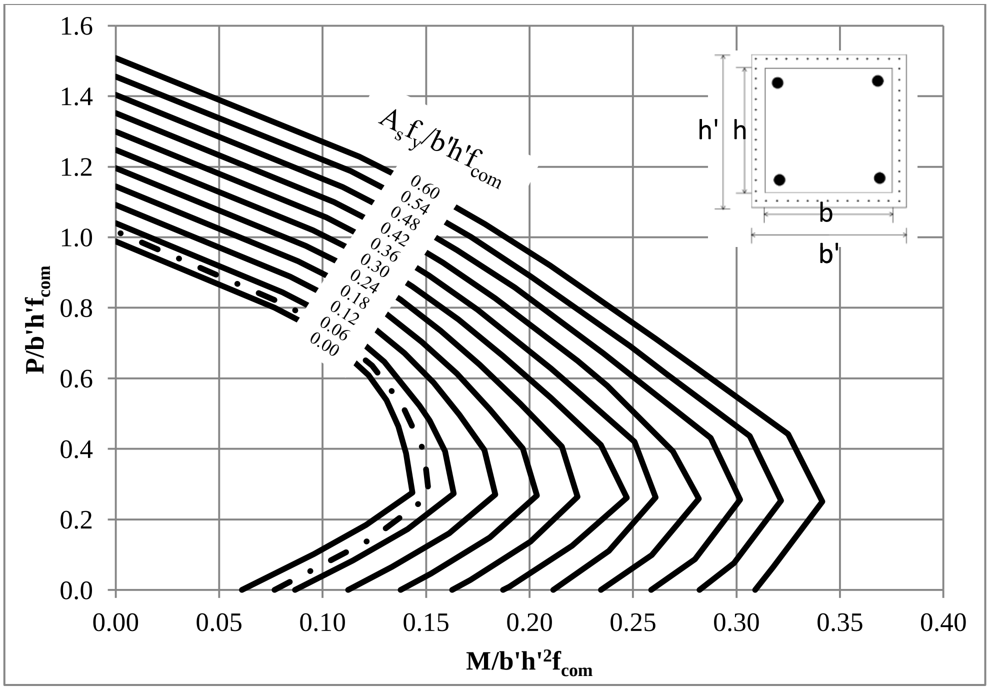

Figure 7-17: The interaction diagram for reinforced concrete columns strengthened using ferrocement jackets (following Eurocode 2)

Note: The dotted line is the lowest requirement volume fraction 1.8% (ACI 549)

Where:

f_{com}	Overall column strength from concrete and matrix properties, $f_{com} = \eta' f_c + (1 - \eta') f_m$
η'	Ratio of concrete to overall section

7.8 Example for using the interaction diagram

Consider a ferrocement column in a two-storey house. The size of the column is 200 × 200 mm. The mesh is 1.6 mm in diameter with 12.5 mm square opening welded mesh. The compressive strength of the matrix is tested as 45 MPa and the mesh yield strength is 380 MPa. The question is whether 6 layers of mesh can resist a 35 kNm bending moment?

Number of opening spaces for each side:

$$200/12.6 = 15.8$$

Then, each side has 16 stands (15+1), and thickness cover is:

$$(200 - 15 \times 12.6)/2 = 5.5 \text{ mm}$$

The value of A_s is the total cross-section area of the welded mesh and the number of layer required is 6, then

$$A_{st} = 6 \times 2 \times (15 + 14) \times \left(\frac{\pi \times 1.6^2}{4}\right) = 700 \text{ mm}^2$$

$$\frac{A_{st} f_y}{bhf_m} = \frac{700 \times 380}{200 \times 200 \times 45} = 0.148$$

The axial load is 200 kN

$$\frac{P}{bhf_m} = \frac{200000}{200 \times 200 \times 45} = 0.111$$

$$\frac{M}{bh^2 f_m} = 0.113$$

Then the value of M is

$$M = (0.113 \times 200 \times 200^2 \times 45) \text{ Nmm} = 40.7 \text{ kNm}$$

The maximum bending moment is 40.7 kNm that is greater than 35 kNm, so the design question is satisfied.

7.9 Ferrocement column guideline

In order to perform calculations for a ferrocement column with square welded mesh reinforcement, an interaction calculation flow chart is proposed. The details for these sections should be based on the Ferrocement Model Code (IFS, 2001) or ACI 318 (ACI, 2008). The following section includes four points (point a, b, c and d) that need to be considered (see Figure 7-6). Firstly, the value of β_1 should be determined.

Find the value of β_1:

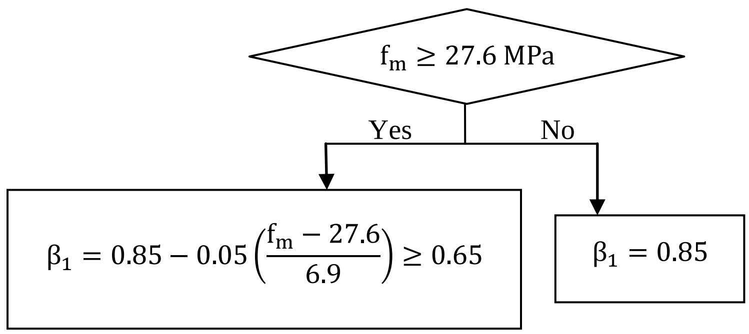

Point a: Moment strength at zero axial force

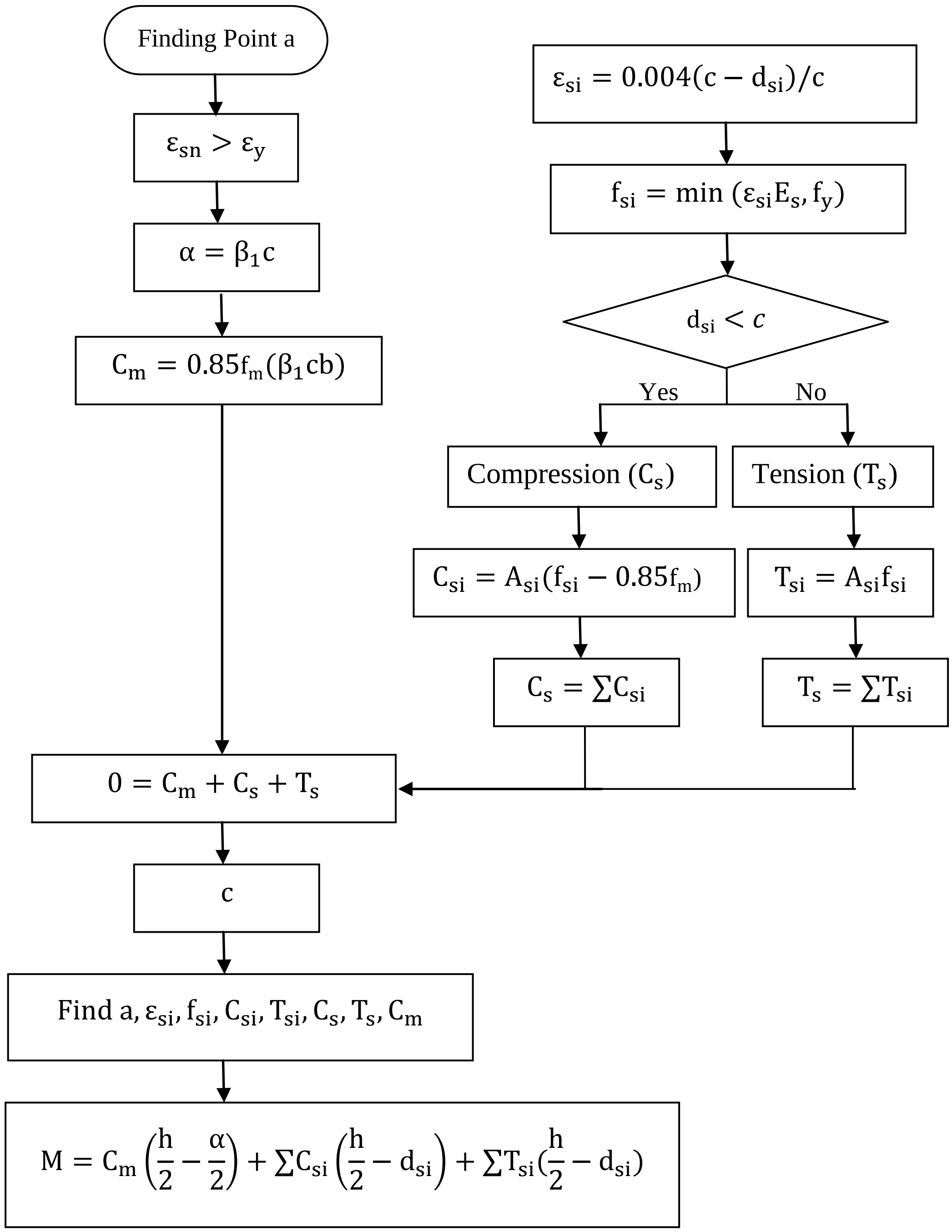

Point b: Axial compression and moment strength at balanced condition

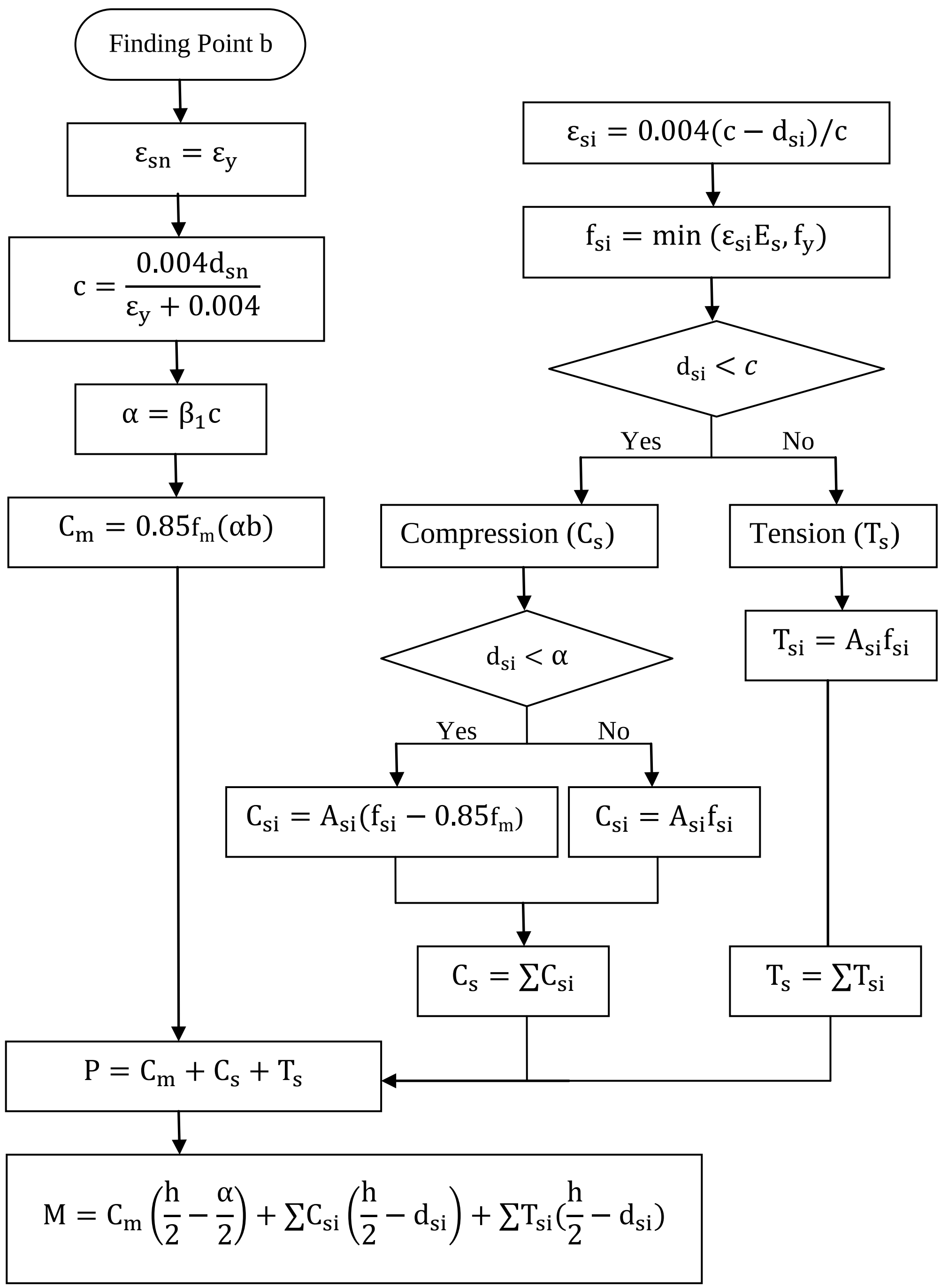

Point bc: Axial compression and moment at zero strain

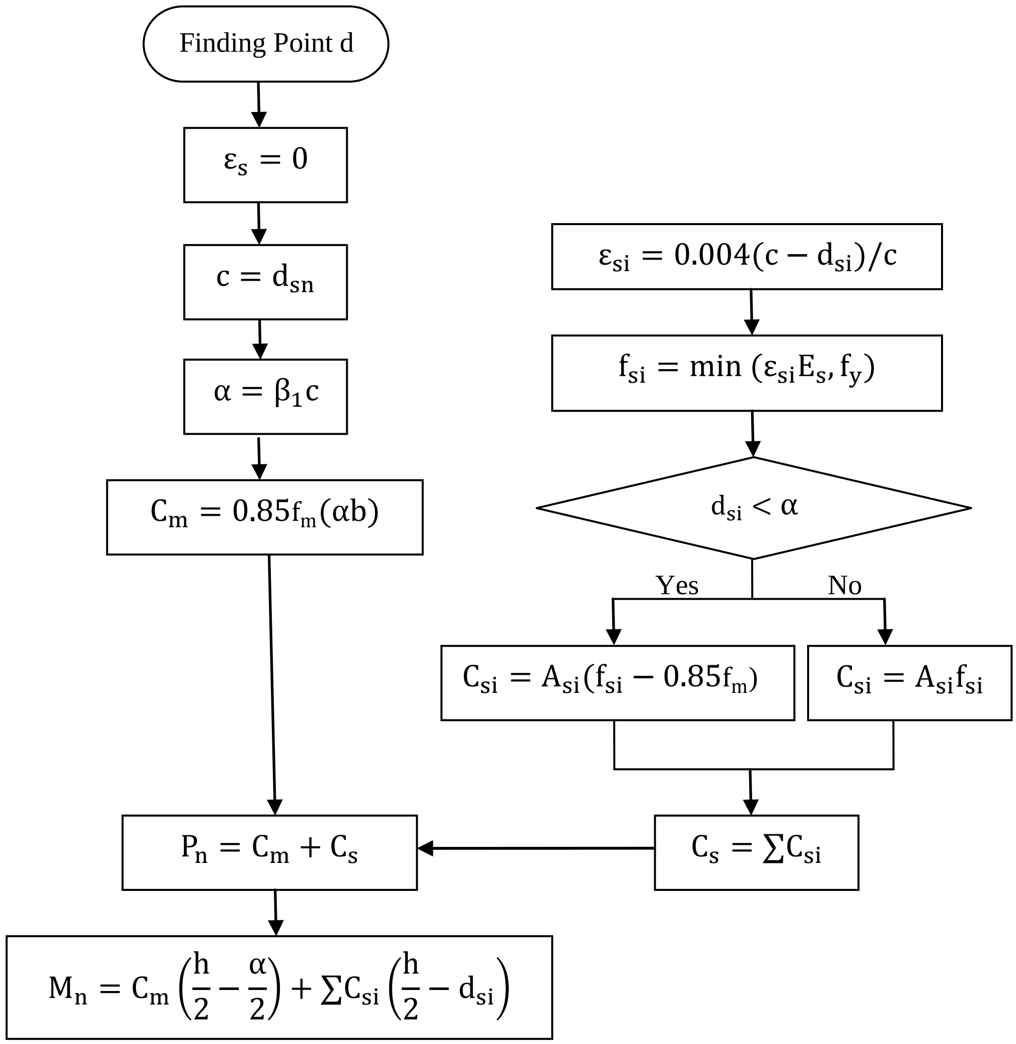

Point c: Axial compression at zero moment

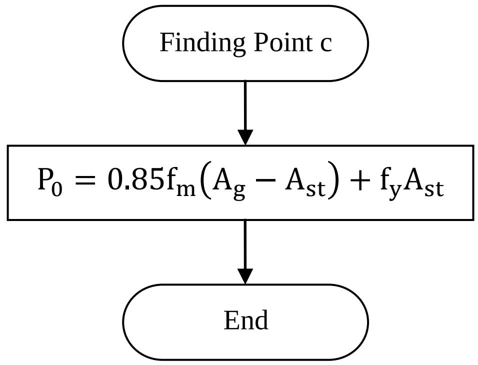

7.10 Summary

In this chapter, design guidelines for ferrocement columns and reinforced concrete columns strengthened using ferrocement jackets have been presented. The following points are emphasized:

- Idealization properties of the reinforcing mesh and matrix are used for design guideline.
- For the theoretical interaction diagram for column design, there are three important points: pure moment, balanced position and pure axial load
- An example (FC4) detailed calculation is shown in this chapter.
- Comparing the theoretical results with ABAQUS simulation results shows that the ABAQUS results are higher, because the mesh in the ferrocement provides confinement. This confinement is not considered in the theoretical calculations, which therefore underestimate the actual values.
- Non-dimensional interaction diagram for ferrocement columns and reinforced concrete columns using ferrocement jacket are presented.
- Calculation flow chart for the column under pure moment, balanced point and pure axial load are presented in this chapter.

CHAPTER 8 Conclusions and recommendations for future studies

This chapter presents a summary of the main conclusions from this study and recommends a number of further studies. Conclusions are drawn from the results and observations of the experimental work and the finite element analysis (FEA) presented in this thesis, considering the effect of different parameters of the ferrocement material.

The present investigation included a set of experimental tests using the following specimens: reinforced concrete column (RC), ferrocement column (FC) and reinforced concrete strengthened columns using ferrocement jacket (RFC).

Design guidelines are presented for FC and RFC columns, which are based on the results of full-scale tests and extensive numerical analyses using FEA. Interaction diagrams for ferrocement columns and reinforced concrete columns strengthened using ferrocement jackets are developed, based on the design of conventional reinforced concrete columns in Eurocode 2 (CEN, 2004a) and ACI 318 (ACI, 2008).

8.1 Summary

8.1.1 Experimental results

Material property tests have been conducted, including concrete, matrix, 12 mm diameter steel bar (longitudinal ribbed bar in RC), 3 mm diameter bar (transverse bar in RC) and welded mesh. The concrete and matrix property tests included compression and split tests using 100 × 200 mm cylinders.

Eight columns were cast: 2 reinforced concrete columns, 4 ferrocement columns and 2 strengthened reinforced concrete columns using ferrocement jackets. For safety and operability, all specimens were tested in a horizontal cantilever position; two Macalloy bars applied a constant axial load (200 kN) and an actuator applied lateral load.

The lateral load was either static or cyclic. For the static load tests, the actuator was moved at 0.5 mm/s. For the cyclic load tests, a load was applied at a frequency of 1 Hz with an amplitude (A) which was set at the displacement value corresponding to 60% of the ultimate load from the static test. Linpots were used to measure the downward movement of the specimens. They were arranged in two parallel lines initially to check for any twist that may have been occurring. A final arrangement of just one row along the length of the column was adopted, as no significant twist was observed. Also, a movement of the top fixed-end plate was observed during the initial test, hence two extra linpots were added in order to calculate an effective support stiffness. This support stiffness was incorporated in the FEA using two springs.

Static column tests:

Firstly, the result of the initial linpots arrangement showed that there was no twisting of the specimen. The support condition was semi-rigid with an effective rotational stiffness of 2075 kNm/rad (the detail calculation is shown in Appendix I). Two linear springs were used in the numerical model to simulate the support flexibility (see §4.3)

Specimen FC2 had the lowest lateral load capacity of 29 kN, whereas Specimen RFC3 had the highest value of 58 kN. The capacity of Specimen FC4 was 20% higher than FC2. RFC2 and RFC3 had significantly increased peak lateral loads than RC, which shows that the ferrocement jacket has a significant potential for strengthening reinforced concrete columns (35.7 kN for RC).

As the end support was not totally restrained, the resulting displacement was split into two parts reflecting: the support rotation effect and the bending-shear effect. For all columns, the support rotation effect dominated until the lateral load reached approximately 90% of the peak load. However, the values of initial stiffness were similar.

The deformation ductility was calculated using the energy balanced method. FC4 and RFC3 have higher values of ductility than FC2 and RFC2, respectively. Higher amounts of mesh results have greater deformation ductility.

Cyclic column tests:

The displacement amplitudes for RC, FC2-C and FC4-C were 14.5 mm, 12.5 mm and 14.0 mm. Results were recorded after 100, 200, 400 and 600 cycles, during cyclic loading. The columns exhibited reduced lateral load capacity with increasing number of cycles. After 600 cycles of loading, the peak load reduced significantly for RC-C and FC2-C, by 21% and 24% respectively. But for FC4-C it just reduced by 11% of the peak lateral load. Then a further 400 cycles were applied, and the capacity reduced to 67%. With higher amounts of mesh, the specimens showed lower load reduction in percentages.

The stiffnesses during cyclic test also reduced with increasing number of cycles. The stiffness for RC-C dropped much quicker than those for the ferrocement specimens. After 600 cycles, the stiffness of RC-C and FC2 showed a similar degradation to 71%, and 79%for FC4-C. Higher amounts of mesh provided higher resistance for both peak lateral load and initial stiffness.

8.1.2 Finite element modelling analysis and parametric studies

The results from the experimental work were used to validate the FEA models. A concrete damaged plasticity (CDP) model was used in this thesis. Concrete and matrix were modelled using C3D8R elements, and the reinforcements were modelled using truss element T3D2. The compressive behaviour of concrete and the matrix were characterized by Eurocode 2 (CEN, 2004a) and Popovics (1973) model, respectively. The tensile behaviour used the Wang and Hsu (2001) model. The reinforcing mesh was embedded in the concrete or matrix section, and for RFC2 and RFC3, the constraint between the concrete surface and the matrix surface was chosen to be a "Tie".

Five plasticity parameters for CDP were analysed and validated, including dilation angle, eccentricity, σ_{b0}/σ_{c0}, K_c and viscosity parameter, also the finite element mesh size and value of spring stiffness were analysed. After conducting a mesh sensitivity analysis, the size of the finite element mesh for concrete and matrix was selected as 30 mm and the reinforcing mesh was selected to be 12.6 mm. The support flexibility was introduced by two springs, the stiffnesses of which were calculated from the measured displacement values.

The calculated load-deflection curves for RC, FC and RFC showed a high degree of correlation with the measured curves (less than 10% differences). The contour plots of strain for each column indicated the position of cracks. For RFC2 and RFC3, the initial stiffness from FEA are higher than experimental tests, possibly because: i) the embedded interaction used in the FEA is too perfect to simulate the realistic cases as bond-slip may occur, ii) material properties cannot be perfectly input in ABAQUS, iii) spring setting in ABAQUS may not totally describe the experimental tests.

Extensive parametric studies were undertaken to investigate the effects of different variables, including column end-conditions, value of axial load, length of column, the material properties (concrete, matrix, main bar, stirrups and welded mesh) and reinforcement detail (amount, arrangement and position) . The support condition was considered as encastre as the rotationally flexible support in the current set up is an artefact of the short column size and the type of reaction frame that was chosen.
Four different grades of concrete or matrix were analysed, C30, C38, C40 and C50 for concrete; and M40, M50, M60 and M62 for matrix. The experimental values

were C38 and M62. Increases in the grade of concrete or matrix, increased the peak lateral load. Also, for the main bar and welded mesh, increasing the material grade also increased the peak lateral load. With increases of the cross-section of the main bar or welded mesh, the lateral load was raised. However, the grade and cross-section of stirrups had negligible affect on the value of the peak load.

Varying the axial load produced significant changes in the value of the peak lateral load. The values of lateral loads and axial loads make up the interaction diagram. The interaction diagrams for ferrocement (FC2 and FC4) are similar; with FC4 having 10% greater lateral load than FC2 at the balanced point. Higher amounts of mesh had greater moments.

8.1.3 Design guide

The idealised properties of the reinforcing mesh and matrix were used for design guidelines. Popovics (1973) model was used for properties of the matrix. For the theoretical interaction diagram for column design, there are three important points: pure moment, balanced position and pure axial load. The position of neutral axis (N.A) needs to be calculated first followed by the calculation of forces for each mesh strand and compressive forces in concrete or matrix. An example of detailed calculation for FC4 is shown in Chapter 7.

The ABAQUS simulations show higher capacity than the theoretical results, because the mesh in the ferrocement provides confinement. This confinement was not considered in the theoretical calculations, which therefore underestimate the actual values to the safe side for design purposes. Dimensionless interaction diagrams for FC and RFC column are presented.

8.2 Conclusion

The main conclusions from this thesis are: Ferrocement may be successfully used to add strength and ductility to columns either when used in place of normal longitudinal reinforcement or when used as a retrofit coating.

1. Higher amounts of mesh result in greater deformation ductility.
2. Higher amounts of mesh provide higher peak lateral loads and initial stiffness.
3. In all cases after cyclic loading the peak-load and stiffness reduced.
4. ABAQUS simulation can successfully predict deflection results.
5. The theoretical values based on ACI are conservative.
6. Non-dimensional interaction diagram for ferrocement columns and reinforced concrete columns using ferrocement jacket are presented.
7. Calculation flow chart for the column under pure moment, balanced point and pure axial load are presented.

8.3 Recommendations for future study

This study highlighted the behaviour of square columns under axial load and moment. Due to financial and time constraints, only five static tests were performed, and more experimental tests are needed changing the shape and dimensions, such as circular or longer columns. Different kinds of mesh (such as woven mesh) of ferrocement also need to be considered. The cyclic load application for RFC column may need to be considered.

The numerical simulation was carried out using ABAQUS, which was available to the author, but alternative numerical simulation software, such as DIANA, may be more suitable because it can show cracking by physical separation of the elements. The cyclic loading tests of ferrocement column also need to be studied by FEA.

The design guideline is limited to a box-section of welded mesh column, and needs to be expanded for ferrocement beams or other sections. Strengthened beams or floors, using ferrocement jackets or ferrocement layers, may need to be tested and modelled and developed into design guidelines.

References

ABAQUS 2009. Version 6.8, ABAQUS Documentation. USA: ABAQUS Inc.

American Concrete Institute (ACI), 2008. *Building Code Requirements for Structural Concrete (ACI 318-08) and Commentary (ACI 318R-05)*. Detroit, American Concrete Institute.

American Concrete Institute (ACI), 1997a. *Guide for Repair of Concrete Bridge Superstructures*. ACI 546.1R-80, Detroit, American Concrete Institute.

American Concrete Institute (ACI), 1988. *Guide for the Design, Construction, and Repair of Ferrocement*. ACI 549, Detroit, American Concrete Institute.

American Concrete Institute (ACI), 1997b. *State-of-The-art Report on Ferrocement*. ACI 549R-97, Detroit, American Concrete Institute.

AHMED, T., ALI, S. & CHOUDHURY, J. Experimental study of ferrocement as a retrofit material for masonry columns, Ferrocement International Symposum, 1994. 269-276.

AL-KUBAISY, M. & NEDWELL, P., 1999. *Behavior and strength of ferrocement rectangular beams in shear*. *Journal of Ferrocement,* 29 (1), 1-16.

ARIF, M. & KAUSHIK, S. K., 1999. *Mechanical behaviour of ferrocement composites: an experimental investigation*. *Cement and Concrete Composites,* 21 (4), 301-312.

BALAGURU, P. N., SHAH, S. P. & NAAMAN, A. E., 1979. *Fatigue behavior and design of ferrocement beams*. *Journal of the Structural Division,* 105 (7), 1333-1346.

BARRERA, A., BONET, J., ROMERO, M. & MIGUEL, P., 2011. *Experimental tests of slender reinforced concrete columns under combined axial load and lateral force*. *Engineering Structures,* 33 (12), 3676-3689.

BARRERA, A. C., BONET, J. L., ROMERO, M. L. & FERN NDEZ, M. A., 2012. *Ductility of slender reinforced concrete columns under monotonic flexure and constant axial load*. *Engineering Structures,* 40 (0), 398-412.

British Stand Institution (BSI), 2006. *Method of specifying and guidance for the specifier*. BS 8500, Londom, British Stand Institution.

British Stand Institution (BSI), 2009. *Testing fresh concrete. Sampling*. BS EN 12350, Lodnon, British Stand Institution.

British Stand Institution (BSI), 2010. *Testing hardened concrete. Shape, dimensions and other requirements for specimens and moulds*. BS EN 12390, London, British Stand Institution.

BSS, http://www.bsspatterdalehall.com/tenacity-of-bolton/gallery/year-8-2009 [Online]. Bolton School Services (BSS).

CAMBODIA, http://www.ewb.org.au/opportunities/50/10205 [Online].

CAPRANI, C., 2006. *Civil Engineering Design (1) Design of Reinforced Concrete Columns*.

CEN, 2004a. *Eurocode 2: Design of Concrete Structures: Part 1-1: General Rules and Rules for Buildings*.

CEN, 2004b. *Eurocode 8: Design of structures for earthquake resistance—Part 1: General rules, seismic actions and rules for buildings*.

DESAYI, P. & JOSHI, A. D., 1976. *Ferrocement load-bearing wall elements*. *Journal of the Structural Division,* 102 (9), 1903-1916.

DETWILER, R. J. & MEHTA, P. K., 1989. *Chemical and physical effects of silica fume on the mechanical behavior of concrete*. *ACI Materials Journal,* 86 (6).

DODSON, V. H. 1990. *Concrete admixtures*, Van Nostrand Reinhold New York.

DRUCKER, D. C. & PRAGER, W., 2013. *Soil mechanics and plastic analysis or limit design*. *Quarterly of applied mathematics,* 10.

EXPANDED-MESH, http://www.makewiremesh.com/Expanded%20Metal%20Mesh.htm [Online].

FAHMY, E. H., ABOU ZEID, M. N., SHAHEEN, Y. B. & GAAFAR, H., 2005. *Behavior of ferrocement panels under axial and flexural loadings*. *The 33rd annual general conference of the canadian society for civil engineering*.

FERROCEMENT.COM, http://ferrocement.com/bioFiber/roofLabContents-y5.en.html [Online].

FERROCEMENT SOCIETY (FS), 2013. *2ND NATIONAL CONVENTION*. Pune, India.

GIONCU, V. & MAZZOLANI, F. 2003. *Ductility of seismic-resistant steel structures*, Taylor & Francis.

HEXAGONAL-MESH, http://fencingwire.net/chichen-mesh [Online].

HOOTON, R., 1993. *Influence of silica fume replacement of cement on physical properties and resistance to sulfate attack, freezing and thawing, and alkali-silica reactivity*. *ACI Materials Journal,* 90 (2).

HUQ, S. & PAMA, R. P., 1978. *Ferrocement in tension: analysis and design*. *Journal of Ferrocement,* 8 (3), 143-168.

International Ferrocement Society (IFS), 2001. *Ferrocement Model Code*. Naaman, AE. Balaguru, P. Nassif, H. Pama, R. Tatsa, E. Austriaco, LR. Hanai, JB. Nedwell, P. Paramasivam, P.

JADFERROCEMENTS.NET, http://www.jadferrocements.net/repairs-rehabilitation-retrofitting.html [Online].

JOHNSTON, C. D. & MATTAR, S. G., 1976. *Ferrocement—Behavior in Tension and Compression*. *Journal of the Structural Division,* 102 (5), 875-889.

KAISH, A. B. M. A., ALAM, M. R., JAMIL, M. & WAHED, M. A., 2013. *Ferrocement Jacketing for Restrengthening of Square Reinforced Concrete Column under Concentric Compressive Load*. *Procedia Engineering,* 54 (0), 720-728.

KHANZADI, M. & RAMESHT, M., 1996. *The effect of cover and arrangement of reinforcement on the behavior of ferrocement in tension*. *Journal of Ferrocement,* 26 (2), 85-94.

KIM, J.-K. & LEE, S.-S., 2000. *The behavior of reinforced concrete columns subjected to axial force and biaxial bending*. *Engineering Structures,* 22 (11), 1518-1528.

MANSUR, M. & ONG, K., 1987. *Shear strength of ferrocement beams*. *ACI Structural Journal,* 84 (1).

MANSUR, M. & PARAMASIVAM, P., 1985. *Ferrocement under combined bending and axial loads*. *International Journal of Cement Composites and Lightweight Concrete,* 7 (3), 151-158.

MORAGE, S. Element De Ferrocemento Para Vivienda social.In: RIVAS, H. W., ed., 10th International Symposium on Ferrocement and Thin Reinforced Cement Composites (FERRO 10), 2012 La Havana, Cuba.

MOURAD, S. & SHANNAG, M., 2012. *Repair and strengthening of reinforced concrete square columns using ferrocement jackets*. *Cement and Concrete Composites,* 34 (2), 288-294.

NAAMAN, A. E. 2000. *Ferrocement and laminated cementitious composites,* Techno press.

NAAMAN, A. E. & SHAH, S. P. Tensile tests of ferrocement, ACI Journal Proceedings, 1971. American Concrete Institute.

NASSIF, H. H. & NAJM, H., 2004. *Experimental and analytical investigation of ferrocement–concrete composite beams*. *Cement and Concrete Composites,* 26 (7), 787-796.

NATHAN, G. & PARAMASIVAM, P., 1974. *Mechanical properties of ferrocement materials*. *Proc. 1st Australian Conj. on Engineering Materials*, 309-31.

NEDWELL, P., 2009. *Ferrocement Lecture Lecture PowerPoint*. *University of Manchester*, 64.

NEDWELL, P., RAMESHT, M. & RAFEI-TAGHANAKI, S. Investigation into the repair of short square columns using ferrocement, FERROCEMENT INTERNATIONAL SYMPOSIUM, 1994. 277-285.

NERVI, P. L., SALVADORI, M. & SALVADORI, G. 1956. *Structures*, FW Dodge Corporation New York.

PAILL RE, A.-M. 1995. *Application of Admixtures in Concrete: State-of-the Art Report*, Taylor & Francis.

PARK, R., PRIESTLEY, M. & GILL, W. D., 1982. *Ductility of square-confined concrete columns*. *Journal of the Structural Division*, 108 (4), 929-950.

PAUL, B. K. & PAMA, R. P. 1978. *Ferrocement*, International Ferrocement Information Center, Asian Institute of Technology Bangkok, Thailand.

POPOVICS, S., 1973. *A numerical approach to the complete stress-strain curve of concrete*. *Cement and concrete research,* 3 (5), 583-599.

RIVAS, H. W. & HERNANDEZ, Y.-L. L. Sistema De Edificios Residenciales Sismoresistentes De Ferrocemento: Una Opcion Paea La Construccion De Viviendas De Interes Social In: RIVAS, H. W., ed., 10th International Symposium on Ferrocement and Thin Reinforced Cement Composites, 2013 La Havana, Cuba.

SHANNAG, M. & MOURAD, S., 2012. *Flowable high strength cementitious matrices for ferrocement applications*. *Construction and Building Materials,* 36, 933-939.

TAKIGUCHI, K., 2003. *An investigation into the behavior and strength of reinforced concrete columns strengthened with ferrocement jackets*. *Cement and Concrete Composites,* 25 (2), 233-242.

TIAN, S., 2013. *Shear Behaviour of Ferrocement Deep Beams.* University of Manchester.

WALKUS, B. & KOWALSKI, T., 1971. *Ferrocement: A survey*. *Concrete Cement-Concrete Association of London*, 48-52.

WANG, T. & HSU, T. T., 2001. *Nonlinear finite element analysis of concrete structures using new constitutive models*. *Computers & structures,* 79 (32), 2781-2791.

WELDED-MESH, http://www.haoyuwire.com/Stainless-steel-welded-mesh.htm [Online].

WOVEN-MESH, http://www.galvanized-wiremesh.com/square-wire-mesh.htm [Online].

YAQUB, M., BAILEY, C., NEDWELL, P., KHAN, Q. & JAVED, I., 2013. *Strength and stiffness of post-heated columns repaired with ferrocement and fibre reinforced polymer jackets*. *Composites Part B: Engineering,* 44 (1), 200-211.

Appendix A. Reinforcement properties

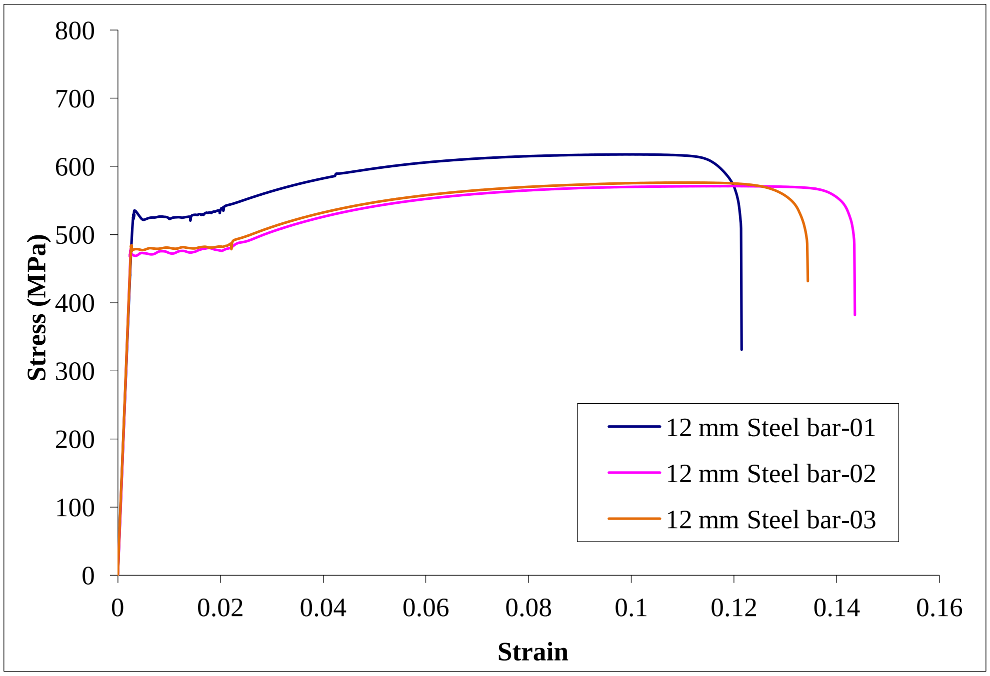

Figure A-1: Stress-strain curves for 12 mm diameter Steel bar

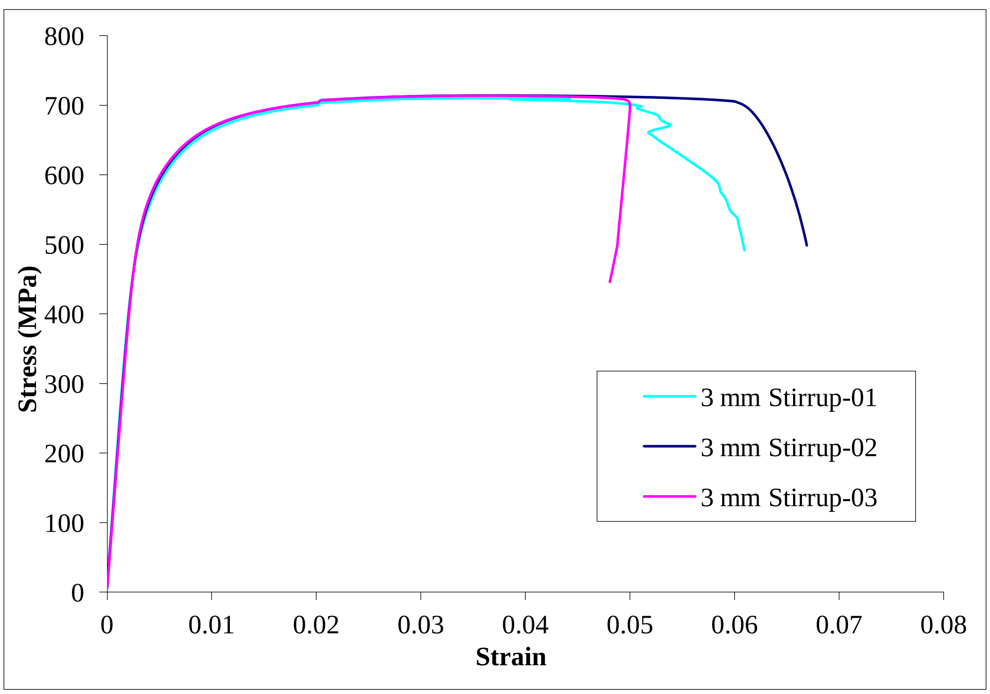

Figure A-2: Stress-strain curves for 3 mm diameter stirrup

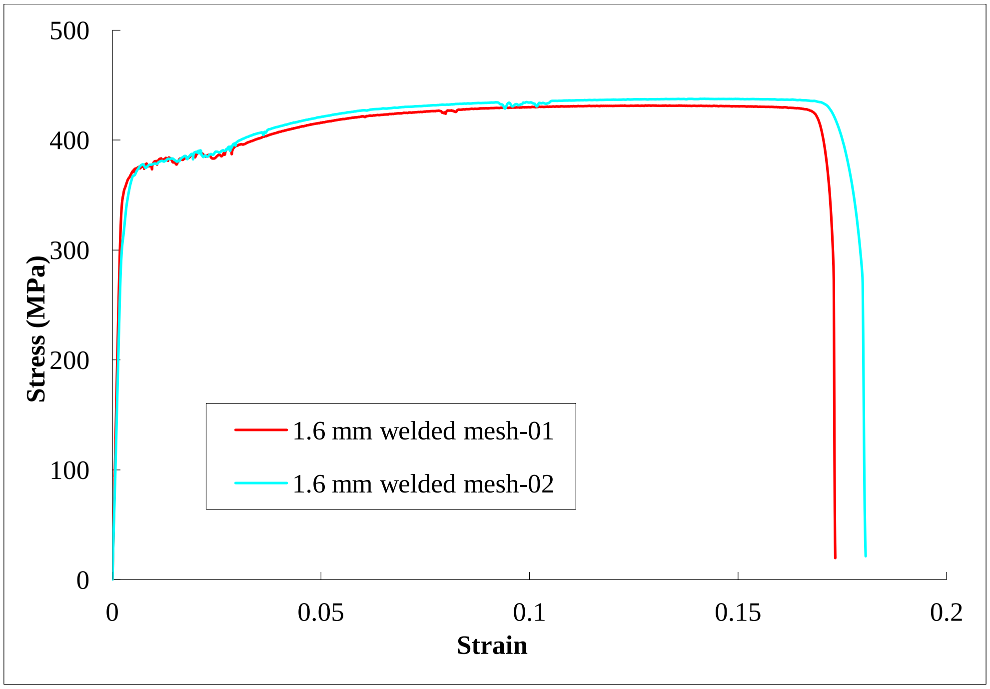

Figure A-3: Stress-strain curves for 1.6 mm diameter welded mesh

Appendix B. The dimensions of the specimens

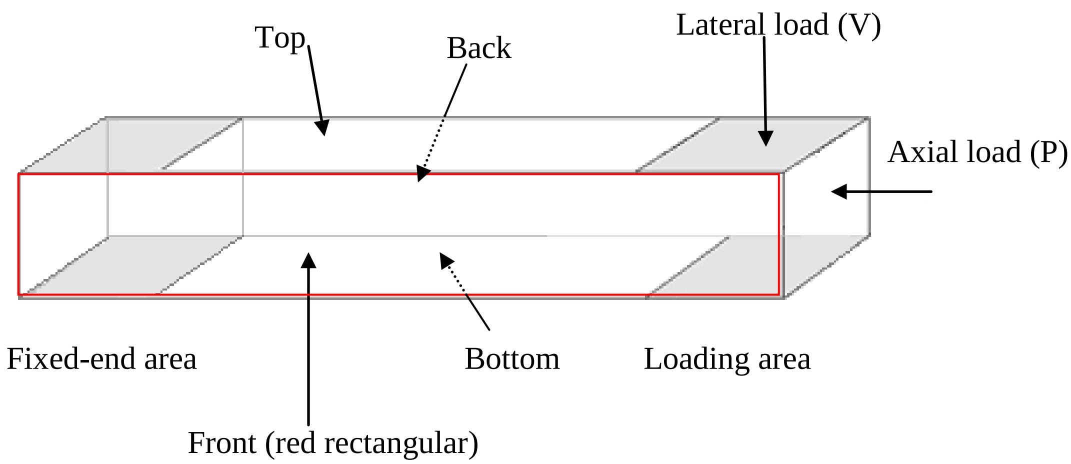

Figure B-4: View of the specimen, showing the top, bottom, front and back

RC view	**Width (mm)**				**Length (mm)**	**Weight (kg)**
	Left	**Middle**	**Right**	**Average**		
Top	150	151	152	151.0	1020	62.3
Bottom	150	151	151	150.7	1021	
Front	150	150	151	150.3	1020	
Back	150	150	151	150.3	1020	

RC-C view	**Width (mm)**				**Length (mm)**	**Weight (kg)**
	Left	**Middle**	**Right**	**Average**		
Top	151	151	152	151.3	1020	61.9
Bottom	151	151	152	151.3	1021	
Front	151	151	152	151.3	1021	
Back	151	151	151	151.0	1020	

FC2 view	**Width (mm)**				**Length (mm)**	**Weight (kg)**
	Left	**Middle**	**Right**	**Average**		
Top	150	151	151	150.7	1020	57.3
Bottom	150	151	151	150.7	1021	
Front	151	151	151	151.0	1021	
Back	150	150	151	150.3	1020	

FC2-C view	Width (mm)				Length (mm)	Weight (kg)
	Left	Middle	Right	Average		
Top	151	151	151	151.0	1020	58.4
Bottom	151	151	151	151.0	1021	
Front	151	151	151	151.0	1021	
Back	150	151	151	150.7	1021	

FC4 view	Width (mm)				Length (mm)	Weight (kg)
	Left	Middle	Right	Average		
Top	151	151	151	151.0	1020	60.6
Bottom	151	151	151	151.0	1020	
Front	151	151	151	151.0	1021	
Back	151	151	151	151.0	1021	

FC4-C view	Width (mm)				Length (mm)	Weight (kg)
	Left	Middle	Right	Average		
Top	151	152	152	151.3	1021	61.6
Bottom	151	151	152	151.3	1021	
Front	151	151	152	151.3	1021	
Back	151	151	152	151	1021	

RFC2 view	Width (mm)						Length (mm)	Weight (kg)
	Left	Left middle	Middle	Right Middle	Right	Average		
Top	181	180	182	181	181	181	1019	96.3
Bottom	178	179	180	180	179	179.2	1020	
Front	179	179	180	181	180	179.8	102	
Back	180	182	181	180	181	180.8	1019	

RFC3 view	Width (mm)						Length (mm)	Weight (kg)
	Left	Left middle	Middle	Right Middle	Right	Average		
Top	181	180	182	181	181	181	1019	97.6
Bottom	178	179	180	180	179	179.2	1020	
Front	179	179	180	181	180	179.8	102	
Back	180	182	181	180	181	180.8	1019	

Appendix C. The specimens after the tests

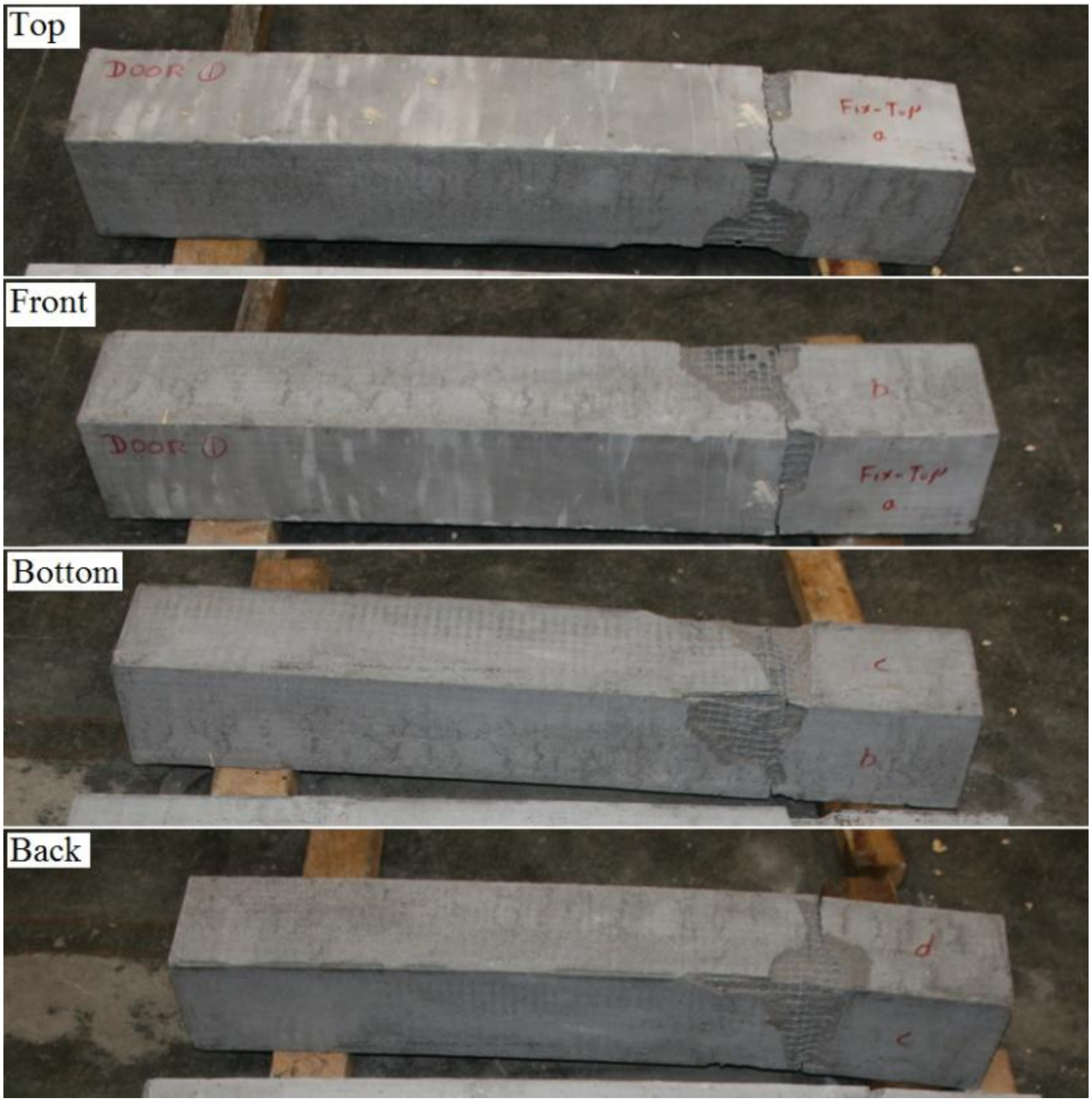

Figure C-5: The two-layer mesh ferrocement failure after testing (FC2)

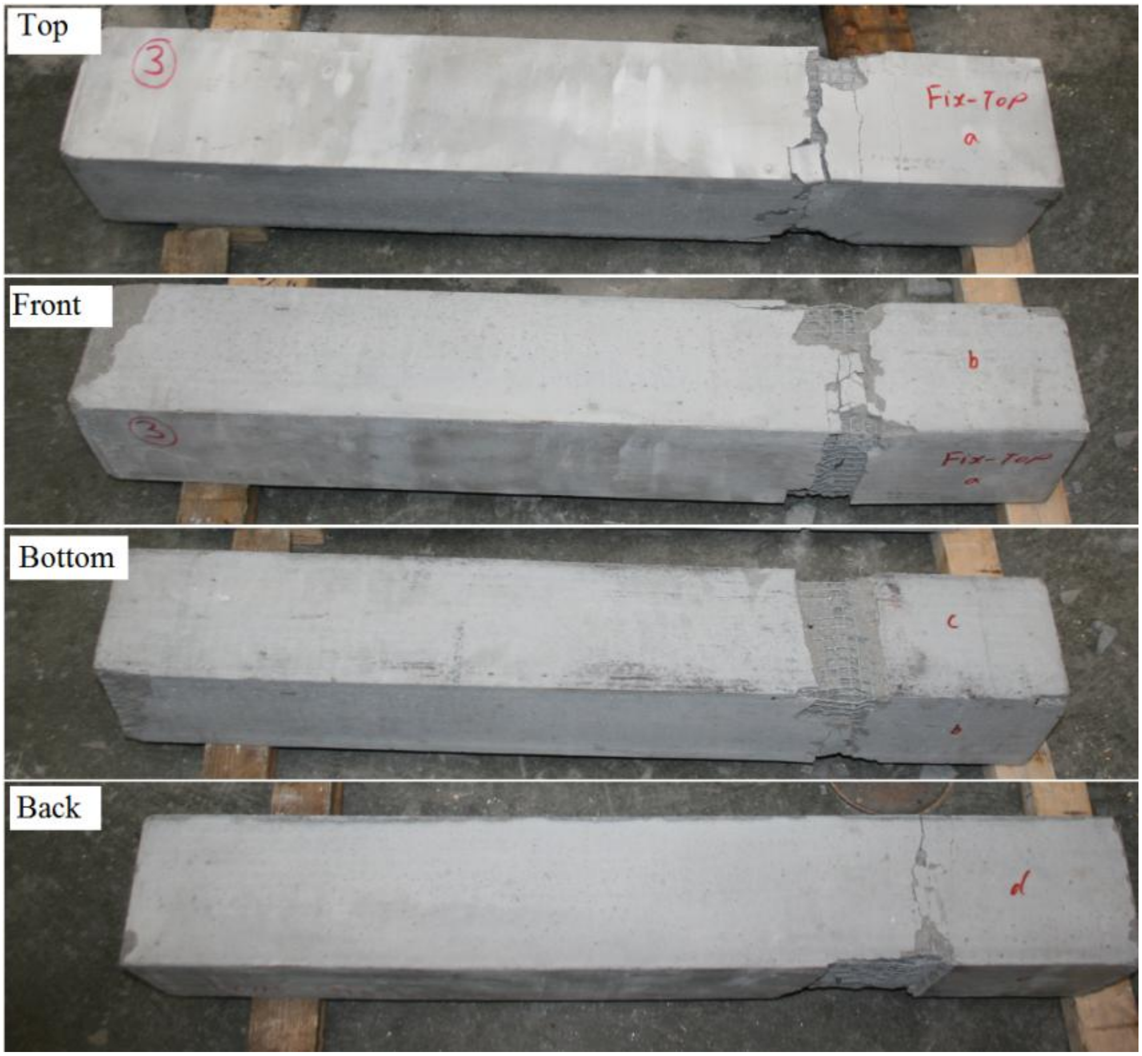

Figure C-6: The four-layer mesh ferrocement failure after testing (FC4)

Figure C-7: The strengthening concrete with two-layer mesh ferrocement failure after testing (RFC2)

Figure C-8: The strengthening concrete with three-layer mesh ferrocement failure after testing (RFC3)

Appendix D. Support rotation and bending-shear effect

Support rotation effect simplified diagram:

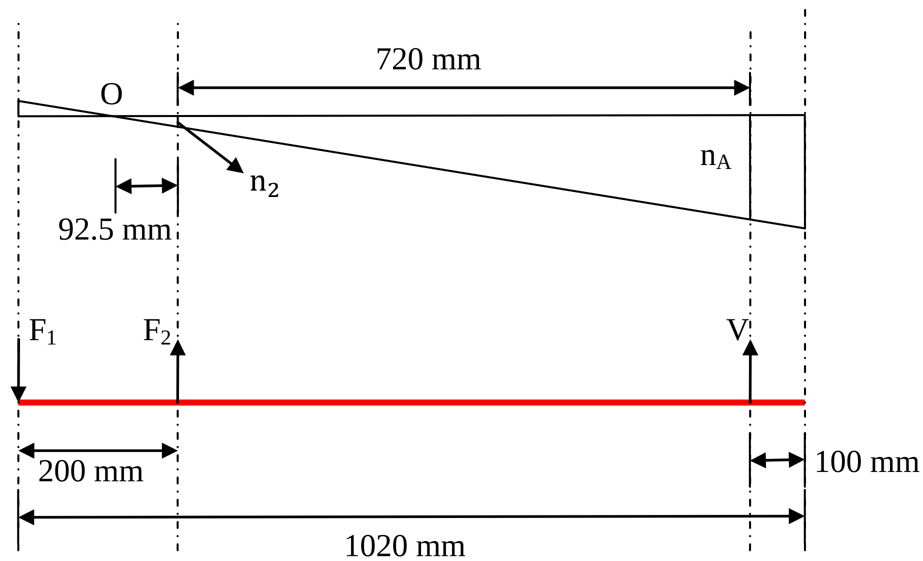

Figure D-9: Simplified support rotation effect diagram

Reinforced concrete (RC):

At 0.33peak load of RC is $0.33 \times 35.7 = 11.9$ kN

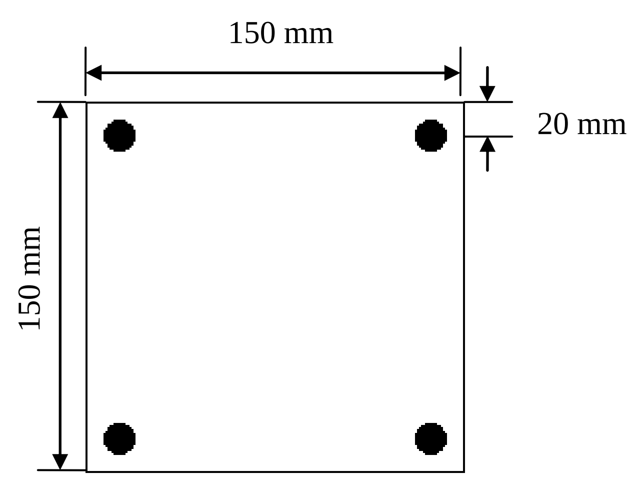

Figure D-10: The cross section of RC

$$n_2 = 9.7/30.5$$

$$\frac{n_2}{n_A} = \frac{92.5}{92.5 + 720}$$

Then:

$$n_A = \mathbf{3.47\ mm}$$

Bending-shear effect: The bending deflection of the specimen acting as a concentrated load working on a cantilever beam, can be calculated as:

$$\Delta_A = \frac{VL^3}{3EI}\left[1 + 0.6(1 + \upsilon)\frac{h^2}{L^2}\right]$$

Where:

L	Length of the cantilever, 812.5 mm
h	Width of column, 150 mm
V	Lateral load, 0.33 of peak load, 12 kN
E	Young's Modulus of composite
I	Second moment area

Young's Modulus of concrete $E_c = 27000\ \mathrm{N/mm^2}$

Young's Modulus of steel bar $E_s = 195000\ \mathrm{N/mm^2}$

Elastic moduli ratio to matrix: $m_s = E_s/E_c = 7.22$

$$A_{sc} = A_{st} = 2 \times \pi \times \frac{12^2}{4} = 226.2\ \mathrm{mm^2}$$

$$I_c = \frac{bh^3}{12} + m_s A_{sc}(0.5h - d_1)^2 + m_s A_{st}(d_2 - 0.5h)^2$$

$$= \frac{150 \times 150^3}{12} + 7.22 \times 226.2 \times (75 - 20)^2 \times 2 = 52068142\ \mathrm{mm^4}$$

Then:

$$\Delta_A = \frac{12000 \times 812.5^3}{3 \times 27000 \times 52068142}\left[1 + 0.6(1 + 0.22)\frac{150^2}{812.5^2}\right] = \mathbf{1.57\ mm}$$

Ferrocement with two-layers mesh (FC2) and four-layers mesh (FC4)

At 0.33peak load of FC2 is 0.33×29.0=9.7 kN

At 0.33peak load of FC4 is 0.33×35=11.6 kN

Assumed the mesh layer is distributed uniformly. The skeleton of welded mesh is simplified as one-layer. The distances of the mesh from the extreme tensile surface are called d_{si} (d_{s1}, d_{s2}, d_{s3},......, d_{s11}, d_{s12}), in which d_{s1} has 3.5 mm (cover), d_{s2} has 3.5+12.6×1=16.1 mm, d_{s3} has 3.5+12.6×2=28.7 mm, etc., the last one is d_{s12}.

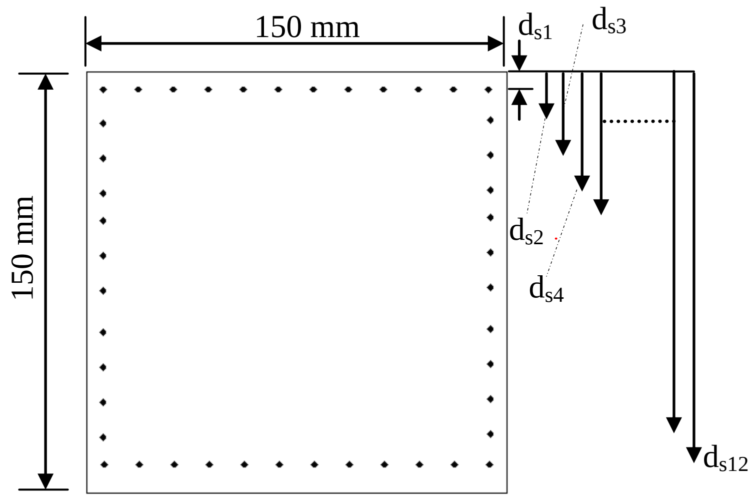

Figure D-11: The cross section for FC

FC2		FC4	
	$n_2 = 9.7/30.5$		$n_2 = 11.6/30.5$
	$\frac{n_2}{n_A} = \frac{92.5}{92.5 + 720}$		$\frac{n_2}{n_A} = \frac{92.5}{92.5 + 720}$
Then:		Then:	
	n_A =**2.82 mm**		n_A =**3.38 mm**

Young's Modulus of matrix		$E_m = 21000\ \mathrm{N/mm^2}$
Young's Modulus of mesh		$E_{mesh} = 175000\ \mathrm{N/mm^2}$
Elastic moduli ratio to matrix	Mesh: m_m=	$\frac{E_{mesh}}{E_m} = 8.33$

Cross-section area (mm^2)		FC2	FC2
Mesh level	A_{s1} and A_{s12}	48.3	96.5
	A_{s2}, A_{s3}, A_{s4},......A_{s11}, A_{s11}	8.04	16.1

$$I_{FC2} = \frac{bh^3}{12} + \sum m_m A_{si}(0.5h - d_{si})^2$$

$$= \frac{150 \times 150^3}{12} + 8.33$$
$$\times [48.3 \times (75 - 3.5)^2 \times 2 + 8.04 \times (75 - 3.5 - 12.6 \times 1)^2 + 8.04$$
$$\times (75 - 3.5 - 12.6 \times 2)^2 + \cdots\cdots + 8.04$$
$$\times (75 - 3.5 - 12.6 \times 11)^2] = 46955108\ \mathrm{mm^4}$$

$$I_{FC4} = \frac{bh^3}{12} + \sum m_m A_{si}(0.5h - d_{si})^2$$

$$= \frac{150 \times 150^3}{12} + 8.33$$
$$\times [96.5 \times (75 - 3.5)^2 \times 2 + 16.1 \times (75 - 3.5 - 12.6 \times 1)^2 + 16.1$$
$$\times (75 - 3.5 - 12.6 \times 2)^2 + \cdots\cdots + 16.1$$
$$\times (75 - 3.5 - 12.6 \times 11)^2] = 517227158\ \mathrm{mm^4}$$

Then:

$$\Delta_{A\ \text{for FC2}} = \frac{9700 \times 812.5^3}{3 \times 21000 \times 46955108}\left[1 + 0.6(1 + 0.22)\frac{150^2}{812.5^2}\right] = \mathbf{1.79\ mm}$$

$$\Delta_{A\ \text{for FC4}} = \frac{11600 \times 812.5^3}{3 \times 21000 \times 517227158}\left[1 + 0.6(1 + 0.22)\frac{150^2}{812.5^2}\right] = \mathbf{1.93\ mm}$$

Reinforced concrete strengthened using a ferrocement jacket: with two-layers mesh (RFC2) and three-layers mesh (RFC3)

0.33 peak load of RFC2 (0.33×50.9=17.0 kN)

0.33 peak load of RFC3 (0.33×57.7=19.2 kN)

Also, assumed the mesh layer is distributed uniformly. The skeleton of welded mesh is simplified as one-layer. Similarly to FC2 or FC4, the distances of the mesh from the extreme tensile surface are called d_{si} (d_{s1}, d_{s2}, d_{s3},......, d_{s14}, d_{s15})

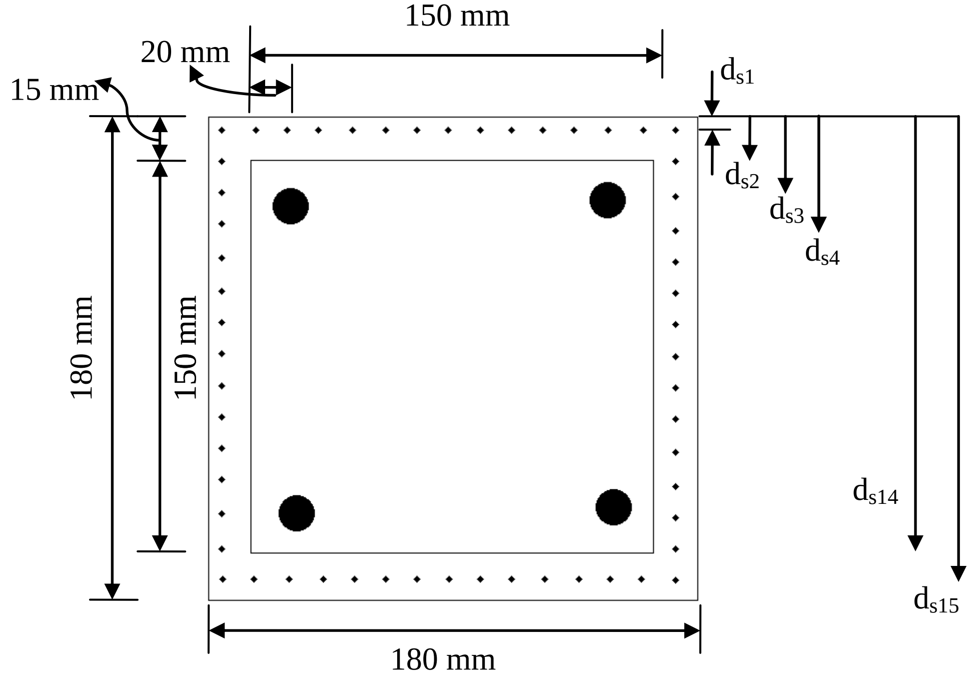

Figure D-12: The cross section for RFC

RFC2		RFC3	
	$n_2 = 17/30.5$		$n_2 = 19.2/30.5$
	$\frac{n_2}{n_A} = \frac{92.5}{92.5 + 720}$		$\frac{n_2}{n_A} = \frac{92.5}{92.5 + 720}$
Then:		Then:	
	n_A =**4.90 mm**		n_A =**5.53 mm**

Young's Modulus of matrix		$E_m = 21000\ N/mm^2$
Young's Modulus of concrete		$E_c = 27000\ N/mm^2$
Young's Modulus of steel bar		$E_s = 195000\ N/mm^2$
Young's Modulus of mesh		$E_{mesh} = 175000\ N/mm^2$
Elastic moduli ratio to matrix	Concrete: m_{m1}=	$\frac{E_c}{E_m} = 1.29$
	Mesh: m_{m2}=	$\frac{E_{mesh}}{E_m} = 8.33$
	Steel bar: m_{m3}=	$\frac{E_s}{E_m} = 9.29$

Cross-section area (mm^2)		RFC2	RFC3
Mesh level	A_{s1} and A_{s15}	96.5	96.5
	A_{s2}, A_{s3}, A_{s4},......A_{s13}, A_{s14}	12.1	16.1

$$I_{RFC2} = I_{matrix} + I_{concrete} + I_{steel\ bar} + I_{mesh} =$$
$$= \left(\frac{180 \times 180^3}{12} - \frac{150 \times 150^3}{12}\right) + 1.29 \times \frac{150 \times 150^3}{12} + 9.29$$
$$\times 226.2 \times (75-20)^2 \times 2 + 8.33$$
$$\times [64.3 \times (90-3.5)^2 \times 2 + 8.04 \times (90-3.5-12.6 \times 1)^2 + 8.04$$
$$\times (90-3.5-12.6 \times 2)^2 + \cdots\cdots + 8.04$$
$$\times (90-3.5-12.6 \times 13)^2] = 122378572\ mm^4$$

$$I_{RFC3} = I_{matrix} + I_{concrete} + I_{steel\ bar} + I_{mesh} =$$
$$= \left(\frac{180 \times 180^3}{12} - \frac{150 \times 150^3}{12}\right) + 1.29 \times \frac{150 \times 150^3}{12} + 9.29$$
$$\times 226.2 \times (75-20)^2 \times 2 + 8.33$$
$$\times [96.5 \times (90-3.5)^2 \times 2 + 12.1 \times (90-3.5-12.6 \times 1)^2 + 12.1$$
$$\times (90-3.5-12.6 \times 2)^2 + \cdots\cdots + 12.1$$
$$\times (90-3.5-12.6 \times 13)^2] = 127353941\ mm^4$$

Then:

$$\Delta_{\text{A for RFC2}} = \frac{17000 \times 812.5^3}{3 \times 21000 \times 122378572}\left[1 + 0.6(1 + 0.22)\frac{180^2}{812.5^2}\right] = \mathbf{1.26\ mm}$$

$$\Delta_{\text{A for RFC3}} = \frac{19200 \times 812.5^3}{3 \times 21000 \times 127353941}\left[1 + 0.6(1 + 0.22)\frac{180^2}{812.5^2}\right] = \mathbf{1.43mm}$$

Comparing the bending-shear effect with Δ_A, shows the results to be quite different. So the author decided to re-calculate with the tensile force of the matrix and concrete ignored.

$$\begin{aligned} I_{RFC2} &= I_{matrix} + I_{concrete} + I_{steel\ bar} + I_{mesh} = \\ &= \left(\frac{180 \times 90^3}{3} - \frac{150 \times 75^3}{3}\right) + 1.29 \times \frac{150 \times 75^3}{3} + 9.29 \times 226.2 \\ &\times (75 - 20)^2 \times 2 + 8.33 \\ &\times [64.3 \times (90 - 3.5)^2 \times 2 + 8.04 \times (90 - 3.5 - 12.6 \times 1)^2 + 8.04 \\ &\times (90 - 3.5 - 12.6 \times 2)^2 + \cdots\cdots + 8.04 \\ &\times (90 - 3.5 - 12.6 \times 13)^2] = 72521384\ \text{mm}^4 \end{aligned}$$

$$\begin{aligned} I_{RFC3} &= I_{matrix} + I_{concrete} + I_{steel\ bar} + I_{mesh} = \\ &= \left(\frac{180 \times 90^3}{3} - \frac{150 \times 75^3}{3}\right) + 1.29 \times \frac{150 \times 75^3}{3} + 9.29 \times 226.2 \\ &\times (75 - 20)^2 \times 2 + 8.33 \\ &\times [96.5 \times (90 - 3.5)^2 \times 2 + 12.1 \times (90 - 3.5 - 12.6 \times 1)^2 + 12.1 \\ &\times (90 - 3.5 - 12.6 \times 2)^2 + \cdots\cdots + 12.1 \\ &\times (90 - 3.5 - 12.6 \times 13)^2] = 77486754\ \text{mm}^4 \end{aligned}$$

Then:

$$\Delta_{\text{A for RFC2}} = \frac{17000 \times 812.5^3}{3 \times 21000 \times 72521384}\left[1 + 0.6(1 + 0.22)\frac{180^2}{812.5^2}\right] = \mathbf{2.1\ mm}$$

$$\Delta_{\text{A for RFC2}} = \frac{19200 \times 812.5^3}{3 \times 21000 \times 77486754}\left[1 + 0.6(1 + 0.22)\frac{180^2}{812.5^2}\right] = \mathbf{2.19\ mm}$$

Appendix E. Test results for all the linpots

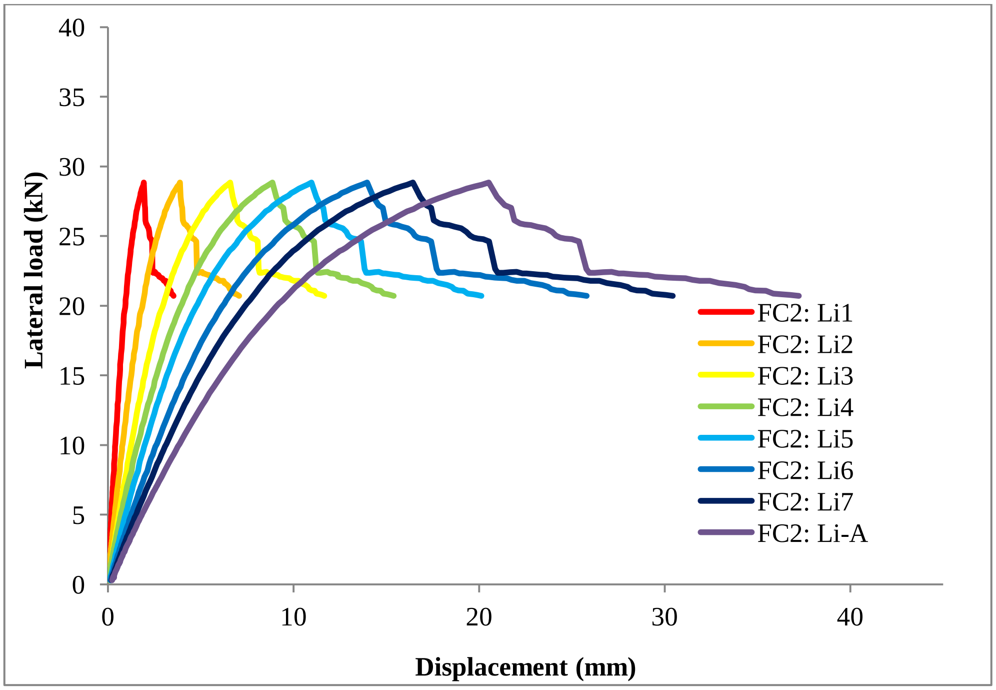

Figure E-13: Load-displacement curves at different positions (FC2)

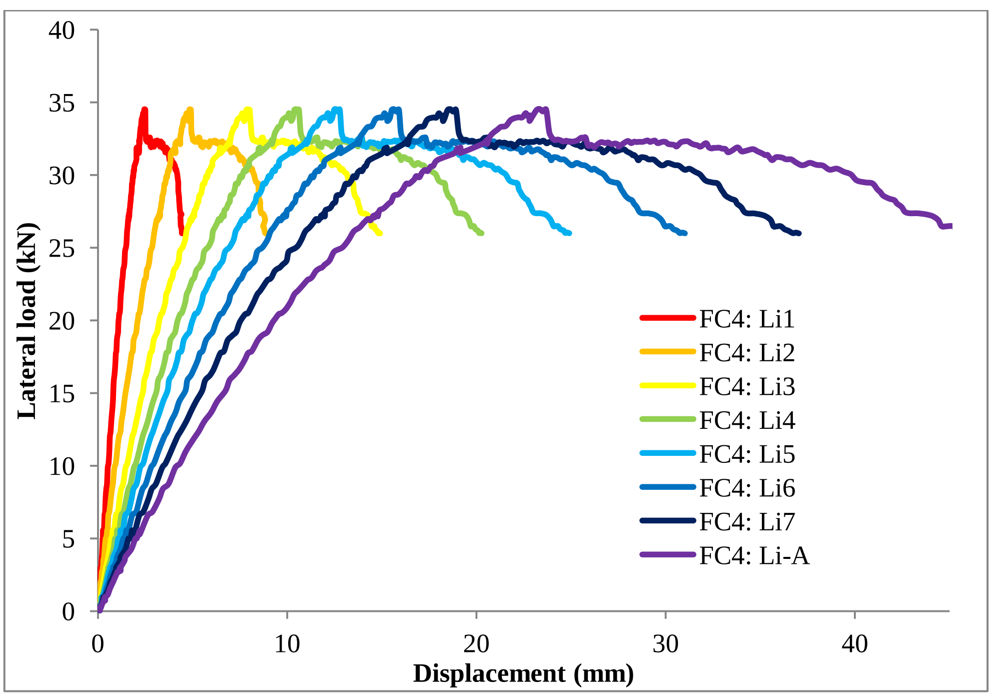

Figure E-14: Load-displacement curves at different positions (FC4)

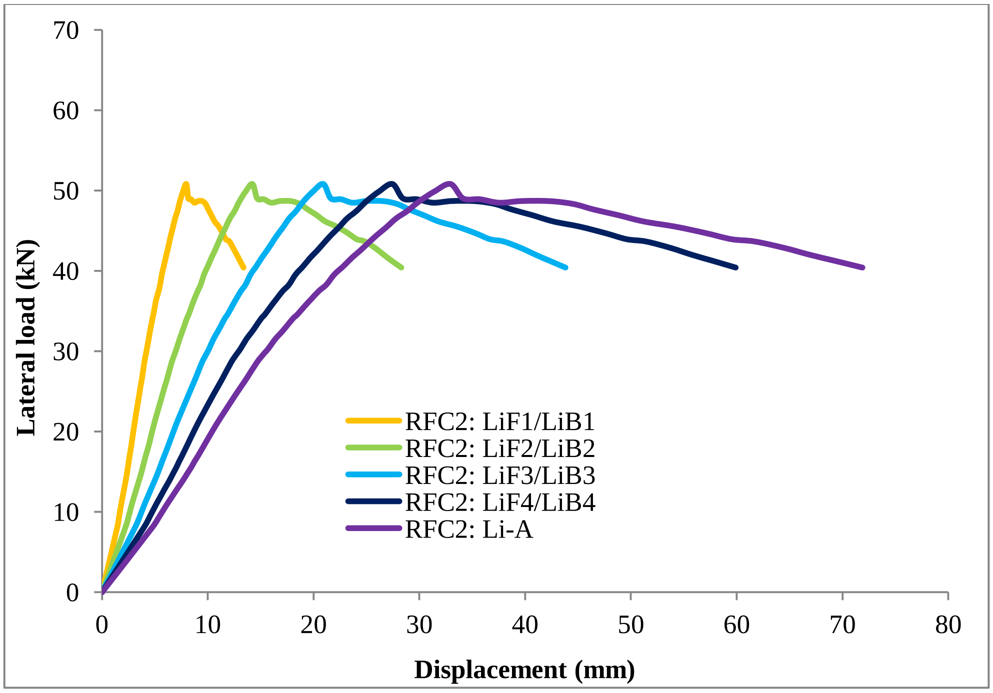

Figure E-15: Load-displacement curves at different positions (RFC2)

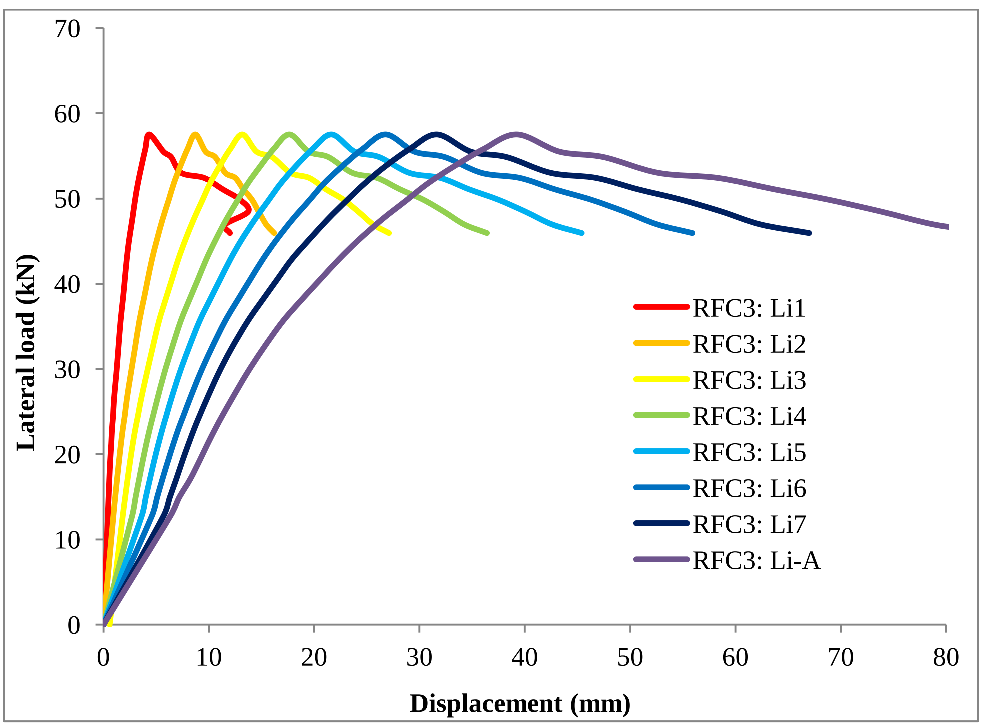

Figure E-16: Load-displacement curves at different positions (RFC3)

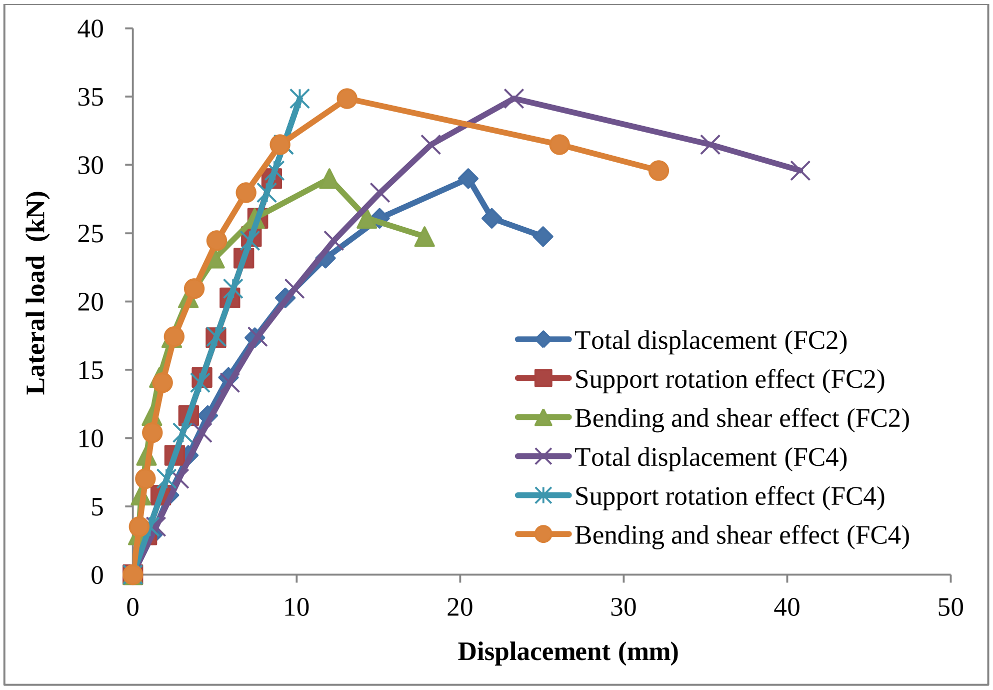

Figure E-17: Load-displacement curves for the support rotation effect and the bending-shear effect at Li-A (FC2 and FC4)

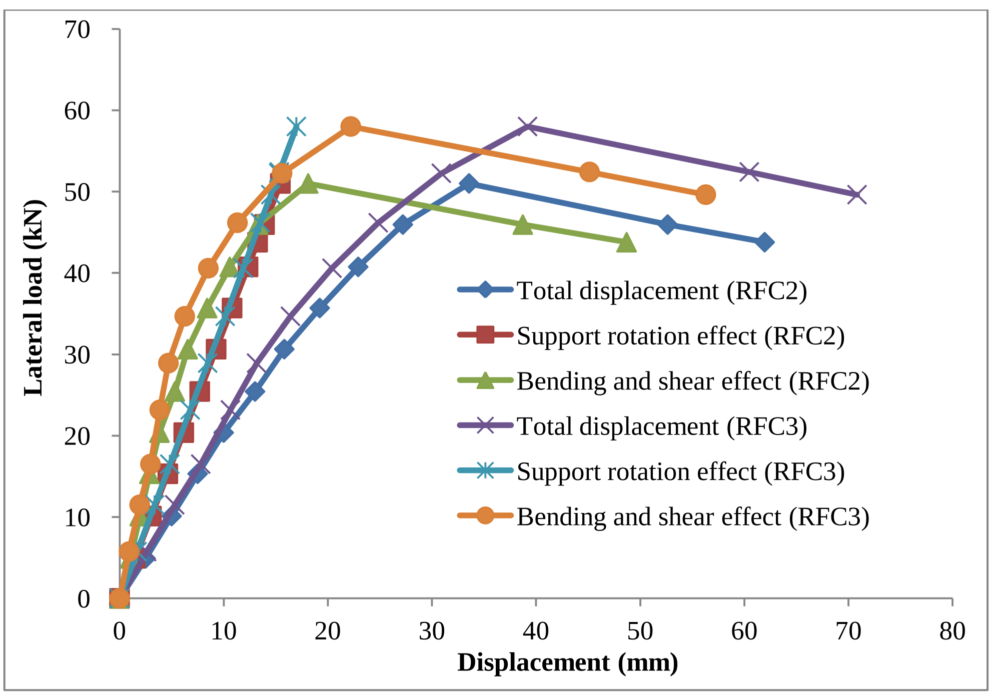

Figure E-18: Load-displacement curves for the support rotation effect and the bending-shear effect at Li-A (RFC2 and RFC3)

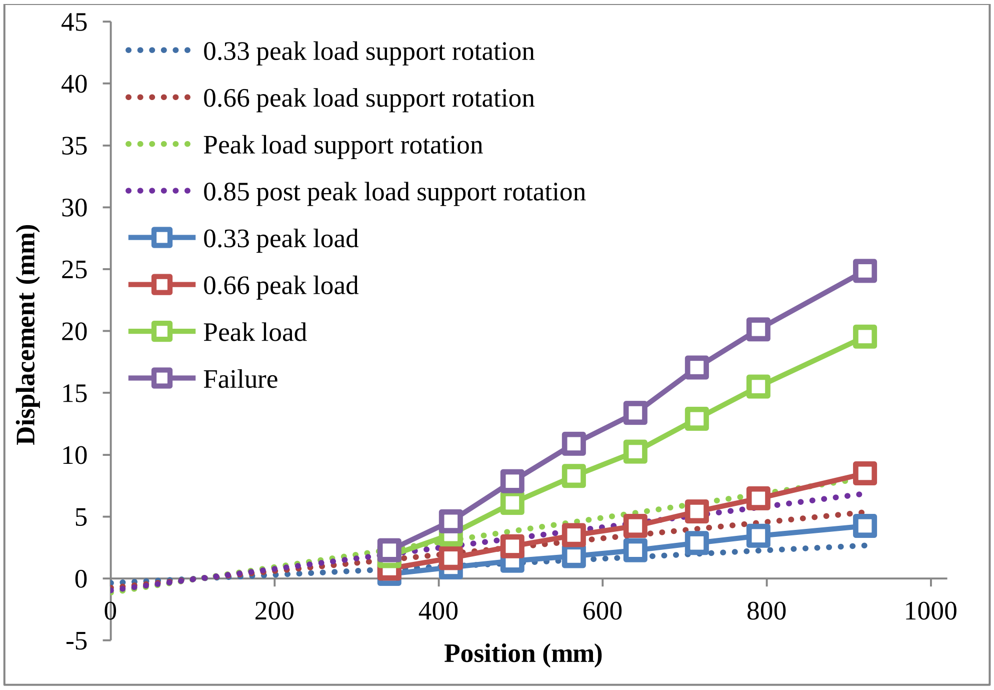

Figure E-19: Displacement for each linpot at different loads (FC2)

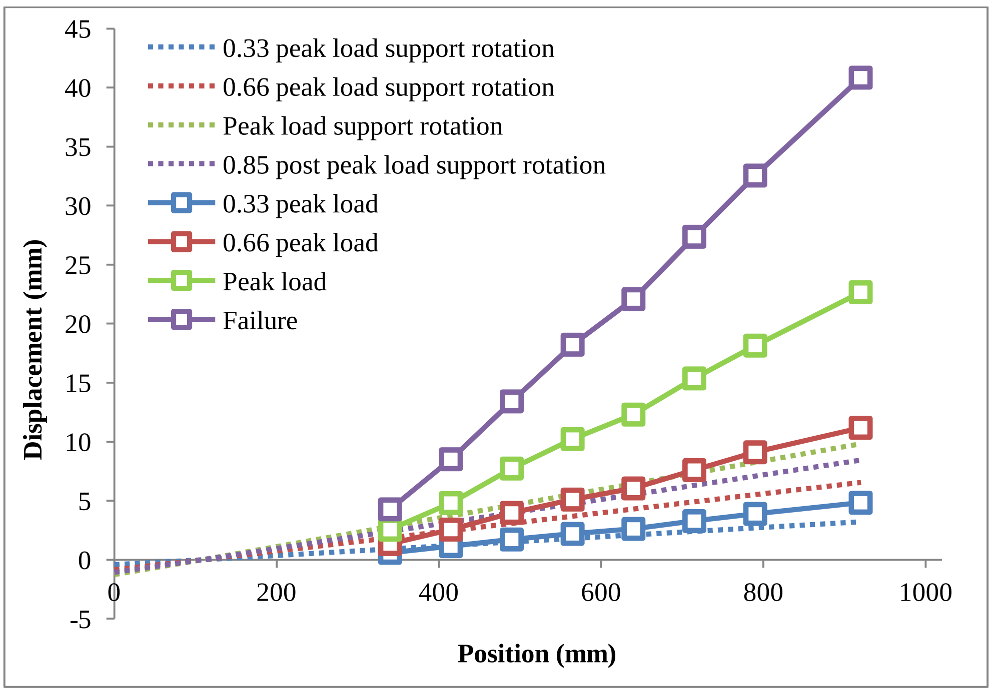

Figure E-20: Displacement for each linpot at different loads (FC4)

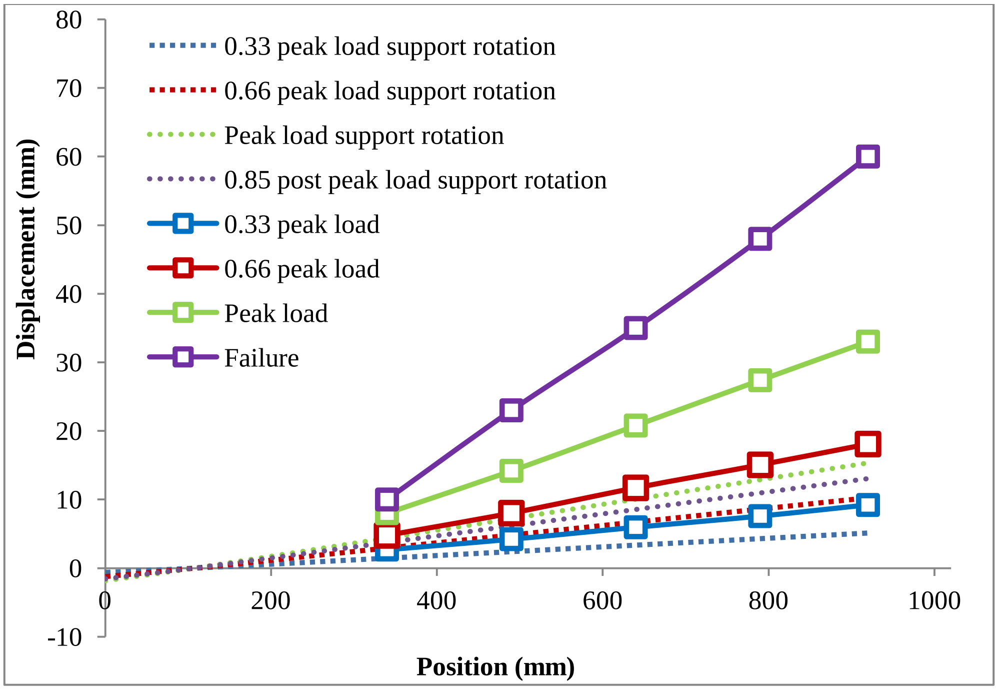

Figure E-21: Displacement for each linpot at different loads (RFC2)

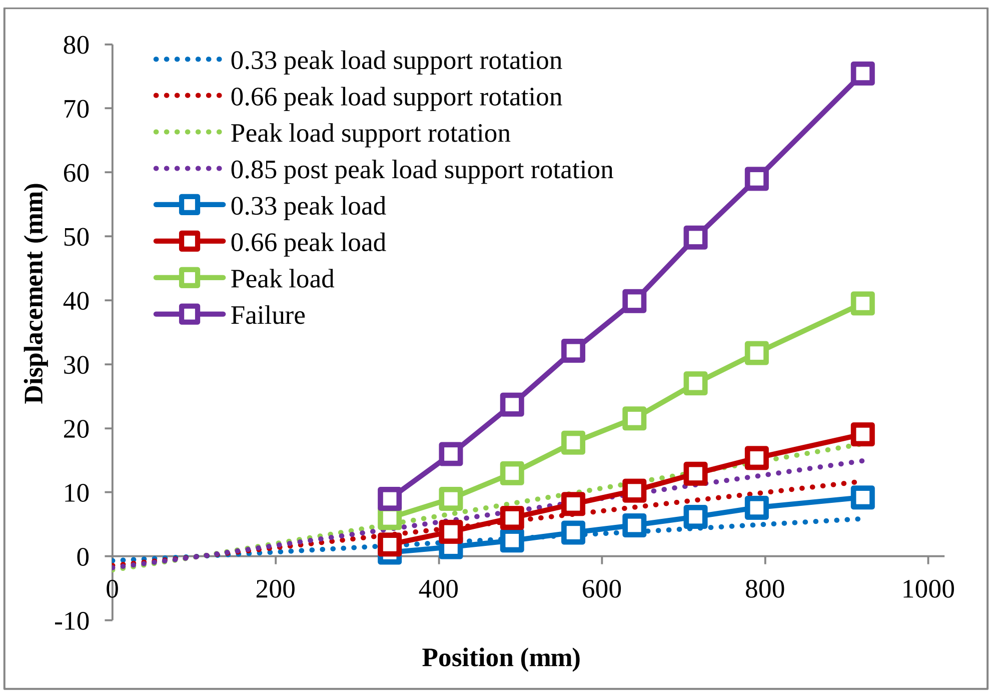

Figure E-22: Displacement for each linpot at different loads (RFC3)

Lateral load and stiffness of RC-C, FC2-C, FC4-C during number of cycles

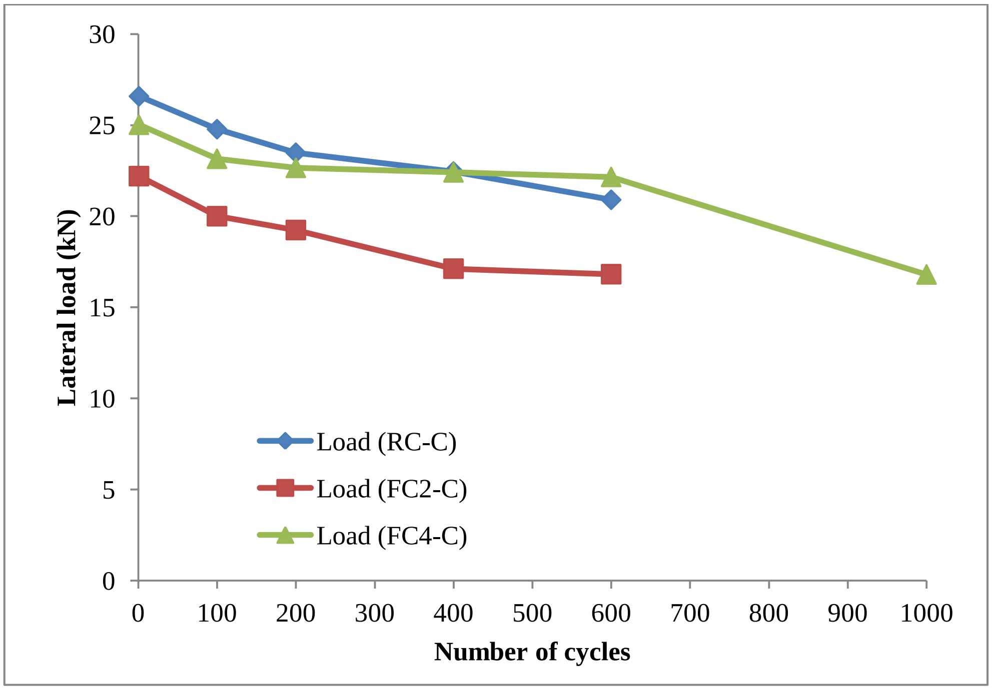

Figure E-23: Lateral load during tests with number of cycles

Table E-1: Result of lateral load and degradation of RC-C, FC2-C and FC4-C during cyclic loading

No. of cycles	**RC-C**		**FC2-C**		**FC4-C**	
	V (kN)	**Degradation (%)**	**V (kN)**	**Degradation (%)**	**V (kN)**	**Degradation (%)**
First	26.6	100%	22.2	100%	25.0	100%
100	24.8	93%	20.0	90%	23.2	93%
200	23.5	88%	19.2	87%	22.7	91%
400	22.5	84%	17.1	77%	22.4	90%
600	20.9	79%	16.8	76%	22.2	89%
1000					16.8	67%

Note: the mark 'V' is lateral load

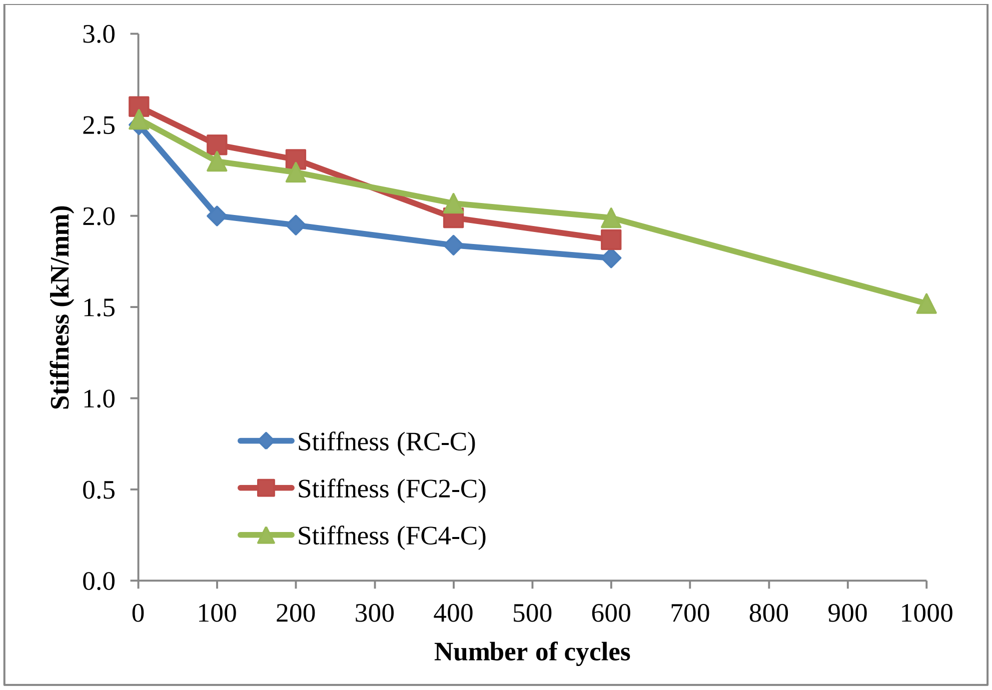

Figure E-24: Stiffness during tests with number of cycles

Table E-2: Result of stiffness and degradation of RC-C, FC2-C and FC4- C during cyclic loading

No. of cycles	**RC-C**		**FC2-C**		**FC4-C**	
	Stiffness (kN/mm)	**Degradation (%)**	**Stiffness (kN/mm)**	**Degradation (%)**	**Stiffness (kN/mm)**	**Degradation (%)**
First	2.50	100%	2.60	100%	2.53	100%
100	2.00	80%	2.39	92%	2.30	91%
200	1.95	78%	2.31	89%	2.24	89%
400	1.84	74%	1.99	77%	2.07	82%
600	1.77	71%	1.87	72%	1.99	79%
1000					1.52	60%

Appendix F. Ductility calculations

Table F-1: Results of the static loading specimens

Specimen	Peak load (kN)	Disp. at peak load (mm)	Ultimate disp. (mm)
RC	35.7	23.9	36.2
FC2	29.0	20.9	25.2
FC4	34.7	23.5	41.0
RFC2	50.8	28.6	62.7
RFC3	57.5	29.5	75.4

Each ductility calculation shows below:

RC:

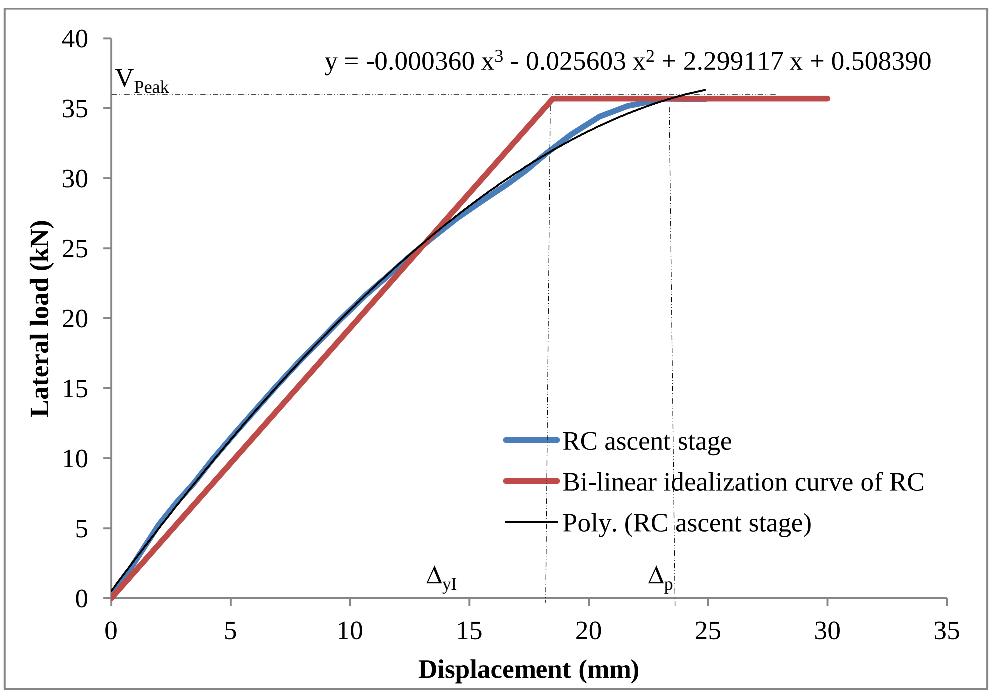

Figure F-25: The bi-linear idealization curve (RC)

So the area of above x-axis equal to the trapezoid:

$$\text{Area} = \int_0^{\Delta_p} (-0.000360\,x^3 - 0.025603\,x^2 + 2.299117\,x$$

$$+ 0.508390\,)\,dx$$

$$= 0.5 \times \Delta_{yI} \times V_{Peak} + \left(\Delta_p - \Delta_{yI}\right) \times V_{Peak}$$

$$= 0.5 \times \Delta_{yI} \times 35.7 + (23.9 - \Delta_{yI}) \times 35.7$$

Put the values in the equation, then: Δ_{yI} =18.6 mm.

The ductility value will be:

$$\mu_\Delta = \Delta_u/\Delta_{yI} = 36.2/18.6 = 1.95$$

FC4: (the FC2 is shown in §4.8)

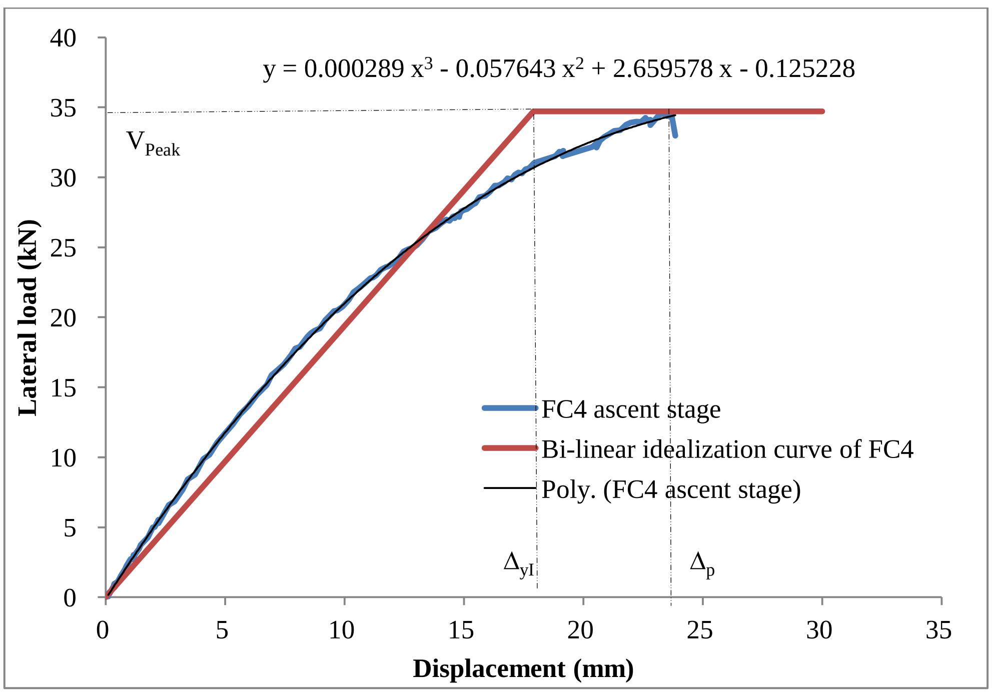

Figure F-26: The bi-linear idealization curve (FC4)

So the area of above the x-axis is equal to the trapezoid:

$$\text{Area} = \int_0^{\Delta_p} (0.000289\, x^3 - 0.057643\, x^2 + 2.659578\, x - 0.125228 + 0.508390)\, dx$$

$$= 0.5 \times \Delta_{yI} \times V_{Peak} + (\Delta_p - \Delta_{yI}) \times V_{Peak}$$

$$= 0.5 \times \Delta_{yI} \times 34.7 + (23.5 - \Delta_{yI}) \times 34.7$$

Put the values in the equation, then: Δ_{yI} =17.9 mm.

The ductility value will be:

$$\mu_\Delta = \Delta_u / \Delta_{yI} = 41/17.9 = 2.29$$

RFC2:

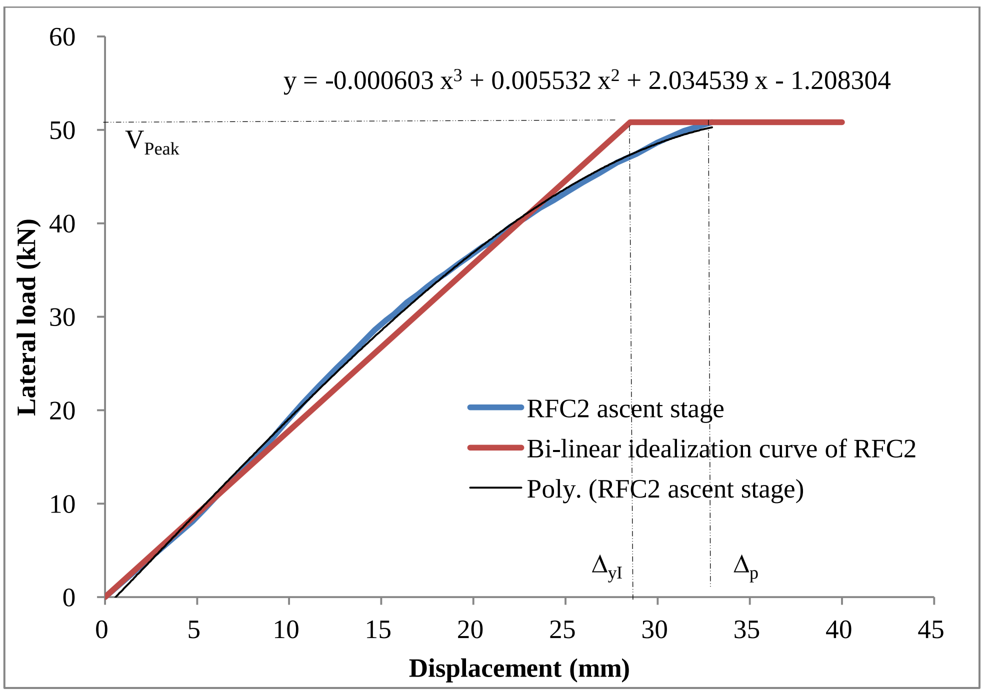

Figure F-27: The bi-linear idealization curve (RFC2)

So the area of above the x-axis is equal to the trapezoid:

$$\text{Area} = \int_0^{\Delta_p} (-0.000603\, x^3 + 0.005532\, x^2 + 2.034539\, x - 1.208304\ ) \, dx$$

$$= 0.5 \times \Delta_{yI} \times V_{Peak} + \left(\Delta_p - \Delta_{yI}\right) \times V_{Peak}$$

$$= 0.5 \times \Delta_{yI} \times 50.8 + (33.6 - \Delta_{yI}) \times 50.8$$

Put the values in the equation, then: Δ_{yI} =28.6 mm.

The ductility value will be:

$$\mu_\Delta = \Delta_u / \Delta_{yI} = 62.7/28.6 = 2.16$$

RFC3:

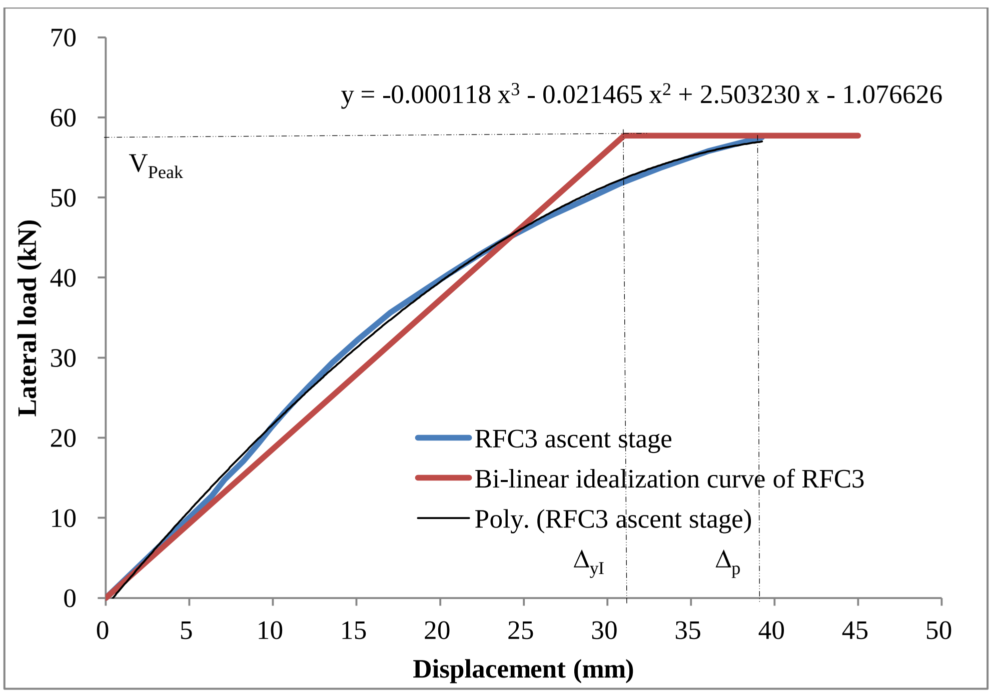

Figure F-28: The bi-linear idealization curve (RFC3)

So the area of above the x-axis is equal to the trapezoid:

$$\text{Area} = \int_0^{\Delta_p} (-0.000118\,x^3 - 0.021465\,x^2 + 2.503230\,x - 1.076626)\,dx$$
$$= 0.5 \times \Delta_{yI} \times V_{Peak} + (\Delta_p - \Delta_{yI}) \times V_{Peak}$$
$$= 0.5 \times \Delta_{yI} \times 57.7 + (39.2 - \Delta_{yI}) \times 57.7$$

Put the values in the equation, then: Δ_{yI} =31.1 mm.

The ductility value will be:

$$\mu_\Delta = \Delta_u/\Delta_{yI} = 70.8/31.1 = 2.28$$

Appendix G. Full details of the changing parameters

Table G-1: Details of the FEM parameters for RC

RC	Axial load (kN)	Concrete property (MPa)	Steel bar property (MPa)	Total area of steel bars (mm^2)	Number of steel bar	Stirrup property (MPa)	Cross-section area of stirrup (mm^2)
Axial load (kN)	0	38	480	452	4	600	7.07
	100	38	480	452	4	600	7.07
	200	38	480	452	4	600	7.07
	300	38	480	452	4	600	7.07
	400	38	480	452	4	600	7.07
	500	38	480	452	4	600	7.07
	600	38	480	452	4	600	7.07
	800	38	480	452	4	600	7.07
Concrete property	200	30	480	452	4	600	7.07
	200	40	480	452	4	600	7.07
	200	50	480	452	4	600	7.07
Steel bar property	200	38	275	452	4	600	7.07
	200	38	355	452	4	600	7.07
	200	38	525	452	4	600	7.07
Total area of steel bars (mm^2)	200	38	480	679	4	600	7.07
	200	38	480	905	4	600	7.07
Number of steel bar	200	38	480	905	8	600	7.07
Size of stirrups	200	38	480	452	4	275	7.07
	200	38	480	452	4	355	7.07
	200	38	480	452	4	525	7.07
Cross-section area of stirrup (mm)	200	38	480	452	4	600	14.1
	200	38	480	452	4	600	28.3

Table G-2: Details of the FEM parameters for FC

FC	End condition	Axial load (kN)	Length of column (mm)	Matrix property (MPa)	Mesh property (MPa)	Cross-section area (mm^2)	Number of layers mesh
End condition	Semi-rigid	200	1020	62	380	2	4
	Rigid	200	1020	62	380	2	4
Axial load (kN)	Rigid	0	1020	62	380	2	2
	Rigid	100	1020	62	380	2	4
	Rigid	200	1020	62	380	2	4
	Rigid	400	1020	62	380	2	4
	Rigid	600	1020	62	380	2	4
	Rigid	800	1020	62	380	2	4
	Rigid	1000	1020	62	380	2	4
Axial load (kN)	Rigid	0	1020	62	380	2	2
	Rigid	100	1020	62	380	2	2
	Rigid	200	1020	62	380	2	2
	Rigid	400	1020	62	380	2	2
	Rigid	600	1020	62	380	2	2
	Rigid	800	1020	62	380	2	2
	Rigid	1000	1020	62	380	2	2
Length of column (mm)	Rigid	200	1275	62	380	2	4
	Rigid	200	1530	62	380	2	4
Matrix property (MPa)	Rigid	200	1020	40	380	2	4
	Rigid	200	1020	50	380	2	4
	Rigid	200	1020	60	380	2	4
Mesh property (MPa)	Rigid	200	1020	62	275	2	4
	Rigid	200	1020	62	355	2	4
	Rigid	200	1020	62	525	2	4
Cross-section area (mm^2)	Rigid	200	1020	62	380	1	4
	Rigid	200	1020	62	380	4	4
Number of layers mesh	Rigid	200	1020	62	380	2	1
	Rigid	200	1020	62	380	2	2
	Rigid	200	1020	62	380	2	3
	Rigid	200	1020	62	380	2	5

Table G-3: Details of the FEM parameters for RFC

RFC	Axial load (kN)	Matrix property (MPa)	Mesh Strength (MPa)	Cross-section area (mm^2)	Number of layers mesh
Matrix property (MPa)	200	40	380	2	2
	200	50	380	2	2
	200	60	380	2	2
	200	62	380	2	2
Mesh Strength (MPa)	200	62	275	2	2
	200	62	355	2	2
	200	62	525	2	2
Cross-section area (mm^2)	200	62	380	1	2
	200	62	380	4	2
Number of layers mesh	200	62	380	2	1
	200	62	380	2	3
	200	62	380	2	4

Appendix H. FC2 and FC4 at different axial loads

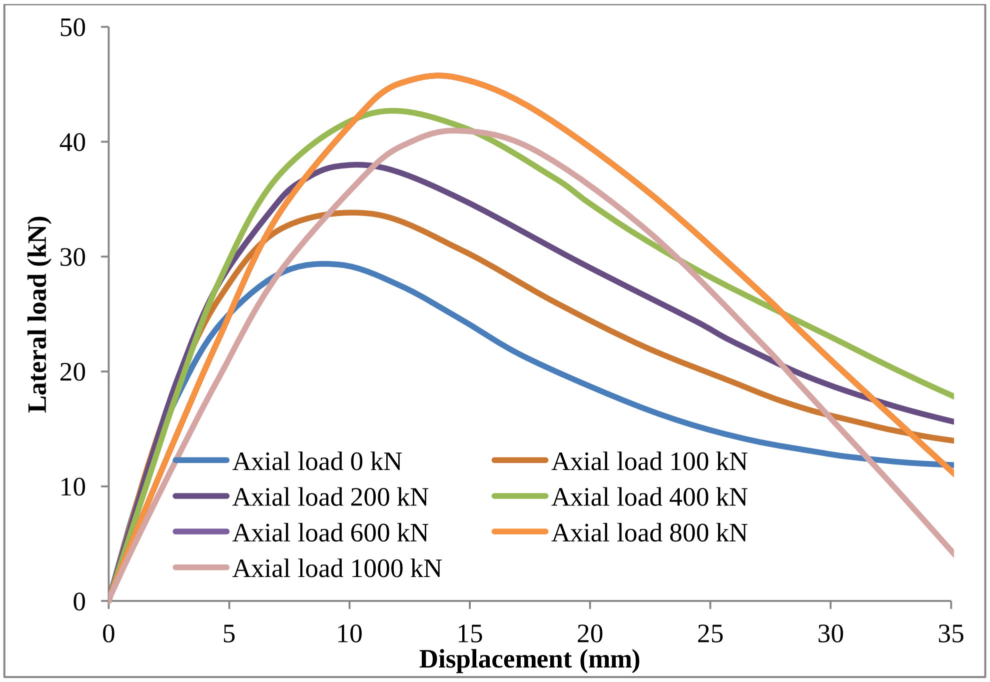

Figure H-29: Load-deflection curves for different axial loads (FC2)

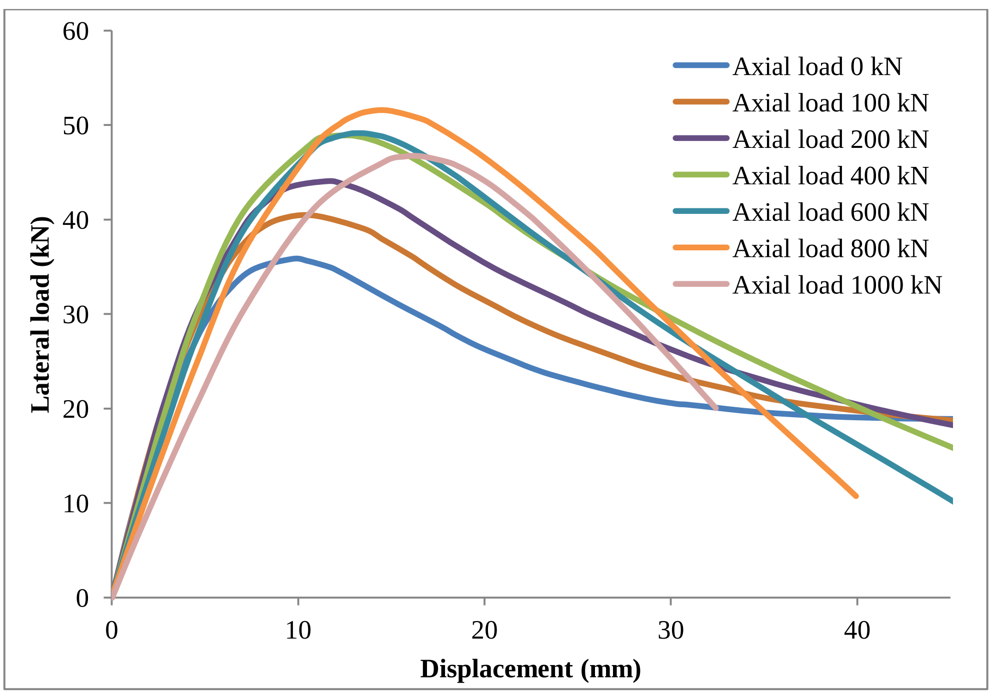

Figure H-30: Load-deflection curves for different axial loads (FC4)

Appendix I. Effective rotational stiffness for support condition

The support condition of experimental test was semi-rigid, the value of effective rotational stiffness calculated by Eq I-1.

$$k_\theta = \frac{M}{\theta} \qquad \text{Eq I-1}$$

Where:

k_θ	Rotation stiffness
M	Moment
θ	Rotation in radian

Then

$$M = V \times L = 34000 \times 812.5 = 27.6 \times 10^6 \text{ Nmm}$$

$$\theta = \frac{n_1 + n_2}{200} = \frac{1.43 + 1.23}{200} = 0.0133$$

The value of n_1 and n_2 are calculated in §4.3

$$k_\theta = (27.6 \times 10^6 / 0.0133) \text{ Nmm/rad} = 2075 \text{ kNm/rad}$$